



TECHNISCHE
UNIVERSITÄT
DRESDEN

Fakultät Physik

Yuliia V. Tymoshenko

NEUTRON SPECTROSCOPY ON BOND-FRUSTRATED HELIMAGNETS

DISSERTATION ZUR ERLANGUNG DES AKADEMISCHEN GRADES
DES DOKTORS DER NATURWISSENSCHAFTEN

Neutron spectroscopy on bond-frustrated helimagnets

Dissertation
zur Erlangung des
akademischen Grades des Doktors der Naturwissenschaften
(Doctor rerum naturalium)

vorgelegt von
Yuliia V. Tymoshenko
geboren am 12. August 1987 in Zaporozhye

Institut für Festkörper- und Materialphysik, TU Dresden
D-01062 Dresden, Deutschland.

Eingereicht am ____ . ____ . 21

Berichterstatter

1. Gutachter: **Prof. Dr. Dmytro S. Inosov**

Institut für Festkörper- und Materialphysik
TU Dresden
D-01062 Dresden

2. Gutachter: **Prof. Joshua Cohn**

Department of Physics
University of Miami
Coral Gables, Florida 33124

Verteidigt am ____ . ____ . 21

To my parents, who gave me the opportunity and strength to wonder

Contents

Introduction	xi
1 Introduction to helimagnetism	1
1.1 New type of magnetic ordering	1
1.2 Symmetric and chiral helimagnets	3
1.3 Helical spin ordering in symmetric helimagnets	5
1.4 Spin waves	7
1.4.1 Spin deviations	7
1.4.2 Linear spin-wave theory	8
1.4.3 Spin waves in ferromagnets and antiferromagnets	9
1.4.4 Spin waves in helimagnets	12
1.4.5 Interactions between spin waves	17
2 Neutron scattering	19
2.1 Introduction	19
2.1.1 Basic properties of thermal neutrons	19
2.1.2 Neutron production	21
2.1.3 Thermal neutron detection	25
2.2 Theory of neutron scattering	29
2.2.1 Scattering cross sections	29
2.2.2 Nuclear scattering	31
2.2.3 Magnetic scattering	37
2.3 Instruments for neutron experiments	41
2.3.1 Kinematics of a scattering experiment	41
2.3.2 The triple-axis spectrometer	43
2.3.3 Time-of-flight spectrometer	47

3	ZnCr₂Se₄	51
3.1	Introduction	51
3.1.1	Chromium spinels	51
3.1.2	Classical phase diagram for chromium spinels	53
3.1.3	Crystal structure and spin-spiral order in ZnCr ₂ Se ₄	56
3.2	SANS measurements	59
3.2.1	Experimental method	59
3.2.2	Results	60
3.2.3	Discussion	63
3.2.4	Summary	65
3.3	Pseudo-Goldstone magnons	65
3.3.1	Instrumental conditions for the experiments	65
3.3.2	ZnCr ₂ Se ₄ magnon spectrum in multi-domain state	67
3.3.3	ZnCr ₂ Se ₄ magnon spectrum in the single-domain state	72
3.3.4	Spin gap of the pseudo-Goldstone magnons	74
3.3.5	Magnon-magnon interactions	76
3.3.6	Summary	78
3.4	Magnetic field evolution of the helimagnon spectrum	79
3.4.1	Instrumental conditions for the experiments	79
3.4.2	TOF measurements	79
3.4.3	TAS measurements	83
3.4.4	Summary	85
3.5	Anisotropy of macroscopic properties	85
3.5.1	Macroscopic properties and magnetism	85
3.5.2	Ultrasound measurements	86
3.5.3	Dilatometric properties	88
3.5.4	Slow relaxation of helimagnetic domains	90
3.5.5	Thermal properties	92
4	Sr₃Fe₂O₇	97
4.1	Introduction	97
4.2	Crystal and magnetic structure of Sr ₃ Fe ₂ O ₇	98
4.3	Inelastic neutron-scattering investigation	99
4.4	Summary	104

5	Iron monophosphide (FeP)	107
5.1	Introduction	107
5.1.1	Phosphides of transition metals	107
5.1.2	FeP magnetic structure	108
5.2	Neutron scattering experiments	109
5.2.1	FeP single crystals	109
5.2.2	FeP reciprocal space overview	112
5.2.3	Neutron diffraction	112
5.2.4	Inelastic neutron scattering	114
5.3	Localised spin approach to magnon spectrum in FeP	120
5.3.1	Motivation	120
5.3.2	Model	122
5.3.3	Classical phase diagram	123
5.3.4	Application to FeP	125
5.3.5	Effect of J_6	126
5.3.6	Dynamics	127
5.3.7	INS spectra of FeP	128
5.4	Summary	132
	Publication List	135
	Bibliography	136
	Acknowledgements	145
	Versicherung	147

Introduction

Screw structures are common in nature. They can be found everywhere, from galactic to microscopic scales. Notable examples are the Double Helix Nebula [1], seashells, horns, flowers, light-harvesting complexes of green plants, DNA molecules, and many others. Therefore, it is natural that we find helical order also on the atomic scale, most prominently as spin arrangement in magnetic materials.

Nowadays it seems incredible, but before the end of the 1950s, it was thought that the magnetic moments in solids can be ordered only in the simple collinear structures — ferromagnetic and antiferromagnetic. However, neutron scattering experiments have shown that MnO_2 has a different type of spin arrangement unseen before — a helical spin structure. This prompted scientists to search for similar spin structures in a wide variety of materials, including both insulators and conductors. It became obvious that a helix is the most fundamental spin structure that includes, as limiting cases, the ferromagnetic and antiferromagnetic states.

Helimagnetic spin order may arise from the frustration among various superexchange interactions. A simple collinear order cannot always satisfy all exchanges in the system, which leads to the formation of a noncollinear long-periodic structure as a kind of energy-minimizing compromise. Exchange interactions can be divided into symmetric and chiral, arising in systems characterized by the absence of an inversion center. The former is the topic to be dealt with in the present thesis.

Often, microscopic theories describing inherently quantum exchange interactions in real systems are extremely complex. Neutron spectroscopy, allowing the direct study of magnetic excitations in a system, is an indispensable tool for testing such models, thereby stimulating their further development.

The results obtained during the work on this thesis are likely universal for a broad class of symmetric helimagnets, opening up a new way of studying weak magnon-magnon interactions experimentally with accessible spectroscopic methods. At the same time, here we demonstrate that the pseudo-Goldstone magnon gap in helimagnets, first measured in

our work, can leave measurable signatures in the low-temperature macroscopic properties of the material, such as thermal transport and specific heat.

We also performed careful measurements of the metallic helimagnet FeP whose spin structure is described by an exotic “double-helix”. The results of our measurements should stimulate theoretical work on the construction of a model describing the complex magnetic dynamics in this system, which is probably a combination of the localized and itinerant magnetic effects.

Layout of the thesis

Chapter 1 starts from the general introduction into the basics of helimagnetism. The main things are discussed, such as the types of helimagnetic order, the nature and fundamental differences between symmetric and chiral helimagnets. After a brief introduction to the theory of spin waves, a derivation of the dispersion of spin waves in symmetric helimagnet is given in the framework of the linear approximation.

Chapter 2 deals with basic aspects of neutron scattering. Here the theoretical ideas and important formulas needed to understand the neutron scattering method and, in particular, neutron spectroscopy are considered. It also gives a brief insight into the production and detection of neutrons. Particular attention is paid to the main neutron instruments used in the work on this thesis, such as triple-axis and time-of-flight spectrometers.

Chapter 3 contains an exhaustive description of our current results on the central project of this thesis – the bond-frustrated helimagnet ZnCr_2Se_4 . We investigated the full spin-wave spectrum of the material in the entire reciprocal space by means of inelastic neutron scattering and estimated the exchange interactions with an accuracy up to the fourth-nearest neighbors. It is shown that the pseudo-Goldstone modes, first measured in our work, have an energy gap, the theoretical description of which requires taking into account physics beyond the linear spin-wave approximation. Thus, they serve as a tempting way to study magnon-magnon interactions using available spectroscopic techniques. Using triple-axis and time-of-flight spectrometers, a systematic study of the magnetic field dependence of the low-temperature magnon spectrum of ZnCr_2Se_4 was carried out. The nonmonotonic character of this dependence was revealed in the vicinity of the recently proposed quantum critical point. A theoretical explanation of the obtained field dependence is a challenge for theorists working in the field of spin waves. Finally, the contribution of the magnetic structure and dynamics to the low-temperature macroscopic parameters of the material is discussed. The data obtained in this research should be applied not only to simple helimagnets but also to a much wider class of materials in which the magnetic propagation vector is spontaneously

chosen from the set of structurally equivalent alternatives at the transition to a magnetically ordered state.

However, the complex unit cell of the pyrochlore sublattice formed by the $S = 3/2$ magnetic Cr^{3+} ions in the spinel structure leads to multiple spin-wave modes that complicate the theoretical calculations. It is therefore important to repeat the experiment on a helimagnetic compound with a simpler structure. In *Chapter 4*, after introducing the sample properties, we present the results of mapping low-energy dispersion in the layered iron oxide $\text{Sr}_3\text{Fe}_2\text{O}_7$. The $S = 5/2$ magnetic moments of $\text{Sr}_3\text{Fe}_2\text{O}_7$ can be regarded as classical, and therefore one can expect well-developed soft modes with a small spin gap. The structure of $\text{Sr}_3\text{Fe}_2\text{O}_7$ is simple tetragonal, with only one magnetic ion per unit cell, which simplifies spin-dynamic calculations, in contrast to the pyrochlore sublattice of ZnCr_2Se_4 . The data presented in the chapter, measured in only a partially domain-selected state, do not allow us to unambiguously judge the presence of pseudo-Goldstone modes in the system but serve as a solid foundation for further measurements.

Chapter 5, after a brief review of current knowledge of iron monophosphide, presents the detailed neutron scattering investigation of its low-energy magnon spectrum. The material is interesting for its exotic “double-helix” spin structure. A simple model is proposed to simulate the spin structure and magnetic excitations in FeP within the local spin approximation. The proposed model reproduces quite well the main details of the experimental spectrum; nevertheless, there are some differences, which may indicate the insufficiency of the localized spin approximation for a detailed description of the system and the possible need to take into account the influence of itinerant magnetic effects.

Chapter 1

Introduction to helimagnetism

1.1 New type of magnetic ordering

Until the middle of the last century, it was assumed that there are only two types of magnetic order in solids — ferromagnetic and antiferromagnetic. This statement was based on the available neutron diffraction data. In all compounds known at that time, the magnetic unit cell either coincided with the crystalline one (ferromagnets) or was a multiple of 2, 4, 8, and so on (antiferromagnets). However, in 1958, at the International Congress on Magnetism in Grenoble, France, Nagamiya gave a talk in which he predicted a helicoidal magnetic order in MnO_2 [2]. This prediction was confirmed by recent puzzling neutron diffraction data that Erickson discussed with Yoshimori during a private communication [3]. He discovered that the magnetic Bragg peaks are located not at the symmetrical points of the Brillouin zone but at the incommensurate positions near the structural peak. This indicates that the studied compound has a long-period magnetic structure, with a period not related to the period of the crystal lattice. The theory developed by Yoshimori [3] provided an interpretation of the MnO_2 data. It turned out that the diffraction data can be successfully described by a screw-type structure with a pitch of $7c/2$. Yoshimori found that the spins located in one ab plane of this crystal point in the same direction, perpendicular to the c axis. When moving from one plane to the next, this direction changes by an angle of $129^\circ (= 5\pi/7)$. Following Yoshimori, this type of spiral rotation is called the proper screw structure Fig. 1.1 (a).

The existence of a helicoidal structure becomes obvious if we assume the existence of anisotropic exchange interactions between the atomic spin moments of the nearest and further neighbors. If we now assume that the exchanges between the nearest and the next-nearest neighbors along a certain direction in the crystal have opposite signs, then the helicoidal ground state is naturally obtained by minimizing the energy. Soon after the

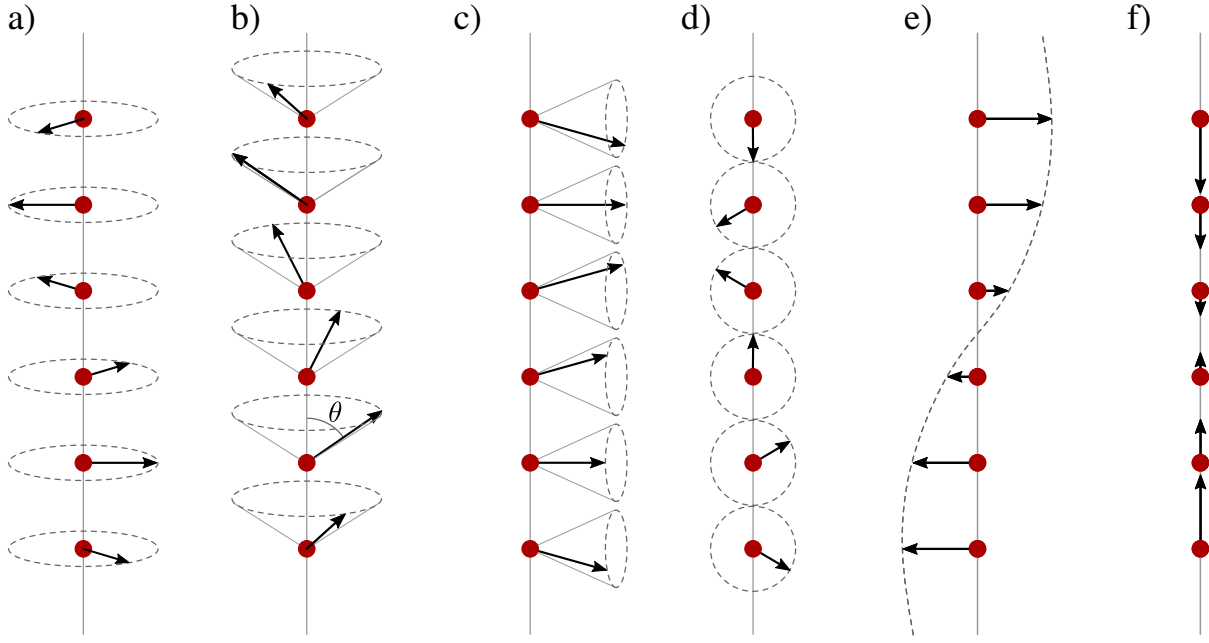


Figure 1.1: Basic types of modulated spin structures. (a) Proper screw, (b) conical screw, (c) transverse conical, (d) cycloidal, (e, f) transverse and longitudinal spin density wave.

discovery of a new helicoidal type of ordering in MnO_2 , neutron diffraction experiments revealed many compounds with magnetic peaks at incommensurate positions of reciprocal space. Shortly after the publication of Yoshimori, Kaplan's paper [4] appeared with a simple interpretation of the neutron diffraction lines of chromium. It is worth noting here that Shibatani [5] soon developed Overhauser's [6] idea and defined the sinusoidal spin structure in chromium as a spin density wave. Around the same time, Villain [7] predicted the possibility of realizing helicoidal order using the molecular field approach.

Despite the fact that scientists have been studying helimagnetic structures for more than seventy years, interest in them continues to this day. In recent years, interest in noncollinear magnetic structures has increased markedly due to advances in the physics of multiferroics [8].

Helicoidal structures belong to a wider class of so-called modulated magnetic structures. These structures can be represented as long-period modulation of simple magnetic structures — ferromagnetic and antiferromagnetic. Some of the basic long-period modulated structures are shown schematically in Fig. 1.1. The arrows indicate the directions of the spin moments of the atoms lying on the ferromagnetic planes perpendicular to the direction of modulation. In all the above structures, the phase difference for two adjacent planes is always constant [9]. Each long-period structure is characterized by a wave vector \mathbf{K} , which is responsible for the translational properties of the system. The translation vector of the

modulated structure can be represented as

$$\mathbf{K} = \mathbf{K}_0 - \mathbf{k}, \quad (1.1)$$

where \mathbf{K}_0 is the reciprocal lattice vector, and \mathbf{k} is the modulation vector. If we apply all the operations of the crystal symmetry group to the vector \mathbf{K} , then we get a star of the wave vector [9]. Considering that all the wave vectors of the star are equivalent, the magnetic moment of the atom in the n -th cell of the crystal can be represented as

$$\mathbf{M}_n = \sum_L e^{i\mathbf{K}_L \mathbf{t}_n} \mathbf{M}_L, \quad (1.2)$$

where the summation is over all rays of the star \mathbf{K}_L and \mathbf{t}_n is the vector of translation into the n -th cell.

Despite the fact that several pairs of magnetic satellites are often observed in neutron diffraction experiments, in most cases, this means that several types of magnetic domains are present in the sample. Each of these domains is modulated in only one direction and is characterized by a pair of vectors \mathbf{K} and $-\mathbf{K}$. Exceptions are some rather exotic structures in which the existence of a multi- k structure is assumed. All modulated structures shown in Fig. 1.1 are single- k and are described by a special case of expression (1.2):

$$\mathbf{M}_n = \mathbf{M}_1 e^{i\mathbf{k} \mathbf{t}_n} + \mathbf{M}_1^* e^{-i\mathbf{k} \mathbf{t}_n}, \quad (1.3)$$

where the magnetic moment of the atom in the first unit cell \mathbf{M}_1 in general is a complex number. The exact form of it determines the type of the modulated structure.

1.2 Symmetric and chiral helimagnets

There are several microscopic mechanisms responsible for the modulation of magnetic structures. In the following, we will confine ourselves to a discussion of helimagnets, which are the main content of this work, but many concepts are also applicable in the case of systems with spin density wave order.

All helimagnets can be divided into two classes – symmetric and chiral, depending on the modulation mechanism. The first class includes systems in which the helimagnetic order of the spins is due to a competition between symmetric exchange interactions and is realized in crystals with an inversion center. For insulators and semiconductors, this is most often a result of frustration among different isotropic superexchange interactions between localized spins. In the case of systems with both localized spins and itinerant electrons (for example, rare-earth metals), these are Ruderman-Kittel-Kasuya-Yosida (RKKY) interactions

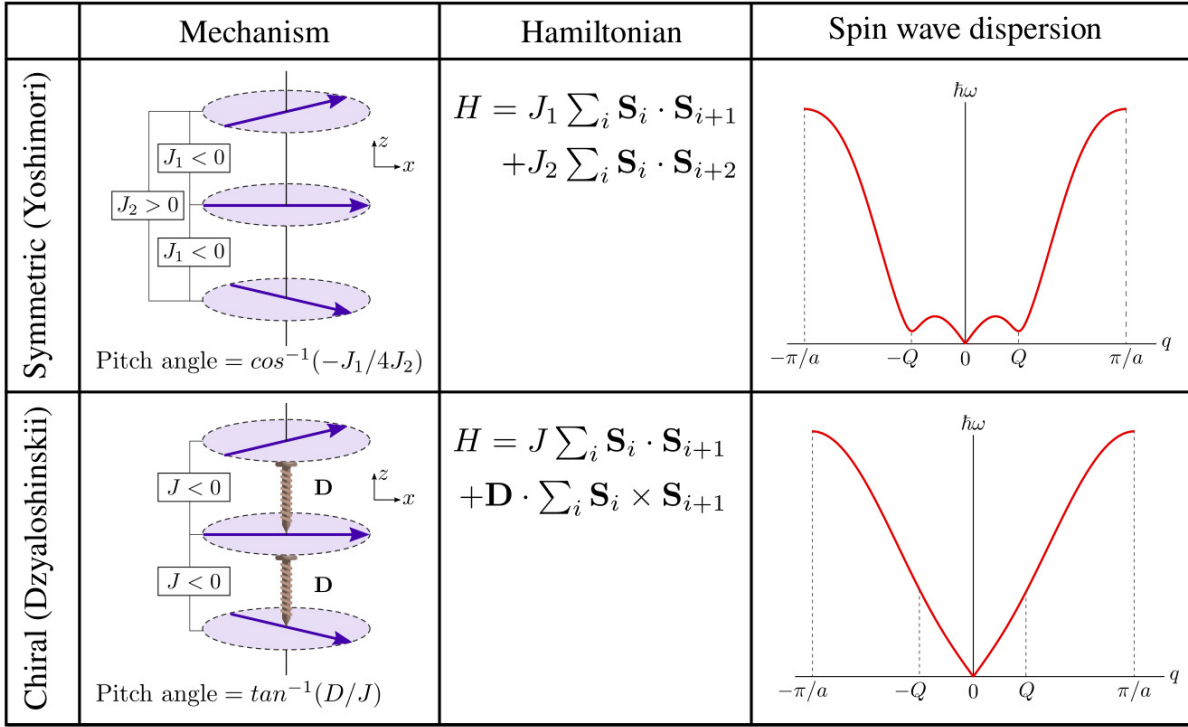


Figure 1.2: Comparison of symmetric and chiral helimagnets.

due to the interaction of magnetic moments mediated by conduction electrons. Symmetric helimagnets are often called Yoshimori-type, after Akio Yoshimori who was the first to give a comprehensive theoretical description [3]. The mechanism leading to the formation of a helicoidal order as a result of the competition of symmetric exchanges between the nearest and the next nearest neighbors in a centrosymmetric system of spins is schematically shown in Fig. 1.2. Ferromagnetic exchange $J_1 < 0$ between nearest neighbors favors the co-aligned ordering of spins, while antiferromagnetic $J_2 > 0$ exchange between the next nearest neighbors tends to order the spins antiparallel. By minimizing the Hamiltonian of the system, we find that the ground state is a helix with a pitch angle $\cos^{-1}(-J_1/4J_2)$. If the ratio of the exchange interaction parameters is $|-J_1/4J_2| \geq 1$, the system falls down in a simple collinear state.

Several years after the discovery of helimagnetism in centrosymmetric crystals, Dzyaloshinsky [10] found another class of helimagnetic structures stabilized by the antisymmetric Dzyaloshinsky-Moriya (DM) interaction [11]. Moriya showed that the microscopic mechanism of antisymmetric exchange is spin-orbit interaction [12]. The antisymmetric DM exchange between spins at positions i and j is $\mathbf{D}_{ij} \cdot \mathbf{S}_i \times \mathbf{S}_j$ term in the expression for the free energy of the system. The constant vector \mathbf{D}_{ij} is called the DM vector, and $\boldsymbol{\chi}_{ij} = \mathbf{S}_i \times \mathbf{S}_j$ is the spin chirality. In systems with an asymmetric electronic structure, the spin-orbit interaction leads to a nonzero contribution from the DM interaction. The antisymmetric coupling can

manifest itself only in systems that do not have an inversion center, while in crystals with a higher symmetry, this coupling vanishes. The DM term favors the canted arrangement of spins and therefore can lead to the helical spin arrangement. Let us turn again to Fig. 1.2 and consider a simple case of the formation of a ferromagnetic spiral due to antisymmetric exchange. The contribution of symmetric ferromagnetic exchange $J < 0$ between nearest neighbors to the energy of the system is minimal for co-aligned spins. At the same time, the antisymmetric interaction $\mathbf{D}_{ij} \cdot \mathbf{S}_i \times \mathbf{S}_j$, since it includes the vector product of spins, prefers the mutually perpendicular orientation of the nearest-neighbor spins. Thus, the helical ground state with the pitch angle $\tan^{-1}(D_{ij}/J)$ is a kind of compromise between symmetric and antisymmetric exchanges. The exact direction of the DM vector \mathbf{D}_{ij} determines the chirality of the spiral.

Regardless of the mechanism of formation, the helicoidal state is always characterized by broken chiral symmetry. The concept of chiral symmetry breaking implies that simultaneously with the broken inversion symmetry (\mathcal{P}), the combination of time-reversal symmetry (\mathcal{T}) with any true spatial rotation (\mathcal{R}) is not broken. Despite the obvious similarity in the magnetic structure, symmetric and chiral helimagnets differ in the level at which the chiral symmetry is broken. In the case of chiral helimagnets, this occurs already at the level of the Hamiltonian, since chirality χ_{ij} is odd under the parity transformation (\mathcal{P}) but even under time reversal (\mathcal{T}). Therefore, the magnetic structure is forced to break the chiral symmetry. On the other hand, in the Yoshimori type helimagnets, chiral symmetry is not broken at the level of the Hamiltonian. Instead, the helimagnetic structure spontaneously breaks the chiral symmetry. Another obvious difference, already laid down at the level of the Hamiltonian, is the lifting of the degeneracy between left- and right-handed helices in chiral systems. Thus, the magnetic structure of chiral helimagnets is protected by the chirality of the crystal, while symmetric helimagnets do not have such protection and are easily fragmented into many domains of different chirality. It is also worth noting the difference in the shape of the magnon dispersion curves in the two types of systems, schematically shown in the third column in Fig. 1.2. While the magnon dispersion in symmetric helimagnets has anomalies at the positions of the propagation vectors $\pm \mathbf{Q}$, the magnon dispersion in chiral helimagnets does not have such anomalies.

1.3 Helical spin ordering in symmetric helimagnets

Following Nagamiya [2], to obtain an expression for the helical spin ordering, consider a system in which classical spins sit on a Bravais lattice with one spin per unit cell. Here

we neglect anisotropy energy and will take into account only Heisenberg exchange forces between separate spins. The exchange energy between spins \mathbf{S}_m and \mathbf{S}_n at the positions \mathbf{R}_m and \mathbf{R}_n has the form:

$$-2J(\mathbf{R}_{mn})\mathbf{S}_m \cdot \mathbf{S}_n \quad (\mathbf{R}_{mn} = \mathbf{R}_m - \mathbf{R}_n). \quad (1.4)$$

Here we assume that the interaction is symmetric: $J(-\mathbf{R}_{mn}) = J(\mathbf{R}_{mn})$. In order to obtain a helical ordering, it is important to notice that the interaction potential is not confined to the nearest neighbors. Let us assume that one atom is at the origin, $J(\mathbf{R}_n) = 0$ if $\mathbf{R}_n = 0$, and the total number of atoms is N . The Fourier transform of the exchange parameters and spins are

$$J(\mathbf{q}) = \sum_n J(\mathbf{R}_n) \exp(-i\mathbf{q} \cdot \mathbf{R}_n), \quad (1.5)$$

$$\mathbf{S}_q = N^{-1/2} \sum_n \mathbf{S}_n \exp(-i\mathbf{q} \cdot \mathbf{R}_n). \quad (1.6)$$

The total exchange energy of the system

$$-\sum_m \sum_n J(\mathbf{R}_{mn}) \mathbf{S}_m \cdot \mathbf{S}_n \quad (1.7)$$

can be written as

$$-\sum_q J(\mathbf{q}) \mathbf{S}_q \cdot \mathbf{S}_{-\mathbf{q}} \quad (1.8)$$

To minimize the Eq. (1.7) or (1.8), we have to assume the condition $\mathbf{S}_n^2 = \text{const} = S^2$ for all n . First we can impose a milder condition

$$\sum_n \mathbf{S}_n^2 = \text{const}, \quad (1.9)$$

or, in Fourier components,

$$\sum_q \mathbf{S}_q \cdot \mathbf{S}_{-\mathbf{q}} = \text{const}. \quad (1.10)$$

Considering the condition (1.10) to minimise the expression (1.8) we need to keep only the \mathbf{q} at which $J(\mathbf{q})$ attains its maximum. If we denote this \mathbf{q} as \mathbf{Q} , we can write the minimum of (1.8) in the form

$$-J(\mathbf{Q})(\mathbf{S}_Q \cdot \mathbf{S}_{-Q} + \mathbf{S}_{-Q} \cdot \mathbf{S}_Q). \quad (1.11)$$

Now, the expression for \mathbf{S}_n can be obtained from (1.6):

$$\mathbf{S}_n = N^{-1/2} [\mathbf{S}_Q \exp(i\mathbf{Q} \cdot \mathbf{R}_n) + \mathbf{S}_{-Q} \exp(-i\mathbf{Q} \cdot \mathbf{R}_n)]. \quad (1.12)$$

Or, in components:

$$\begin{aligned} S_{nx} &= A \cos(\mathbf{Q} \cdot \mathbf{R}_n + \alpha), \\ S_{ny} &= B \cos(\mathbf{Q} \cdot \mathbf{R}_n + \beta), \\ S_{nz} &= C \cos(\mathbf{Q} \cdot \mathbf{R}_n + \gamma), \end{aligned} \quad (1.13)$$

where A, B, α, β , and γ are arbitrary constants. These equations represent a general elliptic helical ordering of spins with wave vector \mathbf{Q} . To satisfy the condition $\mathbf{S}_n^2 = \text{const} = S^2$, spin \mathbf{S}_n rotating must describe a circle at the position \mathbf{R}_n . If we choose the z -axis perpendicular to the plane in which the spin rotates, the equations (1.13) will transform in

$$\begin{aligned} S_{nx} &= S \cos(\mathbf{Q} \cdot \mathbf{R}_n + \alpha), \\ S_{ny} &= S \sin(\mathbf{Q} \cdot \mathbf{R}_n + \alpha), \\ S_{nz} &= 0. \end{aligned} \quad (1.14)$$

These equations represent a helical order of spins on a lattice and the corresponding spin structure is called the *screw structure* after Yoshimori [3]. Expression (1.14) describes a screw structure with an arbitrary angle between the direction of the screw axis and the spin rotation plane. A special case of such a spin structure is a proper screw structure [Fig. 1.1 (a)] in which \mathbf{Q} is perpendicular to the rotation plane. It is worth mentioning the cycloidal structure [Fig. 1.1 (d)] in which they are coplanar.

The helical spin structure is a rather general form of a spin structure. It contains both ferromagnetic ($\mathbf{Q} = 0$) and antiferromagnetic (\mathbf{Q} at the edge of the Brillouin zone) orderings as limiting cases. An important feature of the helical spin structure is that its period is in no way related to the period of the host crystal lattice.

1.4 Spin waves

The central topic of this thesis is neutron scattering by spin waves in helimagnets. This section discusses the main features of spin waves in a solid. For a comprehensive treatment of a spin-wave theory, see Keffer [13].

1.4.1 Spin deviations

Let us consider a ferromagnetic arrangement of localized spins on a Bravais lattice, meaning one atom per unit cell. Assume that each ion on a lattice has spin quantum number S , and spin angular momentum $\hbar\sqrt{S(S+1)}$. Quantum mechanics states that the component of

spin angular momentum measured along any direction has the value $M_S \hbar$, where $M_S = S, S-1, \dots, -S$. It is common to choose the z -axis as the direction of quantization. In a ferromagnet at zero temperature, all spins are aligned, and $M_S = S$. The departure of M_S from the $M_S = S$ value is called a spin deviation.

Spin deviation in a solid can be represented as a sum of deviations caused by a set of traveling sinusoidal waves. These waves are called spin waves. It was first shown by Bloch that the states near the ground state of a ferromagnet can be approximated by superpositions of these sinusoidal spin waves [14]. The spin wave is quantized and its energy is $n\hbar\omega$, where ω is the angular frequency of the wave, n is an integer number. An elementary excitation described by the quantum of the spin wave energy $\hbar\omega$ is called a magnon.

1.4.2 Linear spin-wave theory

To apply a spin-wave theory to a Heisenberg ferromagnet, take the Hamiltonian of the magnetic system in the form

$$H = - \sum_{ll'} J(\mathbf{l}-\mathbf{l}') \mathbf{S}_l \cdot \mathbf{S}_{l'}, \quad (1.15)$$

where \mathbf{S}_l is the spin angular momentum operator of the atom l in units of \hbar , $J(\mathbf{l}-\mathbf{l}') = J(\mathbf{l}'-\mathbf{l})$ is the exchange integral, and $J(0) = 0$ is by definition. The Hamiltonian, written in the form (1.15) assumes that $J > 0$ ensures the minimal energy of a system for co-aligned spins. In the case of an antiferromagnet, $J < 0$ minimizes the energy.

Denote the operators of the x , y , and z projections of the spin angular momentum \mathbf{S}_l as S_l^x , S_l^y , and S_l^z . For a moment, let us constrain our attention to one particular atom l and, for simplicity, drop the subscript l . Define the ladder operators as

$$S^+ = S^x + iS^y, \quad S^- = S^x - iS^y. \quad (1.16)$$

If $|M_S\rangle$ stands for the eigenstate of S^z with eigenvalue M_S , then

$$S^+ |M_S\rangle = \sqrt{(S - M_S)(S + M_S + 1)} |M_S + 1\rangle, \quad (1.17)$$

$$S^- |M_S\rangle = \sqrt{(S + M_S)(S - M_S + 1)} |M_S - 1\rangle. \quad (1.18)$$

Rewrite this using the spin-deviations operator $\hat{n} = S - S^z$, with the quantum numbers $n = S - M_S$:

$$S^+ |n\rangle = \sqrt{2S} \sqrt{n} \sqrt{1 - \frac{n-1}{2S}} |n-1\rangle, \quad (1.19)$$

$$S^- |n\rangle = \sqrt{2S} \sqrt{n+1} \sqrt{1 - \frac{n}{2S}} |n+1\rangle. \quad (1.20)$$

Thus S^+ converts the state $|n\rangle$ characterised by the spin deviation n to the state $|n-1\rangle$ and S^- converts $|n\rangle$ to $|n+1\rangle$. Using the harmonic-oscillator operators a^+ and a acting as

$$a|n\rangle = \sqrt{n}|n-1\rangle, \quad (1.21)$$

$$a^+|n\rangle = \sqrt{n+1}|n+1\rangle, \quad (1.22)$$

we can rewrite (1.19) and (1.20) as

$$S^+ = \sqrt{2S}f(S)a, \quad S^- = \sqrt{2S}a^+f(S), \quad (1.23)$$

where $f(S) \equiv \sqrt{1 - (a^+a/2S)}$. These expressions represent the mapping from the boson creation and annihilation operators to the spin operators and were developed in 1940 by Holstein and Primakoff [15].

To make a linear approximation, first we need to expand $f(S)$ in powers of $1/S$:

$$f(S) = \sqrt{1 - \frac{a^+a}{2S}} = 1 - \frac{a^+a}{4S} + O\left(\frac{1}{S^2}\right). \quad (1.24)$$

In the framework of the linear approximation we restrict ourselves to the first term in the expansion (1.24). Now the spin angular momentum operators for the atom l can be written as

$$S_l^+ = \sqrt{2S}a_l, \quad S_l^- = \sqrt{2S}a_l^+. \quad (1.25)$$

The approximation we have made is equivalent to neglecting terms $(n-1)/2S$ and $n/2S$ in (1.19, 1.20). Thus it is seen that the linear approximation is well suited for small spin deviations, i.e. $n \ll S$. It is exactly true for operator S^+ acting on states $|0\rangle$ and $|1\rangle$ and for operator S^- acting on state $|0\rangle$. As the spin deviations increase, the accuracy of the approximation decreases. When n reaches the S value, the linear approximation becomes completely inapplicable, and the action of the S^+ and S^+ operators leads to the generation of nonexistent states.

In order to obtain an expression for the Hamiltonian (1.15) in the linear approximation, in addition to operators S_l^+ and S_l^- , we need an expression for S_l^z . Since $S_l^z|n\rangle = (S-n)|n\rangle = (S - a_l^+a_l)|n\rangle$, taking into account (1.25) we obtain:

$$S_l^z = S - \frac{1}{2S}S_l^-S_l^+. \quad (1.26)$$

1.4.3 Spin waves in ferromagnets and antiferromagnets

Now we can write the product $\mathbf{S}_l \cdot \mathbf{S}_{l'}$ using S_l^+ , S_l^- , and S_l^z operators and substitute it into the Hamiltonian (1.15):

$$H = - \sum_{ll'} J(1-l') \left(\frac{1}{2}S_l^+S_{l'}^- + \frac{1}{2}S_l^-S_{l'}^+ + S_l^zS_{l'}^z \right). \quad (1.27)$$

To obtain this expression, we took into account that $J(0) = 0$, and any two operators S_l and $S_{l'}$ commute with each other. Spin waves are introduced by the following Fourier expansions

$$a_l = N^{-1/2} \sum_{\mathbf{q}} \exp(i\mathbf{q} \cdot \mathbf{l}) a_{\mathbf{q}}, \quad (1.28)$$

$$a_l^+ = N^{-1/2} \sum_{\mathbf{q}} \exp(i\mathbf{q} \cdot \mathbf{l}) a_{\mathbf{q}}^+, \quad (1.29)$$

where the summation is performed over all wave vectors \mathbf{q} within a Brillouin zone of the reciprocal lattice. We shall refer to $a_{\mathbf{q}}$ and $a_{\mathbf{q}}^+$ as magnon annihilation and magnon creation operators, respectively. Substituting expressions (1.25), (1.26), (1.28), and (1.29) into (1.27), we can obtain the required expression for the Hamiltonian:

$$H = H^0 + \sum_{\mathbf{q}} \hbar \omega_{\mathbf{q}} a_{\mathbf{q}}^+ a_{\mathbf{q}}, \quad a_{\mathbf{q}}^+ a_{\mathbf{q}} = n, \quad (1.30)$$

where

$$H^0 = -S^2 N j(0) = -S^2 N \sum_{\boldsymbol{\rho}} J(\boldsymbol{\rho}), \quad (1.31)$$

$$\hbar \omega_{\mathbf{q}} = 2S(j(0) - j(\mathbf{q})), \quad (1.32)$$

$$j(\mathbf{q}) = \sum_{\boldsymbol{\rho}} J(\boldsymbol{\rho}) \exp(i\mathbf{q} \cdot \boldsymbol{\rho}), \quad (1.33)$$

$$\boldsymbol{\rho} = \mathbf{l} - \mathbf{l}'. \quad (1.34)$$

The term H^0 in Hamiltonian (1.30) is the energy of the ground state in which all $M = S$. The second term is the sum of spin waves with wave vectors \mathbf{q} located within a Brillouin zone, the energy of each of which is $\hbar \omega_{\mathbf{q}}$ and (1.32) is the dispersion relation for spin waves.

Let us consider the simple case of a ferromagnetic chain with interactions only between the nearest neighbors. Assuming that the exchange integral has a constant value, the ferromagnetic magnon dispersion [Fig. 1.3 (a)] relation can be written as

$$\hbar \omega_{\mathbf{q}} = 4JS(1 - \cos qa). \quad (1.35)$$

And in the long wavelength limit, it transforms to

$$\hbar \omega_{\mathbf{q}} = 2JSq^2 a^2 = Dq^2, \quad (1.36)$$

where D is called the spin-wave stiffness constant. The dispersion (1.35) with the dispersion relation $\hbar \omega_{\mathbf{q}} = \hbar^2 q^2 / 2m$ for a free particle of the mass m shows that a magnon with a long wavelength behaves like a particle of effective mass $m^* = \hbar^2 / 4JSa^2$.

Similar to spin waves in ferromagnets, in the case of antiferromagnets, exchange interactions should lead to the excitation of spin waves. However, here we are faced with the

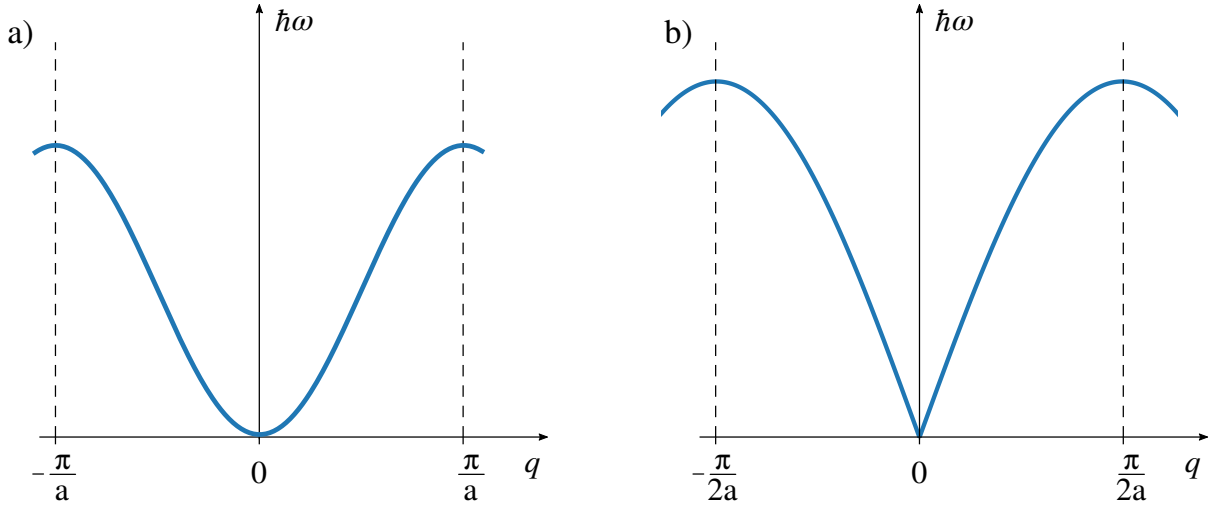


Figure 1.3: Spin wave dispersions in (a) ferromagnetic and (b) antiferromagnetic chains. The exchange integrals are constant and the only nearest neighbours interaction is assumed.

fundamental problem of the unknown ground state. While in the first case the state at 0 K in which all spins are co-aligned is the eigenfunction of the exchange Hamiltonian, in the case of a ferromagnet there is no such unambiguity. Many states are very close in energy and have zero total spin. Each of these states separately is not an eigenfunction of the exchange Hamiltonian and only their combination determines the true ground state. One way to work around this problem is as follows. The state with the minimal classical energy is chosen as the basis for constructing spin waves. This state is determined by minimizing the spin Hamiltonian in which the spin operators are replaced by classical vectors. Subsequent calculations lead to zero-point corrections which, in turn, allow the properties of the approximate ground state to be calculated.

When constructing the theory of spin waves in antiferromagnets and ferrimagnets, it is natural to choose the ordered state of alternately directed spins as an approximate ground state. In what follows, the system is considered as two ferromagnetic sublattices, in each of which the excitation of spin deviations is considered similar to the case of a ferromagnet. Then, following the standard Holstein-Primakoff scheme, the bosonization of the spin angular momentum operators and the transition from direct to momentum space are carried out. The canonical Bogoliubov transformation is used to diagonalize the resulting Hamiltonian and obtain the spin-wave dispersion relations.

In the simple case of a one-dimensional antiferromagnet, the dispersion relation of magnons is

$$\hbar\omega_q = 4JS |\sin qa|. \quad (1.37)$$

This dispersion curve is schematically plotted in Fig. 1.3 (b). In the long wavelength limit, its behavior is linear:

$$\hbar\omega_{\mathbf{q}} = 4JS|qa|, \quad (1.38)$$

in contrast to ferromagnetic magnons, which exhibit quadratic dispersion in the vicinity of the Brillouin zone center. The dispersions (1.35) and (1.37) are schematically plotted in Fig. 1.3. In contrast to spin waves in a ferromagnet, in the vicinity of a zone center, dispersion of the antiferromagnetic magnons is linear.

1.4.4 Spin waves in helimagnets

Now we are ready to consider the spin-wave theory for helimagnets. Let us consider a lattice with inversion symmetry and one magnetic ion per structural unit cell. Suppose, there is some anisotropy energy that distinguishes the Z axis, which we will take as the quantization axis. The spin Hamiltonian has the form:

$$H = -g\mu_B H_0 \sum_l S_l^z - 2 \sum_{l>l'} J(1-l') \mathbf{S}_l \cdot \mathbf{S}_{l'} + D \sum_l (S_l^z)^2, \quad (1.39)$$

where l and l' depict the magnetic ion sites. The first term is the Zeeman energy, and the applied field H_0 is along the Z direction. The second term is the Heisenberg exchange energy, and D is the uniaxial magnetocrystalline anisotropy parameter.

The spiral can be described as

$$S_l^X = S \sin \theta \cos(\mathbf{Q} \cdot \mathbf{l}); \quad S_l^Y = S \sin \theta \sin(\mathbf{Q} \cdot \mathbf{l}); \quad S_l^Z = S \cos \theta, \quad (1.40)$$

with θ the cone angle of Fig. 1.1 (b), and with the axis of the cone, \mathbf{Q} pointed along the Z direction. The absolute value of \mathbf{Q} measures the pitch of the spiral. The antiferromagnetic spiral of Fig. 1.1 (a) is the special case of (1.40) with $\theta = \pi/2$.

To consider spin waves similarly to the case of a ferromagnet, we introduce a new rotating coordinate system, axis ζ of which is co-directed with the equilibrium spin direction at each magnetic site:

$$\begin{aligned} S_l^\xi &= (S_l^X \cos(\mathbf{Q} \cdot \mathbf{l}) + S_l^Y \sin(\mathbf{Q} \cdot \mathbf{l})) \cos \theta - S_l^Z \sin \theta, \\ S_l^\eta &= -S_l^X \sin(\mathbf{Q} \cdot \mathbf{l}) + S_l^Y \cos(\mathbf{Q} \cdot \mathbf{l}), \\ S_l^\zeta &= (S_l^X \cos(\mathbf{Q} \cdot \mathbf{l}) + S_l^Y \sin(\mathbf{Q} \cdot \mathbf{l})) \sin \theta + S_l^Z \cos \theta. \end{aligned} \quad (1.41)$$

In the new coordinate system, spin deviations are introduced identically to the ferromagnetic case and, in the linear approximation have the form:

$$S_l^\zeta = S - a_l^+ a_l; \quad S_l^+ = \sqrt{2S} a_l; \quad S_l^- = \sqrt{2S} a_l^+. \quad (1.42)$$

Further, following the standard procedure, we must substitute expressions (1.42) into Hamiltonian (1.39). After passing to momentum space, the resulting Hamiltonian can be brought into the form:

$$H = C_3 + \sum_{\mathbf{q}} A_{\mathbf{q}} a_{\mathbf{q}}^+ a_{\mathbf{q}} + \sum_{\mathbf{q}} \left(\frac{1}{2} B_{\mathbf{q}} a_{\mathbf{q}} a_{-\mathbf{q}} + \frac{1}{2} B_{\mathbf{q}}^* a_{\mathbf{q}}^+ a_{-\mathbf{q}}^+ \right), \quad (1.43)$$

with

$$C_3 = -g\mu_B H_0 N S \cos \theta - N S^2 \mathcal{J}(\mathbf{Q}) \sin^2 \theta - N S^2 (\mathcal{J}(0) - D) \cos^2 \theta, \quad (1.44)$$

$$A_{\mathbf{q}} = g\mu_B H_0 - \frac{1}{2} S (1 - \cos \theta)^2 \mathcal{J}(\mathbf{Q} + \mathbf{q}) - \frac{1}{2} S (1 + \cos \theta)^2 \mathcal{J}(\mathbf{Q} - \mathbf{q}) \\ - S \sin^2 \theta (\mathcal{J}(\mathbf{q}) - D) + 2S \sin^2 \theta \mathcal{J}(\mathbf{Q}) + 2S \cos^2 \theta (\mathcal{J}(\mathbf{Q}) - D), \quad (1.45)$$

$$B_{\mathbf{q}} = -\frac{1}{2} S \sin^2 \theta (2\mathcal{J}(\mathbf{q}) - \mathcal{J}(\mathbf{Q} - \mathbf{q}) - \mathcal{J}(\mathbf{Q} + \mathbf{q}) - 2D). \quad (1.46)$$

Here $\mathcal{J}(\mathbf{q})$ is given by (1.33).

As the next step, the Hamiltonian (1.43) must be diagonalized to be transformed into a sum of harmonic-oscillator Hamiltonians with no interactions between the oscillators.

The canonical Bogoliubov transformation yields:

$$H = C_3 - \frac{1}{2} \sum_{\mathbf{q}} \bar{A}_{\mathbf{q}} + \sum_{\mathbf{q}} \left(\alpha_{\mathbf{q}}^+ \alpha_{\mathbf{q}} + \frac{1}{2} \right) \epsilon_{\mathbf{q}}, \quad (1.47)$$

$$\epsilon_{\mathbf{q}} = [(\bar{A}_{\mathbf{q}}^2 - |B_{\mathbf{q}}|^2)^{\frac{1}{2}} + H_{\mathbf{q}}], \quad (1.48)$$

$$H_{\mathbf{q}} = \frac{1}{2} (A_{\mathbf{q}} - A_{-\mathbf{q}}), \quad (1.49)$$

$$\bar{A}_{\mathbf{q}} = \frac{1}{2} (A_{\mathbf{q}} + A_{-\mathbf{q}}), \quad (1.50)$$

where the summation is over the entire first Brillouin zone.

Since the Bogoliubov transformation preserves Bose's commutation rules, the eigenvalues $n_{\mathbf{q}}$ of $\alpha_{\mathbf{q}}^+ \alpha_{\mathbf{q}}$ must be 0, 1, 2, 3, and so on. Thus, the energy eigenvalues are given by

$$E_{n_1, \dots, n_N} = C_3 - \frac{1}{2} \sum_{\mathbf{q}} \bar{A}_{\mathbf{q}} + \sum_{\mathbf{q}} \epsilon_{\mathbf{q}} (n_{\mathbf{q}} + \frac{1}{2}). \quad (1.51)$$

It should be noted that due to the various transformations used to obtain Hamiltonian (1.47), the spin waves obtained in this way do not have an obvious connection with the spin deviations. However, despite the loss of the simple connection with a spin, it is customary to refer to all magnetic excitations in ordered magnets as spin waves or magnons.

In the classical limit, the ground state is found by minimizing C_3 . From (1.44) it follows that minimization of C_3 requires a maximum value of $\mathcal{J}(\mathbf{Q})$. The angle of the cone θ is

determined by condition $\partial C_3 / \partial \theta = 0$. In the absence of anisotropy, $\theta = \pi/2$ and the energy of the classical ground state is given by the expression

$$(E_e)_{\text{classical}} = -NS^2 \mathcal{J}(\mathbf{Q}). \quad (1.52)$$

Consider a special case of $\theta = \pi/2$ and $H_0 = 0$. The spin-wave energies can be deduced from (1.48) as

$$\hbar\omega_{\mathbf{q}} = 2S[\mathcal{J}(\mathbf{Q}) - \frac{1}{2}(\mathcal{J}(\mathbf{Q} + \mathbf{q}) + \mathcal{J}(\mathbf{Q} - \mathbf{q}))]^{\frac{1}{2}}[\mathcal{J}(\mathbf{Q}) - \mathcal{J}(\mathbf{q}) + D]^{\frac{1}{2}}. \quad (1.53)$$

To have $\theta = \pi/2$, the uniaxial anisotropy D must be positive. Since the maximum value of $\mathcal{J}(\mathbf{q})$ is reached at $\mathbf{q} = \mathbf{Q}$, it can be seen from (1.53) that the minimum value of the dispersion is at $\mathbf{q} = 0$. This gapless mode corresponds to a uniform rigid rotation of all spins in the ordering plane and is called a phason [16]. In the vicinity of $\mathbf{q} = \pm\mathbf{Q}$, the spin waves dispersion has local minima, the nonzero energy of which is due only to the presence of anisotropy. These two modes are due to spin fluctuations out of the ordering plane. All three modes in the absence of anisotropy are Goldstone modes associated with the spontaneous breaking of continuous symmetry in spin space by a helical long-range order. In the presence of a small easy-plane anisotropy, the modes at $\pm\mathbf{Q}$ acquire gaps, while the central mode remains gapless.

It is important to note that the dispersion relation (1.53) is given in a rotating coordinate system. The transition to the laboratory system will lead to a shift of the dispersion curve by vectors \mathbf{Q} and $-\mathbf{Q}$.

A schematic illustration of the dispersion of spin waves in symmetric and antisymmetric helimagnets is shown in Fig. 1.4. We considered a proper screw spin structure ($\theta = \pi/2$) on a simple tetragonal lattice with one magnetic ion per crystallographic unit cell. In the case of symmetric helimagnet, we limited ourselves to only two exchanges between the nearest and the next-nearest neighbors along the c axis, J_1 and J_2 [see Fig. 1.2]. To introduce the frustration of exchange interactions in the c direction, exchange integral J_1 was chosen ferromagnetic, and J_2 – antiferromagnetic. To model a helimagnet with DM interaction leading to helimagnetism we introduced the ferromagnetic J between nearest neighbors, and \mathbf{D} interaction competing to it as shown in Fig. 1.2. To stabilize the spins in the c plane, a nonzero positive anisotropy was introduced along the c axis.

In both cases, the classical ground state and the spectrum of spin waves were calculated within the framework of the linear spin wave theory using the SpinW software. To trace the evolution of the dispersion curves, I fixed the values of the exchange integrals between the nearest neighbors and gradually increased the absolute values of the competing exchanges. Zero values of J_2 and \mathbf{D} correspond to a simple ferromagnetic ground state with $\mathbf{q} = 0$. In

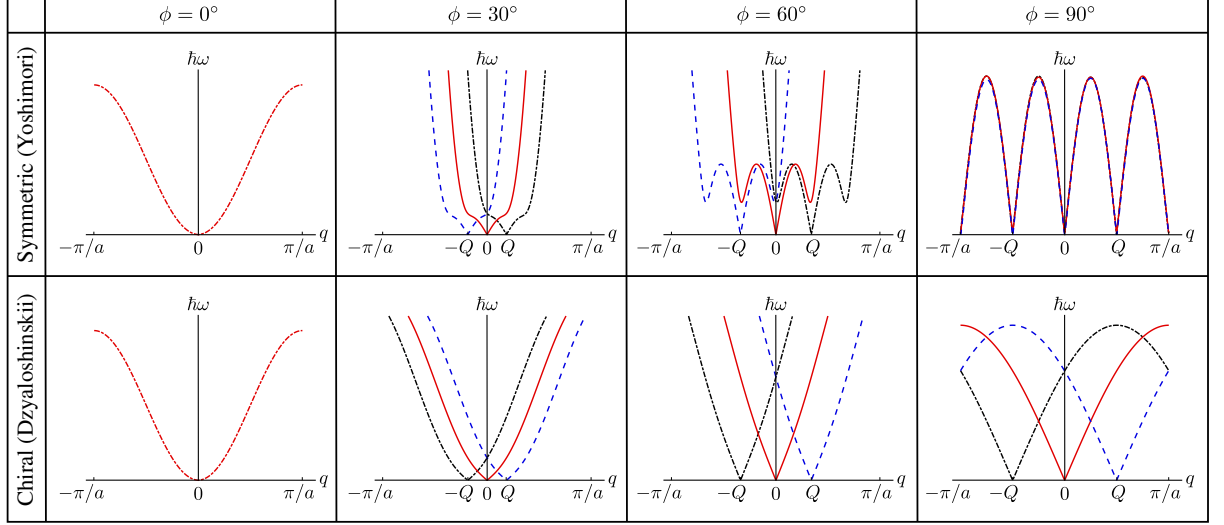


Figure 1.4: Evolution of the dispersion curves for symmetric and antisymmetric helimagnets with increasing competition between exchange interactions leading to the formation of a helix. Angle ϕ is the angle of rotation of the spin direction at the transition between the nearest planes in the direction of the spiral propagation. Dispersion curves are modeled using SpinW software [17].

the case of symmetric helimagnet, the formation of a spiral ground state occurs only when the threshold value of the exchange integrals ratio $|J_1| < 4|J_2|$ is reached. With a further increase in J_2 , the helical pitch Q increases, and the corresponding pitch angle changes as $\cos^{-1}(-J_1/4J_2)$. When $J_2 \rightarrow \infty$ the pitch angle and the helical pitch tend to $\pi/2$ and $\pi/2a$, respectively. In the case of the antisymmetric helimagnet, the formation of a helicoidal ground state occurs immediately when a nonzero value of \mathbf{D} appears and the pitch angle is determined by $\tan^{-1}(D/J)$. The values of the helical pitch and the pitch angle when D tends to infinity coincide with the values for the symmetric case. A characteristic feature of the dispersion curve of symmetric helimagnet is the presence of anomalies at $\mathbf{q} = \pm\mathbf{Q}$, which is absent in the antisymmetric case. The presence of these local minima is described by the previously obtained dispersion relation (1.53).

Neutron scattering experiments make it possible to directly measure the dynamic correlation function $S^{\alpha\beta}(\mathbf{q}, \omega)$. It contains information on the nature and properties of spin excitations in the sample and is defined as the Fourier transform of the space and time correlation function:

$$S^{\alpha\beta}(\mathbf{q}, \omega) = \frac{1}{2\pi\hbar} \int_{-\infty}^{\infty} dt \sum_{\rho} \langle S_0^{\alpha}(0) S_{\rho}^{\beta}(t) \rangle e^{i(\omega t - \mathbf{q} \cdot \boldsymbol{\rho})}, \quad (1.54)$$

where α and β label Cartesian axes and $\langle \dots \rangle$ denotes a ground-state average. The terms with $\alpha = \beta = z$ lead to a correlation function $\langle S_0^z(0) S_{\rho}^z(t) \rangle$ that is independent of time and therefore generate elastic scattering. They are sometimes called longitudinal terms.

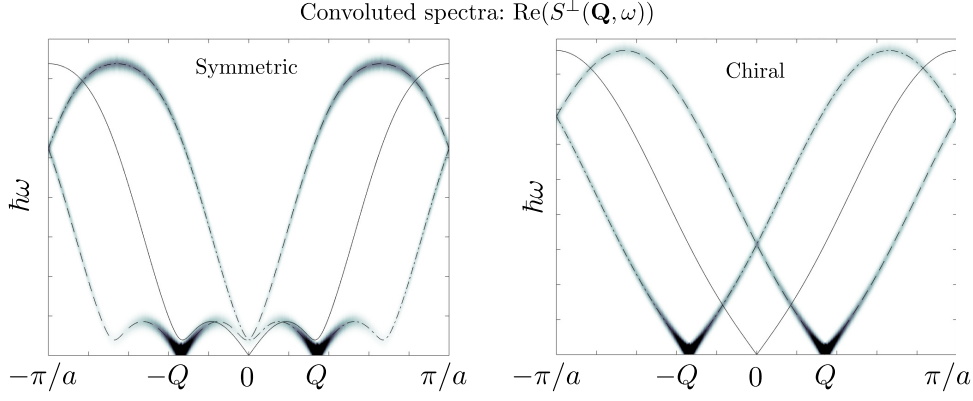


Figure 1.5: Inelastic neutron scattering spectra for the symmetric (left) and antisymmetric (right) helimagnets (see text). The energy resolution is simulated by the convolution of the dynamical correlation function $S^{\alpha\beta}(\mathbf{q}, \omega)$ with a Gaussian function. The thin lines represent the dispersion curves. The spectrum is calculated with SpinW.

The terms with $\alpha, \beta = x, y$ give rise to inelastic neutron scattering and are referred to as transverse terms. The off-diagonal terms cancel out $S^{\alpha\beta}(\mathbf{q}, \omega) = 0$ for $\alpha \neq \beta$, see Ref. [18].

In our case, the role of the ordered spin direction z plays ζ and one-magnon excitations occur in the fluctuations polarized transverse to this direction. The transverse dynamical correlations at $T = 0$ are given by

$$\begin{aligned} S_{1M}^{\xi\xi} &= \frac{\tilde{S}}{2} |u_{\mathbf{q}} + v_{\mathbf{q}}|^2 \delta(\omega - \omega_{\mathbf{q}}), \\ S_{1M}^{\eta\eta} &= \frac{\tilde{S}}{2} |u_{\mathbf{q}} - v_{\mathbf{q}}|^2 \delta(\omega - \omega_{\mathbf{q}}). \end{aligned} \quad (1.55)$$

The delta function in (1.55) leads to the appearance of sharp peaks at the points determined by the dispersion relation $\omega_{\mathbf{q}}$. The effects of intensity smearing due to two-magnon processes are taken into account in \tilde{S} , the value of which is less than S by the value of the corresponding two-magnon corrections. In the case of zero anisotropy D , functions $u_{\mathbf{q}}$ and $v_{\mathbf{q}}$ determining the scattering intensities are given by

$$u_{\mathbf{q}} = \cosh \theta_{\mathbf{q}}; \quad v_{\mathbf{q}} = \sinh \theta_{\mathbf{q}}; \quad 2\theta_{\mathbf{q}} = B_{\mathbf{q}}/A_{\mathbf{q}}. \quad (1.56)$$

Here $A_{\mathbf{q}}$ and $B_{\mathbf{q}}$ are given by (1.45, 1.46) with $\theta = \pi/2$.

The neutron spectra of spin waves in simulated symmetric and antisymmetric helimagnets are shown in Fig. 1.5. In both cases, the spectrum consists of two gapless Goldstone modes emanating from the vectors \mathbf{Q} and $-\mathbf{Q}$.

A characteristic feature of the spectrum of symmetric helimagnet is the M-shape of the central part of the spectrum. The nature of this lies in the form of the dispersion curve, which has two local minima spaced by vectors \mathbf{Q} and $-\mathbf{Q}$ from the central Goldstone mode. We

will find similar spectra further, in the chapters devoted to symmetric helimagnets ZnCr_2Se_4 and $\text{Sr}_3\text{Fe}_2\text{O}_7$. The dispersion curve for an antisymmetric helimagnet does not have such anomalies, which accordingly affects the neutron spectrum.

1.4.5 Interactions between spin waves

Deriving the dispersion relation for a ferromagnet, Bloch considered a single spin wave in a system of perfectly aligned spins [14]. He argued that at low temperatures the eigenstate of a ferromagnet should be very close to a linear superposition of noninteracting spin waves, which is exactly what the linear theory of spin waves gives. The first to test Bloch's hypothesis was Bethe [19], who considered a linear chain with $S = 1/2$. Dyson [20] was the first to tackle the difficult problem of extending calculations to the three-dimensional (3D) case.

Dyson identified two reasons, and two corresponding interactions between spin waves, indicating that the consideration of a linear combination of noninteracting spin waves is not entirely correct. The so-called kinematic interaction occurs because spin-wave states containing more than one spin wave do not form an orthogonal set. The effect of this interaction can be presented as follows. Each excited spin wave decreases the total S^z of the system by one unit \hbar . If $2NS$ spin waves are excited in the system, this will lead to a complete reverse of the magnetization of the system. Spin waves in the system cannot be excited infinitely because of the limited value of S . To take this into account, a repulsive kinematic interaction was introduced. The fact that this interaction is repulsive prevents the accumulation of spin waves at a given spin site.

The reason for the dynamic interaction is that the states containing more than one spin wave do not diagonalize the exchange Hamiltonian. This interaction leads to small shifts in the energies of individual spin waves in the presence of other spin waves. This interaction is attractive since the energy required to reverse a spin is less if the neighboring spins are already partially rotated.

Since, in the framework of the linear theory of spin waves, we deliberately restrict ourselves to only linear terms in expansion (1.24), we obtain spin waves that do not interact with each other. This expansion itself is possible only if the kinematic interaction can be neglected. To establish a connection between Dyson's dynamic interaction and the Hamiltonian of a system, it is necessary to consider the nonlinear terms in (1.24). After making the appropriate transformations, the final Hamiltonian will include coupled spin-wave operators describing processes involving several magnons, and therefore magnon-magnon interactions. The three- and four-magnon terms in the Hamiltonian play an important role in the relaxation and renormalization of spin wave frequencies [21].

Chapter 2

Neutron scattering

2.1 Introduction

2.1.1 Basic properties of thermal neutrons

Neutron scattering is a powerful technique for the investigation of the structure and dynamics of condensed matter. The neutron was discovered in 1932 by James Chadwick, and almost immediately physicists began to develop the fundamentals of neutron diffraction. With the advent of nuclear reactors, high neutron fluxes became available, which contributed to the development of spectroscopy methods. The advantage of using neutrons stems from their basic properties. Some of them are listed in Table 2.1.

The value of the neutron mass leads to several very important consequences that make it an ideal probe for studying condensed matter physics. To produce thermal neutrons one needs to moderate fast neutrons from a reactor or spallation source. The mass of the neutron is almost equal to the proton's one. It means that they can be thermalized by the

Quantity	Value
Mass, m	$1.675 \cdot 10^{-27} \text{ kg}$
Electric charge, q	0
Spin, S	$\frac{1}{2}$
Magnetic dipole moment, μ_n	$-1.913\mu_N$
Lifetime, τ	$886 \pm 1 \text{ sec}$

Table 2.1: Basic properties of neutrons.

collisions with light atoms, such as hydrogen or deuterium. To be diffracted by the crystal, the wavelength of the incoming particle has to be comparable with or smaller than the lattice constant, otherwise, the ordinary refraction will take place. Fortunately, the neutron's mass results in the de Broglie wavelength of the thermal neutrons which fits very well for most of the solids and liquids. Furthermore, thermal neutron energies (1 – 100 meV) are comparable in magnitude with elementary excitations in solids, which makes neutron spectroscopy a unique method for studying phonons and magnons.

The neutron has zero electric charge. This leads to a weak interaction with matter, which allows the neutron to penetrate deep into the sample. From the experimental point of view, it makes possible to easily use various sample environment, such as cryostats, furnaces, pressure cells, etc. Electrical neutrality means the absence of the Coulomb barrier, which must be overcome to approach atomic nuclei. It is worth noting here that the theory of the interaction of neutrons with nuclei is not fully developed. Nevertheless, it is well known that this interaction is very short-range ($\sim 10^{-13}$ cm). This is much smaller than thermal neutron wavelength and interaction can be treated as point-like and scattering is spherically symmetric. It can be characterized by only one parameter — scattering length b . Scattering cross section for a single nucleus equals $4\pi b^2$. Scattering length can be positive or negative, and in general, it is a complex number. The sign is responsible for the phase of the scattered neutron wave in respect to the incident wave. The imaginary part is associated with absorption and becomes noticeable near the nuclear absorption resonance. In contrast to the electron or x-ray scattering, neutrons scattering length does not depend on the number of electrons in an atom and where is no systematic variation across the periodic table. Even among isotopes of the same element, the scattering strength changes somehow randomly.

Neutron has an internal structure and consists of quarks bonded by gluons. It leads to the non-zero magnetic dipole moment of the neutron, which interacts magnetically with unpaired electrons in the atomic electron shell with a strength comparable to that of the nuclear interaction. Neutron's magnetic moment, listed in Table 2.1, makes it a unique probe for studying magnetism.

Spin angular momentum can be $\pm \frac{1}{2}\hbar$. It is possible to prepare a neutron beam with only one spin polarization, spin up or spin down. Polarization neutron analysis is a powerful method for determining magnetic structures, separating magnetic and nuclear scattering, and subtracting incoherent from total scattering.

And the last but not the least important property of the neutron that is worth mentioning is the finite lifetime τ (Table 2.1). A free neutron is not a stable particle and undergoes beta decay into a proton, an electron, and an electron anti-neutrino. Neutron scattering

experiments are possible because the thermal neutron's lifetime is much longer than its traveling time between the production and detection, which is of the order of milliseconds.

2.1.2 Neutron production

Radioactive sources

Portable sources utilize the radioactive decay of unstable elements to produce neutrons. The scheme is similar to the one that Chadwick used to discover the neutron.

The first type of the radioactive neutron sources employs an alpha emitting element to produce ^4He for (α, n) reaction:



As emitter can be used radium, americium, plutonium etc. Because of the short range of alpha particles the source should be made of a mixture of emitter and beryllium for close contact.

Another type of sources are based on (γ, n) photofission reaction. In these sources a radioisotope undergoing gamma decay producing γ particles is used for bombarding beryllium target which leads to the endothermic reaction with the production of a neutron:



The common gamma source is the artificial radioactive antimony isotope ^{124}Sb . The main advantage of this type of source arises from the greater range of gamma particles compared to alpha particles in the (α, n) reaction. As a result, the emitter can be separated from the beryllium target, and the neutron production can be turned on and off.

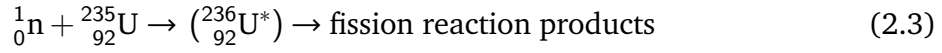
Radioactive neutron sources are in use today for installing and calibrating neutron detectors. The emission rates from such sources are typically from 10^6 to 10^8 neutrons per second, which is too low for most neutron scattering experiments. The more powerful sources, such as nuclear reactors and spallation neutron sources, are employed to produce neutrons for scientific use.

Neutrons from nuclear reactors

The heart of a nuclear reactor is the fission reaction, during which a heavy nucleus splits into two lighter ones, emitting some neutrons, γ -rays, and other subatomic particles.

The typical nuclear reactor working on thermal neutrons consists of four principal components: fuel, moderator, cooling system, and shielding. The fuel is a fissile material,

commonly uranium enriched with its metastable isotope ^{235}U . A typical nuclear fission reaction



excretes a variety of reaction products, such as fissioned nuclei or fission products, neutrinos, gammas, betas, and neutrons [22]. Along with particles, the reaction releases a huge amount of energy, about 200 MeV in each fission.

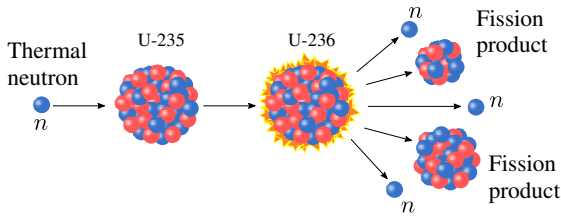


Figure 2.1: Schematic of a fission reaction.

A simplified fission reaction is shown schematically in Fig. 2.1. Following the initial absorption of a thermal neutron by the ^{235}U nucleus, it forms an unstable composite nucleus $^{236}\text{U}^*$, which undergoes fission. The most common is binary fission into fission products with atomic masses of about

95 and 135 u. Also, an average of 2.5 neutrons. These neutrons can be used to further propagate a fission chain reaction or can be employed for neutron scattering experiments. The average kinetic energy of the emitted neutrons is about 2.5 MeV, and the corresponding spectrum is shown in Fig. 2.2. More than 99% of these fission neutrons are emitted within a very short time after a fission event (within 10^{-14} s) and are called *prompt* neutrons. The subsequent radioactive decay of the fission products produces *delayed* neutrons, appearing with noticeable time delay. Although these neutrons account for less than 1 percent of the total number of neutrons emitted, they play a key role in controlling the chain reaction.

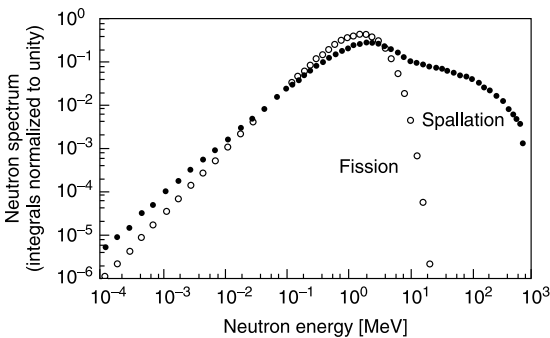


Figure 2.2: Comparison of the thermal neutron fission spectrum of ^{235}U with spallation spectrum. The spallation is measured for tungsten target bombarded by 800 MeV protons [22].

The high-energy neutrons produced during fission are not able to sustain the chain reaction and must be slowed down, or moderated. The fact is that ^{235}U has a negligible capture cross section for high-energy neutrons, while neutrons from the thermal part of the spectrum allow maintaining a chain reaction. The neutrons are slowed down through collisions with light atoms. Because the kinetic energy exchange is most effective between the particles of similar masses, heavy water (D_2O) or graphite are common

moderators used in thermal neutron reactors. The resulting neutrons are in thermal equilibrium with moderator, and their velocity spectrum approaches the Maxwell-Boltzmann

distribution:

$$\phi(v) \propto v^3 \exp\left(-\frac{1}{2}mv^2/k_B T\right), \quad (2.4)$$

where $\phi(v)$ is the flux of neutrons with the velocity v , m is the neutron mass, k_B is the Boltzmann constant, and T is the temperature of the moderator. The typical moderator temperature is kept near 300 K. It corresponds to the energy of about 26 meV, which is, luckily, just the typical energy of elementary excitations in a solid. In some special cases, if neutrons with significantly higher or lower temperatures are required, additional cold or hot moderators can be installed outside the reactor core.

The colossal energy released during the nuclear fission process must be efficiently removed to prevent core overheating, or in the worst case, core meltdown. The achievable rate of cooling limits the power density in the core of the high-flux fission reactors, leading to the limited neutron flux. The need for higher neutron fluxes has led to the development of alternative neutron sources based on the spallation process.

Spallation neutron sources

Spallation reaction is a process of collision of a light projectile (proton, neutron, or light nucleus) with kinetic energy from hundreds of MeV to several GeV with a heavy nucleus (e.g., lead, tantalum), which is usually referred to as target nucleus, with consequent emission of hadrons (mostly neutrons) or nuclear fragments. Modern spallation neutron sources use protons as projectiles.

For the spallation process, it is crucial for the incident proton to have minimal kinetic energy of about 100–150 MeV. For such protons, de Broglie wavelength is of the order of 10^{-13} cm, which is smaller than the size of the target nucleus. In this case, a proton interacts with individual nucleons

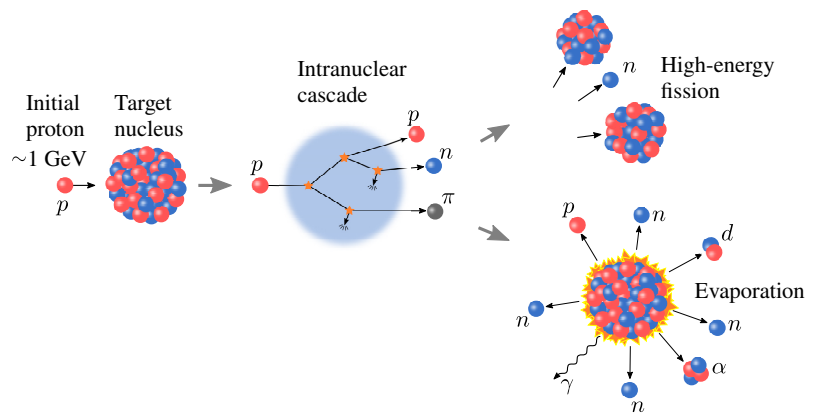


Figure 2.3: Spallation process. After the initial proton collides with a target nucleus, the spallation process can be described in two stages: intranuclear cascade and de-excitation. Neutrons useful for the neutron experiments are released during the second stage. See text for details.

inside the nucleus. After a proton collides with a heavy metal nucleus, two main stages can be distinguished: *intranuclear cascade* and *de-excitation*. The schematic of the spallation

process is shown in Fig. 2.3. When the incident proton hits the target, it undergoes a series of direct interactions with nucleons inside the nucleus – the so-called intranuclear cascade. During this stage, some of the particles (neutrons, protons, and pions) can be ejected from the nucleus in the direction of the projectile and lead to the secondary spallation processes — internuclear cascade. The particles emitted at the intra-nuclear cascade stage have very high kinetic energies — from about 20 MeV to the energy of the incident proton. They cannot be effectively thermalized and therefore are useless for neutron experiments. Sometimes, for modeling the spallation process, an intermediate *pre-equilibrium stage* can be distinguished. Upon this phase, low-energy particles (< 20 MeV) are emitted, but the nucleons inside the target nucleus are not yet in the equilibrium state. When the intranuclear cascade and the pre-equilibrium stage are over, the nucleus remains in a highly excited state. The second stage of the spallation process is de-excitation, or evaporation, when the excited nucleus relaxes by isotropically emitting low-energy particles, such as neutrons, protons, alpha-particles, etc., with the majority of the particles being neutrons. These particles have lower energies (< 20 MeV) and can be thermalized and used for neutron experiments. For some very heavy nuclei, such as lead, tungsten, thorium, and uranium, the high-energy fission can occur during the de-excitation, competing with evaporation. After evaporation, the residual nucleus can be radioactive and decay with the emission of gamma rays.

The net number of neutrons released in one nuclear fission event is about 2.5–3. In the case of spallation, the number of neutrons produced reaches 25–30 for each collision when a target of heavy elements is bombarded with protons with energies of about 1 GeV. Another advantage of a spallation process for neutron production is a smaller amount of energy, released as heat. As was mentioned above, the limit on the neutron flux produced at the nuclear reactor is caused by the cooling system. The amount of heat energy released in the spallation process per one neutron production is four times smaller than for fission neutron. Spallation neutron sources have a big political advantage as far as the target does not require to be made of fissile material. The neutron production can be easily stopped by switching off the proton accelerator power, therefore there is no danger that chain reaction will become uncontrolled. However, despite the obvious advantages of the method, there are also obstacles. First of all, spallation neutrons are much more energetic in comparison to fission ones. The spectra of the spallation and fission neutrons are shown in Fig. 2.2. Intranuclear cascade neutrons reach energies up to a few GeV. They are highly penetrating and can cause difficulties with radiation protection. Another drawback is the markedly higher cost of spallation neutrons compared to the relatively cheap fission production.

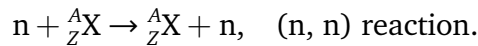
There are two types of spallation neutron sources – pulsed and continuous. Pulsed sources use linear accelerators in combination with proton storage rings (e.g., SNS at Oak Ridge, USA) or synchrotrons (e.g., ISIS in the United Kingdom) to generate high-energy proton beams. The European Spallation Source will not use a storage ring and therefore will produce a long proton pulse. To be able to benefit from such long pulses, special neutron instruments are developed. Continuous spallation sources are based on proton accelerators (e.g., SINQ at Villigen, Switzerland).

2.1.3 Thermal neutron detection

Interaction of neutrons with matter

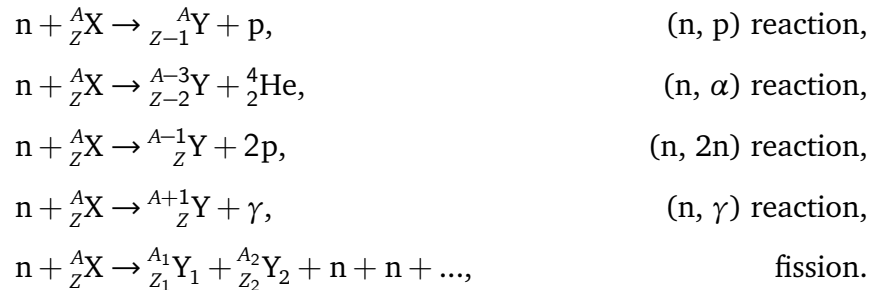
There are two main mechanisms of interaction of neutrons with a nucleus: scattering and absorption [23].

In the first process the initial neutron and nucleus interact with each other and both particles reappear in the scattering products:



Scattering can be elastic or inelastic. Elastic scattering leads to a simple redistribution of the total kinetic energy of the neutron-nucleus system, keeping the total kinetic energy unchanged. When inelastic scattering happens, the neutron transfers to the nucleus a part of its kinetic energy, leaving the nucleus in an excited state. The nucleus can further relax to the ground state emitting gamma particles.

The absorption process causes much more significant changes in the system of interacting particles. The initial neutron disappears being absorbed by the nucleus forming a compound nucleus, which decays either by the emission of subatomic particles or by fission. The typical absorption reactions are:



The absorption process is very important for neutron detection. Zero electric charge of the neutron makes it a very weak probe that does not excessively disturb the sample under investigation. While it is a great advantage for the nondestructive probing of material

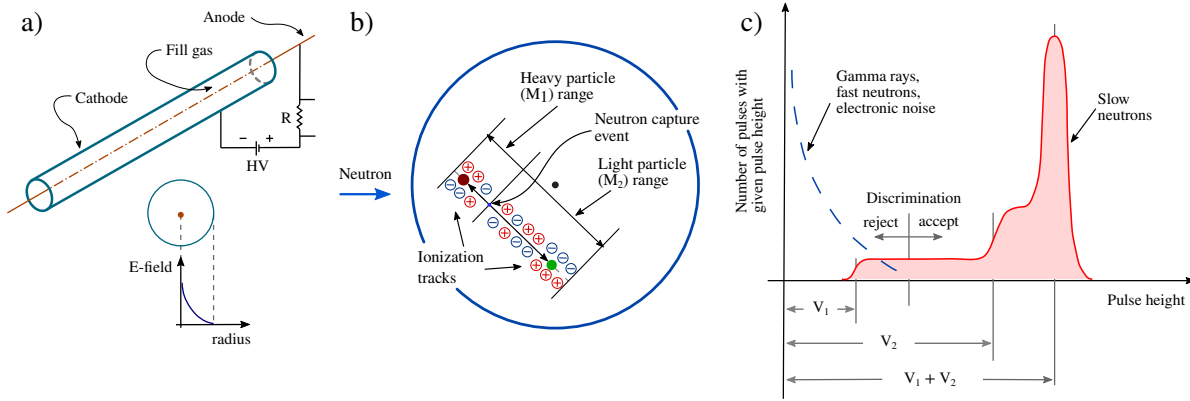
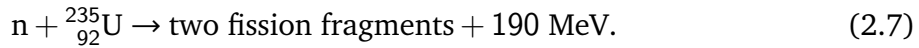
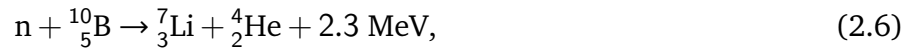


Figure 2.4: (a) Schematic of a cylindrical proportional counter. (b) Ionization tracks in the gas-filled detector. (c) Illustration of the pulse-height distribution and discrimination procedure. Adapted from Ref. [26].

properties, it makes neutron detection quite an intricate task. Thermal neutrons produce negligible ionization and can only be detected by secondary particles emitted after neutron absorption. The most common nuclear reactions which are used for the thermal neutron detection are [24, 25]:



Gas ionization detectors

After the neutron beam is scattered by the sample, it should be detected. A widely used type of thermal neutron detectors is a gas-filled proportional counter. Here we will give basic principles of its operation, more details can be found in Refs. [23, 24, 26]. A schematic drawing of a cylindrical gas detector is shown in Fig. 2.4 (a). It consists of a cylindrical tube, manufactured from either stainless steel or aluminum which works as a cathode [24]. A thin anode wire made of gold-plated tungsten is located along the central axis of the cylinder and held in place by ceramic insulators. There is one (or two, if the detector is position-sensitive) electrical connector attached to the electronic equipment. The tube is hermetically sealed and filled with a mixture of gases. The widely used technology is based on nuclear reactions with either ${}^3\text{He}$ or ${}^{10}\text{B}$ (2.5, 2.6). In this type of detectors, the absorbing material is a gas, ${}^3\text{He}$ or boron trifluoride enriched in ${}^{10}\text{B}$.

To be specific, here we will consider the ${}^3\text{He}$ detectors. After the neutron enters the detector tube, it can be absorbed by the ${}^3\text{He}$ nucleus. ${}^3\text{He}$ decays according to the reaction (2.5) on proton and triton, emitting about 800 KeV. This energy is shared by the reaction products.

It follows from the laws of conservation of energy and momentum that a lighter particle, in our case a proton, takes three times more energy than ^3H . The reaction products, scattering in different directions, ionize gas molecules, forming ionization tracks [see Fig. 2.4 (b)]. Further destiny of the ionized particles depends on the voltage applied to the anode. The electrons move to the anode, accelerating in the electric field which diverges as $1/r$, where r is the distance to the anode wire [Fig. 2.4 (a)]. The positive ions, in turn, move towards the cathode. If the voltage is very low, the electric field in the detector is not strong, electrons and ions move relatively slow, and almost all of them recombine. As voltage increases, the particles move faster and recombination rate decreases, finally reaching the point when all the charge created during the ionization is being collected (Fig. 2.5). This first region is called the recombination region. In the ionization chamber regime, enough voltage has been applied to collect all the electrons before they recombine. Further increase in the voltage does not change a pulse height because the recombination rate is zero and no new charge is produced. At higher voltages, the field is enough to accelerate the electrons until they eventually produce their own ionization in a Townsend avalanche. The output signal is higher, but it is linearly proportional to the energy deposited in the gas. This regime is referred to as a proportional regime and is widely used in neutron scattering instruments. Further increase in voltage leads to the realization of the ionization cascade and the signal is not anymore proportional to the number of neutrons entered the tube, the detector operates in the Geiger-Muller mode. After some critical voltage, a single ionizing event initiates a continuous discharge in the gas and the device cannot be used as a particle detector anymore.

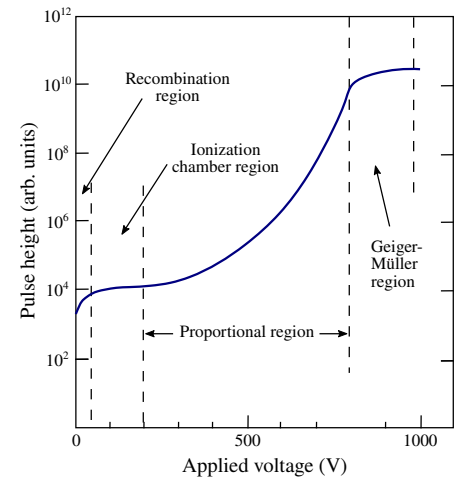


Figure 2.5: Pulse-height vs applied voltage curves to illustrate ionization, proportional, and Geiger-Müller regions of operation. Adapted from Ref. [24].

Even so the signal pulses have the same origin, they can differ in height. Fig. 2.4 (c) shows the schematic of a pulse-height distribution in a ^3He gas-filled detector. The origin of the double-plateau shape of the pulse-height distribution is the wall effect. If the neutron is absorbed by the nucleus near the detector's wall, one of the tracks (or, rarely, both) can hit the wall before it transfers its energy to the gas. The edge of the lower plateau, V_1 , corresponds to the case when the particle with higher energy (triton) hits the wall; the edge of the second plateau, V_2 , marks the energy of the lighter particle (proton). There is a

continuous range of possibilities, from the total loss of energy of one ion, while the other transfers all of its energy to the gas, to the complete deposit of the energies of both particles into the gas, producing a full-height peak ($V_1 + V_2$).

To distinguish neutron capture events from the noise of various origins, the pulse-height discrimination procedure is applied. It is the electronic means by which only the pulses above or below a certain threshold are accepted. The dashed line in Fig. 2.4 (c) shows the low energy pulses from the noise sources. During the low-pulse-height recognition procedure, the minimum pulse value is set, below which all pulses will be ignored. The high-pulse-height discrimination can be useful to separate the background from the fast neutron recoil events or alpha particles from heavy element impurities in the detector wall material [26].

The logical step following the simple gas-filled counter is a position-sensitive detector (PSD). This can be simply done by making anode wire resistive. After the neutron capture event happens, the electric charge is produced whose amplitude is measured at both ends of the detector. The charge measured at the end of the detector is inversely proportional to the distance to the neutron absorption point. By measuring the charges at both ends of the tube, we naturally obtain the position of the neutron along the detector. A close-packed array of individual PSD gas detectors can be built to obtain two-dimensional (2D) spatial resolution. This approach has been implemented in IN5 at ILL and MAPS at ISIS spectrometers.

To measure the intensity and spectrum of the incident neutron beam, any neutron instrument is equipped with a beam monitor, which is commonly a fission chamber. The typical beam monitor fission chamber is a rectangular box filled with gas. The thin layer of the fissile material (usually uranium highly enriched in ^{235}U) is evaporated on the cathode inside of the camera wall and directly exposed to the detector gas. After the absorption of the neutron by the ^{235}U nucleus, the energetic fission fragments ionize the gas. A common fill gas is a mixture of 90% argon and 10% methane [24]. The ionization caused by the fission fragments is detected electronically. Fission chambers work in the ionization chamber mode, no signal amplification needed. It caused by the high energy of the fission fragments producing a sufficient ionization [24]. In some fission chambers, the fissile material and detector gas are not separated. The chamber is filled with gaseous uranium hexafluoride, UF_6 . The advantages of fission chambers, which determine their use for monitoring a direct beam, are the highest insensitivity to gamma radiation, low efficiency, and high transmission.

At present, many methods of neutron detection have been implemented, in addition to gas proportional counters. With the advent of high-intensity pulsed neutron sources, the demand for a PSD capable of rapidly registering high and instantaneous count rates

has grown rapidly. Scintillation detectors are of great interest for these purposes, since their detection mechanism is inherently hundreds of times faster. The spatial resolution of scintillation detectors is also much better than that of gas detectors. This is due to the range of ionizing particles being reduced to a few microns. However, they have a significant drawback — a very high sensitivity to gamma radiation. Therefore, they are rarely used on continuous neutron sources and only if gamma sensitivity is not particularly important. The gamma background can be distinguished in a pulsed neutron source by taking advantage of the time-of-flight method.

2.2 Theory of neutron scattering

Neutrons are scattered by atomic nuclei and unpaired electrons of the magnetic atoms. The corresponding events are called nuclear and magnetic neutron scattering. Neutron scattering intensity is a superposition of these two processes. To interpret experimental data and obtain information about the structure and magnetic dynamics in a system, it is crucial to understand the basic principles of both types of neutron scattering. An exhaustive description of the theory of neutron scattering is given, for instance, in the book of Squires [18]. Here are the basic concepts and formulas that are needed to understand this work.

2.2.1 Scattering cross sections

Any type of scattering can be characterised by a quantity known as a cross section. Consider a beam of monochromatic neutrons incident on a scattering system along the z axis. The schematic of the process geometry is sketched in Fig. 2.6. After interaction with a scattering system, a neutron can be scattered in any direction. If we count the total number of neutrons scattered per second into a full solid angle 4π , the *total scattering cross section* is defined as

$$\sigma_{\text{tot}} = \frac{C}{\eta \Phi}, \quad (2.8)$$

where C and η are the count rate and the efficiency of the detector, Φ is the neutron flux incident on a target.

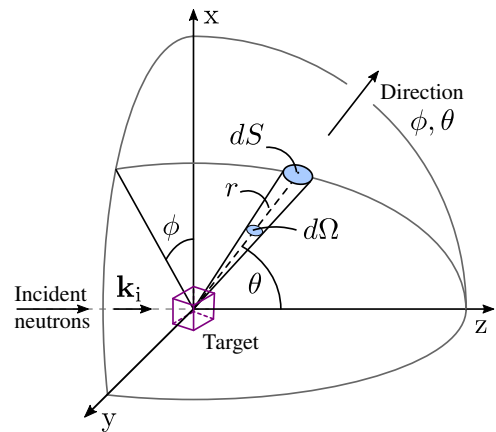


Figure 2.6: Geometry of the scattering process. Adapted from [18].

When we count the number of neutrons scattered per second into a small solid angle $d\Omega$ in the direction (θ, ϕ) , the *differential cross section* is defined by the equation

$$\frac{d\sigma}{d\Omega} = \frac{C}{\eta \Phi \Delta\Omega}, \quad (2.9)$$

where $\Delta\Omega$ is a solid angle in the direction (θ, ϕ) covered by the detector.

If we analyze the energies of the scattered neutrons and count only the ones with final energies between E and $E + \Delta E$, then the corresponding cross section is referred to as the *partial differential cross section*

$$\frac{d^2\sigma}{d\Omega dE} = \frac{C}{\eta \Phi \Delta\Omega \Delta E}. \quad (2.10)$$

The scattering cross sections are exactly the quantities that are measured in neutron scattering experiments. Assume that the incident neutrons, characterized by a wave vector \mathbf{k}_i and a spin σ_i , scatter by the target into a state with \mathbf{k}_f and σ_f . The target is a condensed matter system undergoing a transition from a state λ_i to a state λ_f . In this case, the count rate C in a detector that has the efficiency η and spans the solid angle $d\Omega$ is given by

$$C = \Phi d\Omega \eta \left(\frac{d\sigma}{d\Omega} \right)_{\mathbf{k}_i, \sigma_i, \lambda_i \rightarrow \mathbf{k}_f, \sigma_f, \lambda_f}. \quad (2.11)$$

If we denote the number of transitions per second from the state $|\mathbf{k}_i \sigma_i \lambda_i\rangle$ to the state $|\mathbf{k}_f \sigma_f \lambda_f\rangle$ as $W_{\mathbf{k}_i, \sigma_i, \lambda_i \rightarrow \mathbf{k}_f, \sigma_f, \lambda_f}$, the differential cross section can be written as

$$\left(\frac{d\sigma}{d\Omega} \right)_{\mathbf{k}_i, \sigma_i, \lambda_i \rightarrow \mathbf{k}_f, \sigma_f, \lambda_f} = \frac{1}{\Phi d\Omega} \sum_{\mathbf{k}_f} W_{\mathbf{k}_i, \sigma_i, \lambda_i \rightarrow \mathbf{k}_f, \sigma_f, \lambda_f}. \quad (2.12)$$

To evaluate the sum at the right-hand side of Eq. (2.12) we use Fermi's golden rule — the fundamental result in quantum mechanics,

$$\sum_{\mathbf{k}_f} W_{\mathbf{k}_i, \sigma_i, \lambda_i \rightarrow \mathbf{k}_f, \sigma_f, \lambda_f} = \frac{2\pi}{\hbar} |\langle \mathbf{k}_f \sigma_f \lambda_f | V | \mathbf{k}_i \sigma_i \lambda_i \rangle|^2 \rho_{\mathbf{k}_f \sigma_f}(E_f). \quad (2.13)$$

Here V is the interaction potential between the neutron and the sample, and $\rho_{\mathbf{k}_f \sigma_f}(E_f)$ is the number of the final neutron states \mathbf{k}_f, σ_f in $d\Omega$ per unit energy interval. The use of the golden rule is justified by the legitimacy of the Born approximation. Indeed, first-order perturbation theory is certainly valid for the short-range nuclear potential. In the case of the long-range magnetic scattering potential, the use of the golden rule is supported by the weakness of the potential.

Using a standard technique in quantum mechanics, referred to as box normalisation, and a law of conservation of energy, the master formula of neutron scattering can be derived,

$$\left(\frac{d^2\sigma}{d\Omega dE} \right)_{\mathbf{k}_i \rightarrow \mathbf{k}_f} = \frac{k_f}{k_i} \left(\frac{m_n}{2\pi\hbar^2} \right)^2 \sum_{\lambda_i \sigma_i} P(\lambda_i) P(\sigma_i) \sum_{\lambda_f \sigma_f} |\langle \mathbf{k}_f \sigma_f \lambda_f | V | \mathbf{k}_i \sigma_i \lambda_i \rangle|^2 \delta(E + E_{\lambda_i} - E_{\lambda_f}), \quad (2.14)$$

where m_n is a neutron mass. Here the idea is to interpret an experimental signal by summation over all final states of the sample λ_f and final neutron polarisation states σ_f , and averaging over all initial states λ_i and σ_i , occurring with probabilities $P(\lambda_i)$ and $P(\sigma_i)$ correspondingly. This equation is very general and can be applied to different interaction potentials $V(\mathbf{r})$.

The differential cross section can be expressed as a sum of coherent and incoherent parts:

$$\frac{d^2\sigma}{d\Omega_f dE_f} = \left. \frac{d^2\sigma}{d\Omega_f dE_f} \right|_{\text{coh}} + \left. \frac{d^2\sigma}{d\Omega_f dE_f} \right|_{\text{inc}} \quad (2.15)$$

The coherent scattering cross section depends on the correlation between the positions of the same nucleus at different times, and on the correlation between the positions of different atoms at different times. Therefore, it leads to interference effects. Coherent scattering provides information about the cooperative effects among different atoms. Examples of such processes are elastic Bragg scattering or inelastic scattering by phonons and magnons. Unlike coherent scattering, incoherent scattering depends only on the correlation between the positions of the same atoms at different times and, therefore, does not cause interference effects. The incoherent part of the scattering signal gives information about individual particle motion, such as diffusion.

2.2.2 Nuclear scattering

Although magnetic scattering is studied in this work, nuclear scattering makes the main contribution to the experimental signal. Below we will briefly outline the basic formulas and principles of thermal neutron scattering by nuclei.

Scattering by a single nucleus

The scattering of a neutron by the nucleus is due to the strong interaction. The wavelength of the thermal neutron is of the order of 10^{-8} cm, which is about 4–5 orders of magnitude larger than the range of the strong force. It leads to a spherically symmetric scattered wave. A schematic sketch of the thermal neutron scattering by the single fixed nucleus is shown in Fig. 2.7. The nucleus is at the origin of the coordinate system. If the incident neutron with the wave vector \mathbf{k} along the z axis is written as a plane wave

$$\psi_{\text{inc}} = \exp(ikz), \quad (2.16)$$

scattered wave can be written as

$$\psi_{\text{sc}} = -\frac{b}{r} \exp(ikr), \quad (2.17)$$

where b is a scattering length, the value which is unique not only for each chemical element but even for different isotopes and spin states of the nucleus-neutron system.

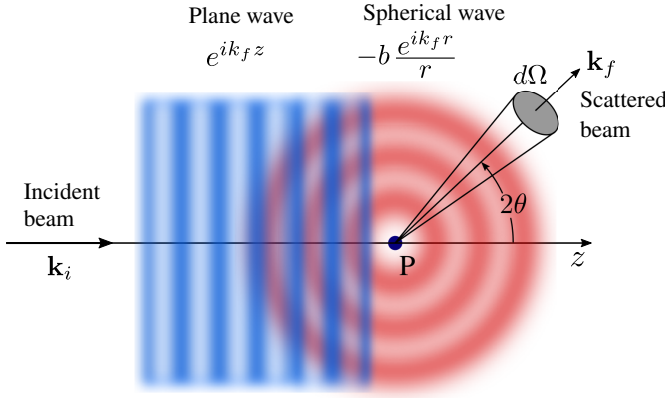


Figure 2.7: Incident plane wave of neutrons scattered by a single point scatterer P .

For simplicity reasons we consider elastic scattering and the wave vectors of the initial and scattered neutrons have the same absolute value. In general, the scattering length is a complex quantity, $b = b_0 + b' + ib''$. Here b_0 is responsible for the scattering on the potential, and $b' + ib''$ for the resonance scattering, happening with the formation of a compound nucleus. For the most nuclei (with the exception of strongly absorbing nuclei such as ^{103}Rh , ^{113}Cd , ^{157}Gd , ^{176}Lu , etc.) the imaginary part of b is very small, and the scattering length can be considered as a real quantity. In the discussion below we will consider only such nuclei.

The differential scattering cross section for scattering of neutrons by a single fixed nucleus is given by

$$\frac{d\sigma}{d\Omega} = b^2. \quad (2.18)$$

The total scattering cross section σ_{tot} is

$$\sigma_{\text{tot}} = 4\pi b^2. \quad (2.19)$$

Nuclear scattering by a general system of particles

We start by ignoring the spin of the neutron for simplicity reasons and specify the neutron state entirely by its momentum. For nuclear scattering, the nuclear potential can be approximated with Fermi pseudopotential:

$$V(\mathbf{r}) = \frac{2\pi\hbar^2}{m_n} b\delta(\mathbf{r}). \quad (2.20)$$

Fourier transform of Eq. (2.20) gives:

$$V(\mathbf{Q}) = \frac{2\pi\hbar^2}{m_n} b, \quad (2.21)$$

where $\mathbf{Q} = \mathbf{k}_i - \mathbf{k}_f$ is a *scattering vector*. Substituting Eq. (2.21) into the master equation (2.14), we obtain an expression for the cross section of the nuclear neutron scattering:

$$\frac{d^2\sigma}{d\Omega_f dE_f} = \frac{k_f}{k_i} \sum_{\lambda_i \lambda_f} P(\lambda_i) \left| \left\langle \lambda_f \left| b \sum_l e^{i\mathbf{Q} \cdot \mathbf{r}_l} \right| \lambda_i \right\rangle \right|^2 \delta(\hbar\omega + E_i - E_f), \quad (2.22)$$

where \mathbf{r}_l are the coordinates of the identical scattering centers. Using a few standard operations, Van Hove (1954) showed that the cross section for a system of N atoms can be written as

$$\frac{d^2\sigma}{d\Omega_f dE_f} = N \frac{k_f}{k_i} b^2 S(\mathbf{Q}, \omega), \quad (2.23)$$

where $S(\mathbf{Q}, \omega)$ is a *scattering function* of the system,

$$S(\mathbf{Q}, \omega) = \frac{1}{2\pi\hbar N} \sum_{ll'} \int_{-\infty}^{\infty} dt \langle e^{-i\mathbf{Q} \cdot \mathbf{r}_{l'}(0)} e^{i\mathbf{Q} \cdot \mathbf{r}_l(t)} \rangle e^{-i\omega t}, \quad (2.24)$$

where we integrate over the time t and the angle brackets $\langle \dots \rangle$ denote the average over initial states. The scattering function gives the probability that a scattering event will result in a change in the energy of the system by $\hbar\omega$ and the momentum by $\hbar\mathbf{Q}$. Equation (2.24) shows that the scattering function depends only on the energy and momentum transferred to the sample, and not on the actual values of the initial and final neutron wave vectors. $S(\mathbf{Q}, \omega)$ contains the information about the positions and motions of atoms in a sample. Therefore, the goal of most neutron scattering experiments is to measure the scattering function and extract the information about the microscopic properties of a system under investigation.

Coherent and incoherent nuclear scattering

To understand the difference between the coherent and incoherent scattering, consider a monoelemental sample. Even in this case, the sample may contain nuclei with different scattering lengths. The fact is that different isotopes of the same chemical element have different values of b . Moreover, if the scattering nucleus has a nonzero spin, the scattering length will vary depending on the mutual orientation of the neutron and the nuclear spins.

Let us assume that there are no correlations between nuclear position and scattering length. In this case, the scattering, which depends on the relative positions of the atoms,

will be determined only by the averaged scattering length \bar{b} . Thus, the coherent scattering cross section is given by

$$\sigma_{\text{coh}} = 4\pi(\bar{b})^2. \quad (2.25)$$

Writing down the total scattering cross section as

$$\sigma_{\text{tot}} = 4\pi\overline{b^2}, \quad (2.26)$$

the incoherent scattering cross section, caused by the random fluctuations in scattering length from site to site, can be obtained as:

$$\sigma_{\text{inc}} = \sigma_{\text{tot}} - \sigma_{\text{coh}} = 4\pi\overline{(b - \bar{b})^2}. \quad (2.27)$$

An effective incoherent scattering length can be written as:

$$b_{\text{inc}} = \sqrt{\overline{b^2} - \bar{b}^2}. \quad (2.28)$$

Coherent nuclear scattering

Examples of coherent nuclear scattering are elastic or Bragg scattering and inelastic phonon scattering. For coherent nuclear scattering, the partial scattering cross section is

$$\left. \frac{d^2\sigma}{d\Omega_f dE_f} \right|_{\text{coh}} = N \frac{k_f}{k_i} \frac{\sigma_{\text{coh}}}{4\pi} S(\mathbf{Q}, \omega). \quad (2.29)$$

In general, if there are correlations between the nuclear positions and scattering length in a sample, they should be taken into account by adding the site-dependent scattering length in $S(\mathbf{Q}, \omega)$.

If the atomic density operator is written in the form

$$\rho_{\mathbf{Q}}(t) = \sum_l e^{i\mathbf{Q} \cdot \mathbf{r}_l(t)}, \quad (2.30)$$

the scattering function (2.24) can be rewritten as

$$S(\mathbf{Q}, \omega) = \frac{1}{2\pi\hbar N} \int_{-\infty}^{\infty} dt e^{-i\omega t} \langle \rho_{\mathbf{Q}}(0) \rho_{-\mathbf{Q}}(t) \rangle. \quad (2.31)$$

Bragg scattering

In the case of coherent nuclear scattering, we consider the time-averaged density operator:

$$S(\mathbf{Q}, \omega) = \delta(\hbar\omega) \frac{1}{N} \left\langle \sum_{ll'} e^{i\mathbf{Q}(\mathbf{r}_l - \mathbf{r}_{l'})} \right\rangle. \quad (2.32)$$

For a Bravais lattice (one atom per unit cell) with the unit cell volume v_0 and reciprocal lattice vectors \mathbf{G} , the scattering function can be written as

$$S(\mathbf{Q}, \omega) = \delta(\hbar\omega) \frac{(2\pi)^3}{v_0} \sum_{\mathbf{G}} \delta(\mathbf{Q} - \mathbf{G}). \quad (2.33)$$

Substituting this into Eq. (2.23), we obtain the expression for the coherent elastic nuclear scattering cross section by an ideally rigid body:

$$\left. \frac{d\sigma}{d\Omega} \right|_{\text{coh}}^{\text{el}} = N \frac{(2\pi)^3}{v_0} (\bar{b})^2 \sum_{\mathbf{G}} \delta(\mathbf{Q} - \mathbf{G}). \quad (2.34)$$

In reality, there are no absolutely rigid bodies and atoms oscillate in the vicinity of the equilibrium positions. This leads to some weakening of the peak intensity. To take these fluctuations into account, it is necessary to add a factor of e^{-2W} to Eq. (2.34), known as the Debye-Waller factor. For small deviations \mathbf{u} of atoms from their equilibrium positions \mathbf{r} :

$$W = \frac{1}{2} \langle (\mathbf{Q} \cdot \mathbf{u})^2 \rangle. \quad (2.35)$$

Let us generalize Eq. (2.34) to the case of a lattice with several atoms per unit cell. If the j th atom in the cell occupies position \mathbf{d}_j , then the coherent elastic differential scattering cross section takes the form:

$$\left. \frac{d\sigma}{d\Omega} \right|_{\text{coh}}^{\text{el}} = N \frac{(2\pi)^3}{v_0} \sum_{\mathbf{G}} \delta(\mathbf{Q} - \mathbf{G}) |F_N(\mathbf{G})|^2, \quad (2.36)$$

where

$$F_N(\mathbf{G}) = \sum_j \bar{b}_j e^{i\mathbf{G} \cdot \mathbf{d}_j} e^{-W_j} \quad (2.37)$$

is a static nuclear structure factor. It contains the information about the atomic positions \mathbf{d}_j within a unit cell. Measurement of structure factors for a number of reflections with their subsequent fit by models for atomic parameters is a standard method of crystallography.

Inelastic nuclear scattering

Inelastic coherent nuclear scattering involves the transfer of energy from a neutron to a scattering system, or vice versa. If the elastic contribution (Bragg scattering) is subtracted from the coherent amplitude of nuclear scattering, then $S(\mathbf{Q}, \omega)$ will correspond to lattice vibrations. An important property of $S(\mathbf{Q}, \omega)$ is the principle of detailed balance:

$$S(-\mathbf{Q}, -\omega) = e^{-\hbar\omega/k_B T} S(\mathbf{Q}, \omega), \quad (2.38)$$

where k_B is the Boltzmann constant, T is the temperature of the scattering system, and the frequency ω is positive. When deriving the Eq. (2.38), it is assumed that for a pair of states of a scattering system, a priori the probabilities that a neutron will transfer the system from one state to another are the same. Since the probability of finding a system in a state with higher energy is $e^{-\hbar\omega/k_B T}$ times lower than in a state with lower energy, then $S(-\mathbf{Q}, -\omega)$ is less than $S(\mathbf{Q}, \omega)$ by the same amount. Thus, the probability of excitation annihilation in the system is lower than the probability of excitation creation and is determined by the statistical weight factor for the initial state. The fluctuation-dissipation theorem establishes a connection between the scattering function $S(\mathbf{Q}, \omega)$ and the imaginary part of the dynamic susceptibility $\chi''(\mathbf{Q}, \omega)$:

$$S(\mathbf{Q}, \omega) = \frac{\chi''(\mathbf{Q}, \omega)}{1 - e^{-\hbar\omega/k_B T}}. \quad (2.39)$$

Equation (2.39) is very useful in the case of phonons, when $\chi''(\mathbf{Q}, \omega)$ does not explicitly depend on temperature. Let us consider the case of one-phonon coherent scattering, that is, a process in which a neutron and a scattering system exchange one quantum of vibrational energy. For a lattice with n atoms per unit cell, there are $3n$ different phonon branches with frequencies $\omega_{\mathbf{q}s}$, where the index s denotes different vibration modes, and vector \mathbf{q} is measured from the nearest reciprocal lattice vector \mathbf{G} . In this case, $\chi''(\mathbf{Q}, \omega)$ takes the form:

$$\chi''(\mathbf{Q}, \omega) = \frac{1}{2} \frac{(2\pi)^3}{v_0} \sum_{\mathbf{G}, \mathbf{q}} \delta(\mathbf{Q} - \mathbf{q} - \mathbf{G}) \sum_s \frac{1}{\omega_{\mathbf{q}s}} |\mathcal{F}(\mathbf{Q})|^2 \times [\delta(\omega - \omega_{\mathbf{q}s}) - \delta(\omega + \omega_{\mathbf{q}s})], \quad (2.40)$$

where

$$\mathcal{F}(\mathbf{Q}) = \sum_j \frac{\bar{b}_j}{\sqrt{m_j}} (\mathbf{Q} \cdot \xi_{js}) e^{i\mathbf{Q} \cdot \mathbf{d}_j} e^{-W_j} \quad (2.41)$$

is a dynamic structure factor. Here ξ_{js} is the polarisation vector for a particular mode s of the j th atom in a unit cell, m_j is its mass, and \bar{b}_j is the average scattering amplitude.

2.2.3 Magnetic scattering

Here we will briefly describe the scattering cross sections due to the magnetic interactions between the neutron and the unpaired electrons in the scattering system.

Magnetic scattering from unpaired electrons

The neutron has a magnetic dipole moment $\mu_n = -\gamma\mu_N\sigma$, where $\gamma = 1.913$, μ_N is the nuclear magneton, and σ is the Pauli spin operator for the neutron. Consider an unpaired electron with momentum \mathbf{p} . Its magnetic dipole moment $\mu_e = -2\mu_B\mathbf{s}$, where μ_B is the Bohr magneton, and \mathbf{s} is the spin angular momentum of the electron. The magnetic field at a point \mathbf{R} from the electron is due to its magnetic dipole moment and the momentum of the electron \mathbf{p} . The potential of a neutron in this field is

$$V(\mathbf{R}) = -\gamma\mu_N 2\mu_B \sigma \cdot \left[\text{curl} \left(\frac{\mathbf{s} \times \hat{\mathbf{R}}}{R^2} \right) + \frac{1}{\hbar} \frac{\mathbf{p} \times \hat{\mathbf{R}}}{R^2} \right], \quad (2.42)$$

where $\hat{\mathbf{R}}$ is a unit vector in the direction of \mathbf{R} .

Substituting the last expression into the master formula for neutron scattering (2.14) and introducing time dependence, one can obtain an expression for the magnetic cross section for neutron scattering by a general system of unpaired electrons:

$$\frac{d^2\sigma}{d\Omega dE} = \frac{k_f}{k_i} \frac{(\gamma r_0)^2}{2\pi\hbar} \sum_{\alpha\beta} (\delta_{\alpha\beta} - \hat{\mathbf{Q}}_\alpha \hat{\mathbf{Q}}_\beta) \int \langle \mathbf{D}_\alpha(-\mathbf{Q}, 0) \mathbf{D}_\beta(\mathbf{Q}, t) \rangle e^{-iEt/\hbar} dt, \quad (2.43)$$

where

$$\mathbf{D}_\beta(\mathbf{Q}, t) = e^{iHt/\hbar} \mathbf{D}_\beta(\mathbf{Q}) e^{-iHt/\hbar} \quad (2.44)$$

is a time-dependent magnetic interaction operator. Here $r_0 = e^2/(m_e c^2) = 0.28179 \times 10^{-12}$ cm, $\delta_{\alpha\beta}$ is the Kronecker delta, scattering vector $\mathbf{Q} = \mathbf{k}_f - \mathbf{k}_i$, and α and β stand for x, y, z . Operator $\mathbf{D}(\mathbf{Q})$ is related to the magnetisation operator $\mathbf{M}(\mathbf{r})$ by

$$\mathbf{D}(\mathbf{Q}) = -\frac{1}{2\mu_B} \int \mathbf{M}(\mathbf{r}) e^{i\mathbf{Q} \cdot \mathbf{r}} d\mathbf{r} = -\frac{1}{2\mu_B} \mathbf{M}(\mathbf{Q}). \quad (2.45)$$

From the Eq. (2.43) it is seen that scattering is dependent on the magnetic fluctuation of the scattering system. This resembles the situation with nuclear scattering, which depends on density fluctuations in the scattering system. However, unlike the latter, magnetic scattering possesses the directional dependence by means of the tensor $(\delta_{\alpha\beta} - \hat{\mathbf{Q}}_\alpha \hat{\mathbf{Q}}_\beta)$. As a consequence, the components of the magnetization are chosen perpendicular to \mathbf{Q} . In some cases, this will make it possible to determine the orientation of the magnetic moments in the sample.

Magnetic scattering from magnetic crystals

Above, we considered the general case of magnetic scattering by an arbitrary many-body system with no assumption about the spatial distribution of unpaired electrons. Now let us consider the case when the unpaired electrons belong to magnetic ions ordered into a crystal lattice. If ions occupy positions \mathbf{R}_j and the spin-orbit interaction is present, then the operator $\mathbf{D}(\mathbf{Q}, t)$ has the form

$$\mathbf{D}(\mathbf{Q}, t) = \sum_j f_j(\mathbf{Q}) \boldsymbol{\mu}_j(t) e^{i\mathbf{Q} \cdot \mathbf{R}_j(t)}, \quad (2.46)$$

where $\boldsymbol{\mu}_j = \frac{1}{2} \mathbf{S}_j$ is the magnetic moment localized at the atom at \mathbf{R}_j in units of μ_B , and $f_j(\mathbf{Q})$ are the atomic form factors:

$$f(\mathbf{Q}) = \frac{g_S}{g} \bar{j}_0(\mathbf{Q}) + \frac{g_L}{g} [\bar{j}_0(\mathbf{Q}) + \bar{j}_2(\mathbf{Q})], \quad (2.47)$$

where

$$\bar{j}_n(\mathbf{Q}) = \int_0^\infty j_n(Qr) |\psi(r)|^2 r^2 dr. \quad (2.48)$$

Here g , g_L , and g_S are the gyromagnetic ratios, j_n are spherical Bessel functions of order n , and $\psi(r)$ are the radial part of the unpaired electron wave functions. The atomic form factor $f_i(\mathbf{Q})$ is the Fourier transform of the magnetic electron density around the atomic center. Assuming that interatomic forces are independent of magnetic moments, the scattering cross section can be written as:

$$\begin{aligned} \frac{d^2\sigma}{d\Omega dE} &= \frac{k_f (\gamma r_0)^2}{k_i 2\pi\hbar} \sum_{\alpha\beta} (\delta_{\alpha\beta} - \hat{\mathbf{Q}}_\alpha \hat{\mathbf{Q}}_\beta) \sum_{jj'} f_j^*(\mathbf{Q}) f_{j'}(\mathbf{Q}) \\ &\times \int \langle \mu_{j\alpha}(0) \mu_{j'\beta}(t) \rangle \langle e^{-i\mathbf{Q} \cdot \mathbf{R}_j(0)} e^{i\mathbf{Q} \cdot \mathbf{R}_{j'}(t)} \rangle e^{-iEt/\hbar} dt, \end{aligned} \quad (2.49)$$

This scattering cross section depends on the correlation between atomic coordinates. This demonstrates the fact that in addition to the magnetic behavior of the scattering system, crystal structure and dynamics also affect magnetic scattering.

Elastic magnetic scattering

In the previous sections, we saw that magnetic scattering depends on the spin-spin correlation function. Let us assume that a decrease in the crystal temperature is accompanied by an ordering of the magnetic moments of the atoms. In this case, the spins become correlated. If the ordering remains unchanged after the scattering event, and the correlations do not

depend on time, then the magnetic scattering is purely elastic. In this case, from Eq. (2.43) we get:

$$\left(\frac{d\sigma}{d\Omega}\right)_{\text{el}} = (\gamma r_0)^2 |\langle \mathbf{D}_\perp(\mathbf{Q}) \rangle|^2, \quad (2.50)$$

where

$$\mathbf{D}_\perp^+ \cdot \mathbf{D}_\perp = \sum_{\alpha, \beta} (\delta_{\alpha\beta} - \hat{\mathbf{Q}}_\alpha \hat{\mathbf{Q}}_\beta) \mathbf{D}_\alpha^+ \cdot \mathbf{D}_\beta. \quad (2.51)$$

If the scattering system is a periodic crystal, we have:

$$\mathbf{R}_j(t) = \mathbf{R}_l + \mathbf{r}_d + \mathbf{u}_j(t), \quad (2.52)$$

where \mathbf{R}_l is the coordinate of the l th unit cell, \mathbf{r}_d is the equilibrium position of the atom within the unit cell, and $\mathbf{u}_j(t)$ is the displacement of the atom from the equilibrium position.

Independently averaging the nuclear and electronic parts of Eq. (2.46), we get:

$$\langle \mathbf{D}(\mathbf{Q}) \rangle = \frac{1}{\gamma r_0} \sum_l \mathbf{F}_M(\mathbf{Q}) e^{i\mathbf{Q} \cdot \mathbf{R}_l}, \quad (2.53)$$

where the summation is carried out over all unit cells. Here $\mathbf{F}_M(\mathbf{Q})$ is a magnetic unit cell structure factor:

$$\mathbf{F}_M(\mathbf{Q}) = \gamma r_0 \sum_d f_d(\mathbf{Q}) \langle \boldsymbol{\mu}_d \rangle e^{i\mathbf{Q} \cdot \mathbf{r}_d} e^{-W_d(\mathbf{Q})}. \quad (2.54)$$

Finally, the elastic differential magnetic cross section can be written as

$$\left(\frac{d\sigma}{d\Omega}\right)_{\text{el}} = \frac{2\pi^3}{v_0} \sum_{\boldsymbol{\tau}_M} \delta(\mathbf{Q} - \boldsymbol{\tau}_M) |\mathbf{F}_{M\perp}(\boldsymbol{\tau}_M)|^2, \quad (2.55)$$

where

$$\mathbf{F}_{M\perp} = \hat{\mathbf{Q}} \times \mathbf{F}_M \times \hat{\mathbf{Q}}, \quad (2.56)$$

and $\boldsymbol{\tau}_M$ is the reciprocal lattice vector of the magnetic structure which can be written as $\boldsymbol{\tau}_M = \boldsymbol{\tau} \pm \mathbf{k}$. The \mathbf{k} vector in a propagation vector of the magnetic structure.

Inelastic magnetic scattering

Consider inelastic magnetic scattering. For this, let us return to the Eq. (2.49), which is the total cross section of magnetic neutron scattering on a crystalline magnetic material. This expression includes the product of the spin-spin and coordinate correlation functions $\mathbf{J}_{ii'}^{\alpha\beta}(t)$ and $\mathbf{I}_{ii'}(\mathbf{Q}, t)$:

$$\begin{aligned} \mathbf{J}_{ii'}^{\alpha\beta}(t) &= \langle \mu_{j\alpha}(0) \mu_{j'\beta}(t) \rangle, \\ \mathbf{I}_{ii'}(\mathbf{Q}, t) &= \langle e^{-i\mathbf{Q} \cdot \mathbf{R}_j(0)} e^{i\mathbf{Q} \cdot \mathbf{R}_{j'}(t)} \rangle. \end{aligned} \quad (2.57)$$

Each of these functions can be expressed as the sum of its value at $t = \infty$ and a time-dependent part:

$$\begin{aligned} \mathbf{J}_{ii'}^{\alpha\beta}(t) &= \mathbf{J}_{ii'}^{\alpha\beta}(\infty) + \mathbf{J}_{ii'}^{\prime\alpha\beta}(t), \\ \mathbf{I}_{ii'}(\mathbf{Q}, t) &= \mathbf{I}_{ii'}(\mathbf{Q}, \infty) + \mathbf{I}_{ii'}'(\mathbf{Q}, t). \end{aligned} \quad (2.58)$$

Using expressions (2.58), the total cross section of magnetic scattering (2.49) can be represented in the form of four terms, each of which corresponds to a certain type of magnetic scattering. The term $\mathbf{J}_{ii'}^{\alpha\beta}(\infty)\mathbf{I}_{ii'}(\mathbf{Q}, \infty)$ is giving rise to the elastic magnetic scattering. The term $\mathbf{J}_{ii'}^{\alpha\beta}(\infty)\mathbf{I}_{ii'}'(\mathbf{Q}, t)$ is responsible for the magnetovibrational scattering. As a result of this kind of scattering, the orientation of the electron spins remains unchanged, that is, the spin system is not excited. At the same time, magnetic interaction leads to the excitation or de-excitation of a phonon in the crystal lattice, thus magnetovibrational scattering is inelastic. The third term $\mathbf{J}_{ii'}^{\prime\alpha\beta}(t)\mathbf{I}_{ii'}(\mathbf{Q}, \infty)$ gives inelastic magnetic scattering. Finally, the last term $\mathbf{J}_{ii'}^{\prime\alpha\beta}(t)\mathbf{I}_{ii'}'(\mathbf{Q}, t)$ describes scattering that excites both the spin and lattice degrees of freedom.

For the general case of a crystal with a few magnetic ions per unit cell, the total magnetic cross section is given by:

$$\begin{aligned} \frac{d^2\sigma}{d\Omega dE} &= \frac{k_f}{k_i} \frac{(\gamma r_0)^2}{4\pi\mu_B^2} \sum_{\alpha\beta} (\delta_{\alpha\beta} - \hat{\mathbf{Q}}_\alpha \hat{\mathbf{Q}}_\beta) (1 - e^{-E/(k_B T)})^{-1} \\ &\times \sum_{dd'} e^{[W_{d'}(\mathbf{Q}) + W_d(\mathbf{Q})]} (\chi'')_{\alpha\beta}^{dd'}(\mathbf{Q}, E), \end{aligned} \quad (2.59)$$

where

$$\begin{aligned} (\chi'')_{\alpha\beta}^{dd'}(\mathbf{Q}, E) &= 4\pi\mu_B^2 f_d^*(\mathbf{Q}) f_{d'}(\mathbf{Q}) (1 - e^{-E/(k_B T)}) \\ &\times \sum_l e^{i\mathbf{Q}\cdot\mathbf{R}_l} e^{i\mathbf{Q}\cdot(\mathbf{r}_{d'} - \mathbf{r}_d)} \frac{1}{2\pi\hbar} \int_{-\infty}^{\infty} \langle \mu_{0d\alpha}(0) \mu_{ld'\beta}(t) \rangle e^{-iEt/\hbar} dt \end{aligned} \quad (2.60)$$

is the imaginary part of the generalized susceptibility $\chi_{\alpha\beta}^{dd'}(\mathbf{Q}, E)$.

Magnetic scattering by spin waves

To evaluate the cross section for magnetic scattering by spin waves, we can utilize the general formula (2.59). For a Bravais crystal, the imaginary part of the generalized susceptibility can be written as

$$\begin{aligned} \chi_{\alpha\beta}''(\mathbf{Q}, E) &= \pi g^2 \mu_B^2 (1 - e^{-E/(k_B T)}) \\ &\times \sum_l e^{i\mathbf{Q}\cdot\mathbf{R}_l} \frac{1}{2\pi\hbar} \int_{-\infty}^{\infty} \langle S_{0\alpha}(0) S_{l\beta}(t) \rangle e^{-iEt/\hbar} dt. \end{aligned} \quad (2.61)$$

After the evaluation of the matrix elements $\langle S_{0\alpha}(0)S_{l\beta}(t) \rangle$, the inelastic neutron scattering cross section from the spin waves can be represented by:

$$\begin{aligned} \frac{d^2\sigma}{d\Omega dE} = & \frac{k_f}{k_i} (\gamma r_0)^2 \frac{(2\pi)^3}{2v_0} \frac{g^2 S}{4} (1 + \hat{\mathbf{Q}}_z^2) f^2(\mathbf{Q}) e^{-2W(\mathbf{Q})} \\ & \times \sum_{\tau \mathbf{q}} \{ \langle n_{\mathbf{q}} + 1 \rangle \delta(\mathbf{Q} - \mathbf{q} - \boldsymbol{\tau}) \delta[E - \hbar\omega(\mathbf{q})] \\ & + \langle n_{\mathbf{q}} \rangle \delta(\mathbf{Q} + \mathbf{q} - \boldsymbol{\tau}) \delta[E + \hbar\omega(\mathbf{q})] \}, \end{aligned} \quad (2.62)$$

where the thermal average of $n_{\mathbf{q}}$ is

$$\langle n_{\mathbf{q}} \rangle = \{ e^{\hbar\omega_{\mathbf{q}}/k_B T} - 1 \}^{-1}. \quad (2.63)$$

The cross section in Eq. (2.62) consists of two terms for one magnon creation and annihilation. The delta functions in the cross section expression lead to the peaks in the inelastic neutron scattering from spin waves which satisfy

$$\mathbf{Q} = \boldsymbol{\tau} \pm \mathbf{q}, \quad (2.64)$$

$$E = \pm \hbar\omega(\mathbf{q}). \quad (2.65)$$

2.3 Instruments for neutron experiments

The main focus of this thesis is neutron spectroscopy. Some of the commonly used instruments for inelastic neutron scattering measurements are briefly described here, in particular, triple-axis (TAS) and time-of-flight (TOF) spectrometers.

2.3.1 Kinematics of a scattering experiment

Any scattering experiment consists in measuring the properties of a neutron beam before and after scattering by a sample. The initial and final beams can be characterized by the wave vectors \mathbf{k}_i and \mathbf{k}_f , respectively. In each act of scattering, the laws of conservation of momentum and energy must be satisfied:

$$\mathbf{Q} = \mathbf{k}_f - \mathbf{k}_i, \quad (2.66)$$

$$\hbar\omega = E_i - E_f = \frac{\hbar^2}{2m_n} (k_i^2 - k_f^2), \quad (2.67)$$

where $k = 2\pi/\lambda$, λ and m_n are wave length and mass of a neutron. According to the expressions (2.66, 2.67), when a neutron is scattered on a crystal, the momentum $-\hbar\mathbf{Q}$ and energy $\hbar\omega$ are transferred to it. If the scattering is elastic, then the energy and, accordingly,

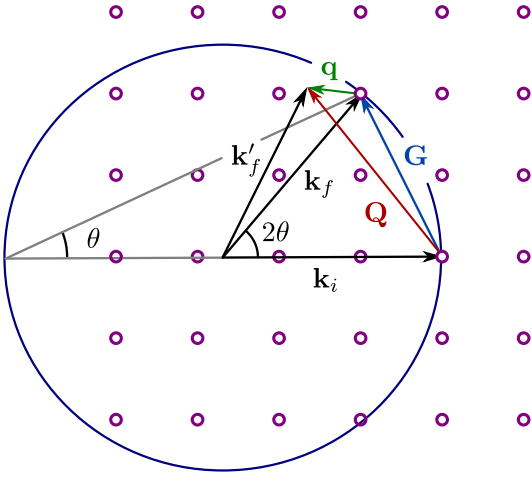


Figure 2.8: Ewald circle.

the absolute value of the wave vector do not change. In the case of inelastic scattering, energy is transferred to the crystal or from the crystal; accordingly, the scattering occurs with energy loss or gain of the neutron.

Understanding neutron scattering experiments requires dealing with reciprocal space. In Fig. 2.8, the points represent reciprocal lattice vectors for a 2D crystalline solid. The direction of the vector \mathbf{k}_i coincides with the direction of the neutron beam incident on the

crystal. Vector \mathbf{k}_i is chosen so that it ends at the origin of the reciprocal space. A circle of radius k_i is centered at the start of vector \mathbf{k}_i . The diffraction conditions are satisfied if this circle passes through some nonzero reciprocal lattice vector \mathbf{G} . The diffracted beam propagates in the direction of vector \mathbf{k}_f , which according to the momentum conservation law is equal to $\mathbf{k}_i + \mathbf{G}$, i.e. its end coincides with the reciprocal lattice point crossed by the circle. This circle is called the Ewald circle, its analog in 3D space is the Ewald sphere.

In a case of elastic scattering, the magnitude of \mathbf{Q} can be expressed as

$$|\mathbf{Q}| = |\mathbf{G}| = 2|\mathbf{k}_i| \sin(\theta), \quad (2.68)$$

where 2θ is the angle between the incident and the final beam for the Bragg condition. This expression represents the well known Bragg's law. If we introduce the lattice spacing d and express the wave number as $k = 2\pi/\lambda$, Eq. (2.68) can be written in the more familiar form:

$$\lambda = 2d \sin(\theta). \quad (2.69)$$

In a diffraction experiment, it is possible to measure any point in reciprocal space. This is achieved by choosing an appropriate value of \mathbf{k}_i and angle θ , which are responsible for the magnitude of vector \mathbf{Q} . The direction of vector \mathbf{Q} in reciprocal space is adjusted by rotating the sample relative to \mathbf{k}_i .

In the case of inelastic scattering, the length of the neutron wave vector changes, $|\mathbf{k}_i| \neq |\mathbf{k}_f|$, thereby providing an energy exchange with the sample. In an experiment on inelastic scattering, one of the vectors ($|\mathbf{k}_i|$ or $|\mathbf{k}_f|$) is fixed, while the other changes. In the case of a single-crystal sample, it is customary to use the relative momentum \mathbf{q} , which is defined in the first Brillouin zone. This is because the energies depend only on the momentum relative to the nearest reciprocal lattice vector. Figure 2.8 illustrates the relationship between the

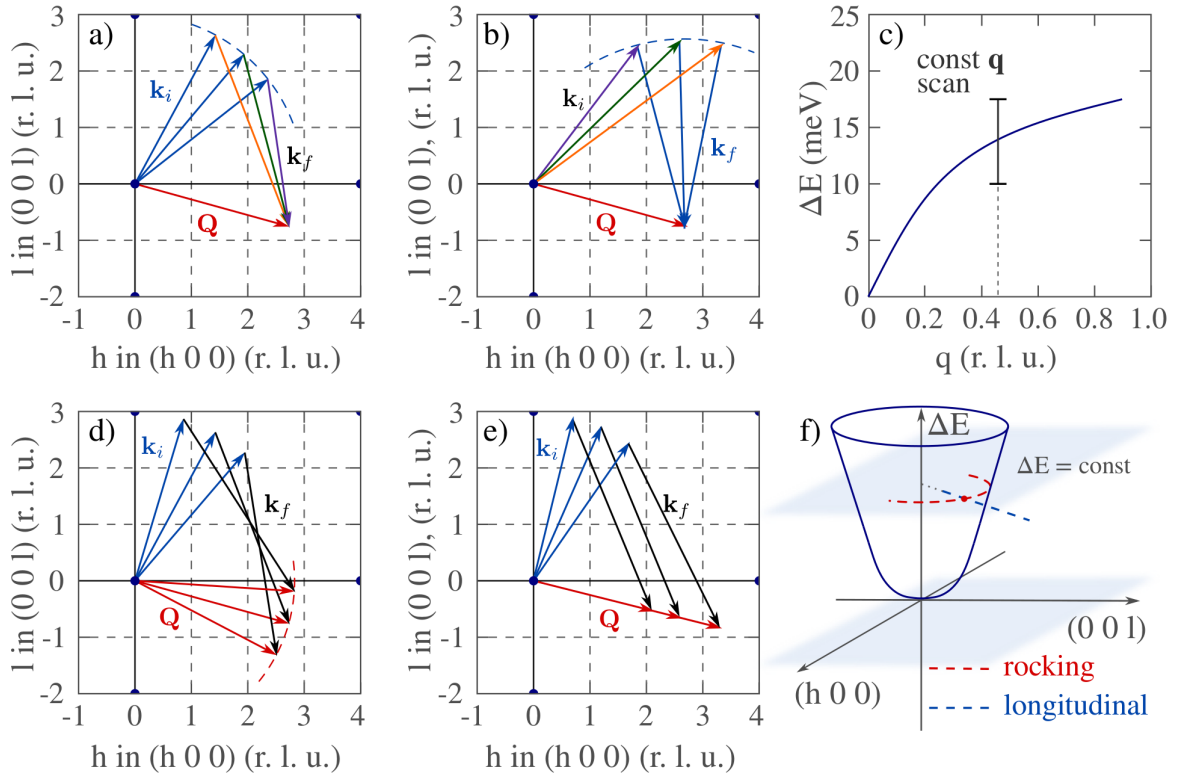


Figure 2.9: Typical TAS scans. Vector diagrams of different scans: (a, b) constant \mathbf{Q} scans with fixed \mathbf{k}_i and \mathbf{k}_f , (d, e) constant E scans with fixed Q (rocking scan) and \mathbf{Q}/Q (longitudinal scan). (c, f) Sketches of the trajectories in the energy-momentum space covered by the corresponding constant- Q and constant- E scans.

momentum transfer vector \mathbf{Q} , reciprocal space vector \mathbf{G} , and vector \mathbf{q} :

$$\mathbf{Q} = \mathbf{G} + \mathbf{q}. \quad (2.70)$$

From the vector diagram in Fig. 2.8, it is seen that every point in reciprocal space \mathbf{Q} can be accessed with an infinite number of combinations of \mathbf{k}_i and \mathbf{k}_f . What combinations are usually preferred in practice and why will be explained below.

2.3.2 The triple-axis spectrometer

Typical scans

During each individual measurement on a classical TAS spectrometer, a signal is measured at one specific point in four-dimensional (4D) energy-momentum space $(\mathbf{Q}, \hbar\omega)$. In a typical experiment, measurements are taken in the form of scans — sequences of measurements of individual points taken in a specific order. There are two main types of scans — constant energy ΔE and constant \mathbf{Q} . These scans are shown schematically in Fig. 2.9. For the

convenience of processing and interpreting the experiment, it is customary to fix the modulus of the wave vector of the incident or scattered beam in scans with constant \mathbf{Q} . Panels 2.9 (a, b) contain vector diagrams for scans with constant \mathbf{k}_i and \mathbf{k}_f , respectively. Panel 2.9 (c) shows the trajectory in the energy-momentum space corresponding to constant- \mathbf{Q} scans. Most of the Brillouin zone is normally measured with constant- \mathbf{Q} scans. If one needs to measure a stiff dispersion mode in the vicinity of the Brillouin zone center, it is reasonable to use the constant- E scans. These scans assume measurements at a fixed value of energy transfer and a simultaneous change in position in reciprocal space. Usually, either the length (rocking scan) or the direction (longitudinal scan) of vector \mathbf{Q} is fixed. Figures 2.9 (d, e) show rocking and longitudinal scans, respectively. Figure 2.9 (f) shows schematically the lines in the energy-momentum space that are covered during each of the constant-energy scans. An elastic rocking scan is commonly used to accurately align the sample at the start of the experiment. For this, the Bragg peak is selected with previously known coordinates in reciprocal space. The instrument and the orientation of the specimen are adjusted in such a way that the vector \mathbf{Q} corresponds to the desired peak, and a rocking scan is performed in the vicinity of the specified point of reciprocal space. Thus, we determine the direction of vector \mathbf{Q} corresponding to the desired structural peak. Continuing to align the sample, a longitudinal scan should be performed. This will make it possible to refine the absolute value of vector \mathbf{Q} corresponding to a given Bragg peak. This procedure, carried out sequentially on several peaks, allows one to determine the orientation of the sample with high accuracy, so necessary for the correct processing of the measurement results. For dispersion mapping, longitudinal scans are performed at nonzero energy transfer values.

Normalization of the counting rates

During the experiment, we count the neutrons arriving at the detector after being scattered by the sample. The detector counting rate determines the scattering function $S(\mathbf{Q}, \omega)$, the determination of which is the goal of most neutron experiments. However, the counting rate of detector Z_{det} depends not only on the scattering function but also on the characteristics of the elements of the spectrometer itself [27]:

$$Z_{\text{det}} \propto I_{\text{init}}(k_i) R_{\text{mono}}(k_i) \frac{1}{k_i} S(\mathbf{Q}, \omega) R_{\text{ana}}(k_f) P_{\text{det}}(k_f), \quad (2.71)$$

where $I_{\text{init}}(\mathbf{k}_i)$ is the intensity of the incident beam at used \mathbf{k}_i , $R_{\text{mono}}(k_i)$ and $R_{\text{ana}}(k_i)$ are the reflectivities of the crystals of the monochromator and analyzer, and $P_{\text{det}}(k_f)$ is the efficiency of the detector. For correct data interpretation, each measurement in the scan must be performed with the same statistics. For this, we use a monitor installed after the

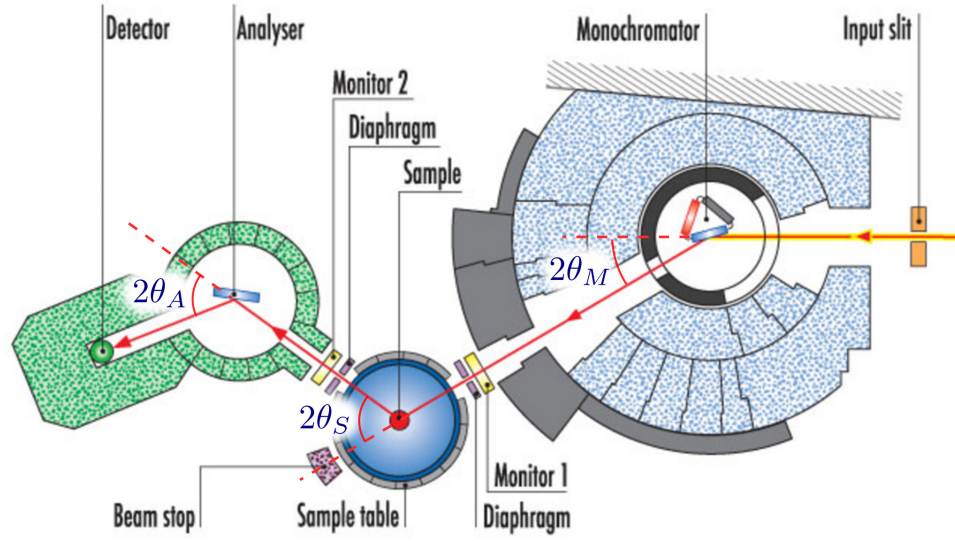


Figure 2.10: The classical setup of a typical triple-axis spectrometer IN8 (ILL, Grenoble). The three axes are the monochromator axis, sample axis, and analyser axis. Adapted from [28].

monochromator and before the sample. Thus, each measurement in the scan is carried out until the monitor detects a certain number of neutrons, which is expected to be:

$$Z_{\text{monitor}} \propto I_{\text{init}}(k_i) R_{\text{mono}}(k_i) \frac{1}{k_i}. \quad (2.72)$$

Thus, because the count rate in the detector is normalized to the monitor, the real count rate in the detector is:

$$Z'_{\text{det}} \propto S(\mathbf{Q}, \omega) R_{\text{ana}}(k_f) P_{\text{det}}(k_f). \quad (2.73)$$

From this formula it can be seen that the count rate of the detector normalized to the monitor depends only on \mathbf{k}_f and does not depend on \mathbf{k}_i . In the case of scans with constant \mathbf{k}_f [see Fig. 2.9 (b)], this dependence disappears, which greatly facilitates data processing.

Instrument components

From its invention by Brockhouse in 1961 to the present day, the three-axis spectrometer has been the most important instrument in neutron spectroscopy. Its uniqueness lies in the ability to measure the scattering function $S(\mathbf{Q}, \omega)$ at almost any point in the four-dimensional (\mathbf{Q}, ω) space. The instrument owes its name to its design, namely the presence of three axes of rotation — the monochromator axis, the sample axis, and the analyser axis. Figure 2.10 shows a simplified diagram of a classic triple-axis spectrometer, namely the

IN8 thermal-neutron spectrometer located at ILL, Grenoble. Let us follow the path of the neutron beam and discuss the main elements of this instrument. A neutron beam coming from a source, such as a nuclear reactor, has a wide spectrum of wavelengths and represents the so-called “white” beam. When the beam hits the monochromator, it is Bragg-reflected from the monochromator crystals (usually these are single crystals of copper, germanium, beryllium, silicon, or pyrolytic graphite). Reflection occurs by Bragg diffraction of the beam on a set of planes determined by the orientation of the monochromator crystal. As a consequence of Bragg’s law, only neutrons of a strictly defined wavelength (reflections of higher orders can be dealt with using special filters) are diffracted by this set of planes, while others pass through the monochromator without scattering or experience incoherent scattering. The angle between the direction of the initial “white” beam and the direction of the monochromatic beam is $2\theta_M$, where θ_M is the Bragg’s angle for the corresponding wavelength and the monochromator orientation. Thus, changing the θ_M and $2\theta_M$ angles of the monochromator, we select neutrons of the required wavelength λ_i , and, accordingly, the wave vector \mathbf{k}_i . The monochromator is surrounded by a heavy shielding with a channel that allows a monochromatic neutron beam to hit the sample. On its way to the sample, the beam passes monitor 1, the purpose of which is to control the number of neutrons hitting the sample and was discussed in more detail in the previous section on the normalization of count rates. The diaphragm is used to cut the beam to the desired size. This is to minimize harmful signals from the surroundings of the sample (e.g. aluminum or copper holder). Having reached the sample, the neutron beam is scattered on it, and the reflected beam, having deviated by an angle $2\theta_s$ from the \mathbf{k}_i direction, continues its way to the detector. In addition to the rotation of the spectrometer elements around the axis passing through the sample table, the design of the instrument provides for the rotation of the sample at a given angle ψ around its axis. This rotation is necessary to control the direction of the incident beam \mathbf{k}_i relative to the direct and, accordingly, the reciprocal space of the sample under investigation. Having passed the second aperture and monitor 2, the diffracted beam enters the analyzer. The rotation of the analyzer selects the angle of reflection θ_A corresponding to the particular final wave vector \mathbf{k}_f . After reflection from the analyzer, the beam finally enters the detector, where it is registered. By varying the angles θ_M , θ_s , ψ , and θ_A , as well as the absolute values of wave vectors \mathbf{k}_i and \mathbf{k}_f accordingly, it is possible to reach any point in the horizontal plane of reciprocal space for any value of energy transfer. This plane is usually called the scattering plane. In practice, however, the reachable region of (\mathbf{Q}, ω) space is limited by considerations of intensity and resolution.

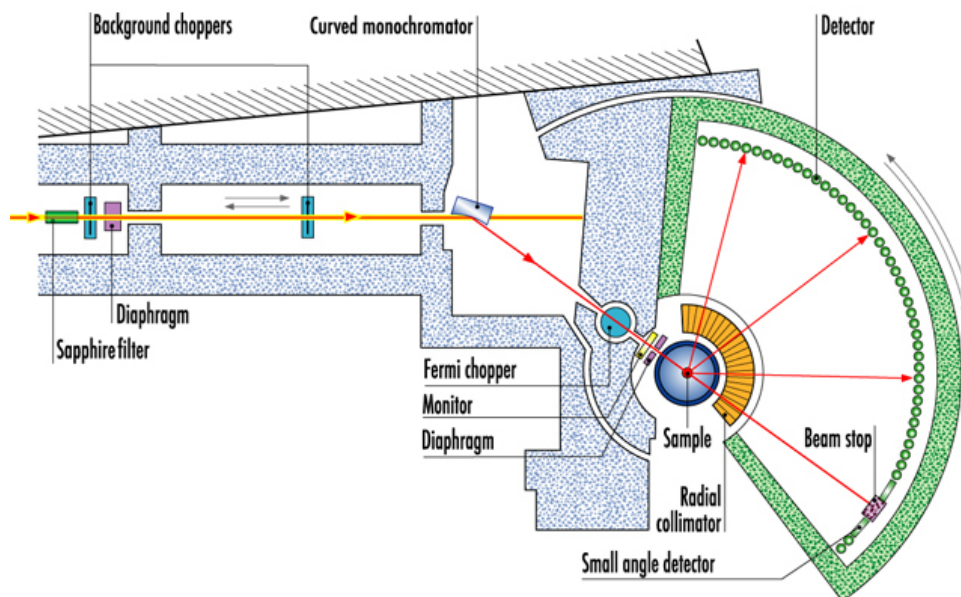


Figure 2.11: The high-flux time-of-flight spectrometer IN4C (ILL, Grenoble). Reproduced from [28].

Today, the control of triple-axis spectrometers is entrusted to a computer. During the pioneering studies of Brockhouse, the adjustment of all three axes of the spectrometer was carried out manually, which required incomparably greater precision and accuracy from the experimenter.

The classic TAS can only work in a step-by-step mode, measuring one single point in the (Q, ω) space per instrument setup and has a long counting time. However, in recent decades, many improvements in the design of spectrometers have been developed, thanks to which it became possible to cover large areas of reciprocal space simultaneously. One concept is to have multiple analyzers that cover a larger solid angle. This allows for increased data acquisition speed and space coverage for each instrument setup. Examples of such solutions are FLATCONE at ILL, MACS at NCNR, RITA-2 at PSI, CAMEA at ESS, and BAMBUS at MLZ [29–33].

2.3.3 Time-of-flight spectrometer

This spectrometer owes its name to the fact that its operation is based on measuring the time of flight (TOF) of scattered neutrons between the sample and the detector, the distance between which is known with high accuracy. Thus, by measuring the time of flight, you can

determine the speed of neutrons v_n . This allows us to calculate their energy:

$$E_n = \frac{1}{2} m_n v_n^2, \quad (2.74)$$

where m_n is the neutron mass.

TOF instruments can be divided into two classes: direct-geometry and indirect-geometry spectrometers. In instruments of the first type, the energy of the incoming beam E_i is selected using a crystal or chopper, and the final energy E_f is measured using a time of flight. In spectrometers with indirect geometry, everything is exactly the opposite — the energy of the incoming beam E_i is measured using the time of flight, the energy of scattered neutrons E_f is determined using a crystal or filter.

Both types of spectrometers are used on both continuous and pulsed neutron sources. Since the method requires knowing the flight time with high accuracy, neutrons must arrive at the sample in the form of short pulses of about $20 \mu\text{s}$ duration. Choppers are used to create the time structure of the neutron pulses on continuous neutron sources. There must be a time between such pulses, sufficient for all the neutrons scattered on the sample to reach the detector.

As an example, consider the schematic drawing of the IN4C time-of-flight spectrometer (ILL, Grenoble) shown in Fig. 2.11. The main components of this spectrometer, which are responsible for the preparation of a monochromatic neutron pulse incident on the sample, are two background choppers, a double-focusing monochromator, and a Fermi chopper. Background choppers are fast-pulsing beam shutters that act as a low-pass filter. In this way, they cut off most of the fast neutrons and gamma rays that can lead to background noise in the measured spectrum. To eliminate fast neutrons, in addition to background choppers, a sapphire filter can be installed in the beam. Following further, a neutron beam with a thermal spectrum falls on a double-focusing monochromator – a mosaic consisting of 55 individual single crystals. Here the selection of neutrons with a strictly defined energy takes place. Thanks to its adjustable double focusing, the monochromator focuses the diverging beam on a small sample surface, thereby providing the high intensity of incoming neutrons. Now the focused monochromatic beam must be split into short pulses. For this, a Fermi chopper is used. The Fermi chopper rotates at speeds of the order of 40,000 rpm, which makes it possible to generate short pulses with a duration of $10\text{--}50 \mu\text{s}$. Striking the sample, a short parallel monochromatic neutron pulse is scattered by the sample. The typical time-of-flight for neutrons between the sample and the detector is $1\text{--}5 \text{ ms}$. The neutron energy loss or gain during scattering by a sample is analyzed by recording the time of arrival of neutrons at the detector, as well as the angle at which they are detected. Using large arrays of detectors, it is possible to obtain a lot of information about the structure and dynamics of the sample.

The TOF spectra measured at various angles are further treated to obtain the scattering function $S(\mathbf{Q}, \omega)$.

Since spallation sources initially produce a short-pulse neutron beam structure, they are ideally suited locations for TOF instruments. The accelerator provides a polychromatic neutron pulse, which is subsequently converted into pulses of the required duration using a chopper.

Summing up, one can say that a triple-axis spectrometer is an ideal tool for studying dispersive excitations in single-crystal samples using energy and momentum scans. This tool can only produce one data point per measurement but with a high \mathbf{Q} resolution and high intensity concentrated in a narrow region of energy-momentum space, making it indispensable for parametric studies (e.g. measurements at a single wave vector as a function of temperature, magnetic field, or pressure). High beam intensity and the possibility of using multianalyser-multidetector systems make TAS a powerful tool for INS measurements.

At the same time, the TOF spectrometers have proven excellent for overview studies of samples across the whole energy-momentum space. These tools are indispensable for getting an overview of the excitation spectrum $S(\mathbf{Q}, \omega)$ with high energy resolution at several fixed values of external parameters. The development of short-pulse spallation sources has provided a significant increase in beam intensity, making TOF an indispensable tool for mapping the energy-momentum space that sometimes leads to unexpected discoveries.

Chapter 3

ZnCr₂Se₄

3.1 Introduction

3.1.1 Chromium spinels

It is hard to overestimate the significance of the frustration concept in the field of modern magnetism. Its essence lies in the competition between dominant terms in a Hamiltonian, that generally destabilizes a physical system, and, in extreme cases, leads to a massive degeneracy of the ground state [34]. These conditions allow higher-order perturbations to become decisive, that otherwise play only a minor role and therefore are very hard to study experimentally. When the perturbations are not sufficient to get rid of the degeneracy completely, the entropic reasons can favor some state among the others via the so-called “order-by-disorder” mechanism [35]. After all, there are systems that preserve extensive degeneracy down to 0 T and fail to order despite strong interactions [36–38]. Thereby, magnetically frustrated systems are characterized by extremely diverse physics and continue to surprise researchers even after a vast amount of studies.

There are two main mechanisms of frustration in defect-free magnetic systems. The first one is based on the geometrical properties of the lattice formed by magnetic ions in a solid. The underlying triangular motifs prohibit simultaneous minimization of energy on all pairwise bonds assuming only nearest-neighbor (NN) coupling. In the second one, two or more inequivalent bonds of comparable strength contest among themselves. From the experimental point of view, the former mechanism is more desirable, as it promotes the frustration by the symmetry of the lattice, whereas the latter one relies on the fine-tuning of the exchange parameters, and therefore can rarely provide order-free states. However, the bond-frustrated systems often possess chiral ground states [3] and exhibit multiferroic properties [39].

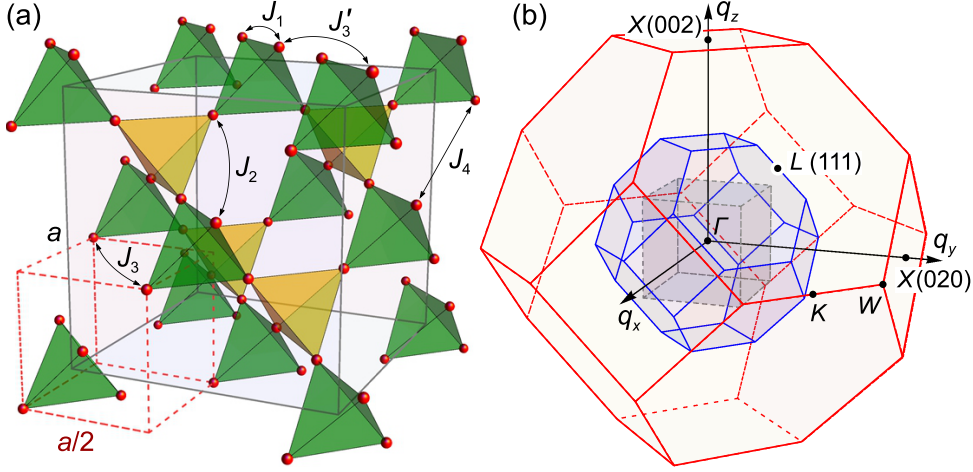


Figure 3.1: (a) Pyrochlore-lattice structure, representative of the magnetic Cr sublattice in ACr_2X_4 spinels. Small spheres represent Cr^{3+} ions. The pyrochlore lattice can be described either as an fcc arrangement of separated Cr_4 tetrahedra formed by NN bonds (large cubic unit cell, solid lines) or as a half-filled fcc lattice of Cr^{3+} ions with a twice smaller lattice parameter (small cubic unit cell, dashed lines). We also show different exchange paths corresponding to $J_1 \dots J_4$ interactions that are discussed in the text. (b) The simple-cubic Brillouin zone with dimensions $2\pi/a$ (central cube), and the two unfolded Brillouin zones corresponding to fcc lattices with parameters a and $a/2$ (truncated octahedra). The high-symmetry points are marked according to the large unfolded zone. Reproduced from Ref. [40].

The pyrochlore lattice is a 3D network of corner-sharing tetrahedra [see Fig. 3.1 (a)], and it attracts a lot of interest as various spin models on this lattice give rise to the simplest 3D frustrated spin systems. Even for classical spins, the Heisenberg model on the pyrochlore lattice hosts a wide range of different ground states. Considering only the antiferromagnetic NN interactions results in a classical spin liquid [41, 42], exhibiting no long-range magnetic order down to zero temperature. This is explained by strong geometric frustration that leads to a highly degenerate classical ground state. However, the inclusion of further-neighbor interactions relieves this frustration and stabilizes various ordered ground states, among them ferromagnetism, single- or multi- \mathbf{q} spin spirals, nematic order, and other exotic phases [43–47].

Chromium spinels provide great opportunities to investigate magnetic interactions between classical spins on the structurally ideal pyrochlore lattice. They belong to a large family of $A^{2+}B_2^{3+}X_4^{2-}$ spinels which crystallize to a cubic $Fd\bar{3}m$ structure. Its A , B , and X ions occupy $8a$ ($1/8, 1/8, 1/8$), $16d$ ($1/2, 1/2, 1/2$), and $32e$ (x, x, x) Wyckoff positions, respectively. Chromium spinels have the general formula ACr_2X_4 , where A and X are non-magnetic ions and Cr^{3+} is the magnetic cation in the $3d^3$ configuration [48]. Cr ions form an undistorted pyrochlore lattice with $S = 3/2$ and $L = 0$. The classical Heisenberg model,

$$H = \sum_{ij} J_{ij} \mathbf{S}_i \cdot \mathbf{S}_j, \quad (3.1)$$

is justified by the negligibly small magneto-crystalline anisotropy [49–51]. Thus we consider throughout the study $J_{ij} \equiv J_n$ if sites i and j are n th neighbors [see Fig. 3.1 (a)].

Depending on the Cr-X-Cr angle, the dominant nearest-neighbor exchange coupling varies from AFM (for $X = \text{O}$) to FM ($X = \text{Se}, \text{S}$) [48]. If dominant NN interactions between the Cr spins residing on a pyrochlore lattice are AFM, the system is geometrically frustrated. However, *ab initio* calculations show that most of Cr-spinels also have non-negligible higher-order exchanges [48]. Generally, this diminishes the frustration and induces an order [46]. Geometrical frustration mechanism is implemented in some chromium oxides, such as ZnCr_2O_4 and CdCr_2O_4 [52, 53]. When the dominant interaction is FM, the lattice becomes geometrically non-frustrated, and unlike in the AFM case, the further-nearest-neighbor exchanges can promote the overall frustration. The bond frustration is responsible for the formation of the helical ground states in ZnCr_2S_4 , HgCr_2S_4 , and ZnCr_2Se_4 far below the Curie-Weiss temperatures [54–58]. In our recent study, the classical phase diagram was constructed taking into account the exchanges up to the 4th nearest neighbor [40], fixing the first one to FM. It shows a rich variety of possible states depending on the relative strength of J_2 and J_3 , among which are collinear FM, single-, and multi- \mathbf{q} spin structures.

To estimate the range and relative strengths of coupling constants J_n in chromium spinels, Yaresko [48] performed *ab initio* calculations to extract exchange parameters up to the 4th nearest neighbor for various compounds of the chromium spinels family. Calculations showed that the NN interaction J_1 changes gradually from antiferromagnetic in some oxides to ferromagnetic in sulfides and selenides, while the next-nearest-neighbor (NNN) interaction J_2 is noticeably weaker than the antiferromagnetic J_3 exchange parameter (see Table 3.1). For the HgCr_2O_4 system, J_1 can be even weaker than J_2 (or comparable, depending on the effective Coulomb repulsion U), so that the third-nearest-neighbor interaction J_3 may become dominant. Therefore, the existing theoretical phase diagram restricted to only NN and NNN interactions [44] appears insufficient for a realistic description of these materials. The importance of the two 3rd-nearest-neighbor exchange paths on the pyrochlore lattice has also been emphasized for the spin- $\frac{1}{2}$ molybdate Heisenberg antiferromagnet $\text{Lu}_2\text{Mo}_2\text{O}_5\text{N}_2$, where J'_3 and J''_3 have opposite signs and dominate over J_2 . It was recently conjectured that this may lead to an unusual “gearwheel” type of a quantum spin liquid [59].

3.1.2 Classical phase diagram for chromium spinels

An inspection of the theoretically predicted exchange parameters for various ACr_2X_4 spinels presented in Ref. [48] reveals non-negligible exchange integrals up to the fourth-nearest

Compound	$J_2/ J_1 $	$J_3/ J_1 $	$J_4/ J_1 $	ground state	Refs.
HgCr_2O_4	0.1714	0.471	0	AFM	[60]
ZnCr_2S_4	0.0395	0.198	-0.014	(00q) spiral	[54]
CdCr_2S_4	0.0065	0.116	-0.015	FM	[61]
HgCr_2S_4	0.0222	0.111	-0.013	(00q) spiral	[55, 56]
ZnCr_2Se_4	0.0102	0.169	-0.018	(00q) spiral	[57, 58]
CdCr_2Se_4	-0.0071	0.101	-0.013	FM	[61]
HgCr_2Se_4	-0.0014	0.109	-0.013	FM	[62]
Experimental values:					
ZnCr_2Se_4	0.0118	0.170	-0.014	this work, [40]	

Table 3.1: Ratios of the exchange constants in different chromium spinels after Ref. [48], taken for a moderate effective Coulomb repulsion $U = 2$ eV. For each compound, its experimentally measured ground state is also given: antiferromagnetic (AFM), ferromagnetic (FM), or proper-screw spin spiral. The bottom row shows experimental values for ZnCr_2Se_4 estimated from our INS data. Reproduced from Ref. [40].

neighbor, J_4 , which is ferromagnetic in all the studied compounds. The third-nearest-neighbor exchange constants are, on the other hand, antiferromagnetic. Note that the pyrochlore lattice exhibits two inequivalent sets of third-nearest neighbors. Following Ref. [48], we treat their corresponding exchange couplings as equal, $J'_3 = J''_3 \equiv J_3$, since deviations are considered to be small. The classical ground state depends only on the ratios between the exchange constants, which can be much more accurately predicted in first-principles calculations than their absolute values. Here we restrict our attention to the sulfides, selenides, and HgCr_2O_4 with ferromagnetic NN interactions, $J_1 < 0$. In Table 3.1, we summarize the calculated ratios $J_2/|J_1|$, $J_3/|J_1|$, and $J_4/|J_1|$ for all seven compounds considered in Ref. [48] (to be specific, we list the ratios for LSDA + U with $U = 2$ eV), along with their experimentally determined ground states.

We determine the classical phase diagram using a direct energy minimization scheme [44]. We consider a pyrochlore lattice (periodic boundary conditions imposed) with typically $L = 8$ unit cells (containing 16 spins) in each spatial direction, resulting in $N = 16 \cdot L^3 = 2^{13}$ spins in total. Starting from a random initial spin configuration, one randomly picks a lattice site i and rotates its spin \mathbf{S}_i antiparallel to its local field defined as $\mathbf{h}_i = \partial H / \partial \mathbf{S}_i = \sum_{j \neq i} J_{ij} \mathbf{S}_j$, thereby minimizing the energy and simultaneously keeping the spins normalized. Once an

energetically minimal spin configuration has been found, the object of interest is the spin structure factor $S(\mathbf{q}) = \frac{1}{N} \left| \sum_j \mathbf{S}_j \exp(i\mathbf{q} \cdot \mathbf{r}_j) \right|^2$ with its magnetic Bragg peaks.

The pure J_1 - J_2 phase diagram already has been computed [44]. As mentioned before, we consider only ferromagnetic J_1 . Table 3.1 reveals that the couplings J_4 of all considered spinels are ferromagnetic and roughly equal, $J_4/|J_1| \approx -0.014$. Thus we restrict our investigation of the phase diagram to $J_4/|J_1| = -0.014$, but we checked for all spinels that the ground state remains unchanged when taking into account the couplings listed in Table 3.1. Therefore we map out the classical phase diagram for $-0.05 \leq J_2/|J_1| \leq 0.2$ and $0 \leq J_3/|J_1| \leq 0.5$ as presented in Fig. 3.2. We find five different phases: ferromagnetic (FM), $(00q)$ proper-screw spiral, cuboctahedral stack (CS), multiply modulated commensurate spiral (MMCS), and the $(\frac{1}{8} \frac{1}{2} \frac{7}{8})$ phase. Quite generally, we have observed for $J_2/|J_1| > 0.1$ and $J_3/|J_1| > 0.1$ that the energy landscape becomes extremely flat. In order to yield reliable results we had to increase system sizes drastically, for some parameter settings we even used $L = 32$ corresponding to more than half a million spins. For dominant $J_1 < 0$ we find FM order, but both antiferromagnetic J_2 and J_3 destabilize the phase. For sufficiently strong $J_3 > 0$ (and not too large J_2) there is a phase transition from the FM to the $(00q)$ helical phase. The wave vector q changes continuously from the phase transition line ($q = 0$) up to a maximal value of $q = 7/8$ for large J_3 (color-coded in increments of $q = 1/8$ in Fig. 3.2). For $J_3 = 0$ and $J_2/|J_1| \geq 0.2$ we find the CS phase of Ref. [44] characterized by Bragg peaks at three of the four $\{\frac{1}{2} \frac{1}{2} \frac{1}{2}\}$ -type q vectors. Finite J_3 stabilizes the phase down to smaller values of J_2 . Further increase of J_3 drives the system into the multi- \mathbf{q} MMCS phase which is also present in a very small parameter range of the J_1 - J_2 phase diagram [44]. This state is characterized by four main Bragg peaks at $(\frac{1}{4} \frac{3}{4} \frac{1}{2})$, $(\frac{3}{4} \frac{1}{4} \frac{1}{2})$, $(\frac{1}{4} \frac{3}{4} \frac{3}{2})$ and $(\frac{3}{4} \frac{1}{4} \frac{3}{2})$, and a subdominant peak at $(\frac{3}{4} \frac{3}{4} 0)$ (or symmetry related combinations of these vectors, respectively). Making J_3 even larger eventually turns the system's ground state into an exotic phase with four dominant Bragg peaks at $\mathbf{q} = (\pm \frac{1}{8} \frac{1}{2} \pm \frac{7}{8})$ and $(\pm \frac{7}{8} \frac{1}{2} \pm \frac{1}{8})$. To our best

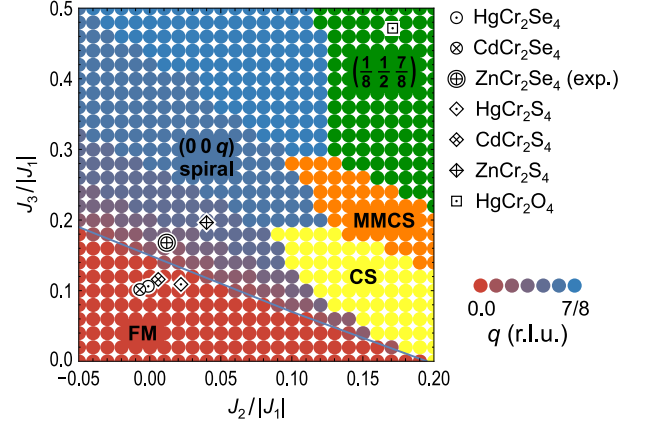


Figure 3.2: Classical J_2 - J_3 phase diagram for $J_1 = -1$ and $J_4/|J_1| = -0.014$ containing five phases: ferromagnetic (FM), $(00q)$ proper-screw spiral with the corresponding q -value shown in color code, the cuboctahedral stack (CS), the multiply modulated commensurate spiral (MMCS), and the $(\frac{1}{8} \frac{1}{2} \frac{7}{8})$ phase. In addition, the location of the seven spinel compounds with ferromagnetic J_1 is indicated by the symbols. For details see the text and Table 3.1. Reproduced from Ref. [40].

knowledge, this phase has not been mentioned before in the literature, and we simply call it the $(\frac{1}{8}\frac{1}{2}\frac{7}{8})$ phase.

The phase diagram in Fig. 3.2 contains all spinels listed in Table 3.1, and it is interesting to compare the results of our calculations with available experimental data. CdCr_2S_4 , HgCr_2Se_4 , and CdCr_2Se_4 have been reported to possess ferromagnetic ground states [61, 62] in agreement with our simulations. HgCr_2S_4 develops a $(00q)$ spiral configuration with a temperature-dependent pitch [55], but the experimental results emphasize a strong tendency to ferromagnetic correlations [56]; in our phase diagram it is located in the FM phase close to the spiral phase. The material of highest interest is, of course, ZnCr_2Se_4 where both experiment and simulation consistently find a $(00q)$ helix with $q = 0.468$ (or 0.28 \AA^{-1}). ZnCr_2S_4 has been reported to host a similar proper-screw spin structure in the temperature range $8 \text{ K} < T < 15 \text{ K}$ with $q = 0.787$ [54], which agrees fairly well with our simulated value $q = 0.625$ based on the coupling constants from Table 3.1. This spinel undergoes a structural phase transition at 8 K with a change of the magnetic order. The only oxide in our list is HgCr_2O_4 , where Bragg peaks corresponding to $\mathbf{q}_1 = (100)$ and $\mathbf{q}_2 = (10\frac{1}{2})$ were measured [60]. The compound undergoes, however, a structural phase transition into an orthorhombic phase [63] for which our pyrochlore description is of course inadequate. Otherwise, according to its exchange couplings, HgCr_2O_4 would be located in the $(\frac{1}{8}\frac{1}{2}\frac{7}{8})$ phase.

We emphasize that our phase diagram, based on the *ab initio* parameters of Ref. [48], agrees fairly well with the available experimental results. The major discrepancies are associated with structural transitions of the spinels ZnCr_2S_4 and HgCr_2O_4 , leading to distortions or even different crystal structures. Since both effects cannot be captured by our simulations, the discrepancies between experiment and theoretical modeling in these particular cases are plausibly understood.

3.1.3 Crystal structure and spin-spiral order in ZnCr_2Se_4

Among the materials listed in Table 3.1, characterized by ferromagnetic NN interactions, only ZnCr_2Se_4 and HgCr_2S_4 host an incommensurate spin-spiral ground state resulting from the band frustration imposed by competition with further-neighbor interactions. The proper-screw spin structure of ZnCr_2Se_4 has a short helical pitch, λ_h , of only 22.4 \AA [57, 64], as compared to that of 42 \AA in HgCr_2S_4 (which in addition increases with temperature to $\sim 90 \text{ \AA}$ at $T = 30 \text{ K}$) [55]. This results in magnetic Bragg peaks in ZnCr_2Se_4 that are sufficiently remote from the commensurate structural reflection, with a propagation vector $(0 \ 0 \ q_h)$, where $q_h \approx 0.28 \text{ \AA}^{-1}$ [57, 64]. Therefore, low-energy magnetic excitations emerging from

different Bragg peaks are easy to resolve, which makes ZnCr_2Se_4 a perfect model material for investigations of low-energy spin dynamics in symmetric (Yoshimori-type) [3,65] helimagnets that are common among multiferroics [39,66]. Moreover, from the comparison of the Néel temperature, $T_N = 21$ K, with the Curie-Weiss temperature $\Theta_{CW} = 90$ K, the frustration ratio of $\Theta_{CW}/T_N = 4.3$ can be estimated, suggesting a considerable degree of frustration in this system [67]. The small single-ion anisotropy energy in ZnCr_2Se_4 is evidenced by the magnetic resonance data [50], by the gapless high-resolution neutron powder spectra down to at least 0.05 meV in energy [68], as well as by the absence of any anisotropy-induced deformation of the spin spiral. According to a recent study [69], such a deformation would lead to the appearance of odd-integer higher-order magnetic Bragg peaks in neutron diffraction that are absent in the neutron-diffraction patterns of ZnCr_2Se_4 [57,64].

ZnCr_2Se_4 crystallizes in the normal spinel ($Fd\bar{3}m$) structure at room temperature having 8 formula units per simple-cubic unit cell with a lattice constant $a = 10.497$ Å [57,70]. Cr^{3+} ions form a pyrochlore magnetic sublattice which consists of corner-sharing tetrahedra [Fig. 3.1 (a)]. The sublattice can be described as a face-centered-cubic (fcc) arrangement of equally oriented Cr_4 tetrahedra (shown in a dark color) or as a half-filled fcc lattice of individual Cr^{3+} ions with a twice smaller unit cell, as shown in Fig. 3.1 with dashed lines. This allows us to introduce a larger unfolded Brillouin zone in reciprocal space, as shown in Fig. 3.1 (b), by analogy with the procedure described for the structurally related compound Cu_2OSeO_3 by Portnichenko *et al.* [71].

Whilst at high temperatures the crystal structure of ZnCr_2Se_4 is cubic, upon crossing the AFM transition the crystal is seen to undergo a distortion which is concurrent with the magnetic transition [72]. Initial measurements indicated that this was a cubic to tetragonal distortion with an c/a ratio of around 0.99920(3) at 4.2 K [72]. Later measurements, however, indicated that the crystal symmetry of the ground state is orthorhombic, where $a \cong b > c$ and [54,73]. The concomitant structural and magnetic phase transitions would suggest that the structural distortion is magnetically driven, which is supported by the observation of a spin-lattice coupling at T_N by ultrasound measurements [74] as well as by neutron diffraction measurements [64]. It is seen that the spin spiral structure propagates along the crystal axis which experiences the maximum distortion at the AFM transition [70,72], which is the c axis in the previous definition.

The distinctive feature of a frustrated system is the presence of short-range correlations way above the ordering temperature. In ZnCr_2Se_4 they were observed by μSR [68] below ~ 70 K. The negative thermal expansion, that appears here at the same temperature scale [75], can also be attributed to the correlated spin fluctuations; this however would also imply the

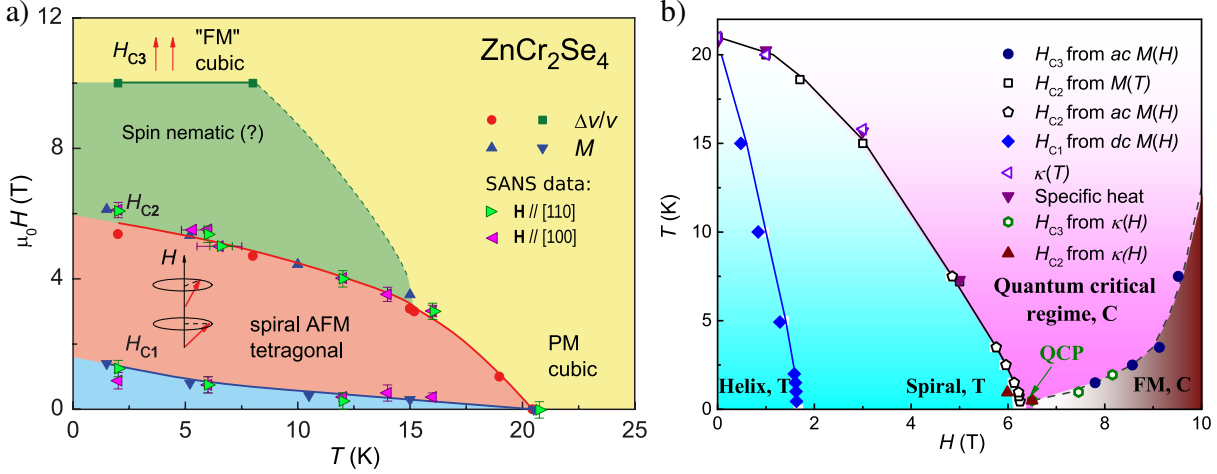


Figure 3.3: (a) Applied magnetic field vs. temperature phase diagram for ZnCr_2Se_4 , reproduced from Ref. [74]. Here we superimpose the phase transition points deduced from our SANS data onto the original graph constructed from magnetisation (M) and sound velocity ($\Delta v/v$) measurements. (b) Phase diagram of ZnCr_2Se_4 resulting from ac and dc magnetic susceptibilities, specific heat, and thermal conductivity measurements. The low-temperature data reveals the presence of a quantum critical point. Reproduced from Ref. [77].

presence of strong spin-lattice coupling. The confirmation of this assumption we find in the excellent study [76], where authors demonstrate the presence of the ferroelectric properties in the compound. On the side, they showed how the structure adapt to the rearrangement of the magnetic spiral from $\mathbf{q} = (q\ 0\ 0)$ to $(0\ q\ 0)$ through the extremely sensitive marker, namely, the electrical polarization.

So far, the origin of the strong spin-lattice coupling in the Cr-spinels remains unclear. In the high-temperature cubic phase, the Cr t_{2g} shell is half-filled, quenching the orbital moment to zero. Thus, no on-site spin-orbit interaction is expected. In the recent NMR study [78], the authors observe the partial transfer of the magnetic moment to the neighboring Se-sites. This mechanism can potentially induce finite orbital component and, therefore, facilitate the spin-lattice interaction. The theory, although confirms this possibility, estimates only insignificant corrections [48].

The magnetic phase diagram of the compound has been investigated with a number of techniques: magnetization, ultrasound [74], and SANS [58]. The summarising phase diagram is shown in Fig. 3.3. Below the ordering temperature, Cr^{3+} spins form an incommensurate helical structure with a propagation vector pointing along the $[001]$ direction (blue and red phases in Fig. 3.3 (a)). In the absence of an external magnetic field, there are three possible domains with mutually perpendicular directions of the spin spirals, corresponding to the cubic crystal symmetry. Upon application of a small magnetic field $H < H_{C1}$, the low-temperature structure acquires the FM component along the field direction. After the field exceeds H_{C1} , the domain selection takes place (blue curve in Fig. 3.3 (a)), favoring the

helix with the smallest angle between the propagation vector and the field. This offers the possibility to prepare a single-domain state either by cooling the sample in a magnetic field or by applying and removing the field at base temperature. Further amplification of the field decreases the conical angle of the magnetic structure until it collapses at the critical value of H_{C2} , which at 2 K is 6 T, although at this field the lattice is nearly ferromagnetically polarised, and at low temperatures with increasing field the system gives way to a new high-field phase which is proposed to be a spin-nematic state [74]. Here, the rate of polarization with the field is greatly reduced in contrast to the spin-spiral state, yet the spin lattice continues to polarise with the increasing field until H_{C3} , where the system then enters the fully saturated ferromagnetic state [74]. Both the domain selection and the saturation transition fields decrease upon heating, but independent from the field direction [58].

The last revision of the phase diagram [77] reveals unusual dynamical properties at the saturation transition that are manifested in the low-temperature T^2 behavior of the specific heat, and a qualitative change in the thermal conductivity. It was shown, that upon decreasing temperature, the high-field transition (at ~ 10 T) approaches the saturation one, with potential merging at 0 K (see Fig. 3.3 (b)). The authors interpret their findings with a field-driven quantum phase transition at 6.5 T.

3.2 SANS measurements

The high-field phase between the saturation transition and the transition to a fully polarised state is of great interest, as it remains uncharacterized in this compound. Initially, this area on the phase diagram was interpreted as a spin-nematic phase [74] but the recent study by Gu *et al.* [77] attributed it to a quantum critical regime. In particular, the arrangement of the unsaturated components of the magnetic moments in real space remains a puzzle. Using neutron scattering we searched for signs of magnetic ordering within this phase to shed light on its character and demonstrate that the unpolarised component of the spins above H_{C2} remain fully disordered without forming any long- or short-range spiral order.

3.2.1 Experimental method

The experiment was performed on a mosaic of co-aligned single crystals of ZnCr_2Se_4 with a total mass ~ 1 g, prepared by chemical transport reactions and characterized as described elsewhere [74]. During the measurements, the magnetic field was applied horizontally, i.e. perpendicular to the neutron beam. We used two orientations of the sample with either the $[100]$ or $[110]$ crystallographic direction pointing along the field, whereas the

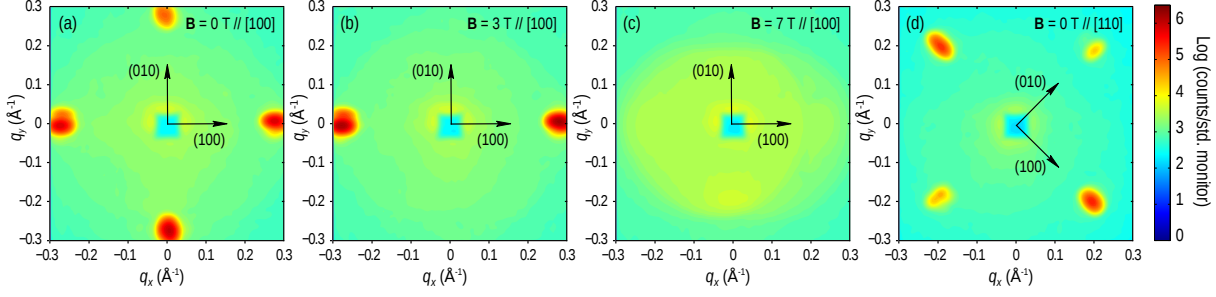


Figure 3.4: Diffraction patterns from the magnetic structure of ZnCr_2Se_4 , measured at a base temperature of 2 K for several magnetic fields. (a)–(c) Diffraction patterns for the magnetic field, aligned along the $[100]$ direction, in applied fields of (a) 0 T, (b) 3 T and (c) 7 T. (d) Diffraction pattern at 0 T for the realigned sample so that the magnetic field could be applied along the $[110]$ direction. Diffraction patterns are a sum over all rocking angles corresponding to the observed Bragg reflections, presented on a logarithmic intensity scale, and the axes q_x and q_y are in the laboratory frame. Reproduced from Ref. [58].

$[001]$ direction for zero rocking angle was pointing along the neutron beam in both cases. These two configurations correspond to the field orientation along the natural propagation vector of the magnetic structure and halfway between two such propagation vectors in neighboring magnetic domains, respectively. For the field parallel to $[100]$, the sample mass was approximately one gram, consisting of six crystals co-aligned with x-ray Laue diffraction and mounted on an aluminum plate. For the field applied parallel to $[110]$, only four crystals from the mosaic were used. These were placed within a cryomagnet with a base temperature of around 2 K and a maximum field of 11 T. Neutron diffraction measurements were performed at the SANS-I instrument of the Paul Scherrer Institute, with the incoming neutron wavelength set to 4.7 \AA . The sample together with the magnetic field was then rocked over the full range of angles corresponding to the accessible Bragg reflections, with background measurements taken above T_N to eliminate all nonmagnetic contributions to the signal. All measurements were taken after cooling the sample to base temperature in zero field and then applying the required magnetic field. The exception to this is a scan at the base temperature which was taken in decreasing field and the following scan in temperature. These exceptions are indicated where applicable.

3.2.2 Results

Figure 3.4 shows a selection of representative neutron diffraction patterns from each of the distinct states and orientations observed during the experiment at the base temperature of 2 K. Each image is a sum over rocking angles in the vicinity of the Bragg condition for each peak, set to a logarithmic intensity scale. Panels (a) – (c) show diffraction patterns from

the first orientation, where the magnetic field was applied parallel to the $[100]$ direction, which is horizontal in these figures. The diffraction pattern in panel (a) was taken in zero field, and we can clearly see the two sets of Bragg reflections resulting from the domains aligned along the $[010]$ and $[100]$ directions, which in this image are vertical and horizontal, respectively. The third set of Bragg peaks, along the one remaining $[001]$ direction, are not accessible within this experimental geometry. Panel (b) is taken in an applied field of 3 T, and it can be seen that domain selection has taken place as only one set of Bragg peaks remains, which belong to the domain whose propagation vector is parallel to the magnetic field. Panel (c) was taken in an applied field of 7 T. This is above H_{C2} , within the region of the phase diagram attributed to a quantum critical regime, and no magnetic signal can be seen in this data. This measurement is also representative of data taken both

elsewhere in the spin-nematic phase and at higher temperatures, within the paramagnetic phase. This indicates that the weak scattering within this data originates from the instrument background. Panel (d) shows the diffraction pattern observed in the second experimental configuration, where the sample was remounted in such a way that the field was also applied horizontally but the crystal axes have been rotated by 45° such that the field is applied along $[110]$, equidistant from the propagation vectors of the two magnetic domains. This diffraction pattern was observed at all fields, throughout the long-range ordered phase below H_{C2} , indicating that the propagation vector is insensitive to the direction of the magnetic field. In this orientation, the domain-selection transition at H_{C1} , was still observed as an increase in the Bragg peak intensity of the two equivalent domains at the expense of the third domain whose propagation vector is orthogonal to the applied magnetic field in Fig. 3.4 (d).

Figure 3.5 presents the intensity of the Bragg reflections within the domains which are preferentially selected at H_{C1} , illustrated in Fig. 3.4 as a function of both field and

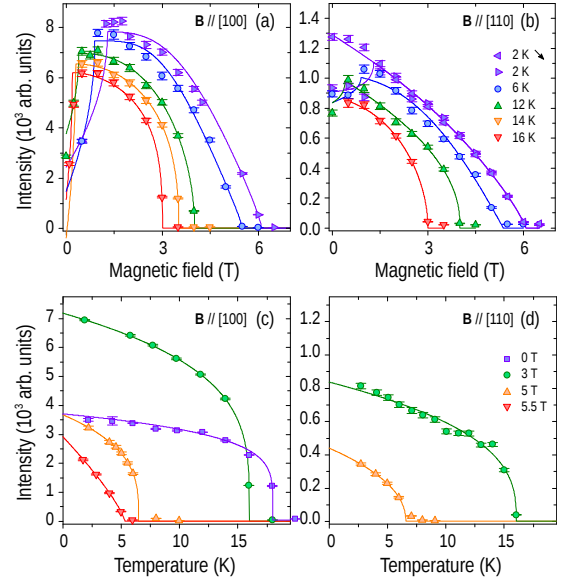


Figure 3.5: Dependence of the magnetic Bragg intensity as a function of both applied magnetic field and sample temperature. (a-b) Intensity of the Bragg reflections as a function of magnetic field applied along (a) the $[100]$ direction and (b) the $[110]$ direction. (c-d) Intensity of the Bragg reflections as a function of temperature for magnetic fields applied along (c) $[100]$ and (d) $[110]$. The lines are a guide for the eyes. Intensity is given in arbitrary units, and is not comparable between the $[100]$ and $[110]$ directions due to a change in sample mass between orientations. Reproduced from Ref. [58].

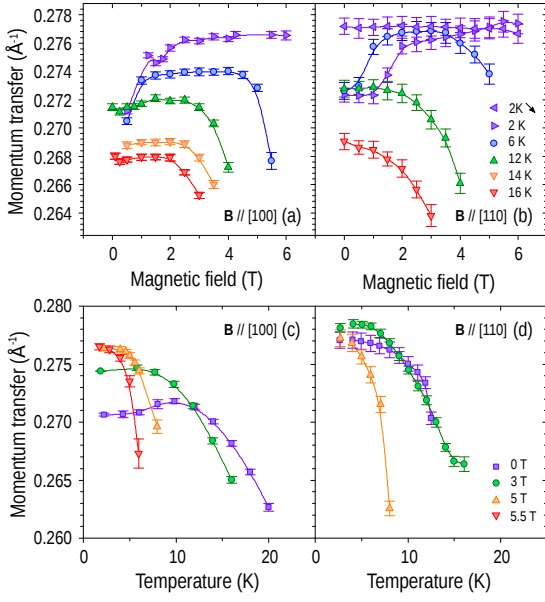


Figure 3.6: The scattering vector of the Bragg reflections from the magnetic structure as a function of both field and temperature. (a) Scattering vector as a function of magnetic field applied along the $[100]$ direction. (b) The same for magnetic field applied along the $[110]$ direction. (c) Scattering vector as a function of temperature for magnetic field applied along the $[100]$ direction. (d) The same for magnetic field applied along the $[110]$ direction. The lines are a guide for the eyes. Reproduced from Ref. [58].

temperature, for magnetic field orientations along both $[100]$ and $[110]$. The data in panel (a) represent the intensity of the Bragg reflections as a function of the magnetic field, applied after zero-field cooling along $[100]$. Here, we see that there is a rapid increase in Bragg intensity at the low magnetic field, in the same region where the domain selection transition takes place. Panel (b) shows the corresponding intensity of the Bragg reflections as a function of the magnetic field applied along the $[110]$ direction. It shows the same behaviour as for the field applied along $[100]$ in panel (a), however the magnitude of the increase in Bragg intensity as a result of domain selection is approximately twice smaller. This is fully consistent with the number of domains selected for each field orientation, which is 1 out of 3 for $\mathbf{H} \parallel [100]$ and 2 out of 3 for $\mathbf{H} \parallel [110]$. These measurements were also taken after zero-field cooling, except

for one scan at 2 K, shown in figure 3.5(b), done with decreasing field. This measurement shows no decrease of intensity across the domain selection transition, and instead, the signal strength increases continuously down to zero field, indicating that the domain distribution is not affected by the removal of a magnetic field. After accounting for the domain selection, for all measurements, we observe a decrease in Bragg intensity as a function of increasing magnetic field until it reaches zero at H_{C2} , with no Bragg scattering observed between H_{C2} and H_{C3} within the covered region of momentum space. Panel (c) shows the intensity as a function of temperature for magnetic fields of 0, 3, 5 and 5.5 T applied along $[100]$. All curves show an order-parameter-like monotonic decrease, with a sharp fall-off in intensity at T_N . Panel (d) displays the diffracted intensity of the Bragg reflections for magnetic fields applied along the $[110]$ direction. This shows the same general behavior as for fields applied along $[100]$, where the intensity falls off with increasing temperature and reaches zero at T_N .

Figure 3.6 shows the propagation vector of the magnetic structure, q , as a function of both applied magnetic field and temperature. Panels (a) and (b) depict q as a function of magnetic field applied along the $[100]$ and $[110]$ directions, respectively, at temperatures of 2, 6, 12, 14 and 16 K. Generally, the changes in q are weak, on the order of a few percent. The most striking feature of the data in both of these panels is the rapid increase in the propagation vector at low fields seen in the low-temperature measurements. This occurs between 1 and 2 T at 2 K, and it is clear from the diffraction patterns that this change in q coincides with the domain-selection transition as the Bragg spots from domains perpendicular to the magnetic field disappear. The location of this transition in a magnetic field is suppressed with increasing temperature, and so it is not seen at higher temperatures. Panel (b) also displays the scan at 2 K in decreasing fields, which expectedly shows no rapid change in q , since domain selection only occurs when applying a magnetic field after zero-field cooling, whereas the removal of the magnetic field at the base temperature does not alter the domain distribution. We see that in both orientations, at higher temperatures, there is a slight decrease in q when approaching the phase transition at H_{C2} . Panels (c) and (d) show q as a function of increasing temperature for the same two magnetic field directions. All these measurements were taken after cooling the sample in zero field, except for the 0 T measurement in panel (d), as this was taken after the decreasing field scan at 2 K shown in panel (b), to remain in the domain-selected state for consistency with the other curves. As a result of this different field history, the shallow maximum seen in the 0 T scan in panel (c), where the magnetic field was applied along $[100]$ after zero-field cooling, is not observed in the same measurement for the field applied along $[110]$ in panel (d), where the domain selection transition was deliberately circumvented. Figure 3.3 (a) shows the magnetic field and temperature phase diagram for ZnCr_2Se_4 , reproduced from Ref. [74]. We have superimposed the data points indicating either domain selection or a phase transition that resulted from the fits to our field- and temperature-dependent SANS measurements onto this diagram. Within the experimental uncertainty, our data for both field directions are in excellent agreement with the previous measurements.

3.2.3 Discussion

Our neutron-scattering measurements revealed that the magnetic signal from the spin-spiral structure always vanishes at the transition line H_{C2} , regardless of whether the system is undergoing a transition to the paramagnetic state or into the proposed high-field state attributed to a quantum critical regime. We observed no other Bragg scattering within the high-field phase. We can, therefore, establish the absence of any long-range order for the

unsaturated component of the spin within this region. From our investigation, we can claim the absence of any such signal within the q -range 0.062 to 0.30 \AA^{-1} , unless it lies outside the $(h\ k\ 0)$ scattering plane, which we consider unlikely given the robustness of the $[1\ 0\ 0]$ propagation direction of the spin-spiral observed throughout our measurements.

We observe the domain selection transition, which can be seen directly in figures 3.4 (a) and (b), in agreement with earlier measurements [74]. Here, domains with propagation vectors perpendicular to the magnetic field are removed, and the Bragg intensity in the selected domains increase rapidly, as seen in figures 3.5 (a) and (b), as a result of the increase in a volume fraction of the remaining domains. Furthermore, this transition is also seen in the length of the scattering vector, q . As the system lowers the number of magnetic domains, q increases, which corresponds to a slight decrease in the length of the spin-spiral structure in real space. In the helimagnetic compound MnSi, an application of pressure causes a shortening of the spin-spiral length [79]. Recalling that in ZnCr_2Se_4 the spin-spiral lies along the axis that undergoes the greatest distortion at T_N [70, 72], these observations suggest that in the multi-domain state the structural distortion induces a strain in the crystal lattice which affects the spin-spiral length, which is then removed upon entering the single-domain state at H_{C1} . In general, both the magnetic structure and the phase transition lines are surprisingly insensitive to the direction of the applied magnetic field. While there is a clear difference in the selection of a single domain for fields applied parallel to $[1\ 0\ 0]$ and the selection of two domains for fields applied along $[1\ 1\ 0]$, beyond this the magnetic field dependence for both orientations are nearly identical. Firstly, the direction of the propagation vector of the magnetic structure is rigid against varying magnetic field directions, only aligning along main crystallographic axes rather than following the field direction. Secondly, the phase diagram is identical regardless of the direction of the applied field, with both the domain selection transition and the spin-spiral transition taking place at the same temperature and field for both $\mathbf{H} \parallel [1\ 0\ 0]$ and $\mathbf{H} \parallel [1\ 1\ 0]$. We illustrate this in figure 3.3 (a). It is clear that the observed transitions fully coincide, within experimental uncertainties, irrespective of the direction of the applied field. This is surprising, as one might expect the projection of the magnetic field on the direction of \mathbf{q} to be important, which differs by a factor of $\sqrt{2}$ between the two experimentally chosen geometries. Even the domain selection transition, which is expected to be sensitive to different angles between the applied field and the propagation vector in different domains, turns out to be fully isotropic in ZnCr_2Se_4 . We note that this behavior is in line with the observation that the magnetization of ZnCr_2Se_4 also seems to be invariant with respect to the direction of the applied magnetic field [76], indicating that the development of the conical spin-structure proceeds at the same rate regardless of the

projection of magnetic field onto the propagation direction of the spiral. We also see that the change of the propagation vector as a function of both field and temperature is similar for both directions of the applied magnetic field, with a reduction in q with increasing field or temperature, shown in figure 3.6. However, the magnetic structure seems more robust against this change in q for fields applied parallel to the crystal axis than for the field applied along $[1\ 1\ 0]$. Therefore, while the precise magnetic structure does weakly depend on the magnetic field direction, the magnetic polarization of the lattice and subsequent transitions do not.

3.2.4 Summary

In summary, we have observed Bragg reflections from the helimagnetic structure in ZnCr_2Se_4 , finding a systematic variation with temperature and field of the spin-spiral pitch length. Particularly, crossing the domain selection transition causes an abrupt jump in the propagation length of the magnetic structure of the order of a few percent. With increasing the field to H_{C2} , we see a gradual order-parameter like decrease in the diffracted neutron intensity in agreement with the observation that the screw-like magnetic structure transforms into a conical spiral as the spin lattice polarises under the application of a field. Whilst previous magnetization measurements have indicated that there still remains an unpolarised component of the spins within the intermediate field phase directly above H_{C2} , we observe no magnetic Bragg reflections within this region, which is concurrent with the hypothesis that this state does not break the translational symmetry of the crystal.

3.3 Pseudo-Goldstone magnons

3.3.1 Instrumental conditions for the experiments

We have used thermal- and cold-neutron time-of-flight (TOF) and triple-axis spectroscopy (TAS) techniques to map out dispersions of magnetic excitations in ZnCr_2Se_4 in a broad range of energies. The advantage of the TOF method is the possibility to obtain data covering the whole 4-dimensional (4D) energy-momentum space $(\mathbf{Q}, \hbar\omega)$ in a single measurement. Further, the combination of data collected with high-energy ($E_i = 20$ and 70 meV) neutrons at the ARCS spectrometer [80] at ORNL, Oak Ridge, and low-energy ($E_i = 3.27$ meV or $\lambda_i = 5$ Å) neutrons at the IN5 spectrometer [81] at ILL, Grenoble, provides an overview of the whole magnon spectrum together with high-resolution imaging of low-energy excitations.

Experiments were performed on a mosaic of the same co-aligned single crystals of ZnCr_2Se_4 with a total mass ~ 1 g, which were used for SANS measurements. For the ARCS experiment (setup 1), the sample was mounted in such a way that the (HHL) plane was horizontal. The experiment was performed without magnetic field in the multi-domain state at the base temperature of $T = 5$ K. We performed rocking scans for incoming neutron energies of 20 and 70 meV, which correspond to the energy resolution of 0.87 and 3.4 meV respectively, defined as the full width at half maximum of the incoherent elastic line. We then processed the data using the HORACE software package [82, 83]. The 4D datasets were symmetrized during data reduction by combining statistics from all symmetry-equivalent directions in the same Brillouin zone.

To confirm the positions of high-energy excitations at certain high-symmetry points of the Brillouin zone, we supplemented our TOF data with thermal-neutron TAS measurements [84] carried out using the IN8 thermal-neutron spectrometer at ILL (setup 2). Here the sample was mounted inside an “orange”-type cryostat in the $(HK0)$ scattering plane, so that the $W(320)$ point could be reached. The spectrometer was operated with the vertically focused pyrolytic graphite (PG) monochromator and analyzer, with the final neutron wave vector fixed to $k_f = 4.1 \text{ \AA}^{-1}$, and a PG filter installed between the sample and the analyzer. The collimation before and after the sample was set to $30'$ and $40'$, respectively. The resulting energy resolution, calculated for this spectrometer configuration at 25 meV energy transfer, was about 4 meV.

The cold-neutron TOF experiment [85] at IN5, ILL (setup 3), was carried out using the same sample placed in the “orange”-type 2.5 T cryomagnet. This time the sample was rotated about the (111) axis so that its $(11\bar{2})$ direction was pointing vertically (parallel to the direction of the magnetic field). Correspondingly, the equatorial scattering plane was spanned by the mutually orthogonal $(1\bar{1}0)$ and (111) vectors. In order to stabilize one helimagnetic domain, we cooled down the sample in a vertical magnetic field of 1.5 T, with $\mathbf{B} \parallel (11\bar{2})$. In this geometry, the $(00q_h)$ ordering vector forms an angle of 35.3° with the field direction, leading to a twice larger projection of the field on this axis as compared to the ordering vectors of the two other domains, $(0q_h0)$ and (q_h00) , that are inclined at 65.9° with respect to the magnetic field. As a consequence, out of the three possible helimagnetic domains, only the one with the propagation vector along the (001) direction is selected by the applied field. When the base temperature of 1.5 K was reached, the magnetic field was switched off, and the measurement was performed in the single-domain state in zero field with the incident neutron wavelength of 5 \AA and the elastic energy resolution of 0.084 meV.

In this scattering geometry, neither of the three propagation vectors lies within the horizontal scattering plane. However, they are sufficiently short to be covered by the out-of-plane acceptance range of the position-sensitive TOF detector bank despite the limitation from the vertical opening angle of the cryomagnet. Therefore, magnetic satellites of the (000), (111), and (222) zone centers could be accessed in this configuration, which would be unfeasible on most instruments restricted to the horizontal scattering plane. During data reduction, the complete dataset was then converted into energy-momentum space using the conventional basis vectors of the simple-cubic crystallographic unit cell, so that the presentation of the data is not affected by the rotated sample mounting. We visualize the obtained results by presenting 2D cuts through the 4D dataset that are taken along high-symmetry momentum directions. To designate points in \mathbf{Q} space, we will use reciprocal lattice units corresponding to the simple-cubic unit cell ($1 \text{ r.l.u.} = 2\pi/a$), whereas high-symmetry points will be marked according to the unfolded Brillouin zone following the standard notation for an fcc lattice [71].

Finally, we performed detailed spin-gap measurements at the cold-neutron TAS PANDA [86] operated by JCNS at MLZ, Garching (setup 4). They were also carried out at zero field in the single-domain state, which was prepared by field-cooling the sample in a field of 2.5 T using the 5 T vertical-field cryomagnet. The same mosaic sample was remounted with its [001] axis pointing vertically, along the magnetic field direction, which resulted in the selection of the domain with the $(00q_h)$ ordering vector, whereas the accessible range of \mathbf{Q} space was restricted to the $(HK0)$ scattering plane spanned by the propagation vectors of the two suppressed domains, $(q_h 00)$ and $(0q_h 0)$. Their Bragg intensities were reduced by a factor of ~ 200 as a result of domain selection. To resolve these wave vectors at low scattering angles (in the vicinity of the direct beam), we operated the spectrometer with the horizontally flat but vertically focused monochromator and analyzer. The final neutron energy was fixed at $E_f = 3.0 \text{ meV}$ ($k_f = 1.2 \text{ \AA}^{-1}$), providing an energy resolution of about 0.1 meV. A cold beryllium filter was used to suppress higher-order contamination from the monochromator.

3.3.2 ZnCr_2Se_4 magnon spectrum in multi-domain state

TOF measurements in the multi-domain state

We will start the presentation of our results with the higher-energy data measured at the ARCS spectrometer in the multi-domain state. Figure 3.7 shows typical energy-momentum cuts along several high-symmetry lines in \mathbf{Q} space that are parallel to the (001) and (110)

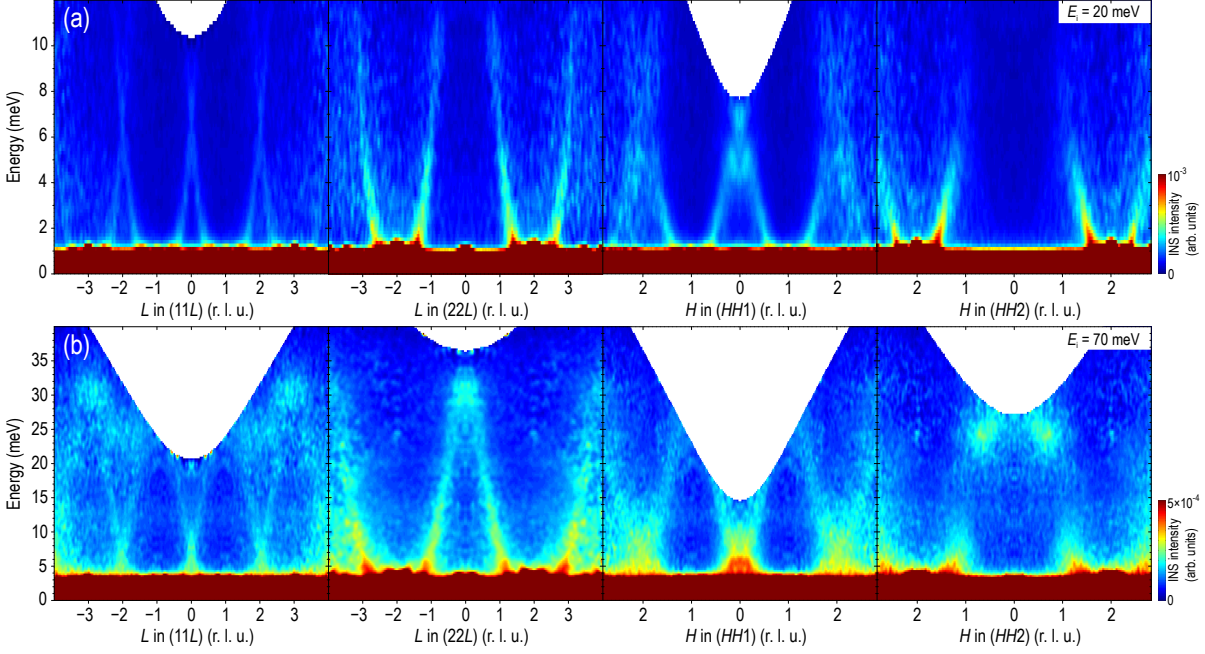


Figure 3.7: Energy-momentum cuts through the TOF data measured at the ARCS spectrometer (setup 1), plotted along high-symmetry directions after symmetrization respecting the cubic crystal symmetry. All the presented data were measured at the base temperature of 5 K with incident neutron energies of 20 meV (top row) and 70 meV (bottom row). The momentum integration range in directions orthogonal to the image was set to ± 0.14 r.l.u. Reproduced from Ref. [40].

directions. Panels (a) and (b) show low- and high-energy datasets ($E_i = 20$ and 70 meV), respectively. In the $(22L)$ and $(HH2)$ cuts, we clearly see intense magnon branches emanating from incommensurate magnetic satellites of the (222) Bragg peak, while similar modes near the (111) and (113) points are noticeably weaker. This behavior of the dynamic structure factors can be explained using the approach of unfolded Brillouin zones, which was detailed in Ref. 71 for another compound with a structurally similar magnetic sublattice. One characteristic energy scale revealed in Fig. 3.7 (a) is given by the crossing point between equivalent magnon branches in the $(11L)$ direction, located at ~ 6.8 meV.

In Fig. 3.7 (b), we additionally observe high-energy modes near the top of the magnon band, between 25 and 35 meV. While there is no energy gap separating the high- and low-energy modes, unlike in Cu_2OSeO_3 [71], the intensity is certainly enhanced near the top of the magnon band, as best seen along the $(HH2)$ direction (rightmost panel). This is reminiscent of the situation in another recently studied helimagnet with a similar pitch of the spin spiral, $\text{Sr}_3\text{Fe}_2\text{O}_7$, where an intense and well separated high-energy magnon branch was observed at a similar energy of 25 meV [87]. However, the low-energy behavior of the spin waves in $\text{Sr}_3\text{Fe}_2\text{O}_7$ is considerably different. There, apart from the steeply dispersing outward branches, we observed M-shaped inner branches of helimagnetic spin waves connecting the incommensurate ordering vectors, which extended up to ~ 4 meV in energy. This form

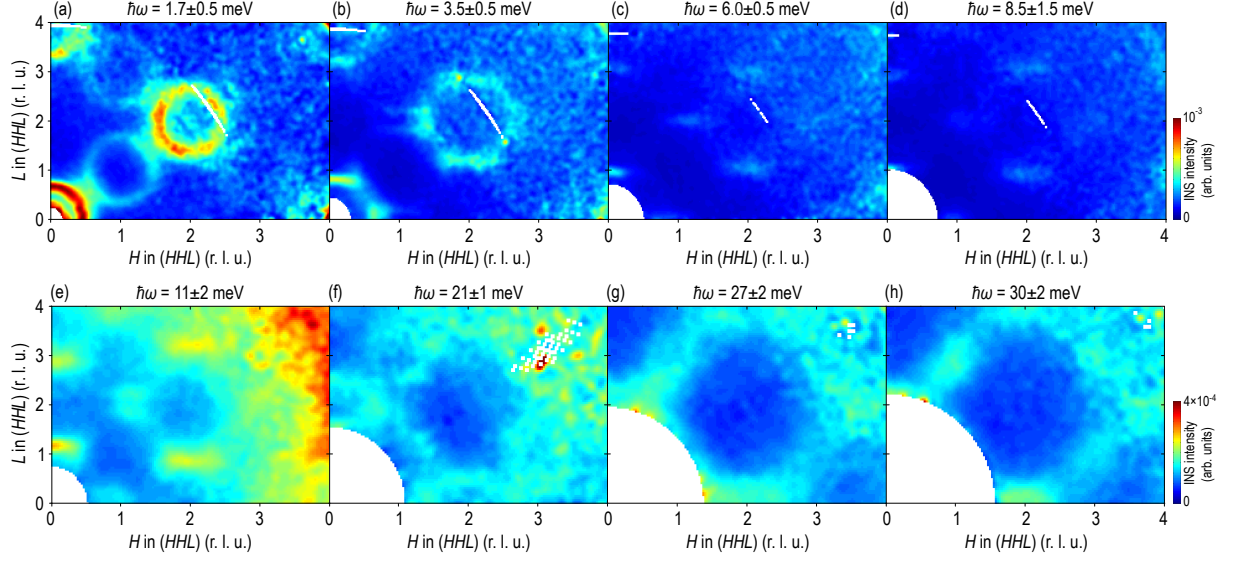


Figure 3.8: Constant-energy slices through the TOF data (setup 1) in the (HHL) plane, integrated within different energy windows as indicated above each panel. The top and bottom rows of panels were measured at the base temperature of 5 K with incident neutron energies of 20 and 70 meV. The out-of-plane momentum integration range was set to ± 0.1 , ± 0.14 , and ± 0.15 r.l.u. for panels (a), (b–d), and (e–h), respectively. The white stripes in some panels originate in regions with no data coverage. Reproduced from Ref. [40].

of spin-wave dispersion, bridging the incommensurate magnetic satellites, is a common feature of helimagnets with symmetric exchange interactions [65]. In the case of ZnCr_2Se_4 , however, this branch occurs at 10 times lower energies, so it cannot be seen in Fig. 3.7 (a) above the elastic line. We will return to the discussion of this low-energy magnon branch when presenting the cold-neutron data.

To visualize the magnon spectrum in \mathbf{Q} space, we are presenting constant-energy cuts in Fig. 3.8. All of them show intensity distributions within the (HHL) plane at different energies, covering wave vectors up to (444) . Here one can observe the complex hierarchy of energy scales in the magnon dispersion. The low-energy cut at 1.7 meV in Fig. 3.8 (a) displays clearly separated rings of scattering intensity around the zone centers. Stronger modes are found near Γ points of the unfolded Brillouin zones, such as $\Gamma(000)$, $\Gamma(222)$, and $\Gamma(004)$, whereas weaker modes appear as replicas shifted by the (111) wave vector to the centers of the folded fcc Brillouin zone [71]. Around 2.5 meV, these two modes start to hybridize, leading to a saddle point in the spin-wave dispersion that can be most clearly seen along the (HHH) direction at the right-hand side of Fig. 3.9 (a). Above the saddle-point energy, the rings of scattering break into separated segments as shown in Figs. 3.8 (b–e). Above 6.8 meV, which corresponds to the crossing of the bands in the $(11L)$ direction in Fig. 3.7 (a), the weaker rings of scattering surrounding the (111) and (113) points cross each other, resulting in a streak of intensity centered at (112) in Figs. 3.8 (c,d). Going

even higher in energy, we observe an elliptical feature surrounding the $X(002)$ point in Fig. 3.8 (f) that finally shrinks in Figs. 3.8 (g,h) into a set of broad peaks corresponding to the top of the magnon band at the unfolded-zone boundary at an energy of ~ 30 meV. What is not seen in this figure is the bottom of the high-energy magnon branch that results in an intense peak centered at 24 meV at the $W(120)$ point, which lies outside of the (HHL) plane but can be well seen in Fig. 3.9 (b). A similar feature was also seen in the spectrum of Cu_2OSeO_3 at the same \mathbf{Q} point and nearly the same energy [71].

For a more comprehensive representation of magnetic excitations in ZnCr_2Se_4 , we put together energy-momentum cuts along a polygonal path which contains all high symmetry directions in \mathbf{Q} space, creating a “spaghetti”-type plot shown in Figs. 3.9 (a,b) for both incident energies. Kinematic constraints lead to the lack of data at high energy transfer in the first Brillouin zone, however these data have better signal-to-noise ratio at low energies. Therefore, in Fig. 3.9 (b) we have overlayed data from the first Brillouin zone on top of those obtained from equivalent points at higher $|\mathbf{Q}|$ to complete the missing parts of the dataset. The stitching lines between high- and low- $|\mathbf{Q}|$ data can be recognized at the left-hand side of the figure.

Experimental determination of the exchange constants

To extract the experimental exchange constants from our data, we compared them with spin-dynamical calculations performed in the framework of linear spin-wave theory (LSWT) using the SPINW software package [17, 88]. The magnon spectrum was calculated using the classical Heisenberg model with interactions up to the 4th shell of Cr neighbors [48]:

$$H = \frac{1}{4} \sum_{i=1}^4 \sum_{n=1}^4 \sum_{j=1}^{z_n} J_n \mathbf{S}_i \cdot \mathbf{S}_j, \quad (3.2)$$

where i numbers Cr sites in the unit cell, and j runs over z_n neighbors in the n^{th} coordination shell around the site i . In our notation, positive J_n stands for AFM coupling between Cr $S = 3/2$ spins. The model does not differentiate between two inequivalent exchange paths for third-nearest neighbors, J'_3 and J''_3 , hence these two exchange parameters were assumed equal. The pitch angle γ between the neighboring magnetic moments of the spin helix can be found by solving the equation that minimizes the energy for classical spins:

$$J_1 + J_2 + 4J_4 + 4(J_2 + 2J_3) \cos(\gamma) + 6J_4 \cos(2\gamma) = 0. \quad (3.3)$$

To enable direct comparison with our ARCS data, we modeled the multi-domain state by averaging the calculated spectra for three possible orientations of the magnetic domains. The calculations were first carried out with the theoretically predicted exchange parameters

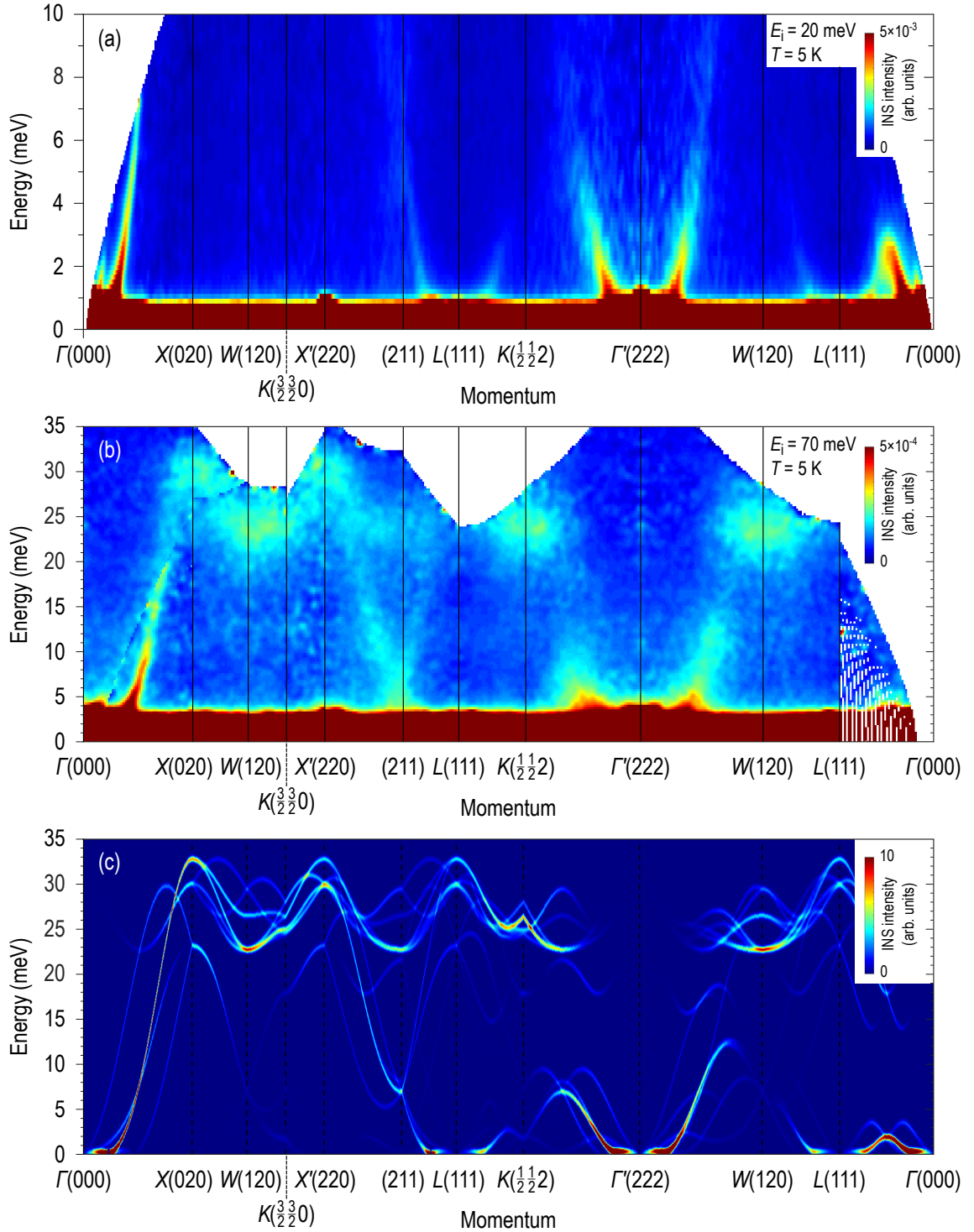


Figure 3.9: (a,b) Energy-momentum cuts through the TOF data, taken with $E_i = 20$ and 70 meV at the ARCS spectrometer (setup 1), combined into a “spaghetti”-type plot that covers all high-symmetry directions of the unfolded Brillouin zone. (c) Results of our spin-dynamical calculations performed using the SPINW software for the exchange constants given in Eq. 3.4, plotted along the same polygonal path in momentum space as the data in panels (a) and (b). The calculations were averaged over three possible domain orientations to mimic the multi-domain spin-spiral state realized in a zero-field experiment. Reproduced from Ref. [40].

from Ref. 48, which were then iteratively adjusted to achieve the best agreement with the measured spectrum. The resulting spectrum is shown in Fig. 3.9 (c) for the following optimized values of exchange constants:

$$\begin{aligned} J_1 &= -2.876 \text{ meV}, & J_2 &= 0.034 \text{ meV}, \\ J'_3 = J''_3 &= 0.490 \text{ meV}, & J_4 &= -0.041 \text{ meV}. \end{aligned} \quad (3.4)$$

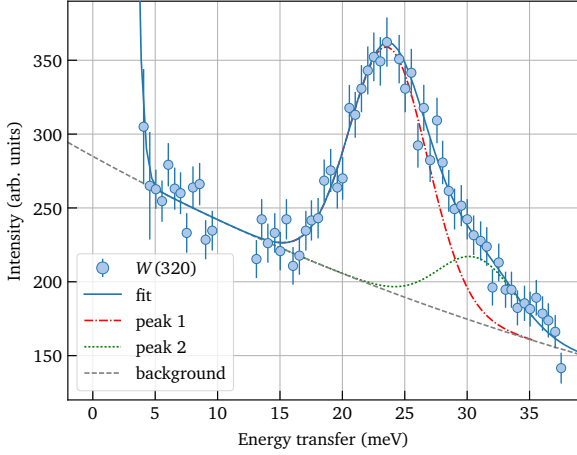


Figure 3.10: A typical energy scan measured at the $W(320)$ point with the IN8 spectrometer (setup 2) in the multi-domain state, revealing two marginally resolved peaks centered at 23.7 meV (dash-dotted line) and 30.8 meV (dotted line), in perfect agreement with our spin-dynamical calculations. Reproduced from Ref. [40].

A closer analysis of the peak shape reveals that it consists of a stronger excitation centered at (23.7 ± 0.2) meV and a weaker one at (30.8 ± 1.2) meV. The strong lower-energy peak originates from the sum of two magnetic domains whose propagation vectors are directed along the y and z cubic axes, whereas the weaker upper peak presumably consists of two unresolved excitations originating from the x -oriented domains. Both the positions and the relative intensities of the two peaks match fairly well with the spin-dynamical calculation results in Fig. 3.9 (c).

3.3.3 ZnCr_2Se_4 magnon spectrum in the single-domain state

We proceed with presenting low-energy data measured at the IN5 spectrometer in the single-domain state prepared by cooling the sample in magnetic field as described in Section 3.3.1. To confirm that our domain-selection procedure was successful, in Fig. 3.11 (a) we show the elastic-scattering intensity map in the $(h1l)$ plane in the vicinity of the (111) structural

The absolute value of the experimental NN exchange constant J_1 is approximately 50% lower than the theoretical prediction. However, the signs of all interactions are well captured by the calculation. Their ratios, listed in Table 3.1, show fair agreement (within 20%) with the results obtained in Ref. 48 for an effective Coulomb repulsion $U = 2$ eV.

As an additional verification of the exchange parameters and the overall correctness of our spin-wave model, in Fig. 3.10 we show a typical energy scan measured at the IN8 thermal-neutron spectrometer at the $W(320)$ wave vector. It reveals an intense peak corresponding to the bottom of the high-energy magnon branch (cf. Fig. 3.9).

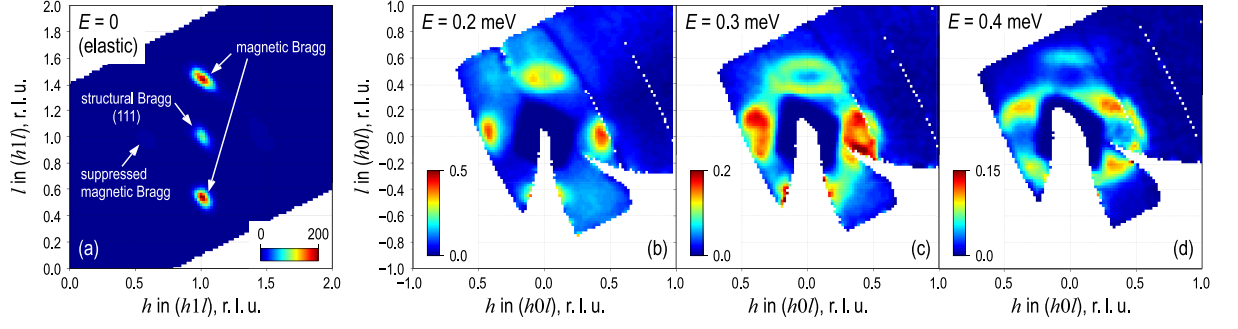


Figure 3.11: Constant-energy cuts through the low-energy TOF data measured at IN5 (setup 3) in the single-domain state. (a) Elastic intensity map in the $(H1L)$ plane, demonstrating the selection of a single magnetic domain with the propagation vector parallel to the c axis. (b–d) Constant-energy cuts at 0.2, 0.3, and 0.4 meV, which show magnetic Goldstone modes emanating from the $(0\ 0\ \pm q_h)$ ordering vectors and pseudo-Goldstone modes at the orthogonal $(\pm q_h\ 0\ 0)$ vectors, which are seen to merge at 0.4 meV. Note different intensity scales in all images. Reproduced from Ref. [40].

Bragg reflection. This plane contains both the $(1\ 1\ 1 \pm q_h)$ ordering vectors, where we observe intense magnetic Bragg peaks, and the $(1 \pm q_h\ 1\ 1)$ wave vectors, where the corresponding peaks are suppressed by two orders of magnitude in intensity. We therefore conclude that all the inelastic spectra obtained from the same dataset originate from a single magnetic domain oriented along the c axis.

The inelastic data shown in Fig. 3.11 (b–d) represent equivalent cuts taken in the vicinity of $\mathbf{Q} = 0$, where the signal-to-background ratio is maximized. The constant-energy maps exhibit two inequivalent types of low-energy spin-wave modes seen as elliptical features emanating from the selected and suppressed ordering vectors. From different sizes of the ellipses it is clear that the dispersion of the two modes is not identical. Moreover, the intensity of the second mode corresponding to the suppressed Bragg reflection appears to be even higher compared to the true Goldstone mode. The two modes merge at 0.4 meV [Fig. 3.11 (d)], resulting in an inflection point (flattening) of the dispersion seen as bright intensity spots along the diagonal directions of the image.

The dispersion of the same low-energy excitations can be seen in Fig. 3.12, where we compare energy-momentum cuts passing through the $(1\ 1\ 1 \pm q_h)$ ordering vectors with orthogonal cuts through the suppressed magnetic Bragg positions [panels (a) and (b), respectively]. In both directions, we observe Goldstone-like magnon modes that appear gapless within the experimental energy resolution. Their dispersion resembles the M-shaped low-energy magnon branch in $\text{Sr}_3\text{Fe}_2\text{O}_7$ [87], with the top of the inner branch reaching to only 0.5 meV for the Goldstone modes in Fig. 3.12 (a) and 0.28 meV for the pseudo-Goldstone modes in Fig. 3.12 (b). A weak spin-wave band dispersing downward towards (111) can be seen in both directions. The nearly twofold difference in the band width of the inner M-shaped

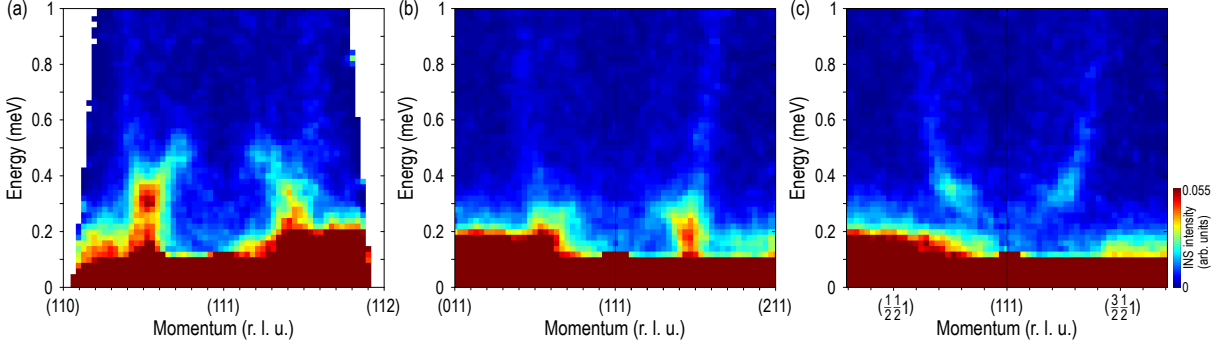


Figure 3.12: Energy-momentum cuts through the IN5 data (setup 3), centered at the (111) wave vector and taken along different directions: (a) along the $(11L)$ line passing through the $(111 \pm q_h)$ ordering vectors of the field-selected domain; (b) average of the equivalent $(1 \pm h 1 1)$ and $(1 1 \pm h 1)$ directions passing through the suppressed $(1 \pm q_h 1 1)$ and $(1 1 \pm q_h 1)$ ordering vectors; (c) along two orthogonal diagonal directions: $(1-h 1-h 1)$ (left) and $(1 \pm h 1 \mp h 1)$ (right), which pass through the 0.35 meV inflection point in the dispersion in the plane orthogonal to the ordering vector. In the right part of panel (c), datasets for positive and negative h have been averaged. Reproduced from Ref. [40].

branch connecting the magnetic Bragg peak with the zone center confirms that the two modes seen in panels (a) and (b) are distinct. The behavior of the steeply dispersing outward branch is, on the other hand, much more isotropic. We also show in Fig. 3.12 (c) diagonal cuts that cross the inflection points of the spin-wave dispersion in the plane perpendicular to the ordering vector. As can be estimated from the image, these inflection points are located at 0.35 meV in energy.

3.3.4 Spin gap of the pseudo-Goldstone magnons

The presented IN5 data indicate that a soft magnon mode persists practically in all momentum directions around the zone center at $|\mathbf{Q}| \approx q_h$, by analogy with the result obtained by Kataoka [89] for conical spin density waves with symmetric exchange interactions. This results in a corrugated Mexican-hat-like dispersion schematically shown in Fig. 3.14. The locus of dispersion minima along different directions forms an approximately spherical surface in \mathbf{Q} space of radius q_h . On this surface, the spin gap $\Delta(\theta, \phi)$ has two distinct minima: at the ordering vector itself ($\theta = 0$), forming the true (gapless) Goldstone mode emanating from the magnetic Bragg peaks (filled dots), and pseudo-Goldstone modes at two orthogonal wave vectors ($\theta = \pi/2$; $\phi = 0$ or $\pi/2$) corresponding to the would-be Bragg peak positions of the suppressed magnetic domains (open dots). The latter are characterized by a small spin gap Δ_{PG} that can be only marginally resolved in our TOF data. Along all intermediate directions, the spin gap is larger, reaching a maximum along the Brillouin-zone diagonals.

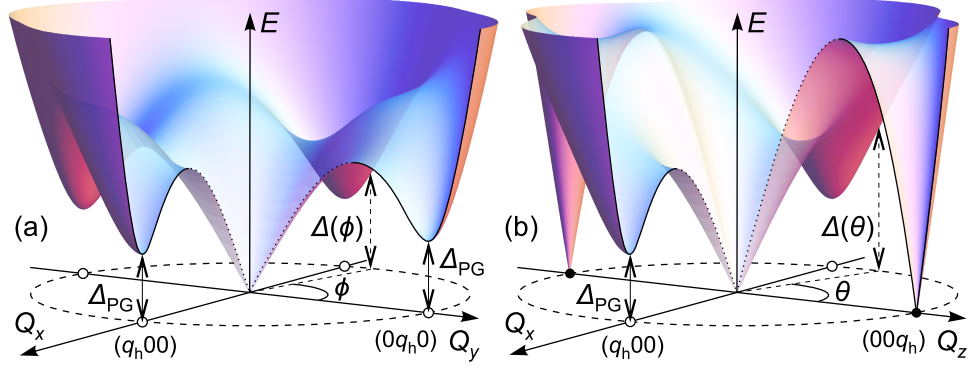


Figure 3.14: Schematic illustration of the low-energy magnon dispersion: (a) in the $(HK0)$ plane orthogonal to the ordering vector and (b) in the $(H0L)$ plane passing through the ordering vector. Here Δ_{PG} denotes the gap of the pseudo-Goldstone magnon branch, ϕ and θ are spherical angles. The filled and open dots represent Bragg peaks of the selected and suppressed magnetic domains, respectively. Reproduced from Ref. [40].

To measure the angular dependence of the spin gap directly, we performed additional measurements at the PANDA spectrometer within the $\theta = \pi/2$ plane along several radial directions relative to the zone center for a number of different ϕ angles. The measurement at each angle was done in three steps. First, we performed an energy scan at $|\mathbf{Q}| = q_h$ (assuming that the locus of the dispersion minima is spherical) to measure the approximate onset energy of magnetic scattering. Then, we did a radial scan at an energy characterized by the maximal slope of the spectrum, in order to find the true location of the dispersion minimum that could slightly deviate from q_h for various angles. Finally, we repeated the energy scan at the new wave vector $|\mathbf{Q}|$ for every angle. These final energy scans are shown in Fig. 3.13 (a). It can be seen that the signal at $\phi = 0$, at the location of the pseudo-Goldstone mode, has a finite energy that is clearly resolved from the elastic line. The maximum of inelastic scattering intensity is observed around 0.15 meV. A

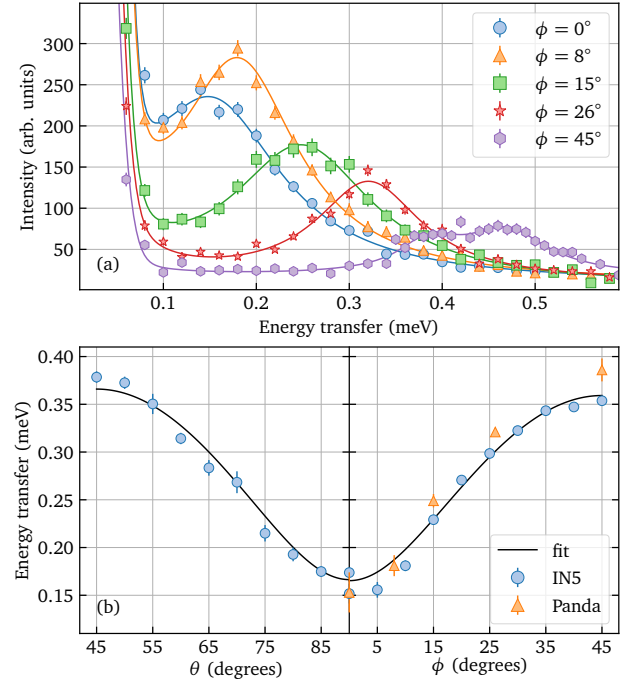


Figure 3.13: (a) Several unprocessed energy scans from the triple-axis spectrometer PANDA (setup 4), measured at the minimum of the spin-wave dispersion in the plane orthogonal to the ordering vector ($\theta = \pi/2$) along different directions with $\phi = 0^\circ, 8^\circ, 15^\circ, 26^\circ$, and 45° . (b) Angular dependence of the minimum energy in the spin-wave dispersion $\Delta(\theta, 0)$ and $\Delta(\pi/2, \phi)$ extracted from the IN5 and PANDA measurements. The solid line is an empirical fit described in the text. Reproduced from Ref. [40].

more robust estimate of the gap energy results from fitting both the IN5 and PANDA data from different radial directions, which resulted in the angular dependence of the spin-gap energy shown in Fig. 3.13 (b). We can see that the results of both TOF and TAS measurements are in good agreement. The accuracy of our spin-gap measurement benefits from the extrapolation of the data taken away from the ordering vector, where the peak is better resolved, toward the low-energy region. We fitted the combined dataset in Fig. 3.13 (b) with the simple empirical function $\Delta(\theta, \phi) = \sqrt{\Delta_{\text{PG}}^2 + A^2 \sin^2 2\phi + B^2 \sin^2 2\theta}$, which resulted in the experimental spin-gap value $\Delta_{\text{PG}} = 0.166(7)$ meV. On the other hand, recent high-resolution powder data on ZnCr_2Se_4 demonstrate a gapless spin-wave spectrum down to at least 0.05 meV [68], which indicates that the anisotropy gap at the ordering vector ($00q_h$) must be negligibly small, at least a factor of 3 smaller than Δ_{PG} .

3.3.5 Magnon-magnon interactions

A remarkable hallmark of the observed pseudo-Goldstone modes is that LSWT predicts them to be gapless in the absence of magneto-crystalline anisotropy [89] at wave vectors where no magnetic Bragg reflections are found below T_N . This is in contrast to magnetic soft modes observed, for example, in $\alpha\text{-CaCr}_2\text{O}_4$ [90], which originate from a proximity to another phase with a different magnetic ordering vector and therefore have a much larger gap that is well captured by LSWT. The existence of gapless modes without an underlying Bragg reflection would violate the Goldstone theorem, yet this contradiction can be resolved by taking into account quantum fluctuation corrections to the linear spectrum.

As long as the low-energy magnon spectrum is concerned, spin systems can be analyzed in the frame of the nonlinear sigma model [91] or mapped onto a one-sublattice Heisenberg model. Therefore, to obtain an estimate of the pseudo-Goldstone spin gap, it is sufficient to consider a simplified model involving $J_1 < 0$, $J_2 > 0$, and $J_4 > 0$ interactions on a simple-cubic lattice,

$$H = J_1 \sum_{\langle i,j \rangle} \mathbf{S}_i \mathbf{S}_j + J_2 \sum_{\langle\langle i,j \rangle\rangle} \mathbf{S}_i \mathbf{S}_j + J_4 \sum_{\langle\langle\langle i,j \rangle\rangle\rangle} \mathbf{S}_i \mathbf{S}_j, \quad (3.5)$$

where the summations are taken over the 1st, 2nd, and 4th nearest neighbors, respectively. This minimal model results in the correct pitch angle $\gamma \approx 0.23\pi$ and similar spin-wave velocities as those realized in ZnCr_2Se_4 for the following values of parameters: $J_2 = 4$ meV, $J_4 = 1.8$ meV, and $J_1 = -4(J_2 + J_4 \cos \gamma)$.

To consider the magnon dispersion in the helical spin structure it is worthwhile to introduce local spin quantization axes x , y , z , such that $z \parallel \langle \mathbf{S} \rangle$ and $y \parallel \mathbf{Q}$. The Holstein-Primakoff transformation in the lowest $1/S$ order followed by the Bogoliubov transformation

yields the magnon Hamiltonian

$$H_m = \sum_{\mathbf{q}} \omega_{\mathbf{q}} \alpha_{\mathbf{q}}^{\dagger} \alpha_{\mathbf{q}}, \quad (3.6)$$

with the dispersion

$$\omega_{\mathbf{q}} = S \sqrt{(J_{\mathbf{q}} - J_{\mathbf{Q}})(J_{\mathbf{q}+\mathbf{Q}} + J_{\mathbf{q}-\mathbf{Q}} - 2J_{\mathbf{Q}})/2}, \quad (3.7)$$

where

$$J_{\mathbf{q}} = \sum_{\mathbf{R}} J_{\mathbf{R}} \exp(i\mathbf{q} \cdot \mathbf{R}). \quad (3.8)$$

This magnon dispersion acquires six zeros at the $(00 \pm q_h)$, $(0 \pm q_h 0)$, and $(\pm q_h 00)$ points.

Quantum fluctuations given by the next orders in the $1/S$ expansion of the Holstein-Primakoff transformation open a gap at the $(0 \pm q_h 0)$ and $(\pm q_h 00)$ points orthogonal to the propagation vector [91–94]. The lowest order of terms which gives such corrections is represented by three- and four-magnon processes shown in Fig. 3.15. Both $\omega_{\mathbf{q}}^{(4)}$ and

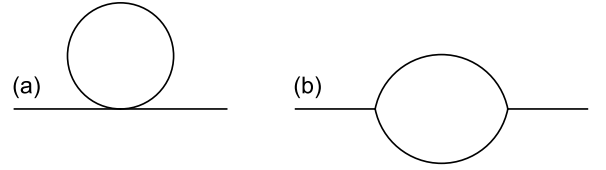


Figure 3.15: The diagrams which give $1/S$ corrections to the spectrum: (a) $\omega_{\mathbf{q}}^{(4)}$ and (b) $\Sigma_{11}(\omega, \mathbf{q})$. Reproduced from Ref. [40].

$\text{Re}\Sigma_{11}(\omega, \mathbf{q})$ terms contribute to the magnon dispersion. The imaginary part of the self-energy term $\text{Im}\Sigma_{11}(\omega, \mathbf{q})$ describes the magnon damping $\Gamma_{\mathbf{q}}$:

$$\tilde{\omega}_{\mathbf{q}} + i\Gamma_{\mathbf{q}} = \omega_{\mathbf{q}} + \omega_{\mathbf{q}}^{(4)} + \Sigma_{11}(\omega, \mathbf{q}). \quad (3.9)$$

We calculated the magnon dispersion $\tilde{\omega}_{\mathbf{q}}$ at the helix propagation vector $\mathbf{Q} = (00q_h)$ and at the orthogonal wave vector $\mathbf{Q}' = (q_h 00)$. Our calculation shows that in the first case the quantum fluctuation corrections cancel out as expected in the $1/S$ expansion theory, whereas at the second vector \mathbf{Q}' a spin-wave gap opens up with a magnitude $\Delta_{\text{PG}} = 0.18$ meV, leading to a pseudo-Goldstone magnon observed in the experiment. The good agreement between the calculated and measured values of the spin gap suggests that the described quantum-fluctuation corrections to the LSWT are fully sufficient to describe the experimentally observed magnon spectrum. It is worth noting that the experimentally measured spin gap is expected to have an additional contribution dictated by the anisotropy energy, which is nonzero in any real material. However, the quantitative agreement of the calculated and measured gap magnitudes indicates that this contribution in ZnCr_2Se_4 is not dominant. Inclusion of a finite single-ion anisotropy term in our model would reduce the estimate of the spin gap from pure quantum-fluctuation effects even further, hence the experimental value of Δ_{PG} should be seen as an upper estimate for the pseudo-Goldstone spin gap in a purely Heisenberg system.

3.3.6 Summary

Using inelastic neutron scattering, we investigated the complete spin-wave spectrum of ZnCr_2Se_4 in the whole of reciprocal space and across two orders of magnitude in energy. We found two distinct types of low-energy magnon modes: the Goldstone mode along the helix propagation vector at $(00 \pm q_h)$ and two pseudo-Goldstone modes at $(\pm q_h 00)$ and $(0 \pm q_h 0)$. Our simulation in the framework of the LSWT provides a perfect description of the spectrum except at the pseudo-Goldstone points, where LSWT predicts a gapless mode, while the experiment shows a gap of the order $\Delta_{\text{PG}} = 0.17 \text{ meV}$. This gap can be quantitatively reproduced in the calculations by including leading-order corrections due to quantum fluctuations arising from magnon-magnon scattering processes.

The scattering channels contributing to the magnon lifetime in insulators are usually very weak and require elaborate time-consuming experiments with a micro-electronvolt energy resolution to be quantified in direct measurements [95]. At the same time, here we demonstrated that the pseudo-Goldstone magnon gap in helimagnets, first measured in our work, represents a well-defined and experimentally accessible quantity of the spin-wave spectrum that carries indirect information about such magnon-magnon interactions. In spite of its relatively simple experimental determination, the spin-gap magnitude Δ_{PG} cannot be expressed analytically as a function of the Hamiltonian parameters and is therefore useful for testing spin-dynamical models beyond LSWT.

The existence of nearly gapless spin-wave modes propagating in the direction orthogonal to the ordering vector is expected to leave measurable signatures in the low-temperature thermodynamic and transport properties of the material, as well as in its response to local probes, at temperatures of the order of $\Delta_{\text{PG}} \ll T_N$. In a cubic system that has two pseudo-Goldstone modes per one Goldstone mode, the contribution of the former would dominate in all processes governed by low-energy magnon scattering, including but not limited to magnetic contributions to the low-temperature specific heat and magnon heat conduction [96]. In the presence of weak anisotropy, a two-gap structure in the magnon density of states is expected. To the best of our knowledge, these effects still await their detection in future experiments performed on samples in the single-domain magnetic state. Our present results should apply not only to simple helimagnets but also to a much broader class of materials in which the magnetic propagation vector is spontaneously chosen from multiple structurally equivalent alternatives upon crossing a transition to the magnetically ordered state.

3.4 Magnetic field evolution of the helimagnon spectrum

3.4.1 Instrumental conditions for the experiments

We have used cold-neutron TOF and TAS techniques to investigate magnetic field dependence of the pseudo-Goldstone mode in the ZnCr_2Se_4 sample [97]. The TOF method allows one to map out the whole four-dimensional energy-momentum space in one measurement, while TAS provides the ability to measure the given points of the reciprocal space with maximal resolution.

The experiments were performed on the same pre-aligned mosaic of single crystals that was used for the previous measurements [40]. The TOF experiment [98] (setup 5) was performed at the LET [99] cold neutron multi-chopper spectrometer at ISIS, UK. The energy of the incoming neutrons $E_i = 2.01$ meV provided us with energy resolution of 0.04 meV, determined as the full width at half maximum of the incoherent elastic line. The sample was placed into the 9 T cryomagnet with its \mathbf{c} axis parallel to the magnetic field and $(HK0)$ scattering plane. This alignment allows us to select the magnetic domain with $(00q_h)$ propagation vector, having propagation vectors $(q_h 00)$ and $(0 q_h 0)$ of two suppressed domains in the accessible range of the reciprocal space. The measurements were done at the base temperature $T = 2$ K in a single-domain state which was prepared by cooling the sample in the magnetic field of 2 T. The domain selection procedure is described in Section 3.3.1. The collected data were processed using the HORACE software package [82, 83]. To improve the statistical quality of the data we combined the signal from symmetrically equivalent reciprocal space points within the same Brillouin zone.

To study a field dependence of the dispersion more carefully, the TOF data was supplemented with TAS measurements (setup 6) which were performed at the THALES [100] low energy spectrometer at ILL, Grenoble. Here the sample was mounted in the 10 T cryomagnet in the same orientation as in TOF experiment – with its \mathbf{c} axis parallel to the magnetic field. The instrument was operated with fixed final neutron energy $E_f = 2.5$ meV ($k_f = 1.1 \text{ \AA}^{-1}$). Pyrolytic graphite PG (002) monochromator and analyzer together with a cold beryllium filter were used to provide a high flux and suppress higher-order contamination from the monochromator. To measure selected points with increased resolution the collimation of the scattered beam was used.

3.4.2 TOF measurements

The main goal of our INS measurements is to investigate the magnetic-field dependence of the previously discovered pseudo-Goldstone magnon modes in ZnCr_2Se_4 [40] and reveal

their relationship to the field-driven QCP suggested by Gu *et al.* [77]. In the paramagnetic phase above T_C , the three pairs of wave vectors $(\pm q_h 0 0)$, $(0 \pm q_h 0)$, and $(0 0 \pm q_h)$ are equivalent because of the cubic symmetry. Helimagnetic order breaks this discrete symmetry by spontaneously selecting one of the cubic directions as the propagation direction of the spin spiral. For the sake of unambiguity, let us assume that this direction is $(0 0 \pm q_h)$. Consequently, all spins forming the helix are constrained to the ab plane. Under the assumption of Heisenberg symmetry, which holds to a very good approximation for Cr^{3+} spins, the system remains invariant under continuous $U(1)$ spin rotations within the ab plane. As a consequence, Goldstone modes emanating from the $(0 0 \pm q_h)$ ordering vectors remain gapless down to the lowest temperatures (the upper limit for the spin gap at these points, set by previous INS experiments, is 0.05 meV [68]).

Under the assumption that the lattice symmetry remains cubic, so that no spin-space anisotropy is imposed by the lattice distortions, linear spin-wave theory (LSWT) predicts gapless magnon modes also at the two orthogonal pairs of wave vectors, $(\pm q_h 0 0)$ and $(0 \pm q_h 0)$, which can be seen as an accidental degeneracy, because in contrast to the true Goldstone modes, the zero spin gap at these points is not enforced by the symmetry of the Hamiltonian. As a consequence, the degeneracy can be weakly lifted by fluctuations, opening up a small magnon gap at the corresponding wave vectors [101] and resulting in pseudo-Goldstone modes that have been experimentally observed in ZnCr_2Se_4 by neutron spectroscopy [40]. In the case of continuous degeneracies, this phenomenon is known as “order by disorder” [102, 103], whereas in ZnCr_2Se_4 the degeneracy is discrete, resulting in one pair of Goldstone and two pairs of pseudo-Goldstone modes, well separated in the Brillouin zone.

According to our spin-wave calculations in zero magnetic field, quantum-fluctuation corrections to the spin-wave spectrum are qualitatively similar to those resulting from LSWT in the presence of weak easy-plane anisotropy (in the plane orthogonal to the spiral direction). Both effects break the cubic symmetry of the magnon dispersions by opening a gap at the pseudo-Goldstone wave vectors while keeping the true Goldstone modes gapless. In the first case, this symmetry breaking is spontaneous, whereas in the second case a preferred axis is explicitly introduced in the magnetic Hamiltonian to reflect the tetragonal distortion resulting from the spin-lattice coupling. On the one hand, experimentally observed pseudo-Goldstone magnon gap $\Delta_{\text{PG}} \approx 0.17$ meV shows reasonable agreement with the theoretical estimate that takes into account quantum fluctuations (three- and four-magnon processes) even in the cubic setting [40]. This offers solid evidence that the anisotropy in the spin-wave spectrum results mainly from quantum-fluctuation corrections beyond LSWT. On the other

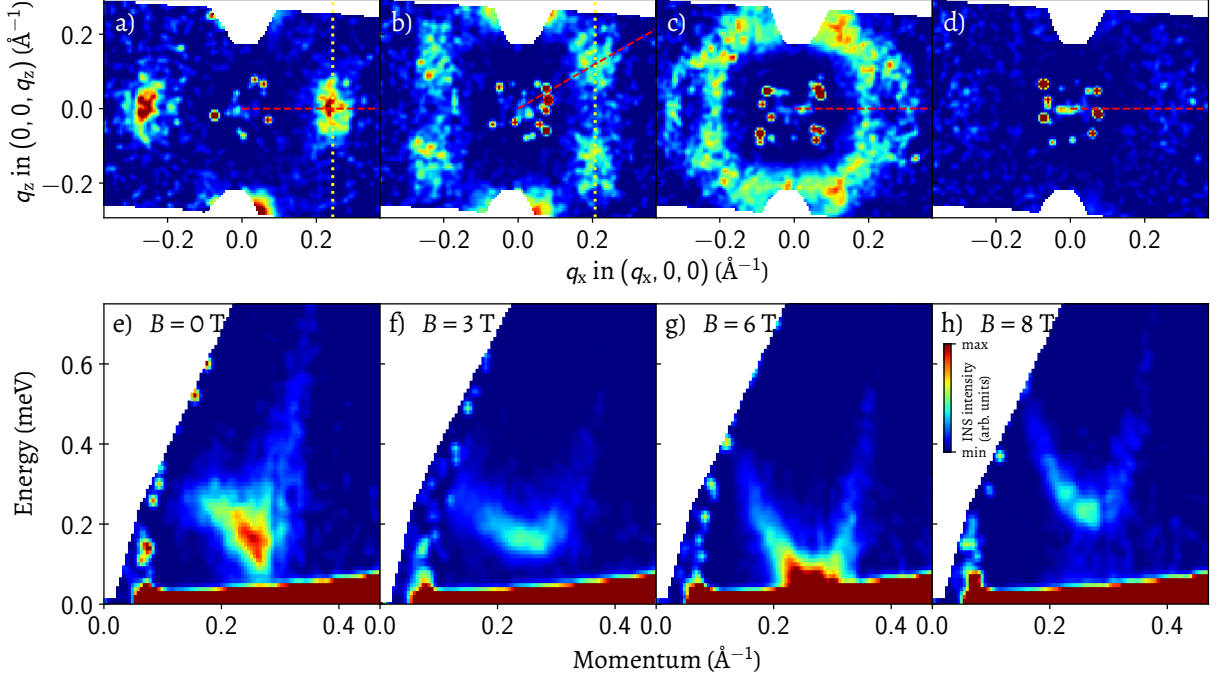


Figure 3.16: The neutron TOF spectrum of ZnCr_2Se_4 , measured in magnetic fields of 0, 3, 6, and 8 T, applied along the [001] direction. The top row of panels (a–d) shows the corresponding constant-energy cuts in the (HOL) plane, integrated within ± 0.03 meV around 0.17 meV energy transfer. The bottom row (e–h) shows energy-momentum cuts along the radial directions connecting the Γ point with the local minimum of the dispersion, as shown with dashed lines in (a–d). Integration ranges in momentum directions orthogonal to the plane of the figure are approximately $\pm 0.05 \text{ \AA}^{-1}$. The vertical dotted lines in (a) and (b) indicate the direction of energy-momentum cuts in Fig. 3.17. Reproduced from Ref. [97].

hand, small easy-plane anisotropy cannot be fully excluded in the presence of a tetragonal lattice distortion, even if our results outlined in Section 3.5 indicate that the corresponding distortions are minor, and due to the smallness of spin-orbit coupling, the resulting spin anisotropy should be negligible. At the qualitative level, the contribution of magnetostrictive distortions to the easy-plane anisotropy and, consequently, to the pseudo-Goldstone gap energy remains unknown. Estimating it from first principles would require more elaborate relativistic calculations, taking into account both lattice and spin degrees of freedom, which are currently beyond reach.

To shed light on this problem, we have measured the low-energy magnon spectrum of ZnCr_2Se_4 in magnetic fields applied along the [001] cubic axis. Figure 3.16 shows representative cuts through the TOF data at 0, 3, 6, and 8 T. The top row of panels [Fig. 3.16 (a–d)] presents constant-energy cuts in the (HOL) plane at 0.17 meV. This energy corresponds to the pseudo-Goldstone magnon gap in zero field [40]. The red dashed lines connect the center of the Brillouin zone with the local minimum in the dispersion. In the panels below [Fig. 3.16 (e–h)], corresponding momentum-energy cuts along these lines are shown.

The spectrum in Figs. 3.16 (a, e) was measured in zero field. In agreement with our previous report [40], we see clear intensity maxima at $(\pm q_h 0 0)$, near the bottom of the pseudo-Goldstone modes. Their positions are equivalent (in the cubic setting) to the ordering vector, which is oriented along the \mathbf{c} axis and cannot be reached in this experimental configuration. The dispersion has a sharp minimum, which is asymmetric even in the direct neighborhood of the ordering vector. On the left side from the minimum, closer to the Γ point, the dispersion forms an arc with a maximum around 0.3 meV. On the right-hand side, the magnon branch rises linearly in energy and has a much steeper dispersion, forming a beak-like shape. The minimum of the dispersion corresponds to the pseudo-Goldstone gap energy. In the constant-energy plane in Fig. 3.16 (a), the magnetic signal appears in the form of sharp spots at $(\pm q_h 0 0)$, with no additional intensity maxima in the field of view.

The application of a 3 T magnetic field, approximately half way to the QCP, qualitatively changes the shape of the dispersion. In the constant-energy plane in Fig. 3.16 (b), the intensity now splits into four spots, which indicates that the dispersion minima are shifted up and down with respect to the $(HK0)$ plane and no longer coincide with the wave vectors equivalent to the magnetic ordering vector in the cubic setting. The momentum-energy cut through one of these minima in the dispersion, shown in Fig. 3.16 (f), reveals a markedly different spectrum to the beak-shaped one in zero field. Even though the spin gap remains nearly unchanged, the dispersion no longer has a cusp and lacks the linear part on the right-hand side, approaching a parabolic shape. The comparison of 0 and 3 T cuts in Fig. 3.17, taken through the corresponding minima in the dispersion along the transverse momentum direction [vertical dotted lines in Fig. 3.16 (a, b)],

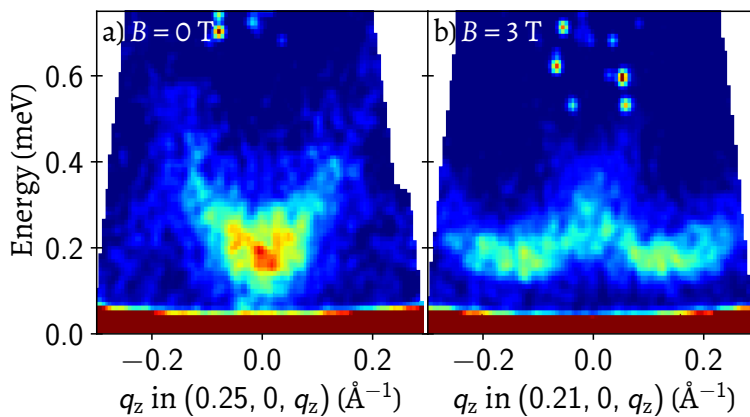


Figure 3.17: The neutron TOF spectrum of ZnCr_2Se_4 . The panels a and b show the energy-momentum cuts taken along the $(00L)$ direction passing through the pseudo-Goldstone magnons for magnetic fields 0 and 3 T respectively. Reproduced from Ref. [97].

indicates that the pseudo-Goldstone mode splits along the magnetic-field direction into two identical soft modes with a parabolic dispersion. The appearance of a crossing point of the two dispersion branches at the center of Fig. 3.17 (b) suggests that there are two different dispersion curves, possibly originating from magnetic domains with opposite chirality.

At a twice higher magnetic field of 6 T, the system is in the immediate proximity to the field-driven QCP, where the incommensurate structure gets suppressed due to the collapse of the conical angle and continuously transforms into the field-polarized FM phase. The corresponding INS spectrum is presented in Figs. 3.16 (c, g). In contrast to the previous cases, the gap in the spin-wave spectrum closes, and a ring of intensity can be seen in the constant-energy cut at 0.17 meV. Despite the proximity of the system to a collinear field-polarized state, spin fluctuations are still concentrated in the neighborhood of a sphere with radius q_h , centered at the origin. Two hollow ellipses can be recognized around $(\pm q_h, 0, 0)$ and $(0, 0, \pm q_h)$, where the gapless Goldstone modes are now located, and the spin-wave dispersion drops below the level of the constant-energy cut. Despite the magnetic field, which breaks the equivalency of the $[100]$ and $[001]$ axes, the spectrum restores its fourfold symmetry in the $(H, 0, L)$ plane at the critical field. The momentum-energy cut in Fig. 3.16 (g), parallel to the q_x direction, shows a nearly symmetric parabolic dispersion curve with a vanishing energy gap. There is a small residual difference in the slopes on opposite sides of the dispersion curve, but neither shows the signs of inflection within the available data range, unlike at smaller fields.

Finally, at even higher fields above B_c , i.e. in the field-polarized FM phase, the spin gap reopens again. This can be well seen in the 8 T data shown in Figs. 3.16 (d, h). The value of the spin gap at this field is above the 0.14–0.20 meV integration range of the constant-energy cut, hence no spin-wave intensity can be seen in Figs. 3.16 (d). The magnon dispersion in the momentum-energy cut in Fig. 3.16 (h) is shaped as a symmetric parabola with an energy gap of 0.25 meV.

3.4.3 TAS measurements

The gap closing without the subsequent formation of the new order corresponding to the wave-vector where it occurred requires more careful study. Therefore, we run additional measurements on the TAS spectrometer THALES with vertical 10 T magnet (setup 6). Due to the technical constraints, we were restricted to $[H, K, 0]$ scattering plane. For each magnetic field we measure energy spectrum at $(\pm q_h, 0, 0)$. The results are shown in Fig. 3.18, where the horizontal axis corresponds to the magnetic field strength, whereas the vertical one represents the neutron energy transfer. The color indicates the intensity of neutron flux. During the measurements we found no appreciable shift in the position of the minimum along $[H, 0, 0]$ direction, therefore, the figure presents the spectrum at a fixed (reciprocal space) point.

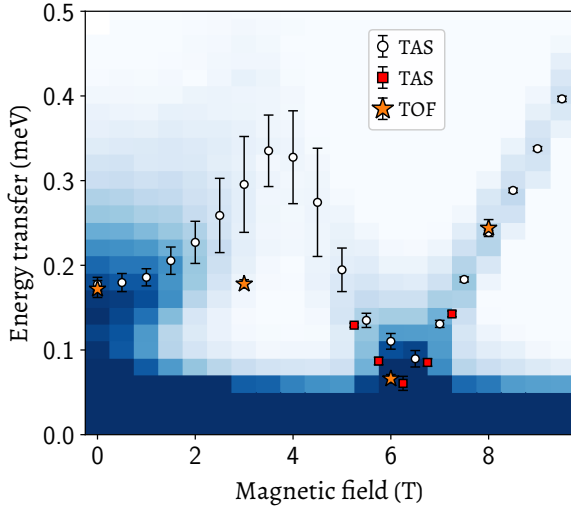


Figure 3.18: Magnetic-field dependence of the INS spectrum at $(q_h 0 0)$, measured as a function of magnetic field applied along the $[001]$ direction. The color map shows INS intensity measured on a TAS instrument (dark-blue color corresponds to high intensity, white to the background level). Open circles show fitted positions of the peak, resulting from Gaussian fits. Red squares show fits of additional TAS data, taken with tighter collimation to improve the resolution (the corresponding raw data are not shown). Orange star symbols correspond to the spin-gap values at the local minimum of the dispersion, extracted from the TOF data. Reproduced from Ref. [97].

branches merge. As long as the field pushes the minima further away, the merge point appears at higher energy, which is what we observe. Although at 0 T and at fields ≥ 6 T, where the minima are unified, the data display the behavior of the gap itself.

The results of the TAS experiment confirm nontrivial field evolution of the magnon spectrum. As we can see, the system is very sensitive to the magnetic field: thus, the application of a small field shifts the spectral weight higher in energy. After 1.5 T the signal becomes substantially weaker, and it is almost gone at 3 T. Approaching 6 T, the signal reappears again although with the reverse tendency: the spectral weight goes down, and at 6.25 T the gap is closing. Further increasing field reopens the gap, with subsequent linear growth.

The white circles on top of the colormap are the positions of the gaussian peaks obtained from the fit of the spectrum. Afterward, we additionally measured intermediate fields around the 6 T with improved collimation. Corresponding peak positions are shown with red triangles. Finally, we add the values of the gap extracted from LET data, shown by yellow stars.

From the TOF data we know that application of 3 T field doubles the local minimum of the dispersion and shifts it from the $(H 0 0)$ direction [see Fig.3.16 (b)]. As we do not have the full coverage of the reciprocal space at the intermediate field values between 0 and 3 T, we assume the splitting happens already after the application of an infinitesimal field. The TAS data reflect this showing the changes in the spectrum already at 0.5 T. Consequently, between 0 and 6 T, the TAS data do not track the local minimum but rather the mode, where the two split

3.4.4 Summary

We investigated the evolution of the magnetic dispersion of ZnCr_2Se_4 in a magnetic field applied along the $[001]$ direction. After the domain-selection procedure, the zero-field low-energy spectrum is determined by the gapless Goldstone modes stemming from the positions of the selected magnetic Bragg-peaks and gapped pseudo-Goldstone modes, which appear at the positions of the suppressed magnetic peaks. Application of a small magnetic field splits each pseudo-Goldstone mode in momentum, making two local minima out of a single one, and shifts them symmetrically from the initial position along the field direction. The new modes have roughly the same gap value, although the minimum is much less pronounced. Being initially proportional to the field, the distance between the split minima saturates at around 4 T, and then decreases. At around 6 T the peaks unite again. Together with the unification, the gap of the modes also decreases and closes completely at 6.25 T. Further increasing the field immediately reopens the gap, and henceforth the gap grows linearly with the field.

When the field approaches 6.25 T, the neutron spectrum becomes symmetric in the $(H\ 0\ L)$ plane, thereby the true- and the pseudo-Goldstone modes are not distinguishable anymore. The specialty of the critical state of the system is that it is characterized by the gapless magnetic excitations which have parabolic-like dispersions, that is more typical for FM-excitations, and usually does not appear at incommensurate positions [see Fig.3.16 (c)].

3.5 Anisotropy of macroscopic properties

3.5.1 Macroscopic properties and magnetism

In the previous sections, we saw that the behavior of the highly anisotropic magnon spectrum, and in particular the pseudo-Goldstone modes, in ZnCr_2Se_4 has an extremely non-monotonic field dependence. In this section, we briefly consider the effect of the magnetic structure and perturbations on the low-temperature macroscopic properties of the sample.

Previous neutron diffraction studies have revealed a correlation between structural and magnetic phase transitions in ZnCr_2Se_4 [70]. The authors argue that the structural phase transition from a cubic to orthorhombic symmetry at T_C is associated with the cooperative displacement of Se^{2-} ions. According to various estimates, this distortion at the lowest measured temperature does not exceed 0.06%–0.08% [68, 72, 73, 75]. In the high-temperature cubic phase, Cr^{3+} ion has no orbital angular momentum, which rejects the Jahn-Teller effect as a possible cause of this displacement. Thus, the structural phase transition should be

associated with an antiferromagnetic transition from the paramagnetic to the helicoidal phase. However, this scenario requires the presence of a spin-orbit interaction, which is not expected in the paramagnetic phase, again, due to the zero orbital angular momentum of Cr^{3+} ion. A possible mechanism for the appearance of a finite orbital moment at the Cr site was proposed based on recent measurements of nuclear magnetic resonance (NMR) [78]. The authors attribute this to a partial transfer of the magnetic moment to the neighboring selenium sites.

3.5.2 Ultrasound measurements

To quantify the lattice anisotropy below the magnetic transition we utilize the ultrasound measurements along and perpendicular to the magnetic propagation vector \mathbf{q}_h .

For these measurements, we polished two opposite $\{001\}$ surfaces of a single crystal. Piezoelectric transducers were glued to the polished surfaces to induce and detect ultrasound vibrations with the generation frequency of 100 MHz and longitudinal polarization. In this configuration, both the wave-vector of the generated sound \mathbf{k}_s , and its polarization were parallel to the $[001]$ cubic axis of the crystal. We chose the mode with the longitudinal polarization of the sound vibrations because, in comparison with the transverse one, it showed robustness against reinstallation of the transducers, as well as decent signal quality.

During the experiment we measured two orientations: the first one allows us to apply the field along $[001]$ axis, whereas in the second one the field direction was $[100]$. To measure sound velocity along the spin-spiral we mounted the ZnCr_2Se_4 sample with its $[001]$ axis pointing vertically, along the magnetic field direction, which results in the selection of the domain with the $(00q_h)$ ordering vector. To change between the orientations we took the sample from the cryomagnet, reoriented it relative to the sample-stick, and inserted it back into the magnet. Each measurement consists of the following steps. Prepare a single-domain state by cooling down the sample in the field of 4 T to the base temperature of 2 K. Do the measurements of the sound velocity upon increasing the temperature up to 30 K. During this measurement, we cross the transition temperature T_N and destroy the single-domain state. When we reach 30 K we reverse the temperature change and proceed with measurements upon cooling. At this stage we start with a multi-domain state and, as far as we do not apply an external magnetic field, the domain selection does not occur, and we measure in a multi-domain state down to the base temperature. The same steps were done for the second orientation in which the ultrasound velocity was measured perpendicular to the spin-spiral propagation vector.

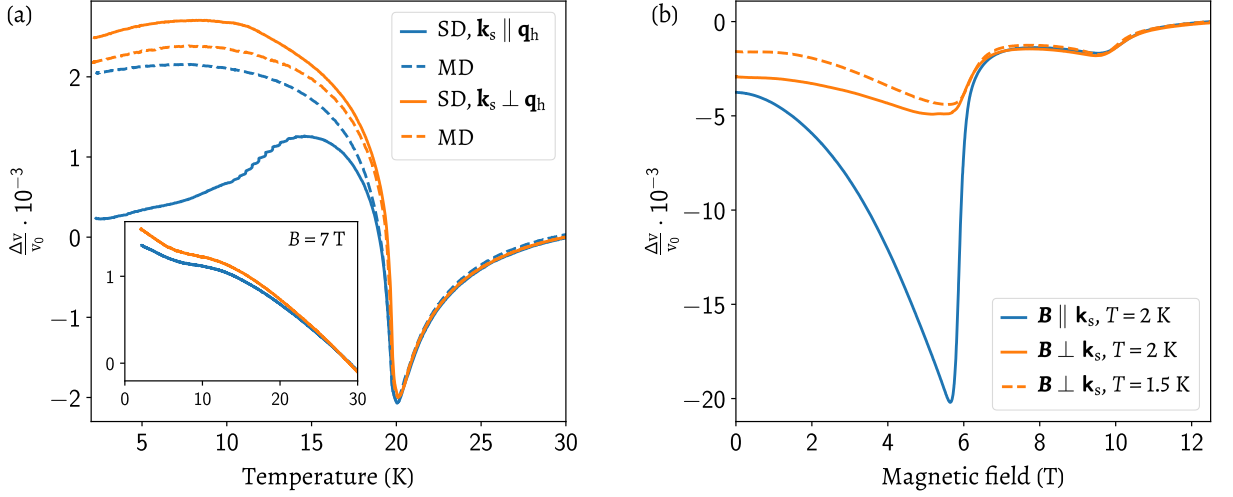


Figure 3.19: (a) The change in the sound velocity of the longitudinal acoustic mode, $\Delta v = v - v_0$, normalized to the value v_0 at 30 K, in the single-domain (SD, solid lines) and multidomain (MD, dashed lines) states. The top and bottom curves correspond to the ultrasound wave vector \mathbf{k}_s perpendicular and parallel to the propagation vector of the spin helix, \mathbf{q}_h , respectively. The inset shows a similar temperature dependence, measured in the field-polarized FM phase at $B = 7$ T for $\mathbf{k}_s \perp \mathbf{B}$ (top curve) and $\mathbf{k}_s \parallel \mathbf{B}$ (bottom curve), for comparison. (b) Magnetic-field dependence of the relative change in the sound velocity, $\Delta v/v_0$, normalized to the respective v_0 values at 12 T. The measurements are done at a constant temperature with the ultrasound wave vector parallel and perpendicular to the magnetic-field direction. Note the tenfold difference in the ranges of the vertical scales between (a) and (b). Reproduced from Ref. [97].

The ultrasound data in Fig. 3.19 (a) show relative changes in the sound velocity, $\Delta v/v_0$, for the longitudinal wave propagating along the $[001] \parallel \mathbf{q}_h$ and $[100] \perp \mathbf{q}_h$ directions, normalized to the respective values in the paramagnetic state at $T = 30$ K. It is clear that the crystal is slightly stiffer in the direction orthogonal to the ordering vector of the spin helix, but the effect is relatively small, on the order of 0.2%. This suggests that the difference in phonon energies and phononic densities of states along the two directions must also be similarly small. For comparison, the inset to Fig. 3.19 (a) shows a similar temperature dependence, measured in the field-polarized FM phase at $B = 7$ T in the directions parallel and orthogonal to the field-induced magnetization. The two curves have been normalized to the respective v_0 values at $T = 30$ K, where the sample remains cubic according to the paramagnetostriction [97]. The observed change in $\Delta v/v_0$ between 30 K and base temperature differs by only $2 \cdot 10^{-4}$ for the two directions of the ultrasound wave vector, which is within the reproducibility margin of our measurements.

The magnetic-field dependence of the relative change in the sound velocity, $\Delta v/v_0$, measured for the same two directions at $T = 2$ K and normalized to the high-field value at 12 T, is plotted in Fig. 3.19 (b). One can see a very pronounced softening of the longitudinal acoustic mode immediately below the critical field, which is much stronger for the acoustic

waves propagating along the magnetic-field direction than perpendicular to it. The maximal value of $|\Delta\nu/\nu_0|$ reaches 2%, which is ten times larger than the corresponding changes at zero field and almost two orders of magnitude larger than the spontaneous magnetostriction, suggesting that magnetic interactions exert a much stronger relative effect on the dynamic than static properties of the lattice. The second anomaly that appears in both field-dependence curves around 10 T represents the previously reported high-field transition that was previously associated either with a spin-nematic phase [74] or with a crossover from the quantum-critical region to the fully field-polarized FM phase [77]. The new phase diagram suggested by Gu *et al.* [77] implies a very strong temperature dependence of this high-field anomaly, so that it merges with B_c in the zero-temperature limit. In contrast, we can see essentially no difference between the 1.5 and 2 K curves in Fig. 3.19 (b), indicating that the crossover to the field-polarized FM phase stays at approximately 10 T at both temperatures, which is hard to reconcile with the newly proposed phase diagram.

3.5.3 Dilatometric properties

To directly measure the structural deformations in the sample as a function of temperature and applied magnetic field, my colleagues from TU Dresden performed accurate measurements using capacitive dilatometry [97]. This method, having a sensitivity to relative changes in the length of the order of 10^{-7} [104], makes it possible to measure changes in the lattice constants with an accuracy unattainable for conventional diffraction methods.

For the measurements, we used the same polished ZnCr_2Se_4 single crystal as for ultrasound measurements. Measurements of the relative change in length $\Delta l/l_0$ were carried out along one of the $\langle 001 \rangle$ cubic axes of the crystal. Depending on the direction of magnetic field (transverse or longitudinal with respect to the chosen axis), it corresponds to either a or c axis, respectively, in the tetragonally distorted structure with $a = b \neq c$. In what follows, we will refer to the two measurement geometries as longitudinal (measurements along the $c \parallel \mathbf{B}$ direction) and transverse (measurements along the $a \perp \mathbf{B}$ direction). All measurements are presented relative to the l_0 value, corresponding to the high-temperature cubic structure at $B = 0$ and $T = 30$ K.

Figure 3.20 (a) shows the temperature dependences of the relative longitudinal and transverse deformation of the sample $\Delta l/l_0$ measured in magnetic fields of 1, 3, 5, and 7 T. Each measurement was carried out after preliminary cooling of the sample in a field of 7 T. Following the phase diagram in Fig. 3.3 (a), all measurements correspond to a single-domain state.

In the paramagnetic ($T > T_C$) and field-polarized FM ($B > B_C$) states, the longitudinal and transverse curves coincide, which indicates isotropic thermal expansion. In the helimagnetic state, the application of an external magnetic field below the critical one leads to a partial polarization of the helix, that is, to the so-called conical spiral. In this case, the deformation of the sample is due to the superposition of two effects — isotropic thermal expansion in the field-polarized FM state and anisotropic spontaneous magnetostriction in the helimagnetic state. The latter effect leads to a splitting of the thermal expansion curves. By extrapolating the data to the zero-field and zero-temperature limit, we obtained an estimate of the tetragonal distortion with $(a - c)/a \approx 3.6 \cdot 10^{-4}$, which is even less than that obtained earlier [68, 72, 73, 75].

To measure the deformation of the sample due to exclusively spontaneous magnetostriction arising from the spiral arrangement of the spins without the contribution caused by the external magnetic field, the sample was brought into a single-domain state by cooling down in a magnetic field of 7 T. When the base temperature of 2 K was reached, the field was ramped down to zero and the temperature dependence of the longitudinal and transverse deformation of the sample was measured. These data, together with the reference curve corresponding to the multi-domain state, are shown in Fig. 3.20 (b). It is immediately evident that the behavior of the curves is fundamentally different from those in Fig. 3.20 (a). One could expect that the single-domain state survives up to T_C , which would result in the order-parameter-like change in both lattice parameters shown with dashed lines, similar to that observed in finite fields [Fig. 3.20 (a)]. However, measured thermal-expansion curves (labeled “FC 0 T \parallel ” and “FC 0 T \perp ”) deviate from this behavior at temperatures above 5 K, as they both converge to the ZFC reference measurement. This behavior of the thermal expansion curves is associated with relaxation

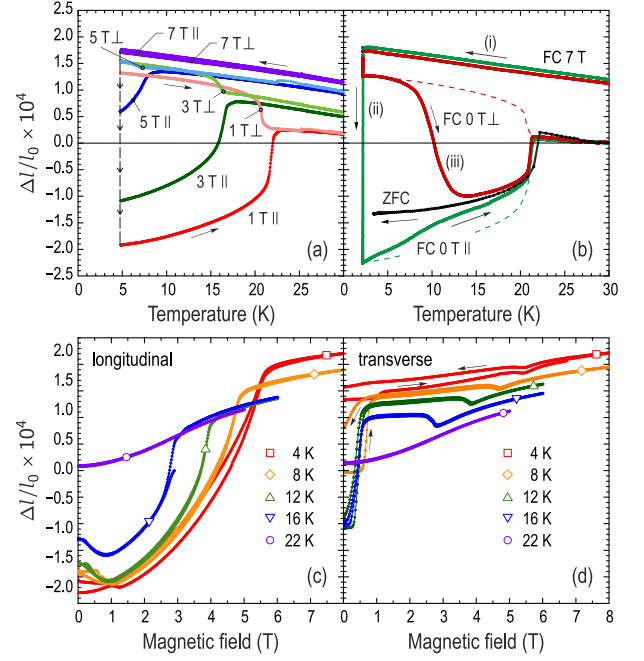


Figure 3.20: (a) Thermal-expansion measurements in longitudinal and transverse magnetic fields above the domain-selection transition. All curves are normalized to the same l_0 value at $T = 30$ K and $B = 0$. (b) Zero-field thermal expansion, measured during zero-field cooling (ZFC) and after field-cooling in a longitudinal (“FC 0 T \parallel ”) or transverse (“FC 0 T \perp ”) field of 7 T. The measurement steps (i), (ii), (iii) are explained in the text. (c, d) Magnetostriction measurements at several constant temperatures for longitudinal and transverse field directions, respectively. Reproduced from Ref. [97].

back to the multidomain state at elevated temperatures on a measurement time scale that was carried out with a temperature sweep rate of 0.1 K/min. The slow magnetic relaxation to the multi-domain state is also revealed in the measurements of magnetostriction at several constant temperatures, which are presented in Figs. 3.20 (c, d) for the longitudinal and transverse field geometries, respectively.

3.5.4 Slow relaxation of helimagnetic domains

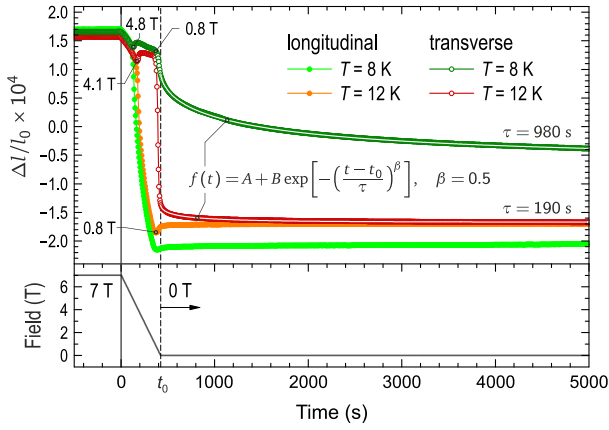


Figure 3.21: Time dependence of the relative change in the sample length $\Delta l/l_0$, measured during and after a rapid linear sweep of magnetic field from 7 T to zero in the transverse and longitudinal directions. The time dependence of magnetic field is plotted at the bottom. At $t < 0$, the sample temperature is stabilized at $T = 8$ or 12 K, and a downward field sweep with 1 T/min starts. After the time $t_0 = 420$ s, when the field reaches zero, slow relaxation towards the multidomain state can be described by a stretched exponential, Eq. (3.10), with $\beta = 0.5$ and the average decay constants $\tau_{8\text{K}} = 980$ s and $\tau_{12\text{K}} = 190$ s (thin white lines). Reproduced from Ref. [97].

Having observed slow magnetic domain relaxation in magnetostriction measurements, we proceed with estimating the functional dependence and characteristic times of such relaxation by following the time-dependent changes in the sample length at a constant temperature. After applying a 7 T field to the sample in either longitudinal or transverse direction and stabilizing the temperature at $T = 8$ or 12 K, we swept the field down to zero with the maximal rate of 1 T/min and followed the time-dependent change in the relative sample length, $\Delta l/l_0$, both during and after the field sweep. The results are plotted in Fig. 3.21, where the bottom panel shows the time dependence of the external field. During the downward field sweep, anomalies in $\Delta l/l_0$ are observed at the critical field (4.8 or 4.1 T, respectively) and at the domain-selection field (0.8 T). As soon as the magnetic field is reduced below the

domain-selection field, slow relaxation towards the multidomain state is observed both in the transverse and longitudinal directions. The relaxation curves cannot be described by a simple exponential function, which implies contributions from processes with a broad spectrum of different relaxation times. Defining the time when magnetic field reaches zero as t_0 , we can describe the relaxation at times $t > t_0$ using the stretched exponential function,

$$f(t) = A + B \exp \left[- \left(\frac{t - t_0}{\tau} \right)^\beta \right], \quad (3.10)$$

with $\beta = 0.5$, where τ is the temperature-dependent decay constant. This model is equivalent to a continuous weighted sum of simple exponential decays with a distribution of relaxation times described by the probability density

$$\rho(\theta) = \frac{1}{2\sqrt{\pi}} \theta^{-1/2} \exp(-\theta/4). \quad (3.11)$$

Relaxation with a stretched-exponential behavior is typical for systems with randomly distributed magnetic domains and is commonly associated with magnetic domain-wall motion. Here it results in the destruction of the single-domain state on the time scale of several minutes or hours (depending on the temperature) with a tendency to restore the cubic symmetry of the sample on the macroscopic scale. At a lower temperature of 8 K, the average relaxation rate is approximately 5 times slower than at 12 K. Apart from that, the two datasets also show a qualitative difference. At the higher temperature of 12 K, both transverse and longitudinal curves relax to the same asymptotic value of $\Delta l/l_0$ at $t \rightarrow \infty$, suggesting that an isotropic multidomain state is fully restored as a result of such relaxation. In contrast, the 8 K datasets relax to different asymptotic values in the transverse and longitudinal directions, which implies that some partial anisotropy in the distribution of magnetic domains survives arbitrarily long after the external field is turned off. A crossover between these two distinct behaviors must therefore take place at some intermediate temperature between 8 and 12 K.

Because every domain wall in a helimagnet costs additional energy, relaxation through nucleation of additional misaligned domains is only possible if some excess energy is already present in the initial state of the system. Indeed, by applying magnetic field to the sample, we only select magnetic domains with a single direction of the magnetic ordering vector, but such domains can still possess different chiralities. One therefore expects that domain walls separating right- and left-handed helical domains are still present in the initial state, carrying excess energy that can be redistributed via nucleation of new magnetic domains with a misaligned orientation of the magnetic ordering vector as a result of relaxation processes facilitated by thermal fluctuation. In other words, a domain wall separating helimagnetic domains with opposite chirality can decay into a larger number of domain walls between domains with orthogonal ordering vectors and either equal or opposite chiralities. It is natural to expect that such processes are governed by the corresponding domain-wall energies that must be different for all three types of domain walls and could be estimated from micromagnetic simulations.

3.5.5 Thermal properties

The anisotropy and nonmonotonic field dependence of the magnon spectrum of ZnCr_2Se_4 manifest themselves in the low-temperature macroscopic thermodynamic properties of the sample. Recently published measurements of the specific heat in ZnCr_2Se_4 [77] have shown behavior that can be regarded as a macroscopic manifestation of the pseudo-Goldstone gap that we see in our inelastic-scattering data [97]. Low-temperature specific heat data in zero field have a pronounced anomaly at temperatures of the order of 0.1–0.3 K. Fitting the specific heat data below 3 K to the exponential function $A\exp(-\Delta_{\text{PG}}/k_{\text{B}}T)$ gives the value of the energy gap $\Delta_{\text{PG}} = 0.186$ meV, which is in perfect agreement with the pseudo-Goldstone magnon gap energy obtained in our INS measurements. Note that the actual spin gap in the system (at the ordering wave vector) is expected to be below this value [40, 68], but because the true Goldstone mode carries only 1/3 of the magnon spectral weight, thermodynamic properties are more sensitive to the pseudo-Goldstone magnon gap. With increasing magnetic field, this anomaly gradually smoothes out and completely disappears at a critical field value of 6.5 T, reappearing again in the 10 T data. This behavior repeats the evolution of the pseudo-Goldstone gap, which closes in a field of about 6.2 T and reopens in the field-polarized ferromagnetic state.

Similar anomalies that resemble the nonmonotonic behavior of the spin gap were also observed in the low-temperature thermal conductivity of ZnCr_2Se_4 as a function of magnetic field and temperature [77]. The zero-field thermal conductivity, $\kappa(T)$, shows a change in behavior around 1 K, which disappears at the critical magnetic field. The corresponding field dependence, $\kappa(B)$, exhibits a nonmonotonic behavior at temperatures below 1 K, with two clear anomalies at the domain-selection field and at the transition to the field-polarized FM phase. In the thermal conductivity experiment from Ref. [77], the magnetic field was applied along one of the $\langle 111 \rangle$ crystallographic axes, while the thermal current was measured in an orthogonal direction [105]. In this geometry, the angle formed by the propagation vectors of all three magnetic domains with the magnetic field is approximately the same, hence the distribution of magnetic domains cannot be well controlled (it would be determined only by small unavoidable misalignments of the field direction). It is therefore unclear whether the thermal conductivity was measured in a single- or multidomain state, and how the thermal current was oriented with respect to the magnetic propagation vector.

The process of heat transfer in a magnetic insulator is due to two mechanisms — lattice thermal conductivity and thermal spin transport. The latter, in the case of a system of localized spins, is the transfer of heat by magnetic oscillations in the system — magnons.

If we consider magnons as essentially an ideal gas, and the phonon and magnon heat-conducting channels — as independent, then the total thermal conductivity is the sum of the contributions of each: $\kappa = \kappa_L + \kappa_m$. The results of ultrasound and dilatometric measurements presented in previous sections showed that in the magnetically ordered state of ZnCr_2Se_4 , deviations from cubic symmetry of both structural parameters and frequencies of acoustic phonons do not exceed 0.1%. This makes it possible to separate the magnon contribution to the thermal conductivity from the lattice contribution by considering the difference in thermal conductivities in directions parallel (κ_{\parallel}) and perpendicular (κ_{\perp}) to the magnetic ordering vector \mathbf{q}_h . Thus the difference, $\Delta\kappa = \kappa_{\perp} - \kappa_{\parallel}$, should be determined exclusively by magnetic effects, which can include magnon heat conduction and anisotropic phonon scattering on magnons and magnetic domain walls [97].

Due to the obvious anisotropy and non-monotonic behavior of the magnon spectrum, as well as the obvious connection with the thermodynamic properties [77], we decided to investigate the directional dependence of the low-temperature thermal conductivity. Our collaborators from the University of Miami conducted an outstanding experiment in which the anisotropic thermal conductivity in the single-domain state of ZnCr_2Se_4 was measured with high accuracy in directions parallel and orthogonal to the magnetic ordering vector in magnetic fields up to 5 T and down to $T \approx 0.6$ K [97].

The measured temperature and field dependences are shown in Fig. 3.22. Measurements in zero magnetic field, shown in Fig. 3.22 (a), did not reveal anisotropy between κ_{\perp}/T and κ_{\parallel}/T , however, when the field is applied, there is a clear discrepancy between the curves at temperatures below 2 K. The thermal conductivity in the direction of propagation of the magnetic helix is greater than in the transverse direction. This difference becomes even more obvious when we consider the relative differences $\Delta\kappa/\kappa \equiv (\kappa_{\perp} - \kappa_{\parallel})/\kappa_{\parallel}$ presented in Fig. 3.22 (b). It can be seen that $\Delta\kappa/\kappa$ reaches values several orders of magnitude higher than the tetragonal distortion of the crystal lattice and by several hundred times the anisotropy in the sound velocity. It could be assumed that a certain phase transition occurs in the system, leading to a decrease in symmetry and, as a consequence, to the appearance of anisotropy. However, neither dilatometry nor ultrasound velocity measurements contains anomalies around this temperature, excluding the possibility of such a transition. Another argument in favor of the hypothesis of the magnetic nature of the anisotropy in thermal conductivity is that the temperature 2 K in energy units coincides with the value of the pseudo-Goldstone energy gap. The low-temperature dependence of κ_{\parallel} and κ_{\perp} on the magnetic field shown in Fig. 3.22 (c), as in the previous experiment, behaves non-monotonically and resembles the field dependence of the energy gap. All curves clearly show a wide peak with a maximum

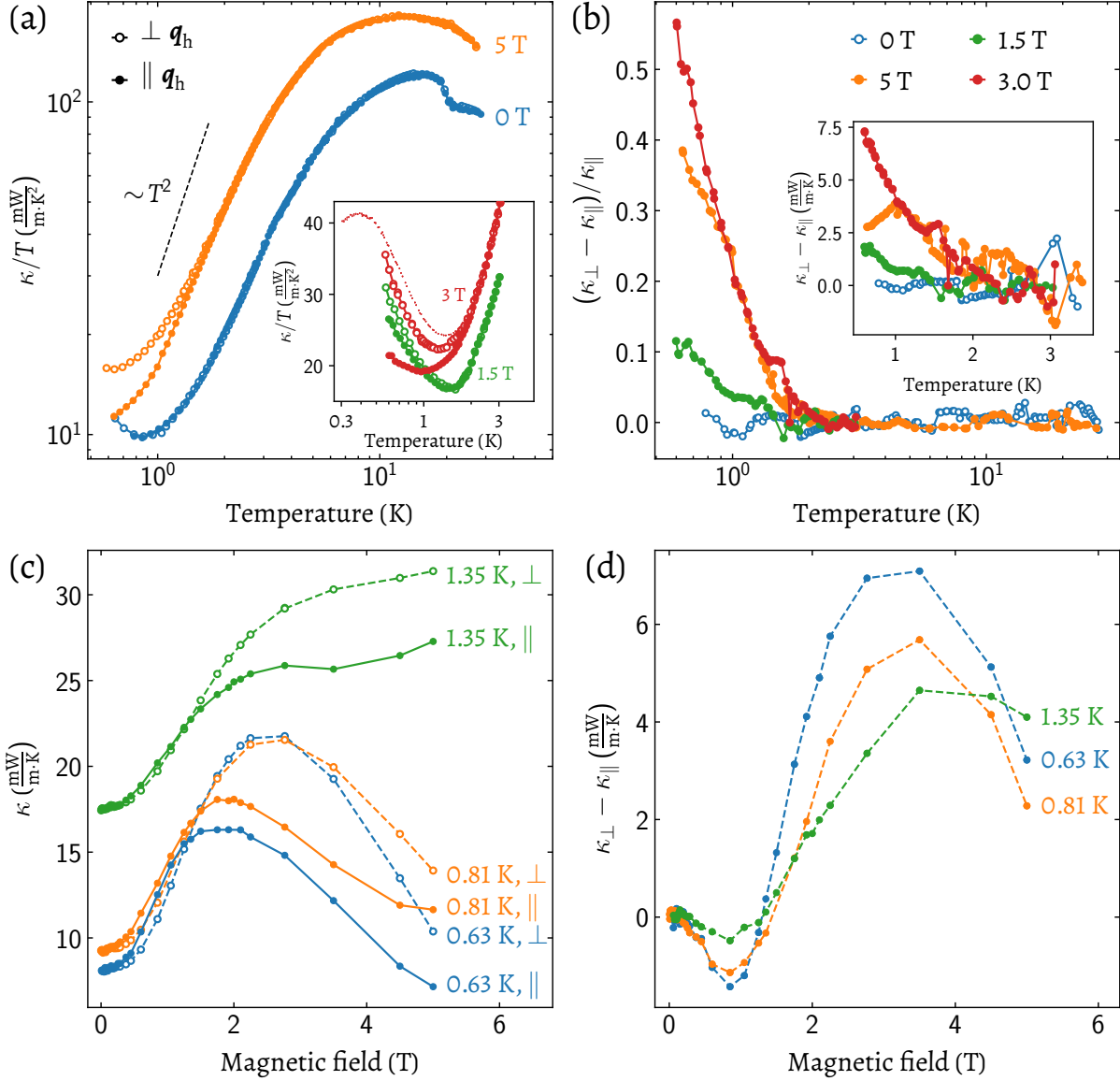


Figure 3.22: Anisotropy of the thermal conductivity with respect to the direction of the magnetic ordering vector. (a) Temperature dependence of κ_{\perp}/T (\circ) and κ_{\parallel}/T (\bullet) at $B = 0$ and 5 T (main panel) and at two intermediate fields of 1.5 and 3 T (inset). The dotted line in the inset shows the 3 T dataset reproduced from Ref. [77], which we recalculated into $\kappa(T)/T$ and normalized by a constant factor to match with our data in the high-temperature region. (b) Temperature dependence of the relative thermal-conductivity anisotropy, $(\kappa_{\perp} - \kappa_{\parallel})/\kappa_{\parallel}$, at different magnetic fields. The inset shows the low- T part of the same data without normalization, i.e. $\kappa_{\perp} - \kappa_{\parallel}$, on a linear temperature scale. (c) Magnetic-field dependence of κ_{\perp} (\circ) and κ_{\parallel} (\bullet) for three different temperatures. (d) Magnetic-field dependence of the thermal-conductivity anisotropy, $\kappa_{\perp} - \kappa_{\parallel}$, resulting from the pairwise subtraction of the data in panel (c). Reproduced from Ref. [97].

at $B \approx 2\text{--}2.5$ T. Fig. 3.22 (d) shows the differences $\Delta\kappa = \kappa_{\perp}(B) - \kappa_{\parallel}(B)$ for each temperature. Several points are worth noting here. First, $\Delta\kappa$ changes sign around 1.5 T for all temperatures. We also see again that the curves flatten to zero as they approach the critical field of the order of 6 T. All curves have a maximum in the vicinity of 3 T, which again prompts thoughts about the behavior of the gap in the magnon spectrum. Comparison

of the curves in Figs. 3.22 (a, c, and d) leads us to the conclusion that the maxima in the field dependences correspond to low-temperature upturns in the $\kappa(T)/T$ temperature dependences. This is especially evident in 1.5 and 3 T datasets in the inset to Fig. 3.22 (a). Comparison with data published by Gu *et al.* [77], which were measured down to slightly lower temperatures, shows that $\kappa(T)/T$ has another peak with a maximum at approximately 0.4 K. This maximum is most pronounced in the transverse thermal conductivity, $\nabla T \perp \mathbf{B}$, and only in the intermediate field range around $B_c/2$, which enhances $\kappa_{\perp}(0.5 \text{ K})$ at least sixfold (according to Ref. [77]) compared to its zero-field value. In higher magnetic fields above the field-induced critical point, the monotonic behavior of $\kappa(T)/T$ is restored [77].

Attempts to estimate the magnetic contribution to the specific heat based on inelastic neutron scattering data have revealed a significant agreement between the calculated and measured values. It is worth noting here that the analytical expression for the magnon dispersion obtained from the neutron data is rather an estimate and does not claim to be accurate. However, despite the inspiring similarity with the measured values, the calculated κ_m does not reproduce several experimental results. First, this is the absence of anisotropy in zero magnetic field, and secondly, the appearance of anisotropy in the experiment only below $T \sim 2 \text{ K}$. The authors discuss magnetic disorder and chiral domain boundaries as possible mechanisms explaining these effects [97].

Chapter 4

$\text{Sr}_3\text{Fe}_2\text{O}_7$

4.1 Introduction

In a crystal with high lattice symmetry, an antiferromagnetic (AFM) or spin-spiral state often selects its ordering vector spontaneously among several structurally equivalent alternatives. For instance, a stripe-AFM state in iron pnictides can form with the $(\pi, 0)$ or $(0, \pi)$ wave vector, whereas the helimagnetic state in the cubic spinel ZnCr_2Se_4 forms in 3 equivalent domains characterized by the ordering vectors $(q_h 0 0)$, $(0 q_h 0)$, and $(0 0 q_h)$. A single-domain state can be stabilized by cooling the system in a magnetic field or under uniaxial pressure. The condensation of paramagnetic excitations into spin waves upon crossing the ordering temperature in the vicinity of the ordering wave vector is well understood. However, what happens at the structurally equivalent wave vectors is less clear. For instance, a recent study performed on iron-pnictide superconductors in the single-domain (detwinned) state indicates that the second wave vector possesses no spin wave up to at least 40 meV [106]. On the other hand, our experiments on the $S = 3/2$ helimagnet ZnCr_2Se_4 show a clear soft mode at the $(q_h 0 0)$ and $(0 q_h 0)$ wave vectors in the single-domain state formed by cooling in a magnetic field applied along the z axis (see. Chapter 3). This soft spin-wave branch appears gapless within the linear spin-wave theory (LSWT) but develops a small energy gap of ~ 0.17 meV due to nonlinear corrections arising from quantum fluctuations. This offers a possibility to estimate the weak effects related to spin-wave scattering processes and to compare them with the theory on a quantitative level. However, the complex unit cell of the pyrochlore sublattice formed by the $S = 3/2$ magnetic Cr^{3+} ions in the spinel structure leads to multiple spin-wave modes that complicate the theoretical calculations. It is therefore important to repeat the same experiment on a helimagnetic compound with a simpler tetragonal structure, with only one magnetic atom per unit cell.

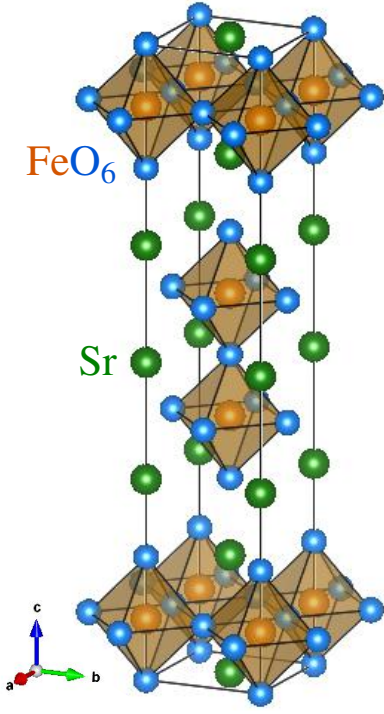


Figure 4.1: $\text{Sr}_3\text{Fe}_2\text{O}_7$ crystal structure. Solid lines illustrate a crystallographic unit cell. The structure is plotted using VESTA software [107] based on refinements in Ref. [108].

The layered iron oxide $\text{Sr}_3\text{Fe}_2\text{O}_7$ with $T_N \approx 115$ K [109] represents the perfect material to study pseudo-Goldstone modes for several reasons. According to our present understanding, the pseudo-Goldstone magnon gap is formed due to the influence of quantum fluctuations. Hence, it should depend on the spin state of the magnetic ion. In a $S = 1/2$ system, the quantum fluctuations are too strong and can destroy the soft mode, whereas, in the classical limit, only a small energy gap opens on top of the gap-less dispersion predicted by LSWT. The $S = 5/2$ magnetic moments of $\text{Sr}_3\text{Fe}_2\text{O}_7$ can be considered as classical, and one can therefore expect well-developed soft modes with a small spin gap. Second, the structure of $\text{Sr}_3\text{Fe}_2\text{O}_7$ is simple tetragonal, with only one magnetic ion per unit cell, which simplifies spin-dynamical calculations in contrast to the pyrochlore-sublattice of ZnCr_2Se_4 . And finally, the tetragonal structure results in only two possible wave vectors for the incommensurate spin spiral, $(\xi \xi 1)$ and $(\xi \bar{\xi} 1)$ with $\xi = 0.141$ (see. Fig. 4.1), as opposed to three

in the cubic structure. The propagation vector of the spin spiral is sufficiently long to be resolved in the spectrum [87]. An additional benefit is that the spin-wave spectrum and exchange interactions in $\text{Sr}_3\text{Fe}_2\text{O}_7$ are well known from previous experiments (performed in the multi-domain state).

4.2 Crystal and magnetic structure of $\text{Sr}_3\text{Fe}_2\text{O}_7$

$\text{Sr}_3\text{Fe}_2\text{O}_7$ is a stoichiometric compound belonging to the Ruddlesden-Popper series with general formula $A_{n+1}M_nO_{3n+1}$, where M is a transition metal. The crystal structure of these compounds consists of 2D perovskite-like layers separated with cations. The number n corresponds to the number of octahedra layers in a perovskite-like slab. These materials attract the attention of researchers due to a wide variety of properties, ranging from superconductivity [110] and electronic nematicity [111] in generally metallic ruthenates to various orbital and magnetic phase transitions in low-temperature insulating manganites.

The bilayer perovskite $\text{Sr}_3\text{Fe}_2\text{O}_7$ crystallizes in a tetragonal structure with 2 formula units per unit cell (space group $I4/mmm$, lattice parameters $a = b = 3.846(4)$ Å and

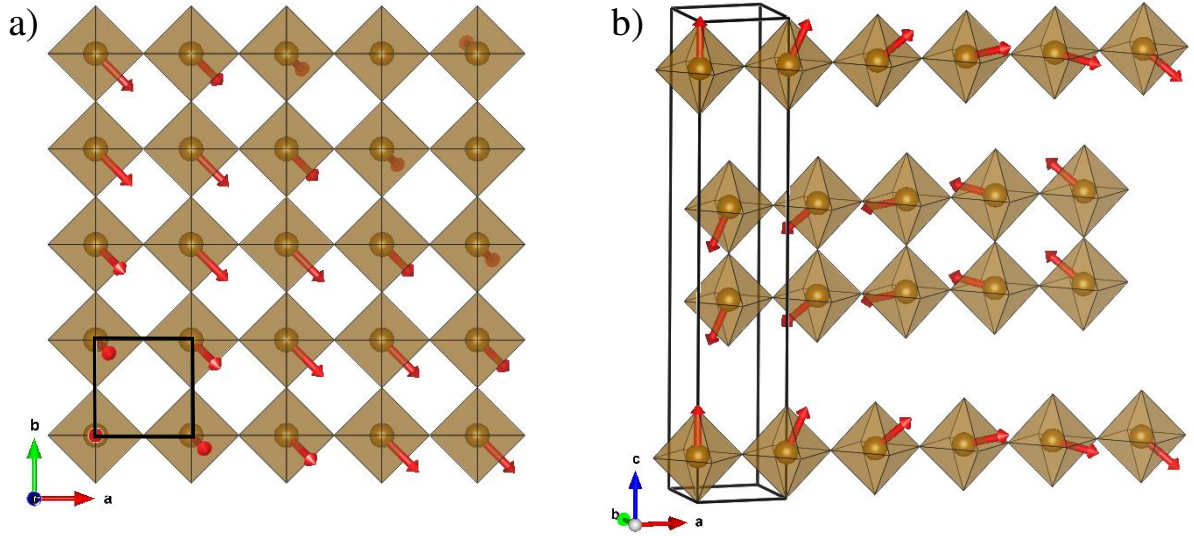


Figure 4.2: Schematic of the helical magnetic structure of $\text{Sr}_3\text{Fe}_2\text{O}_7$. (a) Projection on the ab -plane. All spins are perpendicular to the $[110]$ direction. (b) Side view on a few layers of spins demonstrating a formation of the $k_z = 1$ propagation vector in the c direction. Black solid lines represent the tetragonal unit cell. The structure is plotted using VESTA software [107].

$c = 20.234(2) \text{ \AA}$ (at $T = 390\text{K}$) [87]). This structure is visualised in Fig. 4.1. The magnetic sublattice is formed by Fe^{4+} ions in the $3d^4$ electron configuration with classical spins $S = 5/2$.

$\text{Sr}_3\text{Fe}_2\text{O}_7$ is a helimagnetic material with an incommensurate spin-spiral order below the AFM transition temperature $T_N = 115 \text{ K}$. The helical magnetic ground state with the spin modulation vector $\mathbf{k} = [0.141 \ 0.141 \ 1]$ was determined by means of neutron powder and single-crystal diffraction [87]. The reported magnetic structure is an elliptical helix with $\mu_c = 3.19(5)\mu_B$ component of the magnetic moment smaller than its $\mu_{a,b} = 3.58(11)\mu_B$ components (the corresponding powder diffraction data are $\mu_c = 3.04(5)\mu_B$ and $\mu_{a,b} = 3.53(4)\mu_B$). The schematic drawing of the $\text{Sr}_3\text{Fe}_2\text{O}_7$ magnetic structure is shown in Fig. 4.2. Panel Fig. 4.2(a) shows the view along the c axis. It is seen that all spins are perpendicular to the $[110]$ crystallographic direction. Spins of the iron ions having the same a and b coordinates are co-aligned. The c component of the propagation vector $k_z = 1$ is ensured by the fact that the spins at $(10 \pm z)$ are antiparallel to those at $(0.5 \ 0.5 \ 0.5 \pm z)$ [see Fig. 4.2(b)].

4.3 Inelastic neutron-scattering investigation

Following from the symmetry there are two possible magnetic domains with helices pointing along $(\xi\xi0)$ and $(\xi\bar{\xi}0)$ structurally equivalent directions. The idea of the experiment was

to choose the single magnetic domain by cooling down the sample in a magnetic field and investigate the low-energy magnetic excitations in this material. The main interest was to measure the low-energy dispersion and determine the spin gap of the pseudo-Goldstone modes.

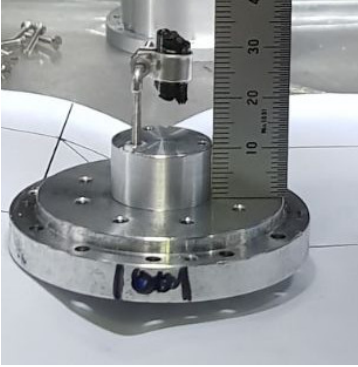


Figure 4.3: $\text{Sr}_3\text{Fe}_2\text{O}_7$ single crystal on the aluminum holder.

The single crystal of $\text{Sr}_3\text{Fe}_2\text{O}_7$ has been grown and characterized by our colleague Darren Peets by the same method as the one used in an earlier study [87, 109]. It is a large fully oxygenated single-grain crystal with a mass of 0.5 gram, which we characterized by x-ray Laue backscattering and magnetization. The field-cooled and zero-field-cooled magnetization data are shown in Fig. 4.4.

Because of the large spin, this sample mass is perfectly sufficient for a TOF measurement. Our main question was whether the 2.5 T field available on IN5 is sufficient to reach the single-domain state by field-cooling. In Fig. 4.4 the field-cooled and zero-field-cooled magnetization curves for the field direction $\mathbf{B} \parallel (1\bar{1}0)$ are shown. One can see that a field of 0.2 T should be already sufficient to select a single helical magnetic domain.

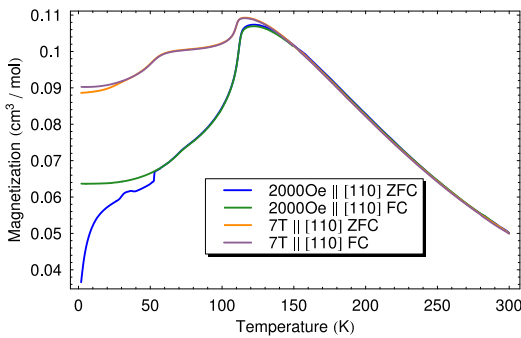


Figure 4.4: Field-cooled (FC) and zero-field-cooled (ZFC) magnetization data.

Inelastic neutron scattering experiment [112] on a single crystal was carried out on direct-geometry time-of-flight (TOF) cold neutron spectrometer IN5 at the ILL (Grenoble). The sample on the aluminum holder (Fig. 4.3) was aligned in the (HHL) scattering plane. It was mounted in the 2.5 T cryomagnet with its $(1\bar{1}0)$ axis pointing vertically along the field direction. In this configuration, field cooling had to result in the selection of the $(\xi\xi\bar{1})$ magnetic domain, whereas the $(\xi\xi 1)$ domain had to be suppressed. The sample is air-sensitive so all alignment was performed in the helium atmosphere. We performed a rocking scan for incoming neutron wavelengths of 3.15 and 4.8 Å, which correspond to the energy resolution of 0.36 and 0.1 meV, respectively, defined as the full width at half maximum of the incoherent elastic line. The measurements were done at the base temperature of 1.8 K.

The sample was cooled down in the magnetic field of 2.5 T. After reaching the base temperature, the magnetic field was switched off, and data was collected. In this scattering geometry, only the propagation vectors of the suppressed domains lie within the horizontal

scattering plane. Fortunately, they are short enough to be covered within the out-of-plane range available with the position-sensitive TOF detector bank, despite the vertical limits of the cryomagnet opening angle. The appropriate reciprocal space coverage and intensity of a signal were found in the vicinity of (005) structural Bragg peak. This Bragg reflection is forbidden by the structure factor, so the intensity from it does not affect the magnetic signal. Here both wave vectors, corresponding to the selected and suppressed magnetic domains, are reachable in momentum and have sufficient energy coverage. Therefore, further investigation was focused around the point (005) in reciprocal space. To denote points in the \mathbf{Q} space, we will use reciprocal lattice elements corresponding to a simple tetragonal unit cell ($1 \text{ r.l.u.}_a = 1 \text{ r.l.u.}_b = 2\pi/a$, $1 \text{ r.l.u.}_c = 2\pi/c$).

In the multi-domain state, if the sample were cooled in zero magnetic field, there would be two equivalent pairs of magnetic reflections ($\mp 0.141, \mp 0.141, 5$) and ($\mp 0.141, \pm 0.141, 5$) of equal intensity. To prepare a single-domain state with only one direction of the spin helix, we cooled down the sample in a magnetic field $\mathbf{B} \parallel (1\bar{1}0)$. As a result, we expected the suppression of the signal intensity at the positions of the ($\mp 0.141, \mp 0.141, 5$) magnetic Bragg reflections corresponding to the suppressed domain. The magnetic Bragg peaks at the ($\mp 0.141, \pm 0.141, 5$) positions should stay well resolvable and intense because the field was parallel to the $(1\bar{1}0)$ direction making the formation of the correspondent domain preferable.

To confirm the domain selection we made the constant-energy cut through the $(H + K, H - K, 5)$ plane (Fig. 4.5) to compare the magnetic Bragg intensities at the two orthogonal wave vectors. It is clearly seen that the intensity of the ($\mp 0.141, \mp 0.141, 5$) Bragg peaks is indeed lower than for the ($\mp 0.141, \pm 0.141, 5$) reflections. However, they are just three times smaller compared to the selected peaks. It indicates that 2.5 T field is not enough for the complete domain selection in this sample. Nevertheless, we performed a series of measurements in this “partially domain-selected state” as well as in the multi-domain state as a reference.

The overview measurements were done with the incoming neutron wavelength of 3.15 \AA . The state was prepared by cooling down the sample in a magnetic field of 2.5 T. We visualize

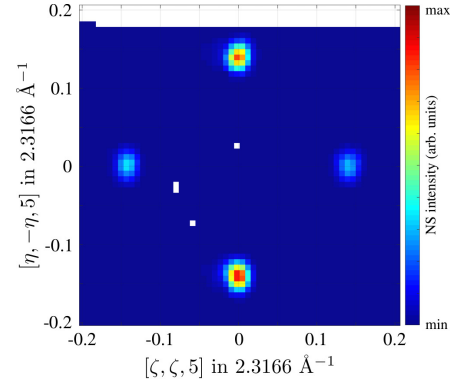


Figure 4.5: Elastic cut through the $(H + K, H - K, 5)$ plane containing both selected and suppressed Bragg peaks. The data were measured at the base temperature of 1.8 K with incident neutron wavelength of 4.8 \AA . The data integrated within $\pm 0.05 \text{ meV}$ energy range and out-of-plane momentum integration range was set to $\pm 0.04 \text{ r.l.u.}$

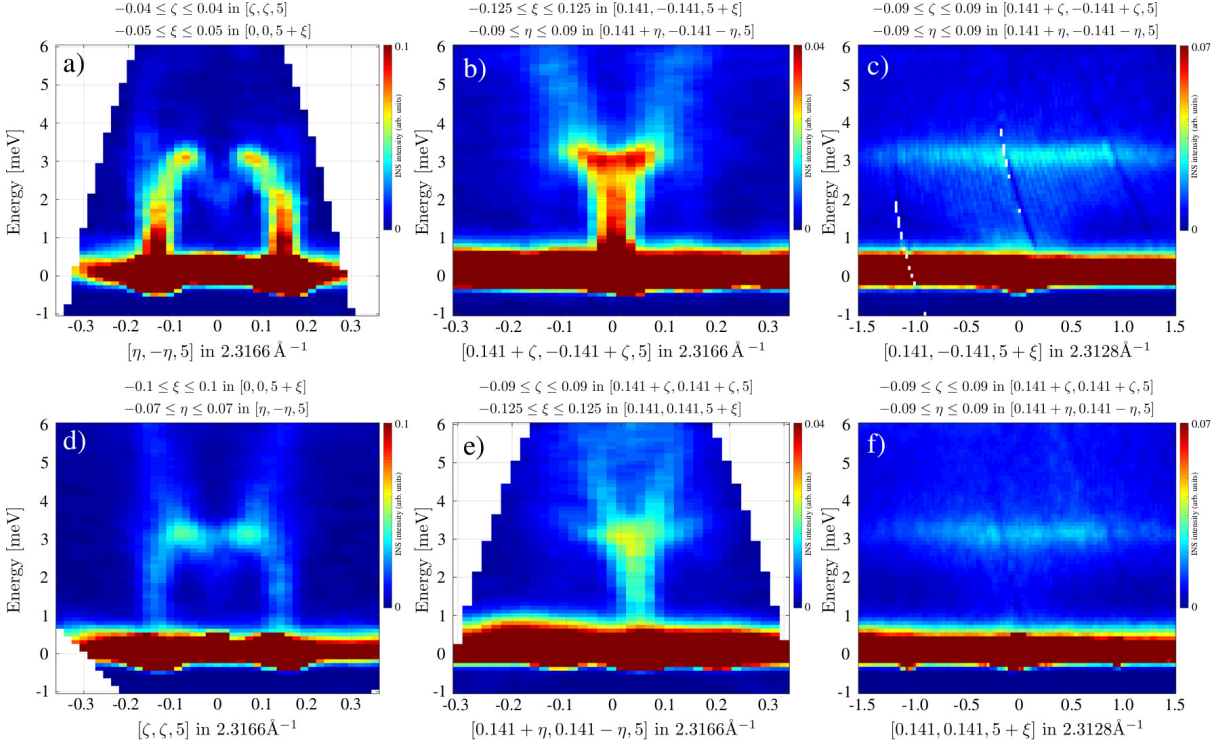


Figure 4.6: Energy-momentum cuts through the selected (a, b, c) and partially suppressed (d, e, f) Bragg peaks. (a, d) Cuts along the direction connecting two magnetic Bragg peak positions. (b) $(HH0)$ cut through the selected magnetic Bragg peak. (d) $(H\bar{H}0)$ cut through the partially suppressed magnetic Bragg peak. (c, f) $(00L)$ cuts through the selected and partially suppressed magnetic Bragg peaks. All the presented data were measured at the base temperature of 1.8 K with incident neutron wavelengths of 3.15 Å. The measurements are done with $B = 0$ T after cooling down in the magnetic field $B = 2.5$ T $\parallel (1\bar{1}0)$. The momentum integration ranges in directions orthogonal to the image are indicated above each panel.

the obtained results by presenting 2D cuts through the 4D data sets. The top and bottom panels in Fig. 4.6 show the cuts through the positions of the selected and suppressed Bragg peaks respectively. The top and bottom panels in each column can be compared in terms of the form of dispersion and signal intensity — the color scales for these pairs are the same and are indicated on each panel. Figs. 4.6 (a, b, c) show cuts through the selected magnetic Bragg peaks along several high-symmetry lines in \mathbf{Q} space that are parallel to the $(1\bar{1}0)$, (110) , and (001) directions. The bottom panels [Fig. 4.6 (d, e, f)] show the equivalent cuts through the suppressed Bragg peaks along the lines parallel to the (110) , $(1\bar{1}0)$, and (001) directions. In the $(H\bar{H}5)$ cut we clearly see intense magnon branches emanating from incommensurate magnetic satellites $(\mp 0.141, \pm 0.141, 5)$ of the (005) Bragg peak. Similar branches originating from the $(\mp 0.141, \mp 0.141, 5)$ suppressed magnetic Bragg peaks are noticeably weaker. This intensity distribution is consistent with the assumption that the domain selection procedure was only partially successful and the resulting state is a superposition of magnetic domains with helices formed along the $(1\bar{1}0)$ and (110)

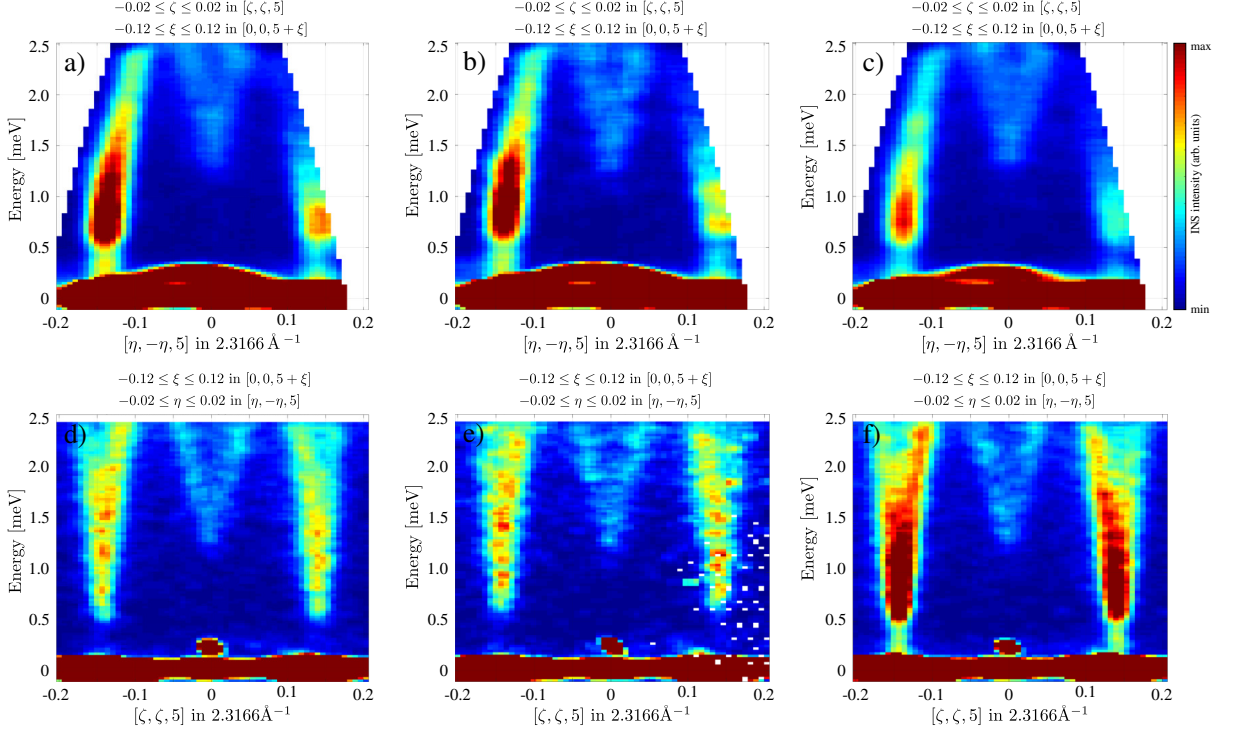


Figure 4.7: Detailed energy-momentum cuts along the directions connecting two selected (a, b, c) and two suppressed (d, e, f) magnetic Bragg peaks. (a, d) $B = 0$ T cuts after domain selection, (b, e) $B = 2.5$ T cuts after domain selection, (c, f) $B = 0$ T cuts in the multi-domain state. All the presented data were measured at the base temperature of 1.8 K with incident neutron wavelengths of 4.8 Å. The momentum integration ranges in directions orthogonal to the image are the same for all datasets and indicated above each panel. (a, b, d, e) Measurements after cooling down the sample in the magnetic field $B = 2.5 \text{ T} \parallel (1\bar{1}0)$, (c, f) measurements after zero-field cooling.

directions. Since the fraction of domains with helixes along the magnetic field applied during the cooling of the sample predominates, the intensity of the signal due to scattering by these domains is higher.

The one characteristic energy scale revealed in Fig. 4.6 is given by the inflection point at the top part of the M-shaped dispersion, located at ~ 3 meV. The results are consistent with the data measured in a multi-domain state [87].

To better resolve the low-energy details of the magnon dispersion we performed measurements with 4.8 Å wavelength, providing a very high energy resolution of 0.1 meV. The correspondent energy-momentum cuts are presented in Fig. 4.7. In addition to measurements in zero magnetic field after the domain selection procedure [Fig. 4.7 (a, d)], we also carried out identical measurements in a field of 2.5 T remaining in a partially single-domain state [Fig. 4.7 (b, e)] and measurements in a multi-domain state [Fig. 4.7 (c, f)]. In contrast to previous measurements [87], thanks to the high resolution of the IN5 spectrometer, we have found the anisotropy gap, which in this sample turned out to be of

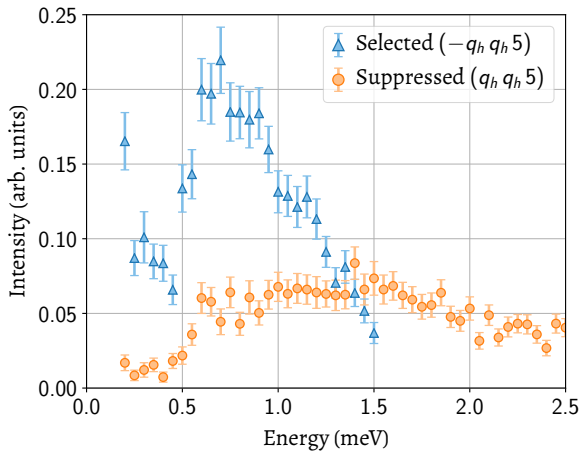


Figure 4.8: One-dimensional energy profiles of the inelastic neutron scattering signal at the positions of the selected (triangles) and suppressed (circles) magnetic Bragg peaks.

helical magnetic order and soft magnon modes at the positions of suppressed Bragg peaks. In the case of $\text{Sr}_3\text{Fe}_2\text{O}_7$, since there is an anisotropy gap, we do not observe gapless modes, but we expect a difference in the size of the gap at the positions of the selected and suppressed magnetic Bragg peaks. Since, as a result of the domain selection procedure, we failed to completely suppress the spiral in one of the directions, the signal at each of the points should be a combination of the Goldstone mode from one domain and the pseudo-Goldstone mode due to the second domain with the orthogonal direction of the spin spiral. To estimate the value of the anisotropy gap, as well as to try to distinguish the internal structure of the dispersion, in Fig. 4.8 we plotted one-dimensional cuts of the data at the suppressed and selected magnetic Bragg peaks. While these cuts give an estimate of the size of the anisotropy gap in the system, no internal structure with two different gaps can be distinguished.

the order of 0.7 meV. The presence of the gap is clearly visible on all panels in Fig. 4.7. Despite only partial suppression of domains in one direction, we still had hope of detecting the presence of pseudo-Goldstone modes in the signal. In accordance with our observations on ZnCr_2Se_4 (Chapter 3), in a sample with several possible equivalent directions of formation of a spin spiral, when choosing a unique direction of the spiral by suppressing domains of other types, magnons are a set of gapless branches arising from magnetic Bragg peaks corresponding to the selected

4.4 Summary

$\text{Sr}_3\text{Fe}_2\text{O}_7$ is a promising material for the study of pseudo-Goldstone magnons, recently discovered in ZnCr_2Se_4 [40]. The latter is the result of physics beyond the linear spin-wave theory and is currently explained by magnon-magnon interactions. To the best of our knowledge, pseudo-Goldstone magnons have so far been discovered only in ZnCr_2Se_4 — a cubic spinel compound with an incommensurate spin-spiral ground state. However, the complex unit cell of the pyrochlore sublattice formed by the $S = 3/2$ magnetic Cr^{3+} ions in the spinel structure leads to multiple spin-wave modes that complicate the theoretical

calculations. It is therefore important to repeat the experiment on a helimagnetic compound with a simpler structure. To observe this type of dispersion, one needs a material with several equivalent directions of formation of a spin spiral. The material should have negligible magnetocrystalline anisotropy and a classical spin, because in the case of spin $1/2$, quantum fluctuations can destroy the soft magnon mode. Also, the helical pitch must be short enough to ensure the propagation vector of the spin spiral is sufficiently long to be clearly resolved in the spectrum. $\text{Sr}_3\text{Fe}_2\text{O}_7$ appeared as a good possibility to investigate pseudo-Goldstone magnons on a simple tetragonal structure with only one magnetic ion per unit cell. The magnetic sublattice of $\text{Sr}_3\text{Fe}_2\text{O}_7$ is formed by the $S = 5/2$ magnetic moments and can be considered as classical. There are only two possible directions for the incommensurate spin spiral with a sufficiently long propagation vector to be clearly resolved in the spectrum.

The goal of the proposed experiment was to measure the pseudo-Goldstone magnon dispersion and determine its spin gap with high-resolution TOF spectroscopy. The data obtained on a simple-tetragonal layered compound with classical spins and one magnetic atom per unit cell would enable a quantitative comparison with spin-dynamical calculations.

We performed a series of measurements on the cold neutron time-of-flight spectrometer IN5 (ILL, Grenoble) and mapped out the low energy dispersion in $\text{Sr}_3\text{Fe}_2\text{O}_7$. The sample was prepared by cooling down in a magnetic field of 2.5 T applied along the $(1\bar{1}0)$ direction. It leads to the partial domain selection and the final state was a superposition of the $(\xi\bar{\xi}1)$ and $(\xi\xi1)$ magnetic domains. Thereby, we conclude that the applied magnetic field is not sufficient for the complete domain selection. Based on the analysis of the intensities of the corresponding Bragg peaks, we found that the fraction of the selected $(\xi\bar{\xi}1)$ domains in the final partially single-domain state was three times higher than the fraction of the suppressed ones. The high-resolution measurements revealed the anisotropy gap in a system of the order of 7 meV which was not resolved in previous neutron studies.

As a result of the partial suppression of one type of magnetic domains, the intensity of the magnetic signal was also redistributed accordingly – we observe an intense signal near the selected wave vectors and less intense branches of dispersion arising from the magnetic satellites corresponding to the suppressed domains. Based on the experience of similar measurements on ZnCr_2Se_4 , for each of the magnetic domains, we expected to find two types of excitation modes. The first type of excitations is characterized by dispersion having a minimum on the wave vectors corresponding to the magnetic order in this particular domain. In ZnCr_2Se_4 , these excitations were found in the form of gapless dispersions, or the so-called Goldstone modes. Since in the case of our system there is anisotropy, these excitations will have a gap. The second type of excitations is pseudo-Goldstone modes —

gapped soft modes having the minima at wave vectors corresponding to the propagation vectors of the spin spirals in the equivalent magnetic domains. These excitations were also found in ZnCr_2Se_4 and, in contrast to the gapless Goldstone modes, they had a spin gap of 0.17 meV. In the case of a sample with an anisotropy gap, it can be assumed that both types of magnons will be gapped, but the gap sizes will be different. In the case of a partial choice of domains, one can expect that two types of magnon dispersions from a superposition of equivalent domains will manifest themselves in the form of an internal structure of the inelastic neutron scattering signal on each of the ordering vectors. However, any attempts to discern any internal structure in the measured data have not led to convincing results.

Obviously, the answer to the question of the presence of pseudo-Goldstone modes in $\text{Sr}_3\text{Fe}_2\text{O}_7$ requires further measurements in the single-domain state prepared using a higher magnetic field. Our group has already made a proposal for such measurements, and we plan to continue this study.

Chapter 5

Iron monophosphide (FeP)

5.1 Introduction

5.1.1 Phosphides of transition metals

FeP belongs to a family of binary compounds with the general formula MX (where M is a transition metal, X is a pnictogen). These compounds have the MnP-type structure and many of them display noncollinear magnetism. One of the most attractive properties is helimagnetism appearing in iron monophosphide and a few other members of the MX family [113]. Another intriguing phenomenon is pressure-induced superconductivity discovered in CrAs and MnP in the vicinity of the magnetically ordered state [114–116].

The orthorhombic FeP crystallizes in a complex crystal structure with 4 formula units per unit cell (space group $Pnma$) [117]. It consists of magnetic Fe^{3+} and non-magnetic phosphorus P^{3-} (Fig. 5.1) that occupy the c positions of the $Pnma$ space group. The unit cell parameters are, at room temperature, $a = 5.17 \text{ \AA}$, $b = 3.09 \text{ \AA}$, $c = 5.77 \text{ \AA}$ [118].

Available resistivity data demonstrate metallic behavior [119, 120]. Susceptibility and specific heat measurements on powder and single-crystalline samples [118–122] show an antiferromagnetic phase transition at about $T_N = 120 \text{ K}$. Other remarkable features seen in susceptibility data are the high level of anisotropy at $T > T_N$ between different crystallographic directions and a broad peak in all curves at about 220 K which indicates the existence of short-range order well above the ordering temperature.

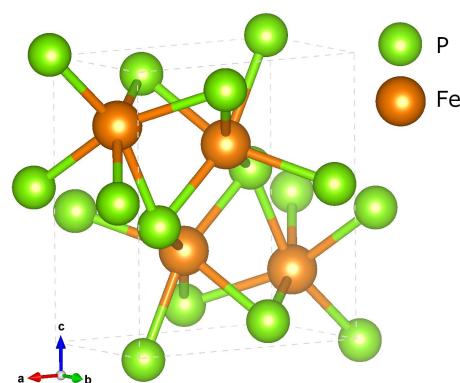


Figure 5.1: FeP crystal structure. The structure is plotted using VESTA software [107] based on data in Ref. [117].

The results of thermal expansion measurements, performed in the temperature range 95–300 K, show the behavior similar to other MnP-type compounds — the thermal expansion coefficient of the b -axis is about six times higher than for other directions [120].

5.1.2 FeP magnetic structure

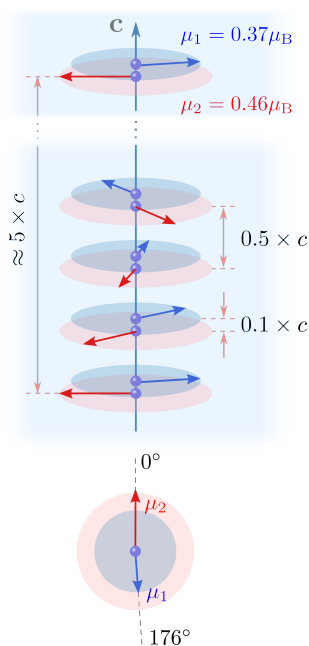


Figure 5.2: Schematic illustration of the FeP helical spin structure propagating along the c axis as proposed by Felcher *et al.* [123]. Iron magnetic moments located in one ab plane are codirectional and have the same magnitude. All iron atoms are projected on the c axis for a visual representation of the spiral structure. Blue and red arrows represent the magnetic moment in the corresponding ab plane.

FeP has an incommensurate helical magnetic ground state, however, the details of the spin structure are still not completely clear. The first spin structure was proposed by Felcher *et al.* in the early 1970s [123]. Neutron diffraction measurements on both powder and single-crystal samples below the Néel temperature revealed a magnetic modulation along the c -axis with a period of $29.2 \text{ \AA} \approx 5 \times c$ and corresponding propagation vector $k_h = 0.22 \text{ \AA}^{-1}$. Similarly to the isostructural MnP [124] and CrAs [125], the magnetic structure was determined as a “double-helix” propagating along the c axis. To obtain a good fit of the diffraction data, authors proposed two different sites for the iron ions with different magnetic moments $0.46\mu_B$ and $0.37\mu_B$. This model is schematically shown in Fig. 5.2. The iron moments lying in the ab plane form ferromagnetic layers perpendicular to the c axis. Spins in the two nearest planes separated by $0.1 \times c$ are nearly antiparallel with the fixed relative angle of 176° . Following the c axis, the direction of spins changes forming a helical structure nearly commensurate with the c axis.

However, following Mössbauer studies performed by several groups [121, 126] result in a long-standing uncertainty concerning the exact details of the spin structure. It was impossible to fit Mössbauer spectra using an easy “double-helix” model proposed by Felcher *et al.* Instead, the authors proposed a modified spiral model with anharmonicity (bunching) of the iron spins and possible modulation of the magnetic moments in the ab plane. According to this model, iron spins are crowding along the a axis. Further detailed studies using polarized neutron diffraction analysis are needed to identify details of the spin structure.

5.2 Neutron scattering experiments

5.2.1 FeP single crystals

Large single crystals of FeP (up to 0.5 g in mass, see Fig. 5.3) of very high crystalline quality were recently grown by our collaborators using chemical vapor transport with iodine transport agent [118]. The optimized temperature regime, reported in details in Ref. [118], allowed them to grow large high-quality single crystals suitable for INS experiments.



Figure 5.3: FeP crystals.

The grown crystals were extensively characterized to confirm their composition, crystal symmetry, unit cell parameters, single crystallinity, magnetic, and transport properties [118]. The elemental analysis and chemical characterization, done by means of energy-dispersive x-ray spectroscopy (EDX), revealed iron and phosphorus in 1:1 proportion corresponding to the FeP stoichiometric composition.

Crystals used for the magnetization, susceptibility, x-ray diffraction, and neutron scattering experiments were aligned using the x-ray Laue backscattering technique. Typical Laue diffractograms are shown in Fig. 5.4. Besides the orientation of a crystal, the Laue method allows us to draw conclusions about the perfection of a sample. In the case of our FeP samples, the spots in the Lauegrams are well resolved, sharp, with intensity concentrated in a small area around the peak. The spots are aligned along the arcs forming symmetric patterns without noticeable artifacts. If we move the crystal in the plane perpendicular to the x-ray beam, the Laue pattern does not change the orientation and positions of the peaks. Therefore, we can conclude that the crystals are of high quality with no twin domains. Also, we considered a possibility of grains inside the samples, which the Laue method cannot detect, but further neutron diffraction experiments confirmed the uniformity of the samples in a bulk.

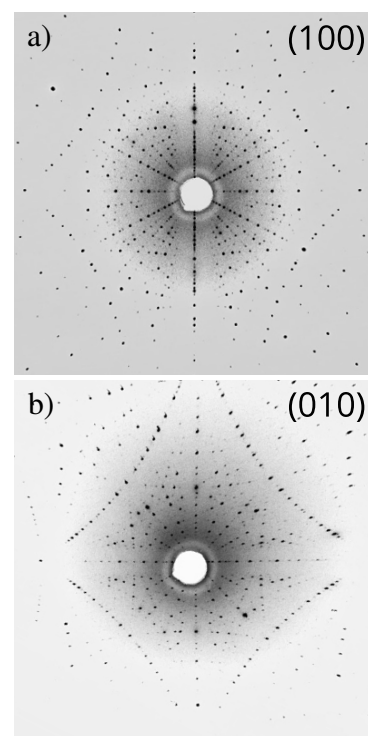


Figure 5.4: Laue patterns of a FeP crystal measured along its a and b crystallographic directions (panels a and b, respectively). Reproduced from Ref. [118].

To check the crystal structure and determine the unit cell parameters, x-ray powder and single-crystal diffraction were utilised. Both methods confirmed the $Pnma$ space group,

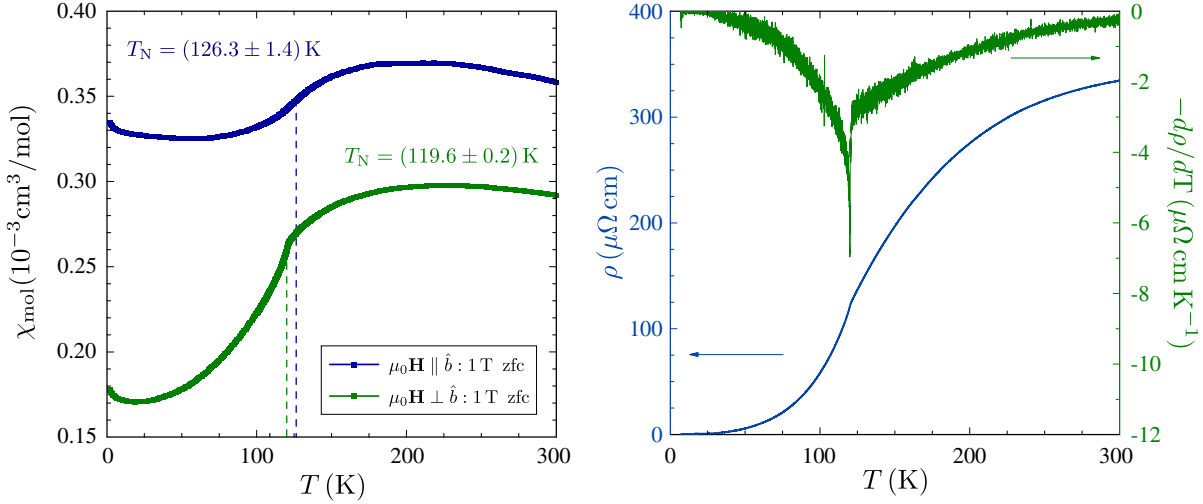


Figure 5.6: Magnetic and transport properties of the FeP single crystal. (a) Temperature dependence of the magnetic susceptibility measured on a single crystal of FeP in an external field of 1 T. (b) Temperature dependence of the electrical resistivity (blue curve) and its derivative (green curve). Reproduced from Ref. [118].

and the refined unit cell parameters ($a = 5.1738(4) \text{ \AA}$, $b = 3.0877(4) \text{ \AA}$, $c = 5.7718(6) \text{ \AA}$) are in good agreement with the previously published results [127].

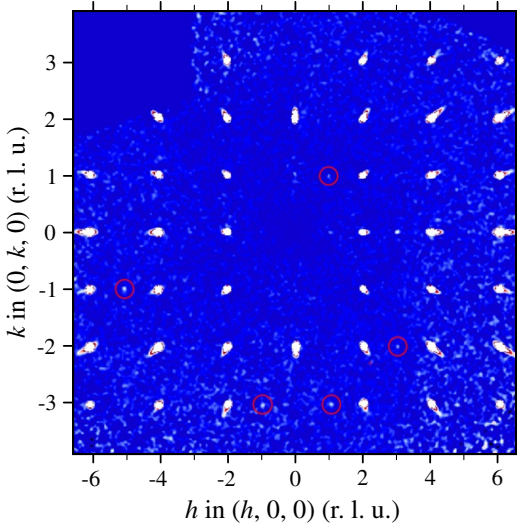


Figure 5.5: Single-crystal x-ray diffraction map of the $(hk0)$ plane measured at $T = 300 \text{ K}$. Red circles mark the Bragg peaks violating the $Pnma$ space group extinction rules. Reproduced from Ref. [118].

The single-crystal x-ray diffraction measurements performed in the wide temperature range 30–300 K confirmed the absence of any structural phase transition. Diffraction pattern of the $(hk0)$ plane measured at 300 K is shown in Fig. 5.5. Well resolved Bragg peaks prove the good quality of the measured crystal. The structure refinement confirmed the $Pnma$ space group. However, after a closer look at the data, one can distinguish weak Bragg peaks with integer Miller indices, which are forbidden by the $Pnma$ group extinction rules [see Fig. 5.5]. These peaks are present at all measured temperatures. On the current stage of the analysis they were ignored during the structure refinement procedure but definitely should be investigated

in the future. The presence of these peaks could originate from some sort of twinning or indicate a lowering of the lattice symmetry and the consequent possibility of the existence of two nonequivalent Fe sites in the unit cell. This possibility requires a closer investigation.

Magnetic susceptibility measurements [Fig. 5.6 (a)] confirm a magnetic phase transition at about 120 K which coincides with the inflection point in the electrical conductivity [Fig. 5.6 (b)]. The magnetic susceptibility was measured at 1 T field on the samples cooled down without application of an external magnetic field. The measurements were done along the b crystallographic direction and perpendicular to it and agree fairly well with the literature [120]. There are several features in the susceptibility data that are worth attention. The high level of the anisotropy and the broad maxima above the Néel temperature suggest a short-range order far above the transition temperature. The behavior of the curves supports the earlier proposed magnetic structure [123] — the susceptibility along the b axis reminds an equally weighted superposition of the parallel and perpendicular susceptibilities of an antiferromagnet. The curve measured along the direction perpendicular to the b axis (it is not indicated in which exact direction it was measured) resembles the superposition with the prevailing perpendicular component. These are in excellent agreement with the proper screw structure propagating in the c direction.

To investigate the magnetic-field dependence of the FeP magnetization in the ordered state, we performed a set of measurements along all principal directions of the sample [Fig. 5.7]. For each orientation the magnetization was measured at 10 K and 2 or 3 K in the magnetic field up to 13 T. The field dependence along the b direction exhibits pronounced oscillations at 3 K. This is a manifestation of the de Haas-van Alphen (dHvA) effect in FeP. The effect was extensively studied in the exhaustive work of Nozue *et al.* [122]. The authors measured the angular dependence of the dHvA branches and discovered that some of them are caused by a magnetic breakdown phenomenon — the tunneling of electrons from one classical orbit in a magnetic field to another. This causes a formation of large closed orbits in reciprocal space lying on surfaces beyond the magnetic Brillouin zone which cannot be captured by the band structure calculations. The authors measured effective masses for a field, aligned parallel to all principal directions, and reported the fairly small electronic specific-heat coefficient $2.86 \text{ mJ K}^{-2} \text{ mol}^{-1}$.

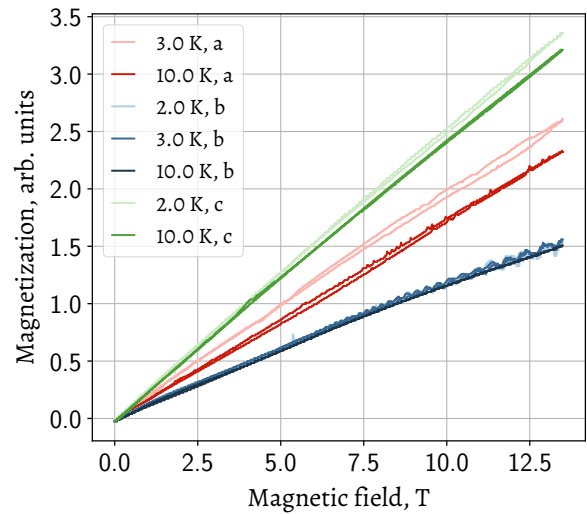


Figure 5.7: Magnetic field dependence of the FeP magnetization along the principal axes of the crystal measured for different temperatures well below the Néel point (unpublished).

5.2.2 FeP reciprocal space overview

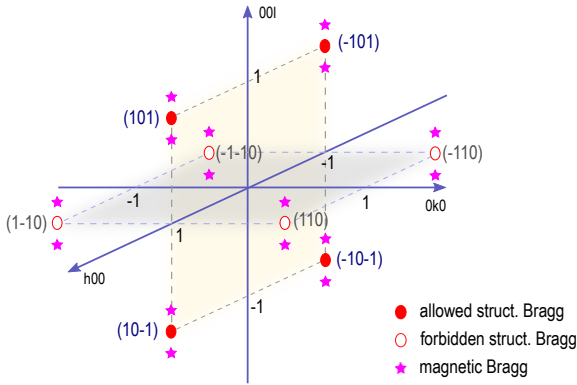


Figure 5.8: Schematic of the reciprocal space of FeP. Closed and open red circles represent structural Bragg peaks allowed and forbidden by the structure factor. Purple stars are at the positions of the magnetic satellites. The (000) Bragg peak is not shown because it is not accessible by our spectrometers.

The theory for the usual (that is, nearly ferromagnetic) helical spin structures is well developed. However, the behavior of the low-energy magnon modes in more exotic antiferromagnetic and ferrimagnetic spin-spiral structures is not fully understood, especially in materials in which neither localized nor itinerant character of the magnetic moments can be clearly established. FeP was investigated by many techniques, but no Q -resolved spin-dynamical studies by inelastic neutron scattering (INS) have been reported so far. The detailed data about the magnon dispersion in FeP help to fill this gap in our

understanding of spin dynamics in itinerant noncollinear magnets, and, in particular, allow us to quantify the relevant energy scales of magnetic interactions in FeP.

We have used thermal time-of-flight (TOF) and triple-axis spectroscopy (TAS) techniques to map out dispersions of magnetic excitations in FeP. To make it easier to orient in the reciprocal space of the sample, let us have a look at its structure. Figure 5.8 illustrates the part of reciprocal space containing wave vectors that will be important in the following study. The structure factor suppresses the intensity of some Bragg reflections allowed by the space lattice. Therefore, we will distinguish two types of the structural Bragg peaks: “allowed” and “forbidden”. As far as the magnetic ground state is an incommensurate helical structure, the reciprocal space includes magnetic Bragg peaks accompanying the structural ones. They are distanced from the positions of the structural Braggs by the propagation vector of the spiral ($00 \pm q_h$). Here we should note that because of the very complex spin structure, the intensity of the magnetic peaks does not exactly follow the structure factor of the lattice. It allows us to observe the intense magnetic satellites around the forbidden structural Bragg reflections.

5.2.3 Neutron diffraction

Single-crystal neutron diffraction measurements were conducted using the E2 diffractometer at HZB, Berlin. It is a flat-cone geometry diffractometer with 2D detectors, which allows

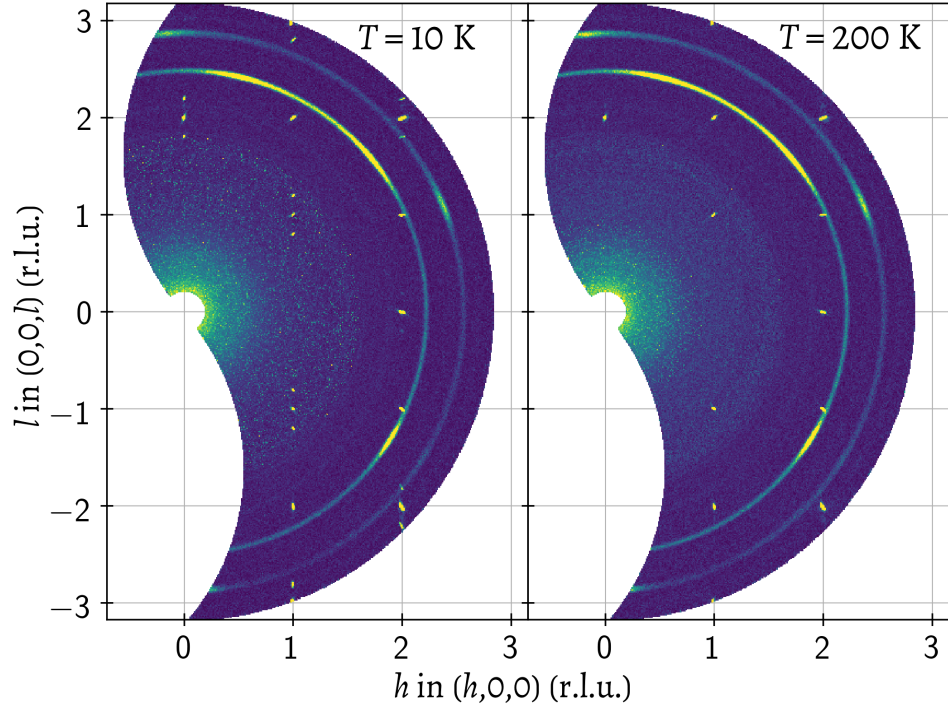


Figure 5.9: Diffraction panels from E2 diffractometer, HZB (setup 1). Left panel contains the data measured at $T = 10$ K. Right panel corresponds to the paramagnetic state at $T = 200$ K. On the low temperature data one can clearly see the appearance of the magnetic satellites at the incommensurate positions $(00 \pm q_h)$ with $q_h \approx 0.2$ r.l.u around the structural Bragg peaks.

measuring out-of-plane peaks. To get the in-plane signal we grouped the signal into eight channels and then integrated the 4th and 5th channels manually. For the E2 experiment (setup 1) the sample was a single crystal of FeP on the aluminum holder. It was mounted in the 7 T cryomagnet with its $[010]$ axis vertical. This crystal orientation allowed us to access the most important high-symmetry directions of the reciprocal space, within the equatorial $(H0L)$ scattering plane. The instrument setup included PG monochromator and $30'$ radial collimation. The measurements were performed with a neutron wavelength $\lambda = 2.41$ Å ($k_i = k_f = 2.62$ Å⁻¹).

The diffraction patterns in the $(h0l)$ scattering plane are shown in Fig. 5.9. We measured two maps above and below the Néel temperature at $T = 200$ K and 10 K, respectively. On the 200 K map there are well-resolved Bragg peaks corresponding to the structural reflections allowed by the structure factor. Concentric circles in both panels are the scattering from the aluminum sample holder. After cooling down the sample below its Néel temperature, additional peaks appear at the incommensurate positions $(00 \pm q_h)$ with $q_h \approx 0.2$ r.l.u. These peaks are magnetic satellites caused by the incommensurate periodic spin structure formed along the c axis below the ordering temperature.

5.2.4 Inelastic neutron scattering

TOF experiments

As the first step in the inelastic neutron study, we performed TOF experiment to get an overview of the excitation spectrum of FeP. The experiment [128] was performed at the MERLIN spectrometer (setup 2) at ISIS, UK. A single crystal of FeP with a mass ~ 0.5 g was mounted in the top-loading closed-cycle cryostat with its a axis vertical, providing $(0\ K\ L)$ scattering plane. We collected the data at the base temperature of 7.5 K utilising neutrons with incoming energies $E_i = 27, 40$, and 60 meV ($\lambda_i = 1.74, 1.43$, and 1.17 Å, respectively). An outcome of the TOF experiment is a data file containing information about a part of the 4-dimensional (4D) energy-momentum space $(\mathbf{Q}, \hbar\omega)$ of the sample. To visualize the data, we make cuts through this space along the directions of interest. Furthermore, it is possible to combine symmetrically equivalent parts of the reciprocal space. In such a way we improve the statistical quality of the data. All the data processing has been done using HORACE software package [82, 83].

The typical energy-momentum cuts are shown in Fig. 5.10. The top panel schematically shows lines in reciprocal space along which the cuts were done. The strongest magnetic Bragg peaks appear as incommensurate satellites around the $(1\ 0\ 1)$ and $(1\ 1\ 0)$ wave vectors. They are clearly inequivalent, as the $(1\ 0\ 1)$ wave vector corresponds to an allowed structural Bragg reflection, while the $(1\ 1\ 0)$ structural Bragg reflection is forbidden. Such a behavior is not surprising, as a collinear ferrimagnet possesses two inequivalent magnetic Bragg peaks at the structural zone center and at the zone boundary, hence when a ferrimagnetic order is twisted into a spiral, both reflections split into a pair of incommensurate peaks.

In the inelastic channel, which we were so far able to map in the three-dimensional $(H\ K\ L)$ space with only limited statistics, several energy scales are clear. The measurements revealed the gapped magnon dispersions emanating from the incommensurate magnetic satellites of the same commensurate wave vector, separated in the L direction [Fig. 5.10 (c, f)]. They can be resolved only at low energies, below ~ 10 meV. After that, they merge into a single broad peak.

The dispersion along the H direction [Fig. 5.10 (a, d)] is also quite shallow, so that the spin waves emanating from the vicinity of $(\bar{1}\ 1\ 0)$ and $(1\ 1\ 0)$ merge around 25–30 meV [Fig. 5.10 (a)]. In contrast, the dispersion along the K direction [Fig. 5.10 (b, e)] rises very rapidly in comparison to the two other orthogonal directions. This means that effective couplings along Y bonds are stronger than along X and Z bonds. The data cover an energy range only up to 35 meV, but from the slope of the dispersion, one can guess the magnon

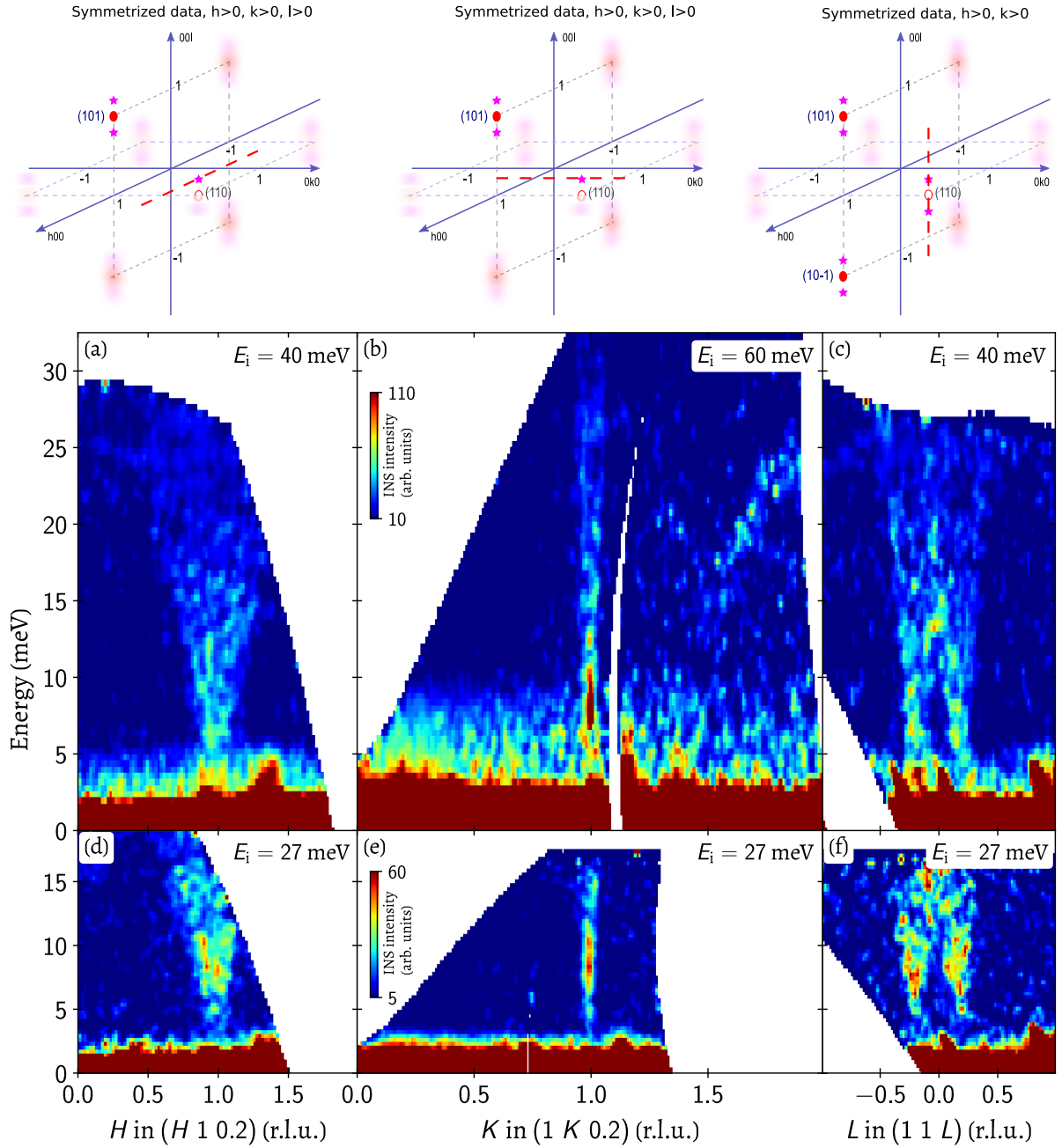


Figure 5.10: Energy-momentum cuts through the TOF data (setup 2) measured at the MERLIN spectrometer, plotted along high-symmetry directions after the symmetrization according to the orthorhombic crystal symmetry. The sketches in the top panel illustrate the directions in reciprocal space (dashed red lines) along which the cuts were done. The blurred spots depict the positions of the peaks which were projected out by the symmetrization. Each sketch describes the data shown on the panels underneath it. All the data were measured at the base temperature of 7.5 K with incident neutron energies of 40 meV (a, c), 60 meV (b) and 27 meV (d, e, f). The momentum integration range in directions perpendicular to the image was set to ± 0.1 r.l.u. for h and l , and ± 0.035 r.l.u. for the k direction.

bandwidth of a few hundred meV. As a side remark, we note that the magnon branch in FeP prominently crosses an optical phonon around 27 meV, as seen in Fig. 5.10 (b), which could be an interesting case for a separate study of magnon-phonon hybridization.

TAS experiments

To resolve the details of the dispersions, we supplemented our TOF data with thermal-neutron TAS measurements performed at IN8 (ILL, Grenoble) and PUMA (MLZ, Munich) spectrometers. In our first IN8 experiment, we performed overview measurements and revealed sharp magnon modes along the $(11L)$ direction in the vicinity of (110) while staying in the (HHL) scattering plane. Subsequently, we complemented these data with measurements at the PUMA spectrometer in the $(H0L)$ scattering plane, where data along the L direction were acquired along the $(10L)$ direction in the vicinity of (101) . However, because of the very steep magnon dispersion in the q_y direction, which was oriented along the out-of-plane direction in both experiments, which has the worst momentum resolution, we could only see clearly the dispersion along L but not along H and K . Therefore, another beamtime was requested at IN8 to complete the measurements in the $(HK0)$ and $(0KL)$ scattering planes. In these configurations, we had better K resolution and were able to reveal the magnon dispersion along H and K directions. All experiments were performed on the mosaic of co-aligned single crystals of FeP with a total mass ~ 1 g.

During the first IN8 experiment [129] (setup 3), the sample was mounted inside an “orange”-type cryostat in the (HHL) scattering plane. In this configuration the (110) forbidden Bragg peak and its magnetic satellites (11 ± 0.2) could be reached. The experimental configuration with PG filter and fixed $k_f = 2.662 \text{ \AA}^{-1}$ was used to achieve a sufficient resolution. Measurements were done at the base temperature of 2 K. In order to map out the magnon dispersion along the $(11L)$ direction, we have measured multiple momentum scans up to 35 meV and a few energy scans to quantify the magnitude of the spin gap at (11 ± 0.2) . To reach higher energies, we changed k_f to 4.1 \AA^{-1} and finished the mapping up to 38 meV. The summarising plot is shown in Fig. 5.11 (a). Here we can clearly see gapped W-shaped magnetic signal extending up to 35 meV. The dispersion is symmetric with respect to (110) Bragg peak both in shape and intensity distribution. It is not surprising because the reciprocal space is symmetric with respect to the $(HH0)$ plane, and both magnetic satellites are equally distanced from the center of the first Brillouin zone. Two branches emanating from the positions of the incommensurate magnetic satellites (11 ± 0.2) have the gap value $\Delta_g \approx 7$ meV. The gap value indicates a significant anisotropy in the system. The outer branches of the dispersion are possibly back-folded at 0.5 r.l.u. This back-folding is not well resolved because of the arc-shaped signal of non-magnetic origin. This signal at around 27 meV is an optical phonon which we already have seen in Fig. 5.10 (b, c). Another noticeable but unwanted signal — a sharp, well defined straight diagonal line crossing the picture. It is a so-called “spurion”. Such artifacts frequently appear because of the nonideal

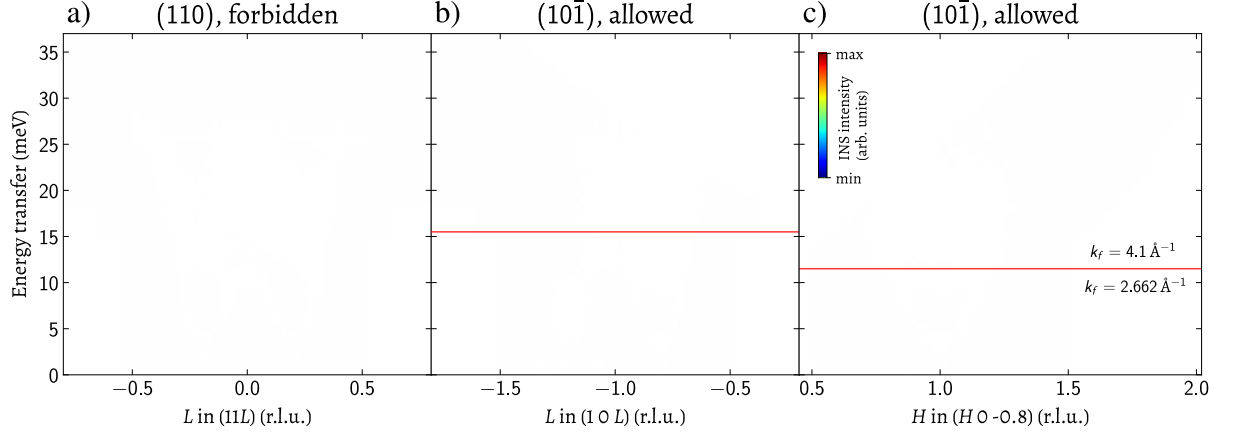


Figure 5.11: Low temperature magnon dispersions in FeP along the $(00L)$ and $(H00)$ directions mapped out with the thermal-neutron spectrometers IN8 (setup 3) (a), and PUMA (setup 4) (b, c). The measurements were conducted with fixed $k_f = 2.662 \text{ \AA}^{-1}$ (below the horizontal red line) and k_f to 4.1 \AA^{-1} above it.

behavior of various sample environments or spectrometer components. This spurious signal makes it almost impossible to resolve the internal structure of the middle part of the dispersion at this wave vector.

Figure 5.11 (b, c) shows the results of the complementary experiment at the TAS spectrometer PUMA. In this experiment (setup 4), the sample was mounted in the standard cryostat with its b axis vertical, providing $(H0L)$ scattering plane. This alignment was chosen to be able to reach the $(10\bar{1})$ allowed magnetic Bragg peak and its magnetic satellites $(10-0.8)$ and $(10-1.2)$. The measurements were performed at the temperature of 3.5 K. To reach a compromise between intensity and resolution, the instrument was operated with PG002 monochromator and analyzer in the double-focusing mode. Measurements were performed with fixed $k_f = 2.662 \text{ \AA}^{-1}$ up to 15 and 12 meV for L and H scans, respectively. To obtain sufficient momentum coverage for higher energies, we changed k_f to 4.1 \AA^{-1} , which naturally entails lower resolution. Just as during the IN8 experiment, we carried out a series of momentum scans at different energies. We mapped out the dispersion along H and L directions. This time we investigated magnetic satellites of the $(10\bar{1})$ Bragg peak. The dispersion in L direction [Fig. 5.11 (b)] demonstrates the same behavior as around the (110) forbidden Bragg but the intensity distribution is different. The branches emanating from $(10-0.8)$ are noticeably more intense than the ones around $(10-1.2)$. It is a consequence of the magnetic form factor, which diminishes with a momentum transfer. In Fig. 5.11 (c), the H dependence of the dispersion stemming from $(10-0.8)$ is shown. From the comparison of the $(11L)$ and $(H0-0.8)$ data, we can conclude that the magnon dispersion behavior is the same in the vicinity of forbidden and allowed structural Bragg peaks.

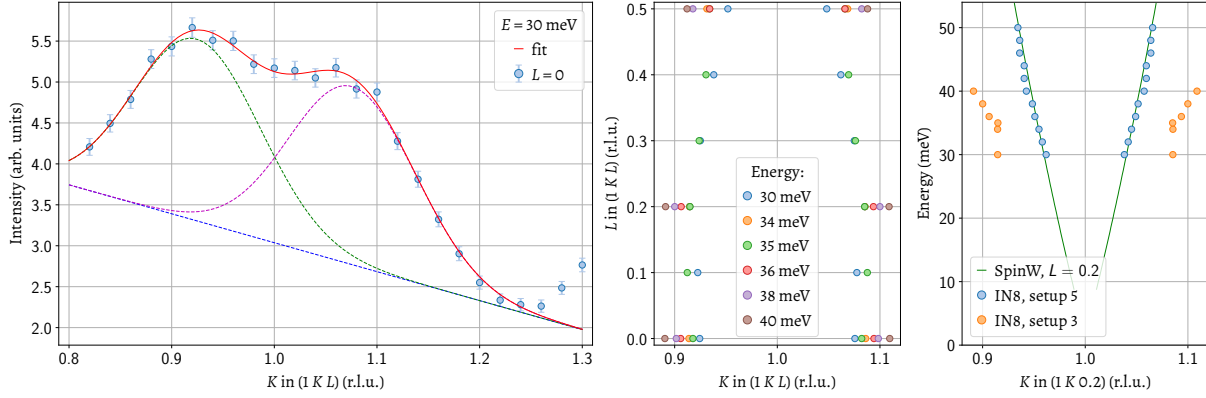


Figure 5.12: Out of the (HHL) scattering plane measurements of FeP at the IN8 spectrometer (setup 3). (a) Typical raw momentum scan along $(1KL)$ at $L = 0$ and $E = 30$ meV. Red curve is a fit of the data with two Gaussians (green and purple dashed lines) and a linear background (blue dashed line). (b) $(1KL)$ constant energy dispersion profiles obtained from the Gaussian fits of the data. (c) Energy-momentum profiles of the magnon dispersion along the $(1K0.2)$ direction measured IN8. Orange and blue circles correspond to the data measured in the setup 3 and setup 5. The green line is a $(1K0.2)$ dispersion modelled with SpinW (see Section 5.3 for details).

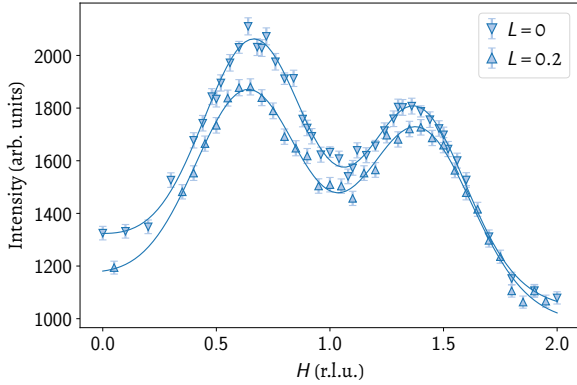


Figure 5.13: Two H scans centered at (110) , measured at 40 meV at $L = 0$ and $L = 0.2$ (to reach finite L , one of the sample goniometers had to be tilted). The solid lines are fits with two Gaussians.

IN8 spectrometer has a software feature that allows one to easily navigate out of the scattering plane using the goniometers installed under the cryostat. It allowed us to make measurements outside the (HHL) scattering plane and investigate the magnon dispersion along K -direction. We made a series of K -scans at different L and fixed $H = 1$ r.l.u. in the vicinity of (110.2) magnetic satellite for energies between 30 and 40 meV. The typical scan for $L = 0$ and $E = 30$ meV is shown in Fig. 5.12 (a). For

every single scan, we made a fit with two Gaussians and a linear background. The L -coordinates of the Gaussian peak centers correspond to the dispersion positions at a given energy. We summarised these fits in Fig. 5.12 (b). This plot can be interpreted as a set of the $(1KL)$ constant-energy cuts of the dispersion at different energies, and one can observe its energy evolution. The proportions between the reciprocal lattice units are preserved, and it is seen that dispersion along K is much steeper than along L . The out-of-plane measurements can give a general impression of the dispersion's behavior, but the resolution is quite low to expect accurate values. The next IN8 experiment (setup 5) revealed that the dispersion in the K direction is even steeper and the interactions in FeP are highly anisotropic. In

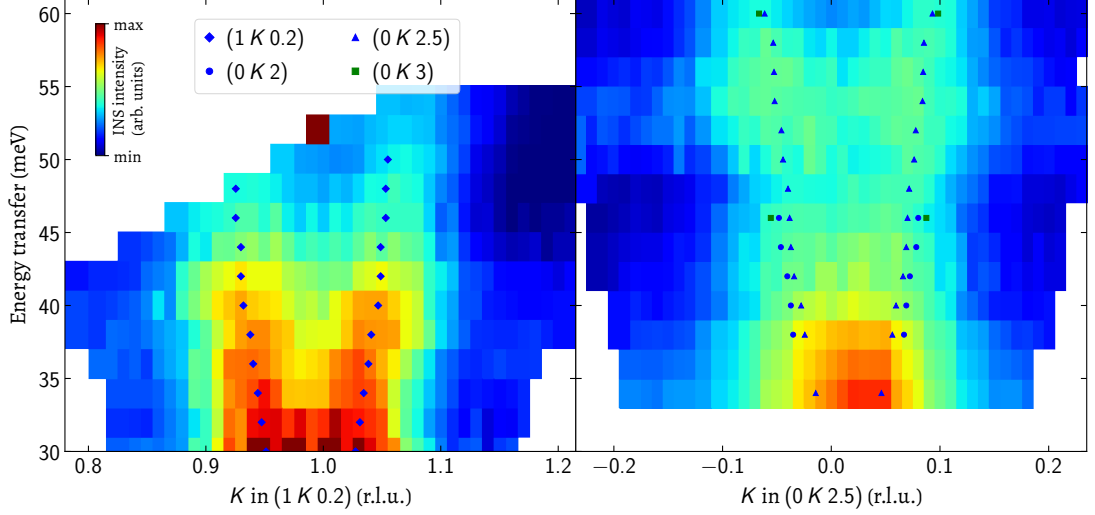


Figure 5.14: Measured intensity along the $(1 K 0.2)$ and $(0 K 2.5)$ directions, presented as a color map. The markers represent the Gaussian fits of the data measured along K direction at different L and H values.

Fig. 5.12 (c), the energy-momentum dispersion profiles are shown for setups 3 and 5. The green line is a $(1 K 0.2)$ dispersion modeled with SpinW software and will be discussed in Section 5.3.

During the next experiment [130] at IN8 (setup 5), we used the same pre-aligned array of FeP single crystals. The measurements were started with the sample mounted in the $(H K 0)$ plane, and after two days the sample was re-oriented into $(0 K L)$. In the first case, the measurements were done near the structurally forbidden (110) reflection that has two magnetic satellites. Both H - and K -scans were performed. In the second case, the measurements were carried out near the structurally allowed (002) and (013) wave vectors. Here we mostly performed K scans at several L values and at different energies up to 70 meV. We chose the experimental configuration with PG filter and fixed $k_f = 4.1 \text{ \AA}^{-1}$ in order to have access to higher energies. All measurements were done at the base temperature of 1.5 K. Due to the improved momentum resolution along K , we could clearly resolve the magnon peaks both along the H direction [see Fig. 5.13 for an example] and along the K direction [Fig. 5.15].

The steepness of the dispersion along the K direction leads to the fact that the dispersion at high energies is almost independent of L . In Fig. 5.14 we summarize the data collected along the $(1 K 0.2)$ and $(0 K 2.5)$ directions in the form of a color map. The fitting results for the peak positions are overlaid as data points for different values of L . They show a linear dispersion and nearly coincide within the accuracy of the fit. By extrapolation, a magnon bandwidth of about 500 meV can be estimated for this momentum direction. Higher background in the energy range between 50 and 55 meV is due to an optical phonon.

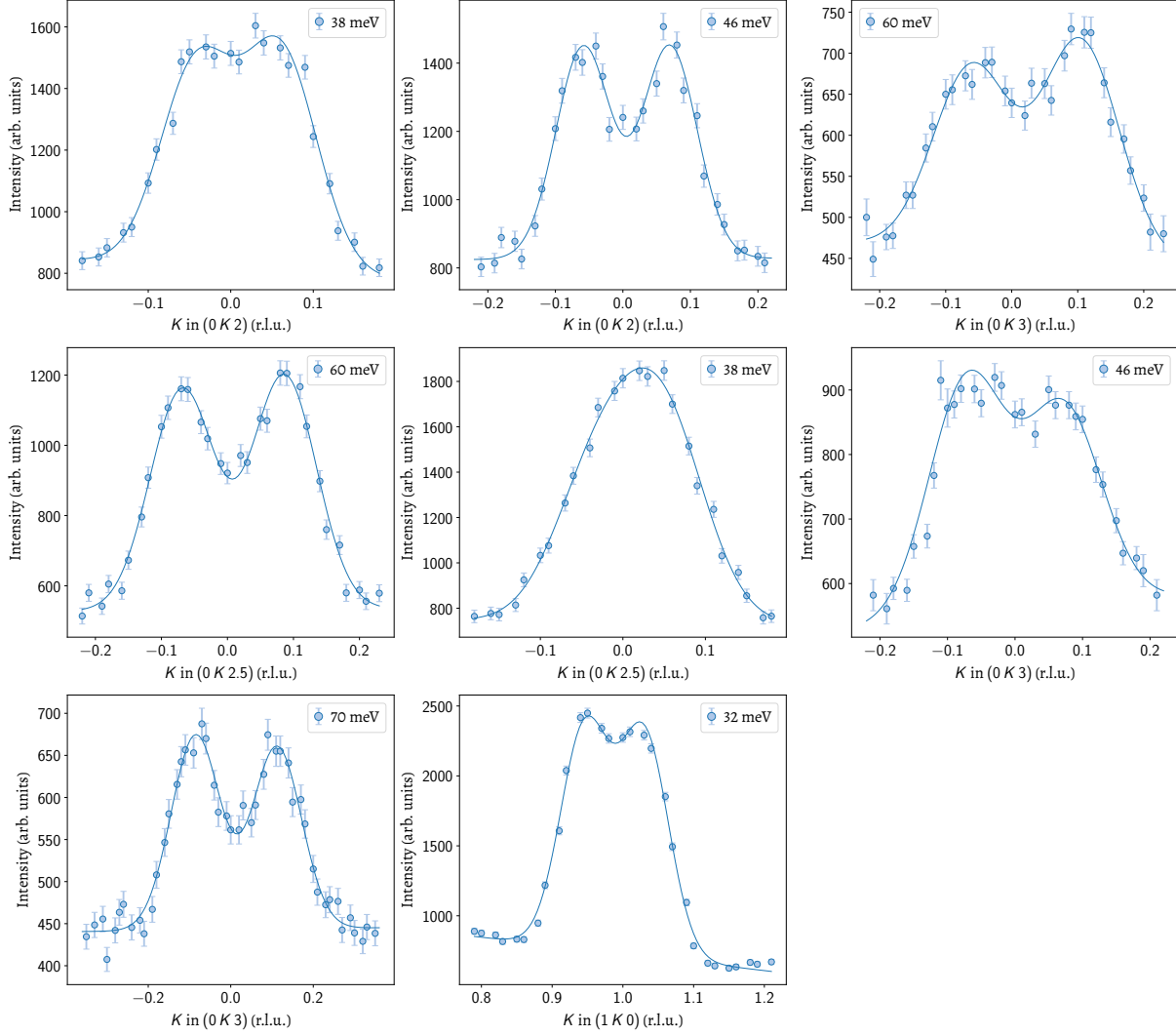


Figure 5.15: Several representative momentum scans along the K direction, revealing the splitting of two magnon branches at high energies. The solid lines are fits with Gaussians.

5.3 Localised spin approach to magnon spectrum in FeP

5.3.1 Motivation

FeP attracted our attention because of its exotic spin structure — so-called “double helix”. This structure was proposed by Felcher [123], but its exact details are still not fully understood. Our collaborators performed *ab initio* calculations for this system and estimated the energies of a few collinear magnetic ground states. To illustrate these states let me consider the magnetic sublattice of iron phosphide. There are 4 crystallographically equivalent Fe sites in the FeP unit cell. In Fig. 5.16 (a) they are shown with colors: red, green, yellow, and blue. Sites are sorted according to their z coordinate, so the red one has the smallest $z = 0.2$, then goes the green one with $z = 0.3$, and so on. The sites of each color form the set of

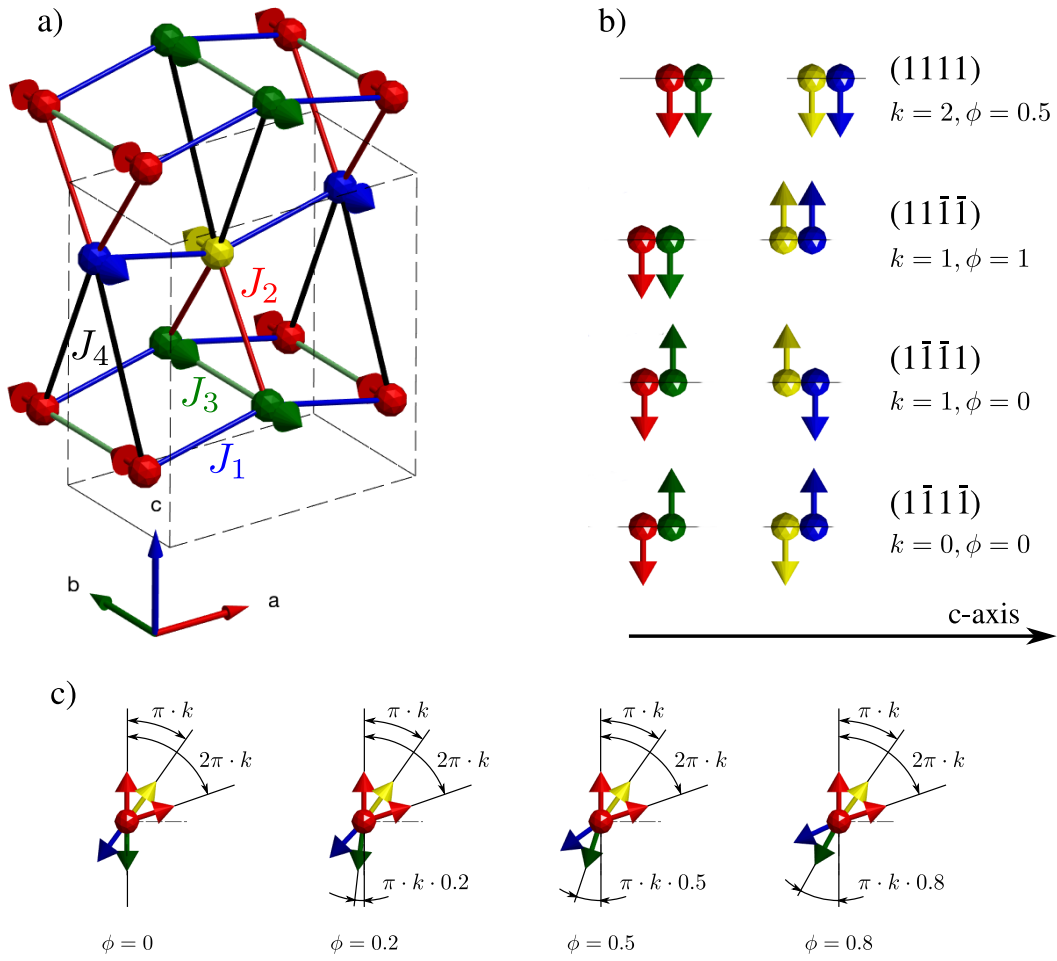


Figure 5.16: Schematic of the possible spin structures of FeP. (a) AFM spin ordering on the FeP magnetic sublattice. The dashed cuboid represents a unit cell. The four exchange integrals are shown by the lines and labels of the same colors: first-, second-, third-, and fourth-NN — J_1, J_2, J_3 , and J_4 , respectively. (b) Several commensurate spin configurations with corresponding k and ϕ parameters. Each arrow represents a FM layer. (c) Illustration of spin arrangements for $k = 0.2$ and different ϕ values according to our parametrisation (see text).

ferromagnetic (FM) layers in the ab plane. In Fig. 5.16 (b) each arrow represents a FM layer. The final incommensurate magnetic structure with propagation vector along the c axis can be constructed by stacking red, green, yellow, and blue FM layers one by one with appropriate rotation of the magnetization vector. In Fig. 5.16 (a), a commensurate antiferromagnetic (AFM) structure ($k = 0$) is shown.

All collinear spin structures with $k = 0$ can be described by the 4-dimensional structure vector. The index of a coordinate corresponds to the Fe site in the same order as it was introduced above. The value of each coordinate can be either 1 or -1 . In Fig. 5.16 (b) several configurations are shown with the appropriate structure vectors. The results of DFT calculations [131] give us the energies of the following states:

- $E(1111) = -2.2 \text{ meV}$
- $E(1\bar{1}\bar{1}1) = -7.6 \text{ meV}$
- $E(11\bar{1}\bar{1}) = -7.4 \text{ meV}$
- $E(1\bar{1}1\bar{1}) = -14.3 \text{ meV}$

The question that can be asked is whether it is possible to describe the magnetic structure and magnon spectrum in FeP using the local-spin approximation, despite the metallic behavior of resistivity and susceptibility. In the following investigation, we will try to address this question. The numerical analysis was done using the Matlab-based SpinW software [17].

5.3.2 Model

Assuming that the magnetic behavior in FeP can be described in the local-spin approximation, the effective spin Hamiltonian can be constructed. The minimum set of exchange parameters which can roughly reproduce the DFT results consists of J_1 and J_2 — exchange integrals between the first- and second nearest-neighbors (NN) [blue and red lines in the Fig. 5.16 (a)]. Since the third-NN exchange (green) does not influence the energy differences between the states considered in the DFT study, its value is irrelevant. We fixed $J_3 = -1 \text{ meV}$ to stabilize FM layers, according to the previously proposed structure. $J_1 = J_2 = 0.5 \text{ meV}$ roughly reproduces the energy differences obtained in DFT.

So far the model is non-frustrated and therefore can only have collinear solutions. From the experiment, we know that the ground state of FeP is a helical structure with a propagation vector along the c direction. To be able to capture this behavior, the model has to be extended to include incommensurate solutions. For this one needs to introduce frustration. If the forth-NN exchange J_4 is added (black), it starts to compete with J_2 (red). Both exchanges couple the spins in the c direction, so one can expect an appearance of incommensurability in the required direction.

In this study, we constructed a magnetic phase diagram of the model as a function of J_2 and J_4 exchange parameters. During the calculation, we minimized classical spin energy, with respect to the spin structure. To describe different spin configurations we introduce two parameters, k and ϕ . To illustrate their meaning, we schematically show several spin arrangements for a fixed k and different ϕ values in Fig. 5.16 (c). The angle between two red arrows is the angle by which the whole spin structure rotates from one unit cell to another. It is determined only by the parameter k and is equal to $2\pi k$. Now we will describe the spin arrangement within the unit cell. To define it we utilize both parameters. From the symmetry of the problem, it follows that the angle between the red and yellow arrows is exactly equal to πk — half the angle between two adjacent red arrows. The same symmetry considerations lead to equal angles between the pairs of arrows “red-green” and

“yellow-blue”. we expressed this angle as $\pi + \pi k \phi$. This form can be interpreted as the AFM order of spins (π) plus some deviation ($\pi k \phi$). The deviation is given by the parameter ϕ — the fraction of the angle between the red and yellow arrows. This choice was motivated by the DFT calculations and the previously proposed FeP spin structure. The latter states that the angle between the spins inside “red-green” and “yellow-blue” pairs is 176° . Varying k and ϕ , one can get all possible collinear spin structures. The relevant ones are shown in Fig. 5.16 (b) with corresponding values of k and ϕ .

The phase diagram we will present goes far beyond the problem initially motivated by FeP and covers a wide range of exchange parameters $-1.5J_1 \leq J_2 \leq 1.5J_1$ and $-1.5J_1 \leq J_4 \leq 1.5J_1$, containing both FM and AFM exchanges.

Since classical ground state depends only on the ratios between the exchange parameters, all energetic variables are normalized by J_1 . Furthermore, we added a small single-ion anisotropy in the c direction. It prompts the spins to rotate in the ab plane, whereby favoring the helical-like structure among other possible incommensurate solutions (e.g. cycloidal).

5.3.3 Classical phase diagram

To construct a $J_2 - J_4$ phase diagram for the system, we fixed the AFM value of the J_1 exchange parameter. For each set of exchange parameters in the range $-1.5J_1 \leq J_2 \leq 1.5J_1$ and $-1.5J_1 \leq J_4 \leq 1.5J_1$, we calculated the energies of the states with $0 \leq k \leq 2$ and $0 \leq \phi \leq 1$. Figure 5.17 (a) shows the energy landscape for $J_2 = J_1$ and $J_4 = 1.5J_1$. Here both J_2 and J_4 are AFM and the solution falls into the pure $(1\bar{1}1\bar{1})$ state with $k = 0$ and $\phi = 0$ (star marker). Note that for $k = 0$ the parametrisation does not distinguish states with different ϕ values. Now let us follow the evolution of the ground state of the system upon decreasing J_4 . While J_4 stays positive (AFM), the system favours the same $(1\bar{1}1\bar{1})$ state. Even when it becomes zero, the state is preserved. Upon further decrease of J_4 it turns into FM ($J_4 < 0$) which leads to competition with AFM J_2 . Nevertheless, the effect is not immediate: only after a certain critical value, the incommensurability emerges. Fig. 5.17 (b) shows a similar landscape but for $J_4 = -0.22J_1$ where the minimum appears at $k = 0.15$ and $\phi = 0.65$. That means that the first-NN are tilted one against another more than the second-NN (e.g. green and yellow arrows). Equal tilting would correspond to $\phi = 0.5$. According to our results, the transition happens discontinuously. The further increase in the accuracy of the calculations did not lead to the smooth dependence. This suggests that we are observing a first-order phase transition. A very large negative J_4 suppresses the J_2 influence, and the system tends to a marginal commensurate state. Fig. 5.17 (c) depicts the classical ground-state energy (black dots) vs. the propagation parameter k for different

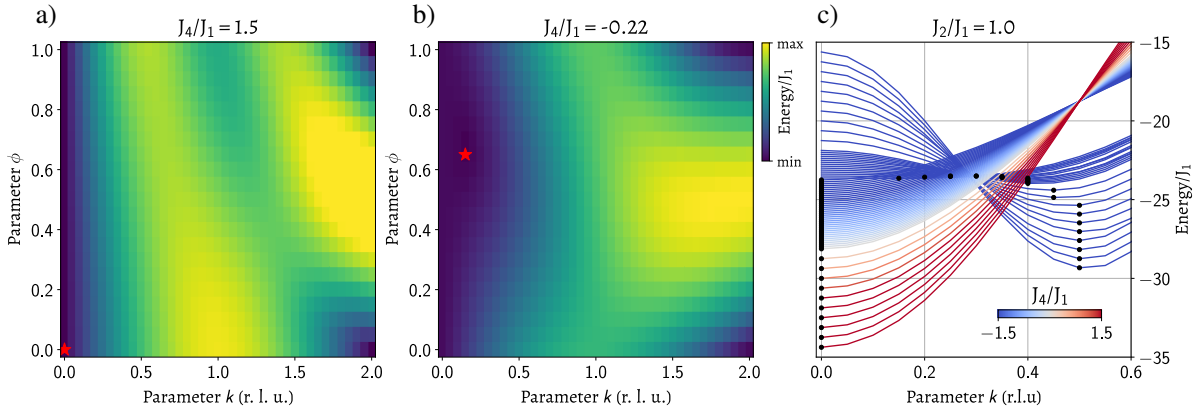


Figure 5.17: The results of calculations for $J_2 = J_1$. a, b) $\phi - k$ energy maps for two states with $J_4 = 1.5J_1$ and $-0.22J_1$. Red stars depict positions with minimal energies. c) Energy- k dependence for different J_4/J_1 states. Every curve has a fixed ϕ corresponding to the ground state value for this particular set of exchange parameters. States with minimal energies are marked with black dots.

J_4 values. Antiferromagnetic J_4 values correspond to the commensurate states with $k = 0$. Further decrease of the J_4/J_1 ratio leads to the emergence of incommensurability. The incommensurability parameter k shows very rapid J_4 dependence for low ferromagnetic J_4 values and slows down for large ones.

Combining all ground states for each set of exchange parameters, we constructed the final phase diagrams which are shown in Fig. 5.18. Here we want to emphasize that the J_3 value does not affect the ground-state order, therefore it was fixed to $J_3 = -2J_1$ to stabilize the ferromagnetic order in the ab plane. The possible commensurate spin configurations are shown in Fig. 5.18 (a).

The first diagram depicts k as a function of the J_2 and J_4 parameters following by a similar diagram for the parameter ϕ . Notice that the phase diagram is symmetric to the line connecting the upper left and lower right corners of the picture. But the symmetry in the shape of the regions on the diagram does not lead to symmetry in the corresponding phases.

There are four different phases marked with Roman numerals in the diagrams. The whole regions II and III correspond to the commensurate collinear states. Region II contains states with $k = 0$ and $\phi = 0$, region III — states with $k = 1$ and $\phi = 0$. As the parameter k is responsible for the rotation of the unit cell as a whole, integer k values point on the FM arrangements of the unit cells with respect to each other for both regions. At the same time, the internal spin structures are different but in both cases collinear. Regions I and IV are more complex. First, let us consider region I. When J_2 has large FM values, the spins in the “green-yellow” pairs favor FM alignment. At the same time, strong AFM J_4 leads to the AFM order within the “red-blue” pairs. Both factors together give the internal spin structure shown on the Fig. 5.18 (a) (I). The calculated $k = 1.5$ means the AFM arrangement

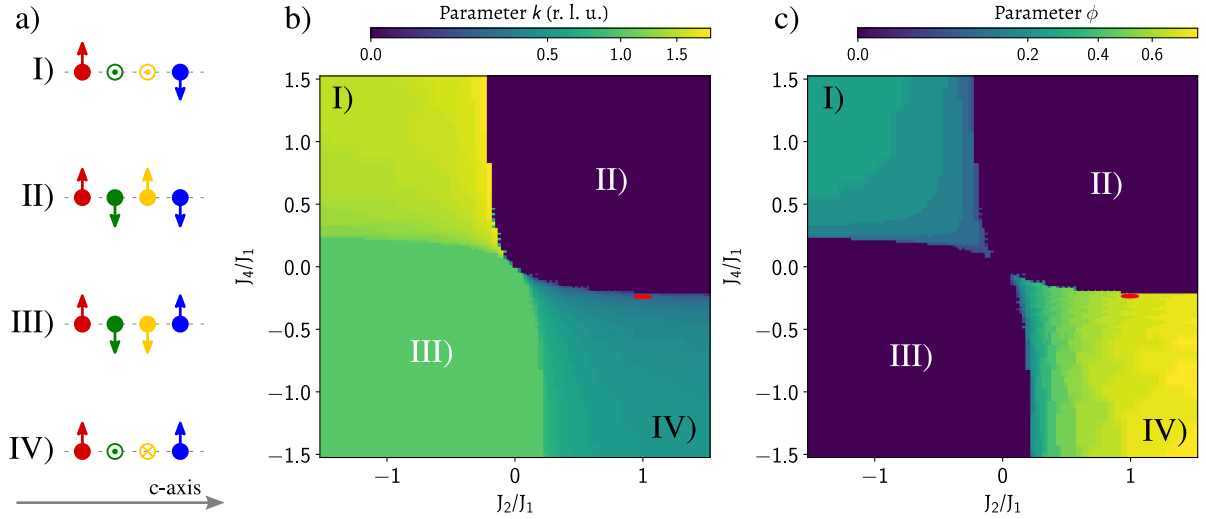


Figure 5.18: Calculated phase diagrams of the spin ordering on the FeP magnetic sublattice. (a) Schematic of the possible commensurate structures. (b, c) Classical $J_2 - J_4$ phase diagrams containing four commensurate phases: I, II, III, IV. The regions with incommensurate states are separating the areas with a commensurate order. In addition, the location of the realistic FeP compound is indicated by the red marks.

between the unit cells. When we decrease the FM J_2 an incommensurability in the c direction emerges. The evolution of the k and ϕ parameters during such change of the J_2 is shown on the second panel in Fig. 5.19. The same considerations for the IV region lead to the spin arrangement is shown in Fig. 5.18 (a) (IV) and AFM ordering of the unit cells. The transition between regions happens discontinuously in both k and ϕ . We observe the same behavior crossing other borders between the regions of the phase diagram [Fig. 5.19].

Summarising these results, we conclude that the localized-spins approach to our system produces a rich phase diagram with a wide variety of spin states including incommensurate ones. Helical states are induced by introducing the 4th NN exchange (between red and blue spins). They take place within limited ranges of exchange parameters separating the areas with commensurate order. It is important to pay attention to the very sensitive dependence of k parameter on the exchange interactions. Such a steep dependence suggests that quantum phenomena and/or higher-order corrections can significantly influence the exact degree of incommensurability.

5.3.4 Application to FeP

Now we can project the real FeP compound on the phase diagram. The only firmly established experimental fact concerning FeP spin structure is the value of its helical pitch ($k = 0.2$ r. l. u.). It was confirmed in neutron diffraction measurements conducted by two independent groups [118,123]. There are several regions on the phase diagram which can satisfy this value

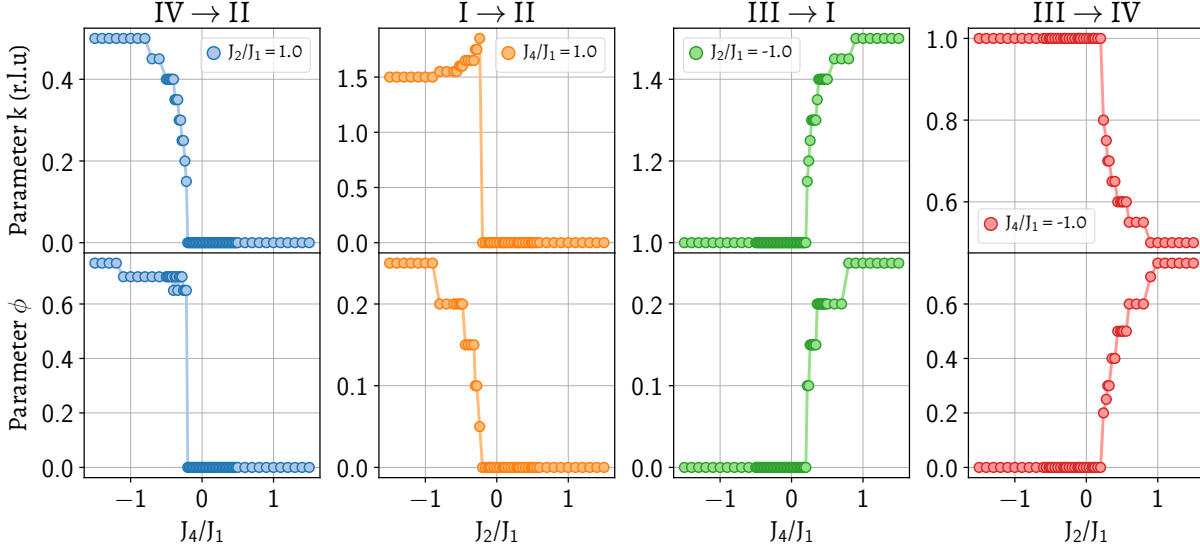


Figure 5.19: 1D cuts through the phase diagrams in Fig. 5.18 (b, c) for J_2 and J_4 equal $\pm J_1$. Different panels illustrate the transitions between the separate commensurate phases of the diagrams.

of k . All of them are situated close to the boundaries of phases II and III. However, the results of DFT calculations on FeP impose constraints on the values of exchange interactions ($J_2 \approx J_1$, FM J_4). The residual locations are marked with the red signs in Fig. 5.18. This area matches with $J_2 \approx J_1$ and $J_4 \approx -0.24J_1$, and the corresponding parameters are $k = 0.2$ r.l.u. and $\phi = 0.65$. This result is in good agreement with the experimentally measured propagation vector of the spiral and with the DFT calculations. Parameter $\phi = 0.65$ roughly corresponds to the angle 203° between the closest neighboring spins in the c direction (e.g. red and green). It differs from the previously proposed value (176°). This may indicate that our model is not able to describe all details of the behavior of FeP or that the later model is not completely correct.

5.3.5 Effect of J_6

As the next step, we investigate the stability of the solutions to the possible effects of the exchanges with farther neighbors. J_5 (the diagonal exchange between the red and green spins) brings nothing new to my study as it is equivalent to an effective tuning of J_2 . The next nontrivial exchange is J_6 [Fig. 5.20]. It couples red with yellow and green with blue spins which were not directly coupled before. We start from the configuration suggested by the DFT and diffraction experiments [red markers in Fig. 5.18 (a, b)] with $J_2 = J_1$, $J_3 = -2J_1$, and $J_4 = -0.24J_1$. Fixing these exchanges, we vary J_6 in a wide range, including both FM and AFM values. For every set of exchange parameters, we find a state with minimal energy — the ground state, characterized by k and ϕ parameters.

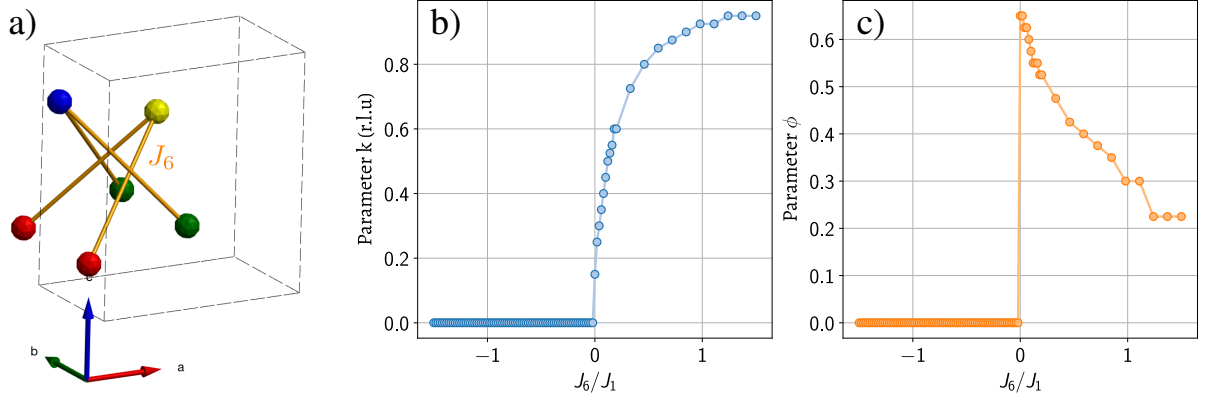


Figure 5.20: (a) Schematic illustration of the J_6 . (b, c) J_6 dependence of the k and ϕ parameters. The calculations were done with fixed $J_2 = J_1$, $J_3 = -2J_1$, and $J_4 = -0.24J_1$.

The resulting J_6 dependences of k and ϕ are shown in Fig. 5.20 (b, c). We found that $J_6 = 0.01J_1$ reproduces the propagation vector deduced from the experiment. Parameter ϕ stays unchanged too. The value $0.01J_1$ is within the numerical error of my calculations. From this, we can conclude that the solution does not depend on the J_6 and we can skip it for further analysis.

5.3.6 Dynamics

Now, when we have an estimation of the exchanges in the system, we can examine its magnon spectrum. To reproduce the energy scale comparable with the experiment, we multiplied the exchanges by some arbitrary number. It is allowed because the classical ground state depends only on the ratios of the exchange parameters.

To reproduce the neutron spectra, we calculated dynamical spin-spin correlation functions for a few directions in reciprocal space using linear spin wave theory. Typical spectra for different incommensurate regions of the phase diagram are shown in Fig. 5.21. The finite energy resolution is simulated by convolution with a Gaussian function.

One can notice that spectra can be divided into two groups. The first group includes A and D spectra that look the same. The spectrum consists of two magnon bands well separated in energy. It reminds the situation when spins form strongly bonded clusters that are weakly connected. However, in our case, the role of “spin clusters” is played by chains of spins strongly FM coupled along the b direction. The second group consists of B and C. According to our knowledge, the FeP spectrum belongs to the second one. These spectra are characterised by two intense magnon branches emanating from the magnetic ordering vectors $\mathbf{q}_m = (0, 0, \pm 0.2)$ r.l. u. In contrast to the previous case, here we have a single band of excitations that appears in a W-shaped form.

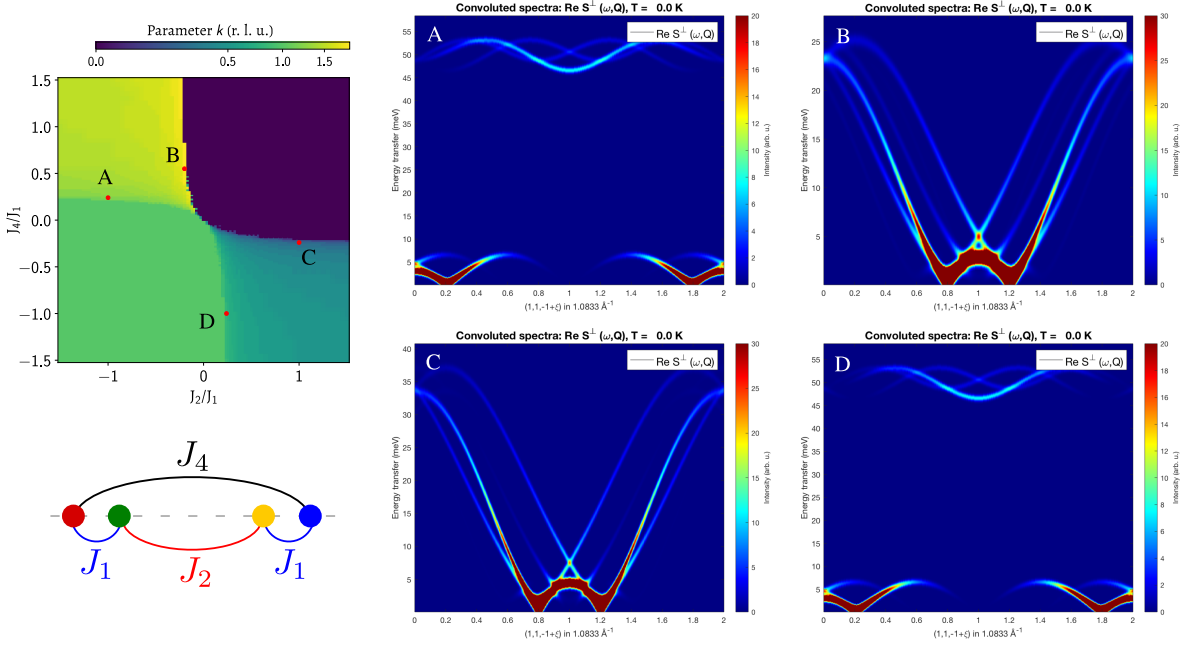


Figure 5.21: Simulated spectra for different incommensurate regions of the phase diagram.

5.3.7 INS spectra of FeP

Now we can compare the results of the SpinW simulations with real neutron data [Fig. 5.22 (a, d)] collected at the TAS spectrometers IN8 (ILL, Grenoble) and PUMA (MLZ, Munich). For better agreement with the measured spectra, we scaled the exchange parameters, keeping the ratios between them. The J_3 exchange can be scaled independently because it does not influence the ground-state order. This is allowed by the fact that the spin structure in the ground state depends only on the ratio of the exchange parameters but not on their actual value. The final exchange integrals which we used in the model are:

- $J_1 = 7.2 \text{ meV}$
- $J_2 = J_1 = 7.2 \text{ meV}$
- $J_3 = 5.25J_1 = -37.8 \text{ meV}$
- $J_4 = -0.24J_1 = -0.41 \text{ meV}$

Any neutron spectrum measured along a given direction in reciprocal space has a finite momentum resolution in all three dimensions. The resulting data along $(00L)$ is an integral within finite ranges along $(H00)$ and $(0K0)$. To compare my model with the data, we integrated the simulated spectrum in directions orthogonal to the direction of interest. The integration ranges were set to ± 0.01 r.l. u. along all directions, and the resulting dispersions are shown in Fig. 5.22 (b, e). The spectrum along $(11L)$ consists of a well resolved W-shaped magnon signal with two minima at $\mathbf{q}_m \approx (0, 0, \pm 0.2)$ r.l. u. and a weakly dispersed arc-shaped phonon branch at about 25 meV. The stripe crossing the image is a spurion: the width is lower than the instrument resolution and it does not follow the symmetry of the

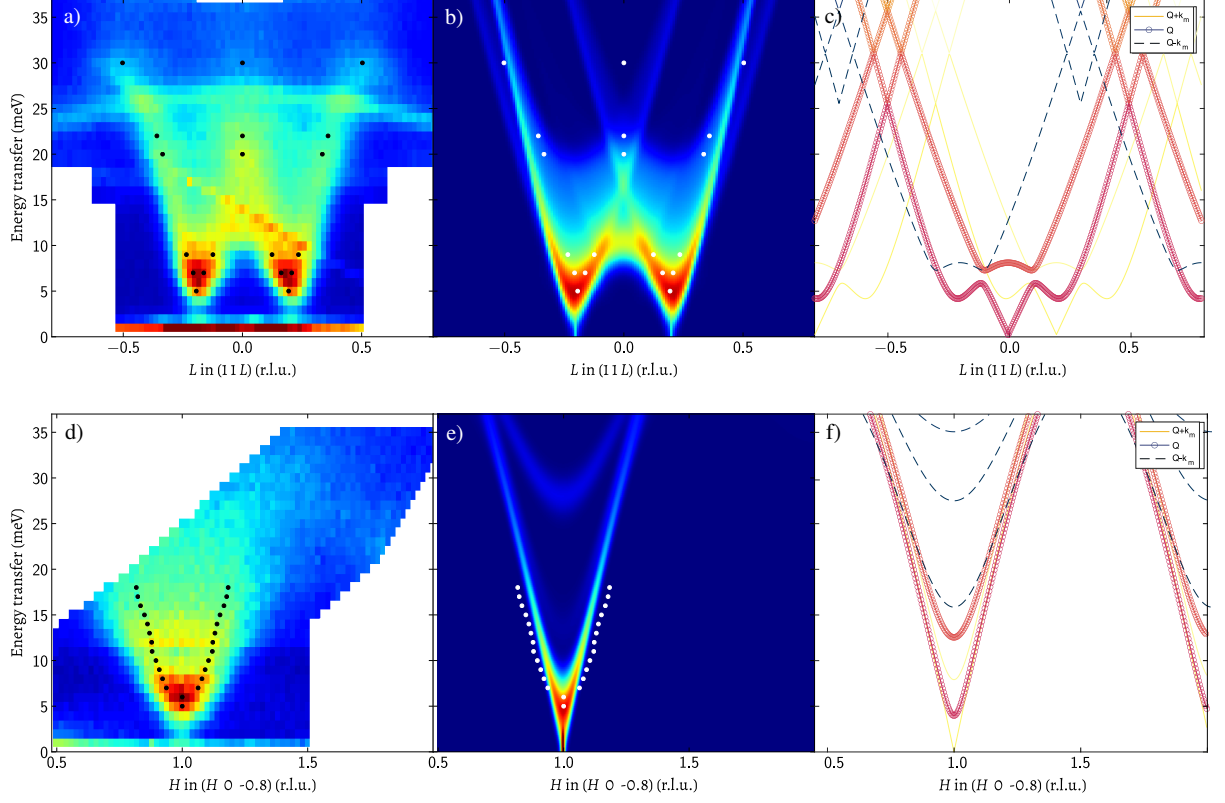


Figure 5.22: (a, d) Experimental colormap of the neutron spectrum of FeP along $(11L)$ (IN8, ILL) and $(H0-0.8)$ (PANDA, MLZ). The black and white dots show the intensity maxima obtained from the fitting with two Gaussians. (b, e) SpinW simulation of the magnon spectra along $(11L)$ and $(H0-0.8)$. (c, f) Spin-wave dispersions calculated with SpinW.

crystal. In $(H0-0.8)$ direction the dispersion is V-shaped signal emanating from the position of the $(10-0.8)$ magnetic Bragg peak. The instrument resolution was not sufficient to clearly resolve separate branches thus we see a vague intensity in the middle part. The dots in the figures show the intensity maxima obtained from fitting with two Gaussians. To compare the modelled dispersion along $(1K0.2)$ with the IN8 data [see Fig. 5.12 (c) and 5.23 (f)]. Though the model captures the main features of dispersion, the calculated spectrum is narrower. Further tuning of the exchange parameters did not improve the resemblance of the two spectra. Nevertheless there are noticeable similarities between the experimental [Fig. 5.22 (a, d)] and simulated [Fig. 5.22 (b, e)] spectra. First of all, it is the W-shape of the signal along $(11L)$ and the positions of the dispersion minima. In the measured spectra, the signal intensity reaches its maximum at about 7 meV and drops markedly toward lower energies. It resembles an anisotropy effect in the system. However, this gap may also be an artifact due to the final instrument resolution. Despite the absence of anisotropy in our model, we observe a similar intensity distribution caused by simulations with finite resolution. Since we calculated only magnetic perturbations in the system, the phonon is not reproduced.

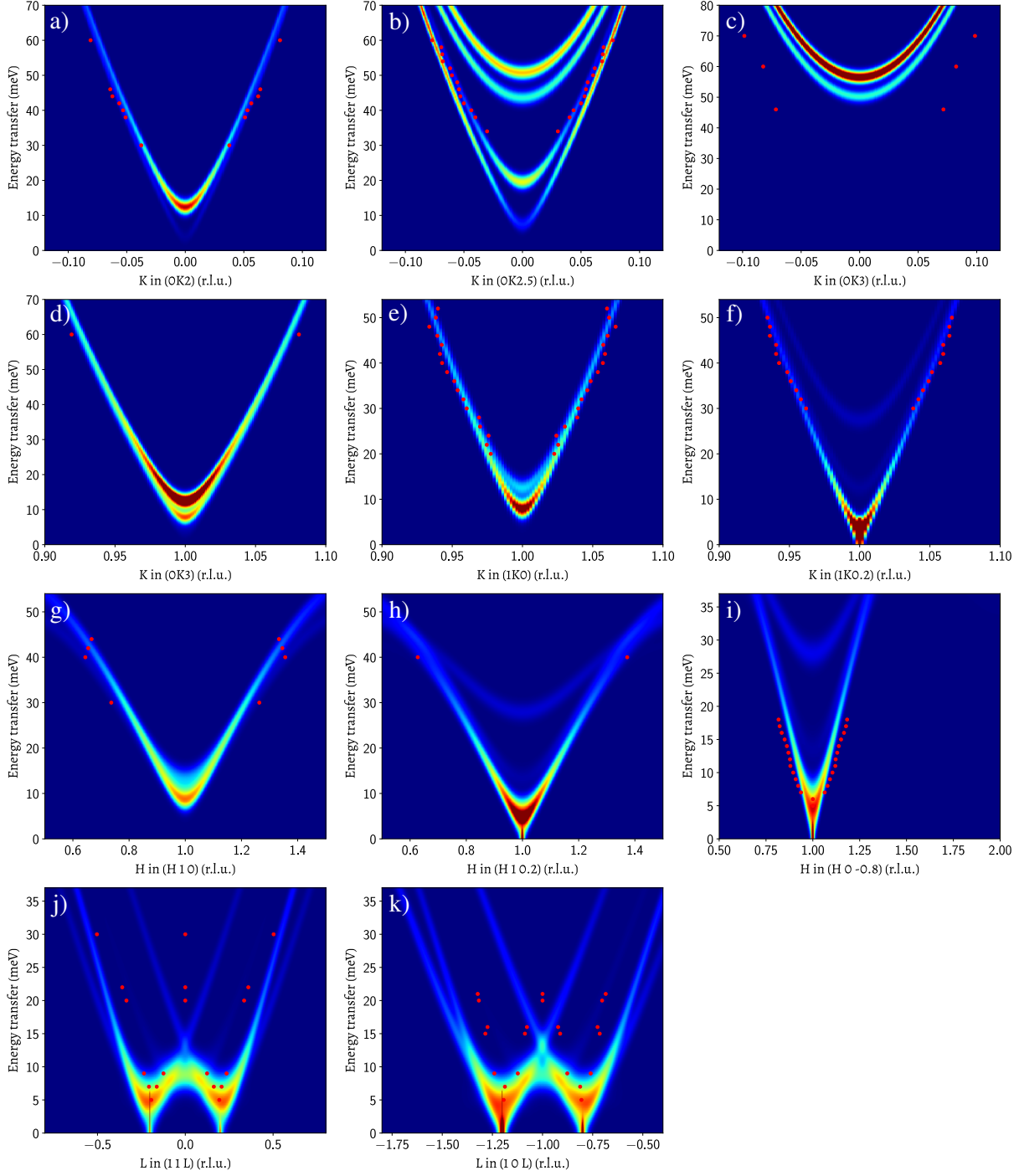


Figure 5.23: The overview of the SpinW simulated spectra of FeP. The red dots depict the experimental results obtained from our neutron spectroscopy measurements.

The presence of the spurion makes it tricky to extract the energy and internal structure near the saddle point in the middle. However, signal broadening in this region as a result of finite resolution in the K direction along which the magnons are very steep is well reproduced. Another possible feature of the $(11L)$ dispersion is a bend of the side branches around ± 0.5 r.l.u. Their visibility and resolution is hampered by the presence of the phonon but can still be distinguished. This bending does not occur in the simulated spectrum. If we

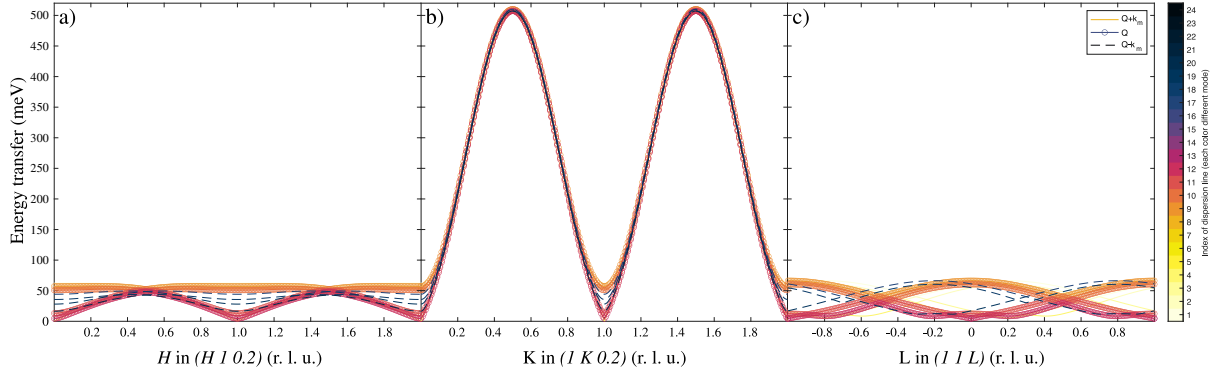


Figure 5.24: Spin wave dispersions calculated with SpinW along (a) $(H\ 1\ 0.2)$, (b) $(1\ K\ 0.2)$, and (c) $(1\ 1\ L)$ directions passing through the $(1\ 1\ 0.2)$ magnetic satellite.

consider the dispersion curves in Fig. 5.22 (c), we see that they intersect exactly at 0.5 r.l.u., moreover, the energy of the intersection is roughly the same as in the experimental spectrum. Within the framework of the local-spin approximation, these branches do not feel each other. A possible manifestation of the itinerant behavior of FeP may be the hybridization of the dispersion curves, which leads to the bending of the spectrum at 0.5 r.l.u.

To have an exhaustive comparison of the modeled and experimental results, we fitted the data from TOF experiments and plotted them over the simulated color maps [Fig. 5.23]. The experimental results nicely agree with simulated dispersions in the vicinity of structural and magnetic Bragg peaks [Fig. 5.23 (a, b, d, e, f, g, h, i)]. The only discrepancy is in the dispersion along the L direction [Fig. 5.23 (j, k)]. The modeled dispersion branches are too wide in this direction and do not reproduce the possible bending of the measured dispersion [see Fig. 5.22 (a)]. It can be the reason for the noticeable disagreement along the $(0\ K\ 3)$ direction in Fig. 5.23 (c) — the modeled dispersion branches go up in energy very fast along the L direction and overestimate the energy of the saddle point in the dispersion. As far as a visible dispersion curve along the K direction is a cut of a 4D energy-momentum space in the direction orthogonal to L , the energy of the dispersion in K is directly connected to the slope of the outer branches of the dispersion along L . The data measured along the K direction at different L [see Fig. 5.14] show almost no L dependence. If the branches of the dispersion were as strongly dependent on the value of L as the model predicts, the dispersion along K would be strongly dependent on the L value.

Another obvious problem — the energy of the middle bridge at $(1\ 1\ 0)$ and $(1\ 0\ \bar{1})$. The model predicts the value which is fairly lower than the experimental value. Of course, scaling of the exchange parameters can lead to a corresponding increase in the slope of the dispersion branches and, as a consequence, to an increase in the energy of the central intersection, but this leads to a decrease in agreement in other directions. Now it is clear that to obtain a good agreement with the experimental results, it is crucial to reproduce

a bending of the dispersion's branches along the L direction. Hopefully, it can be done by adding one more exchange interaction along the c direction and will be done in future work.

The last thing which we want to discuss here is the bandwidth of the magnon excitations in FeP. The model gives a magnon bandwidth of about 50–60 meV along the H and L directions, and almost ten times larger in K [Fig. 5.24]. It agrees with the experimentally observed behavior of the dispersion curves — the excitations along the K direction are much steeper than in other orthogonal directions. Here the question may be asked: why does a material with a rather three-dimensional crystal structure have such anisotropic magnetic couplings?

5.4 Summary

In this chapter, we gave a short outlook of the current knowledge about iron monophosphide. The material is interesting because of its exotic double-helix spin structure. FeP has been investigated for a long time by many groups and techniques but the exact details of its structure and the microscopic mechanism of magnetism remain unclear. Recently our collaborators succeeded in growing high-quality big single crystals suitable for inelastic neutron studies.

We performed a series of measurements and mapped out the magnon dispersion in a wide range of energies and momentums. The data covers the energy range up to ~ 30 meV where the spin waves show up well-defined. The magnetic branches in the $(0K0)$ direction is much steeper than along two other principal axes. Our modelling gives the magnon bandwidth of the order of ~ 60 meV in $(H00)$ and $(00L)$, whereas the dispersion in $(0K0)$ goes further up to ~ 520 meV. The existence of such a high anisotropy in a fairly 3D material is an open question and definitely requires further research.

To interpret the data, we applied the local spin approximation approach to model the spin structure and magnetic excitations in FeP. The phase diagram of the FeP magnetic sublattice is constructed in a wide range of exchange parameters up to the fourth nearest neighbor. When constructing the model, we used the minimum number of parameters, which leads to a high degree of generality. Taking into account the neutron diffraction and spectroscopy data, as well as DFT calculation results, we found that FeP spin structure and magnon spectrum can be partially reproduced using a simple parametrization and varying the exchange parameters. In addition to a similar spectrum shape, we were able to reproduce the distribution of the signal intensity. In the experimental data, the neutron scattering intensity has a pronounced maximum at energies of the order of 7 meV and

rapidly decreases as the energy decreases. This may be due to the presence of anisotropy in the system, leading to the opening of the energy gap in the spectrum of magnetic excitations. However, and our model directly demonstrates this, such an intensity distribution can be obtained by considering the finite resolution of the instrument. Thus, the question of the existence of an energy gap in the magnon spectrum of FeP remains open. Moreover, the absence of magnetic Bragg peaks of the second and higher orders in the diffraction data is more likely in favor of a harmonic helicoid structure, which, in turn, suggests the absence of anisotropy in the plane of spin rotation. Despite the fact that the proposed model reproduces fairly well the main details of the experimental spectrum, there are still some differences. In particular, the possible bending of magnon branches along $(1\ 1\ L)$ at about 0.5 r.l. u. In the framework of the linear spin wave theory, this should not happen. Perhaps this indicates insufficiency of the localized spin approximation to describe the system in detail and the need to take into account the possible influence of itinerant magnetic effects.

Such a combined approach is widely used for the description of the magnetic excitations in many systems. It reminds the situation with iron-arsenide superconductors. Their parent compounds have an antiferromagnetic ground state [132–136], but its microscopic origin remains debated. There is complementary evidence favouring both localized [137–141] and itinerant [142–146] mechanisms. The inelastic neutron scattering experiments on CaFe_2As_2 [147, 148], parent compound of the “122” iron-arsenide family of superconductors, revealed the magnon spectrum in the AFM ordered state. Its low-energy part, up to 100 meV, can be fitted to a local-moment Heisenberg Hamiltonian. However, the dispersion above 100 meV and up to the maximum energy of about 200 meV appears broader in energy and momentum than the instrument resolution. This was explained by the damping of spin waves by particle-hole excitations [147]. The magnon spectrum is characterized by the large in-plane anisotropy which cannot be explained within the localized picture. All these facts lead to the conclusion that magnetism in iron-based superconductors has a complex microscopic origin, and both localized and itinerant effects play important roles [148].

Another possible solution is to include further-neighbor exchange interactions in the model and try to reproduce the experimental results while staying within the localized spin approach.

Further theoretical study is needed to find out the microscopic mechanisms responsible for the magnetic behavior in FeP. To determine the details of the magnetic structure, neutron experiments with a polarisation analysis are planned by our group.

Publication List

- A. S. Cameron, Y. V. Tymoshenko, P. Y. Portnichenko, J. Gavilano, V. Tsurkan, V. Felea, A. Loidl, S. Zherlitsyn, J. Wosnitza and D. S. Inosov; *Magnetic phase diagram of the helimagnetic spinel compound ZnCr_2Se_4 revisited by small-angle neutron scattering*, [J. Phys.: Condens. Matter](#) **28**, 146001 (2016).
- Y. V. Tymoshenko, Y. A. Onykienko, T. Müller, R. Thomale, S. Rachel, A. S. Cameron, P. Y. Portnichenko, D. V. Efremov, V. Tsurkan, D. L. Abernathy, J. Ollivier, A. Schneidewind, A. Piovano, V. Felea, A. Loidl, D. S. Inosov; *Pseudo-Goldstone magnons in the frustrated $S = 3/2$ Heisenberg helimagnet ZnCr_2Se_4 with a pyrochlore magnetic sublattice*, [Phys. Rev. X](#) **7**, 041049 (2017).
- A. S. Cameron, Y. S. Yerin, Y. V. Tymoshenko, P. Y. Portnichenko, A. S. Sukhanov, M. C. Hatnean, D. Mc K. Paul, G. Balakrishnan, R. Cubitt, A. Heinemann, D. S. Inosov; *Rotation of the magnetic vortex lattice in Ru_7B_3 driven by the effects of broken time-reversal and inversion symmetry*, [Phys. Rev. B](#) **100**, 024518 (2019).
- L. Zhang, Y. A. Onykienko, P. M. Buhl, Y. V. Tymoshenko, P. Čermák, A. Schneidewind, J. R. Stewart, A. Henschel, M. Schmidt, S. Blügel, D. S. Inosov, Y. Mokrousov; *Magnonic Weyl states in Cu_2OSeO_3* , [Phys. Rev. Research](#) **2**, 013063 (2020).
- D. S. Inosov, Y. O. Onykienko, Y. V. Tymoshenko, A. Akopyan, D. Shukla, N. Prasai, M. Dorr, D. Gorbunov, S. Zherlitsyn, D. J. Voneshen, M. Boehm, V. Tsurkan, V. Felea, A. Loidl, J. L. Cohn; *Magnetic-field dependence of low-energy magnons, anisotropic heat conduction, and spontaneous relaxation of magnetic domains in the cubic helimagnet ZnCr_2Se_4* , [Phys. Rev. B](#) **102**, 184431 (2020).
- A. S. Sukhanov, S. E. Nikitin, M. S. Pavlovskii, T. C. Sterling, N. D. Andryushin, A. S. Cameron, Y. V. Tymoshenko, H. C. Walker, I. V. Morozov, I. O. Chernyavskii, S. Aswartham, D. Reznik, D. S. Inosov; *Lattice dynamics in the double-helix antiferromagnet FeP* , [Phys. Rev. Research](#) **2**, 043405 (2020).

Bibliography

- [1] M. Morris, K. Uchida, and T. Do, *Nature* **440**, 308 (2006).
- [2] T. Nagamiya, Helical spin ordering—1 theory of helical spin configurations, volume 20 of *Solid State Physics*, pages 305 – 411, Academic Press, 1968.
- [3] A. Yoshimori, *J. Phys. Soc. Jpn.* **14**, 807 (1959).
- [4] T. A. Kaplan, *Phys. Rev.* **116**, 888 (1959).
- [5] A. Shibatani, K. Motizuki, and T. Nagamiya, *Phys. Rev.* **177**, 984 (1969).
- [6] A. W. Overhauser and A. Arrott, *Phys. Rev. Lett.* **4**, 226 (1960).
- [7] J. Villain, *J. Phys. Chem. Solids* **11**, 303 (1959).
- [8] T. Kimura, *Annu. Rev. Mater. Res.* **37**, 387 (2007).
- [9] Y. A. Izyumov, *Soviet Physics Uspekhi* **27**, 845 (1984).
- [10] I. E. Dzyaloshinsky, *J. Exp. Theor. Phys.* **19** (4), 960 (1964).
- [11] I. Dzyaloshinsky, *J. Phys. Chem. Solids* **4**, 241 (1958).
- [12] T. Moriya, *Phys. Rev.* **120**, 91 (1960).
- [13] F. Keffer, *Spin Waves*, pages 1–273, Springer Berlin Heidelberg, Berlin, Heidelberg, 1966.
- [14] F. Bloch, *Z. Physik* **61**, 206 (1930).
- [15] T. Holstein and H. Primakoff, *Phys. Rev.* **58**, 1098 (1940).
- [16] R. Coldea, D. A. Tennant, and Z. Tylczynski, *Phys. Rev. B* **68**, 134424 (2003).
- [17] S. Toth and B. Lake, *J. Phys.: Condens. Matter* **27**, 166002 (2015).

- [18] G. L. Squires, *Introduction to the Theory of Thermal Neutron Scattering*, Cambridge University Press, 3 edition, 2012.
- [19] H. Bethe, *Z. Physik* **71**, 205 (1931).
- [20] F. J. Dyson, *Phys. Rev.* **102**, 1217 (1956).
- [21] R. M. White, *Quantum Theory of Magnetism*, chapter The Dynamic Susceptibility of Strongly Interacting Systems, pages 237–279, Springer Berlin Heidelberg, Berlin, Heidelberg, 2007.
- [22] J. J. Duderstadt and L. J. Hamilton, *Nuclear Reactor Analysis*, John Wiley & Sons, Inc., 1 edition, 1976.
- [23] N. Tsoulfanidis and S. Landsberger, *Measurement and Detection of Radiation, Fourth Edition*, CRC Press, 4th edition, 2015.
- [24] D. Reilly, N. Ensslin, H. J. Smith, and S. Kreiner, editors, *Passive nondestructive assay of nuclear materials*, NUREG/CR-5550, LA-UR-90-732, US Nuclear Regulatory Commission, Washington, DC, 1991.
- [25] B. T. M. Willis and C. J. Carlile, *Experimental Neutron Scattering*, Oxford University Press, 2009.
- [26] J. M. Carpenter and C.-K. Loong, *Elements of Slow-Neutron Scattering Basics, Techniques, and Applications*, Cambridge University Press, 2015.
- [27] T. Brückel, D. Richter, A. W. G. Roth, and R. Zorn, editors, *Neutron Scattering. Experiment Manual of the JCNS Laboratory Course held at Forschungszentrum Jülich and at the Heinz-Maier-Leibnitz Zentrum Garching*, volume 107, 2015.
- [28] <https://www.ill.eu>.
- [29] M. Kempa et al., *Physica B: Condens. Matter* **385-386**, 1080 (2006).
- [30] K. Lefmann et al., *Physica B: Condens. Matter* **385-386**, 1083 (2006).
- [31] J. A. Rodriguez et al., *Meas. Sci. Technol.* **19**, 034023 (2008).
- [32] Freeman, P. G. et al., *EPJ Web of Conferences* **83**, 03005 (2015).
- [33] J. A. Lim et al., *J. Phys.: Conf. Ser.* **592**, 012145 (2015).
- [34] A. P. Ramirez, *Annu. Rev. Mater. Sci.* **24**, 453 (1994).

- [35] D. Bergman, J. Alicea, E. Gull, S. Trebst, and L. Balents, *Nat. Phys.* **3**, 487 (2007).
- [36] S. T. Bramwell and M. J. P. Gingras, *Science* **294**, 1495 (2001).
- [37] C. Castelnovo, R. Moessner, and S. L. Sondhi, *Nature* **451**, 42 (2008).
- [38] L. Balents, *Nature* **464**, 199 (2010).
- [39] T. Kimura, *Annu. Rev. Condens. Matter Phys.* **3**, 93 (2012).
- [40] Y. V. Tymoshenko et al., *Phys. Rev. X* **7**, 041049 (2017).
- [41] R. Moessner and J. T. Chalker, *Phys. Rev. Lett.* **80**, 2929 (1998).
- [42] O. Benton, L. D. C. Jaubert, H. Yan, and N. Shannon, *Nat. Commun.* **7**, 11572 (2016).
- [43] J. N. Reimers, A. J. Berlinsky, and A.-C. Shi, *Phys. Rev. B* **43**, 865 (1991).
- [44] M. F. Lapa and C. L. Henley, *arXiv:1210.6810* (2012).
- [45] E. Takata, T. Momoi, and M. Oshikawa, *arXiv:1510.02373* (2015).
- [46] T. Okubo, T. H. Nguyen, and H. Kawamura, *Phys. Rev. B* **84**, 144432 (2011).
- [47] P. H. Conlon and J. T. Chalker, *Phys. Rev. B* **81**, 224413 (2010).
- [48] A. N. Yaresko, *Phys. Rev. B* **77**, 115106 (2008).
- [49] K. Siratori, *J. Phys. Soc. Jpn.* **30**, 709 (1971).
- [50] P. Zhang et al., *Appl. Phys. Express* **9**, 102401 (2016).
- [51] K. Aoyama and H. Kawamura, *Phys. Rev. Lett.* **116**, 257201 (2016).
- [52] S.-H. Lee, C. Broholm, T. H. Kim, W. Ratcliff, and S.-W. Cheong, *Phys. Rev. Lett.* **84**, 3718 (2000).
- [53] H. Ueda, H. A. Katori, H. Mitamura, T. Goto, and H. Takagi, *Phys. Rev. Lett.* **94**, 047202 (2005).
- [54] F. Yokaichiya et al., *Phys. Rev. B* **79**, 064423 (2009).
- [55] J. Hastings and L. Corliss, *J. Phys. Chem. Solids* **29**, 9 (1968).
- [56] V. Tsurkan et al., *Phys. Rev. B* **73**, 224442 (2006).
- [57] R. J. Plumier, *J. Appl. Phys.* **37**, 964 (1966).

- [58] A. S. Cameron et al., J. Phys.: Condens. Matter **28**, 146001 (2016).
- [59] Y. Iqbal et al., Phys. Rev. Materials **1**, 071201 (2017).
- [60] M. Matsuda et al., Nat. Phys. **3**, 397 (2007).
- [61] N. Menyuk, K. Dwight, R. J. Arnott, and A. Wold, J. Appl. Phys. **37**, 1387 (1966).
- [62] P. Wojtowicz, IEEE Transactions on Magnetism **5**, 840 (1969).
- [63] H. Ueda, H. Mitamura, T. Goto, and Y. Ueda, Phys. Rev. B **73**, 094415 (2006).
- [64] J. Akimitsu, K. Siratori, G. Shirane, M. Iizumi, and T. Watanabe, J. Phys. Soc. Jpn. **44**, 172 (1978).
- [65] Y. Togawa, Y. Kousaka, K. Inoue, and J.-i. Kishine, J. Phys. Soc. Jpn. **85**, 112001 (2016).
- [66] Y. Tokura and S. Seki, Adv. Mater. **22**, 1554 (2010).
- [67] T. Rudolf et al., New J. Phys. **9**, 76 (2007).
- [68] P. Zajdel et al., Phys. Rev. B **95**, 134401 (2017).
- [69] G. Abdul-Jabbar et al., Nat. Phys. **11**, 321 (2015).
- [70] M. Hidaka, N. Tokiwa, M. Fujii, S. Watanabe, and J. Akimitsu, Phys. Stat. Sol. (b) **236**, 9 (2003).
- [71] P. Y. Portnichenko et al., Nat. Commun. **7**, 10725 (2016).
- [72] R. Kleinberger and R. de Kouchkovsky, C. R. Acad. Sci. Paris, Ser. B **262**, 628 (1966).
- [73] M. Hidaka et al., Phys. Stat. Sol. (b) **236**, 570 (2003).
- [74] V. Felea et al., Phys. Rev. B **86**, 104420 (2012).
- [75] J. Hemberger, H.-A. K. von Nidda, V. Tsurkan, and A. Loidl, Phys. Rev. Lett. **98**, 147203 (2007).
- [76] H. Murakawa, Y. Onose, K. Ohgushi, S. Ishiwata, and Y. Tokura, J. Phys. Soc. Jpn. **77**, 043709 (2008).
- [77] C. C. Gu et al., Phys. Rev. Lett. **120**, 147204 (2018).
- [78] S. Park et al., Sci. Rep. **9**, 16627 (2019).

- [79] B. Fåk, R. A. Sadykov, J. Flouquet, and G. Lapertot, *J. Phys.: Condens. Matter* **17**, 1635 (2005).
- [80] D. L. Abernathy et al., *Rev. Sci. Instrum.* **83**, 015114 (2012).
- [81] J. Ollivier and H. Mutka, *J. Phys. Soc. Jpn.* **80**, SB003 (2011).
- [82] T. Perring, R. A. Ewings, and J. V. Duijn, HORACE software at <http://horace.isis.rl.ac.uk>.
- [83] R. Ewings et al., *Nucl. Instrum. Methods Phys. Res. Sect. A: Accel. Spectrom. Dect. Assoc. Equip.* **834**, 132 (2016).
- [84] A. Cameron et al., Magnetic excitation spectrum of the helimagnetic spinel compound ZnCr_2Se_4 . Institut Laue-Langevin (ILL), 2017, doi:10.5291/ILL-DATA.4-01-1472.
- [85] Y. V. Tymoshenko, D. S. Inosov, P. Y. Portnichenko, and Y. O. Onykiienko, Resolving helimagnon excitations in the long-pitch helimagnetic insulator Cu_2OSeO_3 . Institut Laue-Langevin (ILL), 2016, doi:10.5291/ILL-DATA.4-01-1521.
- [86] A. Schneidewind and P. Čermák, *J. Large-Scale Res. Facilities* **1**, A12 (2015).
- [87] J.-H. Kim et al., *Phys. Rev. Lett.* **113**, 147206 (2014).
- [88] S. Toth, *SpinW software*, <http://horace.isis.rl.ac.uk>.
- [89] M. Kataoka, *J. Phys. Soc. Jpn.* **56**, 3635 (1987).
- [90] S. Toth et al., *Phys. Rev. Lett.* **109**, 127203 (2012).
- [91] A. I. Milstein and O. P. Sushkov, *Phys. Rev. B* **84**, 195138 (2011).
- [92] A. V. Chubukov, S. Sachdev, and T. Senthil, *J. Phys. Condens. Matter* **6**, 8891 (1994).
- [93] A. L. Chernyshev and M. E. Zhitomirsky, *Phys. Rev. Lett.* **97**, 207202 (2006).
- [94] A. L. Chernyshev and M. E. Zhitomirsky, *Phys. Rev. B* **79**, 144416 (2009).
- [95] S. P. Bayrakci, T. Keller, K. Habicht, and B. Keimer, *Science* **312**, 1926 (2006).
- [96] N. Prasai et al., *Phys. Rev. B* **95**, 224407 (2017).
- [97] D. S. Inosov et al., *Phys. Rev. B* **102**, 184431 (2020).
- [98] D. S. Inosov et al., Nature of the new field-induced magnetic phase in ZnCr_2Se_4 , STFC ISIS Neutron and Muon Source, 2018, doi:10.5286/ISIS.E.90594650.

- [99] R. Bewley, J. Taylor, and S. Bennington, Nucl. Instrum. Methods Phys. Res. Sect. A: Accel. Spectrom. Dect. Assoc. Equip. **637**, 128 (2011).
- [100] Y. V. Tymoshenko et al., Non-monotonic behavior of the spin gap in ZnCr_2Se_4 in magnetic field. Institut Laue-Langevin (ILL), 2019, doi:10.5291/ILL-DATA.4-05-734.
- [101] J. G. Rau, P. A. McClarty, and R. Moessner, Phys. Rev. Lett. **121**, 237201 (2018).
- [102] Villain, J., Bidaux, R., Carton, J.-P., and Conte, R., J. Phys. France **41**, 1263 (1980).
- [103] C. L. Henley, Phys. Rev. Lett. **62**, 2056 (1989).
- [104] M. Rotter, H. Müller, E. Gratz, M. Doerr, and M. Loewenhaupt, Rev. Sci. Instrum. **69**, 2742 (1998).
- [105] X. Sun (private communication).
- [106] X. Lu et al., Science **345**, 657 (2014).
- [107] K. Momma and F. Izumi, J. Appl. Crystallogr. **44**, 1272 (2011).
- [108] S. Dann, M. Weller, and D. Currie, J. Solid State Chem. **97**, 179 (1992).
- [109] D. C. Peets et al., Phys. Rev. B **87**, 214410 (2013).
- [110] T. M. Rice and M. Sigrist, J. Phys.: Condens. Matter **7**, L643 (1995).
- [111] C. M. Puetter, J. G. Rau, and H.-Y. Kee, Phys. Rev. B **81**, 081105 (2010).
- [112] D. S. Inosov, Y. O. Onykiienko, and Y. V. Tymoshenko, Pseudo-Goldstone magnon in the single-domain state of $\text{Sr}_3\text{Fe}_2\text{O}_7$. Institut Laue-Langevin (ILL), 2016, doi:10.5291/ILL-DATA.4-01-1589.
- [113] K. Motizuki, H. Ido, T. Itoh, and M. Morifuji, *Electronic Structure and Magnetism of 3d-Transition Metal Pnictides*, Springer-Verlag Berlin Heidelberg, 2010.
- [114] W. Wu et al., Nat. Commun. **5**, 5508 (2014).
- [115] J.-G. Cheng et al., Phys. Rev. Lett. **114**, 117001 (2015).
- [116] C. Y. Guo et al., Phys. Rev. B **98**, 024520 (2018).
- [117] R. W. G. Wyckoff, *Crystal Structures*, Interscience, New York, 1963.
- [118] I. O. Chernyavskii et al., Phys. Rev. Materials **4**, 083403 (2020).

- [119] D. Bellavance, M. Vlasse, B. Morris, and A. Wold, *Journal of Solid State Chemistry* **1**, 82 (1969).
- [120] B. Westerstrandh, L. Lundgren, U. Gäfvert, and B. Carlsson, *Physica Scripta* **15**, 276 (1977).
- [121] L. Häggström and A. Narayanasamy, *Journal of Magnetism and Magnetic Materials* **30**, 249 (1982).
- [122] T. Nozue, H. Kobayashi, N. Kimura, H. Aoki, and T. Kamimura, *J. Phys. Soc. Jpn.* **70**, 192 (2001).
- [123] G. P. Felcher, F. A. Smith, D. Bellavance, and A. Wold, *Phys. Rev. B* **3**, 3046 (1971).
- [124] G. P. Felcher, *J. Appl. Phys.* **37**, 1056 (1966).
- [125] H. Watanabe, N. Kazama, Y. Yamaguchi, and M. Ohashi, *J. Appl. Phys.* **40**, 1128 (1969).
- [126] A. V. Sobolev et al., *J. Alloys Compd.* **675**, 277 (2016).
- [127] S. Rundqvist and P. Nawapong, *Acta Chem. Scandinavica* **19**, 1006 (1965).
- [128] D. S. Inosov et al., Magnon spectrum of helimagnet PtMnGa, STFC ISIS Neutron and Muon Source, 2018, doi:10.5286/ISIS.E.RB1820021.
- [129] D. S. Inosov, A. Sukhanov, Y. O. Onykienko, Y. V. Tymoshenko, and A. Cameron, Spin-wave dispersion in the itinerant helimagnet FeP. Institut Laue-Langevin (ILL), 2019, doi:10.5291/ILL-DATA.4-01-1599.
- [130] D. S. Inosov, Y. O. Onykienko, Y. V. Tymoshenko, and A. Kulbakov, Low energy spin-wave dispersion in the itinerant helimagnet FeP. Institut Laue-Langevin (ILL), 2020, doi:10.5291/ILL-DATA.4-01-1657.
- [131] A. Yaresko (private communication).
- [132] Y. Kamihara, T. Watanabe, M. Hirano, and H. Hosono, *J. Am. Chem. Soc.* **130**, 3296 (2008), PMID: 18293989.
- [133] X. H. Chen et al., *Nature* **453**, 761 (2008).
- [134] M. Rotter, M. Tegel, and D. Johrendt, *Phys. Rev. Lett.* **101**, 107006 (2008).
- [135] C. de la Cruz et al., *Nature* **453**, 899 (2008).

- [136] J. Zhao et al., Nat. Mater. **7**, 953 (2008).
- [137] J. Dai, Q. Si, J.-X. Zhu, and E. Abrahams, Proc. Natl. Acad. Sci. USA **106**, 4118 (2009).
- [138] C. Fang, H. Yao, W.-F. Tsai, J. Hu, and S. A. Kivelson, Phys. Rev. B **77**, 224509 (2008).
- [139] C. Xu, M. Müller, and S. Sachdev, Phys. Rev. B **78**, 020501 (2008).
- [140] F.-j. Ma, Z.-y. Lu, and T. Xiang, Frontiers of Physics in China **5**, 150 (2010).
- [141] E. Manousakis, J. Ren, S. Meng, and E. Kaxiras, Solid State Commun. **150**, 62 (2010).
- [142] J. Dong et al., EPL (Europhysics Letters) **83**, 27006 (2008).
- [143] T. Yildirim, Physica C: Superconductivity **469**, 425 (2009).
- [144] I. I. Mazin and M. D. Johannes, Nat. Phys. **5**, 141 (2009).
- [145] T. Kariyado and M. Ogata, J. Phys. Soc. Jpn. **78**, 043708 (2009).
- [146] M. J. Han, Q. Yin, W. E. Pickett, and S. Y. Savrasov, Phys. Rev. Lett. **102**, 107003 (2009).
- [147] S. O. Diallo et al., Phys. Rev. Lett. **102**, 187206 (2009).
- [148] J. Zhao et al., Nat. Phys. **5**, 555 (2009).

Acknowledgements

First of all, I would like to thank my supervisor, Dmytro Inosov, with whom I have been working for nearly six years. Dmitry's natural curiosity, joy for science, and optimism are very contagious. In addition to careful scientific supervision, I would like to thank him for his friendly support in the foreign country.

Sample preparation, neutron measurements, and data processing require excellent technical skills, a deep understanding of physical processes, and extensive programming experience. I am very grateful to my colleague Pavlo Portnichenko for his help in the experimental part of neutron scattering. Special thanks to Yevhen Onykienko for generously sharing his skills in programming, data analysis, and especially for his talent to explain complex things in understandable words. I also want to thank Alexandr Sukhanov for interesting discussions and new ideas. And of course, thanks to my dear officemate Alistair Cameron whose charming smile has lifted my spirits for five years in any situation!

Neutron scattering experiments require large, high-quality crystals. Therefore, special thanks go to Alois Loidl, Viorel Felea, Vladimir Tsurkan, Darren Peets, and Igor Morozov for growing the samples that allowed us to carry out our experiments.

I also thank our collaborators Joshua Cohn, Dmitri Efremov, Matthias Dörr, Sergei Zherlitsyn, and Stephan Rachel.

I express my gratitude to neutron teams at ISIS (RAL, Harwell), ILL (Grenoble), FRM-II (MLZ, Garching), and SNS (ORNL, Oak Ridge) neutron facilities, in particular to Helen Walker, David Voneshen, Alexandre Ivanov, Jacques Ollivier, Martin Boehm, Astrid Schneidewind, Peter Čermák, Jitae Park, Doug Abernathy, and all the beamline scientists for technical help and fruitful discussions. Thank you very much for welcoming us warmly and preventing us from destroying the equipment and creating complete chaos in the laboratories!

All these years I felt like a part of a large friendly team of the Institute of Solid State and Materials Physics. I really appreciate the friendship and support of all my colleagues and friends, in particular our tireless and patient secretaries, in particular Tatjana Schoffer, Elke Wachsmuth, and Kerstin Novak. It is difficult to overestimate the support of Sergey

Granovsky, who is always ready to help with technical issues, or just make a pleasant company at lunch!

I credit Dmytro Inosov for a careful proofreading of this thesis.

In science, as in any other creative work, there are moments of emotional ups and downs. I am very happy that throughout this time my beloved, close, and reliable friends have always been with me — Margarita Iakovleva, Olga Ziabkina, Ekaterina Pärschke, Cliò Agrapidis, Ziba Zangeneh-pourzdeh, Elena Dukhnitskaya, and Richard Hentrich.

A very special thank you to my boyfriend Yevhen for the warmth and support. A heartfelt thanks to my beloved cat Ozzy who put his furry paws on the typing of this thesis!

And of course, the biggest thanks go to my parents Svetlana and Victor for always loving, believing in me, supporting me, and giving me a good education.

Versicherung

Hiermit versichere ich, dass ich die vorliegende Arbeit ohne unzulässige Hilfe Dritter und ohne Benutzung anderer als der angegebenen Hilfsmittel angefertigt habe; die aus fremden Quellen direkt oder indirekt übernommenen Gedanken sind als solche kenntlich gemacht. Die Arbeit wurde bisher weder im Inland noch im Ausland in gleicher oder ähnlicher Form einer anderen Prüfungsbehörde vorgelegt. Bis zum jetzigen Zeitpunkt habe ich keinerlei erfolglose Promotionsverfahren absolviert.

Die vorliegende Dissertation wurde am Institut für Festkörper- und Materialphysik der Fakultät Physik der Technischen Universität Dresden unter Leitung von Prof. Dr. Dmytro S. Inosov angefertigt.

Ich erkenne hiermit die Promotionsordnung der Fakultät Physik der Technischen Universität Dresden vom 23.02.2011 an.

(Ort, Datum)

(Unterschrift)